EXPERIMENTAL INVESTIGATIONS ON SMALL-STRAIN STIFFNESS PROPERTIES OF PARTIALLY SATURATED SOILS VIA RESONANT COLUMN AND BENDER ELEMENT TESTING

by

PHAYAK TAKKABUTR

Presented to the Faculty of the Graduate School of

The University of Texas at Arlington in Partial Fulfillment

of the Requirements

for the Degree of

DOCTOR OF PHILOSOPHY

THE UNIVERSITY OF TEXAS AT ARLINGTON

August 2006

ACKNOWLEDGMENTS

The author would like to thank his supervising professor, Dr. Laureano R. Hoyos, for all his guidance and unconditional support throughout the course of this research effort.

Thanks are also extended to the other members of his thesis committee, Drs. Anand Puppala, Syed Qasim, Ali Abolmaali, and Danny Dyer, for their valuable advice and review of this manuscript. In addition, the author would like to thank the faculty and staff of the Department of Civil and Environmental Engineering at The University of Texas at Arlington for their valuable assistance during his graduate studies.

The author also would like to thank all the geotechnical engineering graduate students in this institution for all their help and support. Special thanks are also extended to the Thai group and the India group for their worthy friendship and the good times.

Finally, and most of all, the author would like to thank his parents and his sisters for all their love, encouragement, and great support. It is the best thing in his life to be a part of their family.

July 21, 2006

ABSTRACT

EXPERIMENTAL INVESTIGATIONS ON SMALL-STRAIN STIFFNESS PROPERTIES OF PARTIALLY SATURATED SOILS VIA RESONANT COLUMN AND BENDER ELEMENT TESTING

Publication No._________

Phayak Takkabutr, Ph.D.

The University of Texas at Arlington, 2006

Supervising Professor: Laureano R. Hoyos

A comprehensive series of resonant column (ASTM D 2325-68), bender element (ASTM C 778), pressure plate (ASTM D 4015-92), and filter paper (ASTM D 5298) tests were conducted on compacted specimens of poorly graded sand (SP) and high plasticity clay (CH) in order to assess the influence of key environmental factors, namely compaction-induced matric suction and K_o stress state, on small-strain stiffness properties of partially saturated soils. Compaction-induced matric suction in all test specimens was estimated via soil-water characteristic curves (SWCC) for each type of soil.

The research work was accomplished in six broad stages. During *Stage I*, a modified pressure plate extractor device was developed for assessing SWCC under anisotropic stress sates. Results from a series of SWCC tests on SP and CH

specimens were used to assess the Fredlund and Xing's SWCC model parameters for each type of soil.

During *Stage II*, resonant column (RC) tests were conducted on SP and CH specimens, at different compaction-induced suctions and isotropic confinements, in order to devise correlations between small-strain stiffness properties, i.e. shear modulus (G_{max}) and material damping (D_{min}), and matric suction (ψ).

During *Stage III*, bender element (BE) tests were conducted on SP and CH specimens for the same experimental variables as in *Stage II*. Results were used to investigate the influence of suction on bender element performance as compared to resonant column testing.

During *Stage IV*, bender element (BE) tests were conducted on SP and CH specimens at different compaction-induced suctions and K_o stress states. Results were used to devise a correction factor for RC results, on the basis of initial compaction-induced suction, for any given K_o stress condition.

During *Stage V*, a series of RC and BE tests were conducted on SP and CH specimens using a resonant column device with self-contained bender elements. Results were used to further substantiate the experimental findings and correlations devised in *Stages II*, *III* and *IV*.

Finally, during *Stage VI*, bender element tests were conducted on SP and CH specimens sheared at different vertical strain levels in order to assess the influence of vertical strain level on suction loss and menisci regeneration patterns.

TABLE OF CONTENTS

ACKNOWLEDGMENTS iii

ABSTRACT iv

LIST OF FIGURES xii

LIST OF TABLES xxii

Chapter

1. INTRODUCTION 1
   - 1.1 Background and Importance 1
   - 1.2 Objective and Scope 5
   - 1.3 Organization 8

2. LITERATURE REVIEW 10
   - 2.1 Introduction 10
   - 2.2 Significance of Shear Modulus as Material Property 10
   - 2.3 Nonlinear Soil Behavior 15
   - 2.4 Methods to Measure Shear Modulus 18
     - 2.4.1 Direct Field Methods 19
       - 2.4.1.1 Seismic Reflection Method 19
       - 2.4.1.2 Seismic Refraction Method 20
       - 2.4.1.3 Seismic Cross-Hole Shear Wave Test 21
       - 2.4.1.4 Seismic Downhole/Uphole Method 22
       - 2.4.1.5 Spectral Analysis Wave Technique (SASW) 23
       - 2.4.1.6 Seismic Flat Dilatometer Test 23

2.4.1.7 Suspension Logger Method 24
2.4.2 Indirect Field Methods 24
2.4.2.1 In Situ Measurements 24
2.4.2.2 Hardin's Empirical Equation 25
2.4.3 Laboratory Methods 26
2.4.3.1 Cyclic Triaxial Test 26
2.4.3.2 Resonant Column Test 28
2.4.3.3 Bender Element Test 29
2.5 Advantages of Laboratory Methods Over Field Methods 29
2.6 Fundamentals of Unsaturated Soil Mechanics 30
2.6.1 Properties of Unsaturated Soils 32
2.6.1.1 Unsaturated Soil Profile 32
2.6.1.2 Capillarity 33
2.6.1.3 Soil Suction 35
2.6.1.4 Soil Water Characteristic Curve 38
2.6.2 Measurement of Total Suction 44
2.6.2.1 Psychrometer (Direct Measurement) 44
2.6.2.2 Filter Paper (Indirect Measurement) 45
2.6.3 Measurement of Matric Suction 46
2.6.3.1 Direct Measurement Methods 47
2.6.3.2 Indirect Measurement Methods 49
2.7 Review Previous Studies 50
3. FUNDAMENTALS OF RESONANT COLUMN, BENDER ELEMENT, PRESSURE PLATE, AND FILTER PAPER TESTING TECHNIQUES 57
3.1 Introduction 57

3.2 RC Testing 58

3.2.1 Basic RC Test Configuration 58

3.2.2 Shear Modulus (G) 60

3.2.3 Material Damping Ratio (D) 62

3.2.4 Shearing Strain (γ) 64

3.2.5 Resilient Modulus (M_r) 65

3.2.6 Basic Components of RC Testing Device 66

3.2.6.1 Confining Chamber 66

3.2.6.2 Torsional Drive Mechanism 67

3.2.6.3 Torsional Motion Monitoring System 69

3.2.7 Frequency Response Measurement System.......................... 69

3.2.8 Apparatus Assembly 71

3.3 BE Testing 77

3.3.1 Introduction 77

3.3.2 Advantages of Bender Elements
over Other Laboratory Methods.. 78

3.3.3 Working Mechanism 80

3.3.4 Equipment Details 81

3.3.5 Near-field Effects 84

3.3.6 Time of Flight 85

3.3.6.1 Travel Time of First Direct
Arrival in the Output Signals 85

3.3.6.2 Travel Time between Characteristic
Peaks off Input and Output Signals 86

3.3.6.3 Travel Time by Cross-Correlation
of Input to Output Signals 86

3.3.6.4 Travel Time Using the Second
Arrival in the Output Signals 87

3.3.7 Small Strain Shear Modulus
Measurements Using Bender Element 89
3.3.8 Damping Ratio Measurements
Using Bender Element 94
3.3.8.1 Half-Power Method 94
3.3.8.2 Circle-Fit Method 96
3.3.9 Basic Components of BE Testing Device 98
3.3.10 Apparatus Assembly 102
3.4 RC/BE Testing in RC Chamber 105
3.5 PPE Testing with Radial Confinement 112
3.5.1 Introduction 112
3.5.2 Conventional PPE Device 112
3.5.3 Modified PPE Device 115
3.6 FP Testing 120
4. EXPERIMENTAL VARIABLES AND PROCEDURES 122
4.1 Introduction 122
4.2 Properties of Testing Soil 123
4.2.1 Clay 123
4.2.2 Sand 124
4.3 Experimental Variables 126
4.4 Standard Proctor Compaction Curves 130
4.5 Specimen Preparation Method 131
4.5.1 RC, BE, and RC/BE Specimen Preparation 131
4.5.2 Saturation of Ceramic Plate and PPE
Specimen Preparation 132
4.6 Filter Paper Testing Measurement 136
5. EXPERIMENTAL PROGRAM AND TEST RESULTS 142

5.1 Introduction 142
5.2 Specimen Notation 142
5.3 Experimental Program and Procedure 144
5.4 SWCCs from Modified PPE 146
5.4.1 Controlled Radial Confinement Condition 146
5.4.1.1 SWCC for Sand 146
5.4.1.2 SWCC for Clay 147
5.4.2 Constant K_0 Stress State Condition 148
5.4.2.1 SWCC for Sand 148
5.4.2.2. SWCC for Clay 149
5.4.3 Variable K_0 Stress State Condition 150
5.4.3.1 SWCC for Sand 150
5.4.3.2. SWCC for Clay 151
5.5 RC Response 152
5.5.1 Typical RC Test Result 152
5.5.2 Sand 153
5.5.3 Clay 161
5.6 BE Response 168
5.6.1 Typical BE Test Result 168
5.6.2 Isotropic Condition 169
5.6.2.1 Sand 169
5.6.2.2 Clay 177
5.6.3 K_0 Stress State Condition 184
5.6.3.1 Sand 184
5.6.3.2 Clay 192

5.7 RC/BE Response 199
5.7.1 Sand 199
5.7.2 Clay 214
5.8 Assessment of Vertical Strain-Induced Suction Loss and Menisci Regeneration Patterns 228
5.8.1 Sand 228
5.8.2 Clay 236
5.9 Summary 243
6. EMPIRICAL MODELS FOR SMALL-STRAIN STIFFNESS PROPERTIES 244
6.1 Introduction 244
6.2 Soil-Water Characteristic Curve 244
6.3 Soil-Water Characteristic Curve Models 246
6.4 SWCC Results and Models 247
6.5 Empirical Models for Shear Modulus and Damping Ratio 252
6.5.1 Isotropic Condition 253
6.5.2 Comparison of RC and BE Testing 259
6.5.3 K_0 Stress State Condition 264
6.5.4 Correction Factor for Any K_0 268
6.6 Summary 274
7. SUMMARY, CONCLUSIONS, AND RECOMMENDATIONS 275
7.1 Summary 275
7.2 Main Conclusions 276
7.3 Recommendations for Future Work 280
REFERENCES 281
BIOGRAPHICAL INFORMATION 289

LIST OF FIGURES

Figures Page

1.1 Idealization of Unsaturated Soil under Non-static Loading 2

1.2 Experimental Program and Modeling Flow Chart 7

2.1 Variation of Shear Stress versus Shear Strain 11

2.2 Variation of Soil Stiffness with Shear Strain 14

2.3 Loading-Unloading at Different Strain Amplitudes 16

2.4 Secant Modulus and Material Damping Ratio as Function of Maximum Strain 17

2.5 Seismic Reflection Method 19

2.6 Seismic Refraction Method 20

2.7 Seismic Cross-Hole Shear Wave Test 21

2.8 Seismic Down-Hole Method 22

2.9 Unsaturated Soil Profile 32

2.10 Water in a Capillary Tube 34

2.11 Typical Suction Profiles below an Uncovered Ground Surface: (a) Seasonal Fluctuation; (b) Drying Influence on Shallow Water Condition; (c) Drying Influence on Deep Water Table Condition 37

2.12 Total, Matric, and Osmotic Suction Measurement on Compacted Regina Clay 39

2.13 Possible Water Saturation Stages 40

2.14 External and Internal C-52 Sample Chamber 45

2.15 Wescor Dew Point Microvoltmeter (HR 33T) for Psychrometer Test 45

2.16 Contact and Noncontact Filter Paper Method for Measuring Matric and Total Suction 46

2.17 The BAT-Piezometer 48

2.18 Schematic of a Null Type Pressure Plate 49

2.19 Variation of Shear Modulus and Mean Net Stress 52

2.20 (a) Schematic Cell Design; (b) Experimental Setup 53

2.21 Shear-Wave Velocity versus Degree of Saturation for Different Materials: (a) Clean Glass Beads (Deionized Water); (b) Mixture of Kaolinite and Glass Beads; (c) Granite Powder; (d) Sandboil Sand 54

3.1 Idealization of a Fixed-free RC Device 58

3.2 Typical Frequency Response Curve from a RC Test 59

3.3 Bandwidth Method for Determination of Material Damping Ratio, D 63

3.4 Concept of Shearing Strain (γ) for Hollow Soil Column under Torsion 64

3.5 Base Plate and Fully Assembled Confining Chamber 66

3.6 Base Pedestal Tightly Secured onto Base Plate 67

3.7 Top and Side Views of the Torsional Drive Mechanism (Driver) 68

3.8 Cylindrical Cage Supporting Set of Drive Coils 68

3.9 SR785 Dynamic Signal Analyzer and 4102 Charge Amplifier Box 69

3.10 Dynamic Analyzer and Charge Amplifier Interacting with RC Device 70

3.11 Specimen with Membrane and O-rings Resting on Base Pedestal 71

3.12 Inner Water-Bath Acrylic Cylinder Fitted into the Base Pedestal 72

3.13 Application of Water Bath between Acrylic Cylinder and Soil Specimen 72

3.14 Stainless Steel Cylindrical Cage Attached to Base Plate 73

3.15 Assembling of Torsional Drive Mechanism (Driver) 73

3.16 Application of Isotropic Confining Air-Pressure From HM-4150 Panel 74

3.17 Pre-setting of the SR785 Dynamic Signal Analyzer prior to RC Testing 75

3.18 Analyzer, Amplifier and Panel Interacting with RC Device 75

3.19 Dynamic Analyzer Interacting with PC-Based Computer Terminal 76

3.20 Typical Set of Transmitter and Receiver Bender Elements 77

3.21 Schematic Representation of Principle of Bender Elements 80

3.22 Series and Parallel Connected Piezoceramic Bender Elements 83

3.23 Schematic of Piezoceramic (a) Single Sheet and (b) Double Sheet “Bender Element” 91

3.24 Typical Transmitted and Received Signals from Monitor 93

3.25 Typical Amplitude Measurement from BE Test 95

3.26 Typical Resonant Curve with Variables for Half-Power Method 96

3.27 Nyquist Plot Used in the Circle-Fit Method 97

3.28 Triaxial and Bender Element Setup 98

3.29 Arbitrary Waveform Generator and Receiving Signal Converter 99

3.30 Bender Element on the Triaxial Cell Base 100

3.31 Triaxial Pressure Cell with Bender Element 101
3.32 Chiseled Sample Surfaces 102
3.33 Specimen with Membrane and O-rings Resting on Base Pedestal 103
3.34 Triaxial Chamber Filled up with Water 104
3.35 Couple Bender Elements for RC/BE Testing 105
3.36 Sealed 50 Psi Bulkhead Connectors 106
3.37 RC/BE Device Setup 106
3.38 Chiseled Sample Surfaces for RC/BE Test 107
3.39 Base Pedestal with Bender Element 108
3.40 Specimen and O-rings Resting on Base Pedestal 108
3.41 Torsional Driver over Cylindrical Cage 109
3.42 Wires and Connections in Confining Chamber 110
3.43 Top View of RC/BE Chamber 110
3.44 Resonant Column with Bender Element Setup 111
3.45 Typical SWCC for Silt with Suction Parameters 113
3.46 Model 1500 15-Bar PPE Device: (a) Sample Retaining Rings, (b) Sealed Vessel 114
3.47 Modified 15-Bar PPE Device: (a) Confining Ring, (b) Assembled Ring, (c) Ring Inside PPE Vessel, (d) Sealed Vessel 116
3.48 SWCC Testing: (a) Air Pressure Application, (b) Radial Confinement Application 117
3.49 SWCCs Measurement from Conventional and Modified PPE Devices 118
3.50 The Repeatability of SWCCs from Modified PPE 118
3.51 Schematic of Modified PPE Device Setup 119
3.52 The Schleicher & Schuell No. 589-WH Filter Paper 120

3.53 Filter Paper Wetting Calibration Curve 121

4.1 Grain Size Distribution for Clay 124

4.2 Grain Size Distribution for Sand 125

4.3 Schematic of PPE under Controlled Radial Confinement Condition 127

4.4 Schematic of PPE under Constant K_0 Stress State and Variable K_0 Stress State Condition 127

4.5 Piece of Heavy Steel Resting of Top of Porous Stone 128

4.6 Standard Proctor Compaction Curves for Clay and Sand 130

4.7 Split Miter Box with Clamps Used for Compaction 131

4.8 Compaction of Specimen Using U.S. Army Corps Hammer 132

4.9 Clayey Specimen Compaction Tools for PPE Testing 133

4.10 Compaction of Clayey Specimen for PPE Testing 134

4.11 Compacted Clayey Specimen for PPE Testing 134

4.12 Confining Ring Seated on the Ceramic Plate 135

4.13 Tamping Compaction for Sand 135

4.14 A Full Soaking Arrangement with Stainless Steel Setup 136

4.15 Two Halves Soil Specimens with Filter Paper Apparatus 137

4.16 Schleicher & Schuell No. 589-WH Filter Paper in Between Two Larger Protective Filter Papers 137

4.17 Two Pieces of Soil Samples Taped Together 138

4.18 Soil Specimen in Glass Jar with Rolled Stainless Steel Net on Top 139

4.19 Filter Paper Resting on Top of Rolled Stainless Steel Net Using Tweezers 139

4.20 Glass Jar Secured Tightly with Lid 140

4.21 Filter Paper Removed from Glass Jar Using Tweezers 140

4.22 A Tin with Wet Filter Paper inside Small Scale Balance 141

5.1 SWCC at Different Net Radial Confinement under Controlled Radial Confinement for Sand 146

5.2 SWCC at Different Net Radial Confinement under Controlled Radial Confinement for Clay 147

5.3 SWCC at Different K_0 under Constant K_0 Condition for Sand 148

5.4 SWCC at Different K_0 under Constant K_0 Condition for Clay 149

5.5 SWCC at Different Initial K_0 Stress State under Variable Suction Dependent K_0 Condition for Sand 150

5.6 SWCC at Different Initial K_0 Stress State under Variable Suction Dependent K_0 Condition for Clay 151

5.7 Typical Response at Low-Amplitude Shearing Strain Level 152

5.8 Variation of Average Shear Modulus with Confinement for Sand (RC) 160

5.9 Variation of Average Damping Ratio with Confinement for Sand (RC) 160

5.10 Variation of Average Shear Modulus with Confinement for Clay (RC) 167

5.11 Variation of Average Damping Ratio with Confinement for Clay (RC) 167

5.12 Typical BE Test Result for Shear Modulus Determination 168

5.13 Typical BE Test Result for Damping Ratio Determination 168

5.14 Variation of Average Shear Modulus with

Confinement for Sand (TX/BE) 176

5.15 Variation of Average Damping Ratio with Confinement for Sand (TX/BE) 176

5.16 Variation of Average Shear Modulus with Confinement for Clay (TX/BE) 183

5.17 Variation of Average Damping Ratio with Confinement for Clay (TX/BE) 183

5.18 Variation of Average Shear Modulus with K_0 Stress State for Sand (TX/BE) 191

5.19 Variation of Average Damping Ratio with K_0 Stress State for Sand (TX/BE) 191

5.20 Variation of Average Shear Modulus with K_0 Stress State for Clay (TX/BE) 198

5.21 Variation of Average Damping Ratio with K_0 Stress State for Clay (TX/BE) 198

5.22 Variation of Shear Modulus with Confinement For Sand w=0% (RC/BE) 206

5.23 Variation of Damping Ratio with Confinement For Sand w=0% (RC/BE) 206

5.24 Variation of Shear Modulus with Confinement For Sand w=5% (RC/BE) 207

5.25 Variation of Damping Ratio with Confinement For Sand w=5% (RC/BE) 207

5.26 Variation of Shear Modulus with Confinement For Sand w=10% (RC&BE) 208

5.27 Variation of Damping Ratio with Confinement For Sand w=10% (RC/BE) 208

5.28 Variation of Shear Modulus with Confinement For Sand w=15% (RC/BE) 209

5.29 Variation of Damping Ratio with Confinement For Sand w=15% (RC/BE) 209

5.30 Variation of Shear Modulus with Confinement For Sand w=20% (RC/BE) 210

5.31 Variation of Damping Ratio with Confinement

For Sand w=20% (RC/BE) 210

5.32 Variation of Shear Modulus with Confinement
For Sand w=24% (RC/BE) 211

5.33 Variation of Damping Ratio with Confinement
For Sand w=24% (RC/BE) 211

5.34 Variation of G with Confinement Using RC
Method for Sand (RC/BE) 212

5.35 Variation of G with Confinement Using BE
Method for Sand (RC/BE) 212

5.36 Variation of D with Confinement Using RC
Method for Sand (RC/BE) 213

5.37 Variation of D with Confinement Using BE
Method for Sand (RC/BE) 213

5.38 Variation of Shear Modulus with Confinement
For Clay w=13% (RC/BE) 220

5.39 Variation of Damping Ratio with Confinement
For Clay w=13% (RC/BE) 220

5.40 Variation of Shear Modulus with Confinement
For Clay w=17% (RC/BE) 221

5.41 Variation of Damping Ratio with Confinement
For Clay w=17% (RC/BE) 221

5.42 Variation of Shear Modulus with Confinement
For Clay w=20% (RC/BE) 222

5.43 Variation of Damping Ratio with Confinement
For Clay w=20% (RC/BE) 222

5.44 Variation of Shear Modulus with Confinement
For Clay w=23% (RC/BE) 223

5.45 Variation of Damping Ratio with Confinement
For Clay w=23% (RC/BE) 223

5.46 Variation of Shear Modulus with Confinement
For Clay w=27% (RC/BE) 224

5.47 Variation of Damping Ratio with Confinement
For Clay w=27% (RC/BE) 224

5.48 Variation of G with Confinement Using RC

Method for Clay (RC/BE) 225

5.49 Variation of G with Confinement Using BE Method for Clay (RC/BE) 225

5.50 Variation of D with Confinement Using RC Method for Clay (RC/BE) 226

5.51 Variation of D with Confinement Using BE Method for Clay (RC/BE) 226

5.52 Variation of Shear Modulus from RC and TX/BE 227

5.53 Variation of Shear Modulus of RC and BE from RC/BE 227

5.54 Time Variation in Shear Modulus of Sand at Different Vertical Strain Levels 235

5.55 Time Variation in Shear Modulus of Clay at Different Vertical Strain Levels 242

6.1 Typical SWCC for Silt with Adsorption And Desorption Curves 245

6.2 Typical SWCC for Sandy, Silty, and Clayey Soil 245

6.3 Experimental and Predicted SWCC for Sand 249

6.4 Experimental and Predicted SWCC for Clay 250

6.5 SWCC Model for Sand and Clay 251

6.6 Normalized G by Confinement with Matric Suction for Sand (RC) 254

6.7 Normalized G by Confinement with Matric Suction for Sand (TX/BE) 254

6.8 Normalized G by Confinement with Matric Suction for Clay (RC) 255

6.9 Normalized G by Confinement with Matric Suction for Clay (TX/BE) 255

6.10 Normalized D by Confinement with Matric Suction for Sand (RC) 257

6.11 Normalized D by Confinement with Matric Suction for Sand (TX/BE) 257

6.12 Normalized D by Confinement with Matric Suction for Clay (RC) 258

6.13 Normalized D by Confinement with Matric Suction for Clay (TX/BE) 258

6.14 The Variation of G_{RC} and G_{BE} for Sand and Clay 262

6.15 The Variation of D_{RC} and D_{BE} for Sand and Clay 262

6.16 The Variation of G_{RC} and $G_{BE\ Corrected}$ for Sand and Clay 263

6.17 The Variation of D_{RC} and $D_{BE\ Corrected}$ for Sand and Clay 263

6.18 Variation of Shear Modulus with K_0 Stress State for Sand (TX/BE) 265

6.19 Variation of Shear Modulus with K_0 Stress State for Clay (TX/BE) 265

6.20 Variation of Damping Ratio with K_0 Stress State for Sand (BE) 267

6.21 Variation of Damping Ratio with K_0 Stress State for Clay (TX/BE) 267

6.22 Variation of $G_{Ko}/G_{Ko=1}$ with K_0 Stress State For Sand (TX/BE) 271

6.23 Variation of $G_{Ko}/G_{Ko=1}$ with K_0 Stress State For Clay (TX/BE) 271

6.24 Variation of $D_{Ko}/D_{Ko=1}$ with K_0 Stress State For Sand (TX/BE) 272

6.25 Variation of $D_{Ko}/D_{Ko=1}$ with K_0 Stress State For Clay (TX/BE) 272

6.26 Comparisons between Shear Modulus from Experiment and Model 273

6.27 Comparisons between Damping Ratio from Experiment and Model 273

LIST OF TABLES

Tables Page

2.1 Existing Models from Previous Studies 55

4.1 Basic Engineering Properties of Testing Clay 123

4.2 Basic Engineering Properties of Testing Sand 125

4.3 Experimental Variable Used for RC, BE, RC/BE, and PPE Testing 129

5.1 Notation Symbols Used for Identification of all Test Specimens 143

5.2 Dry Unit Weight and Compaction Moisture Contents 144

5.3 RC Test Results of Sand at w = 0% 154

5.4 RC Test Results of Sand at w = 5% 155

5.5 RC Test Results of Sand at w = 10% 156

5.6 RC Test Results of Sand at w = 15% 157

5.7 RC Test Results of Sand at w = 20% 158

5.8 RC Test Results of Sand at w = 24% 159

5.9 RC Test Results of Clay at w = 13% 162

5.10 RC Test Results of Clay at w = 17% 163

5.11 RC Test Results of Clay at w = 20% 164

5.12 RC Test Results of Clay at w = 23% 165

5.13 RC Test Results of Clay at w = 27% 166

5.14 BE Test Results of Sand at w = 0% 170

5.15 BE Test Results of Sand at w = 5% 171

5.16 BE Test Results of Sand at w = 10% 172

5.17 BE Test Results of Sand at w = 15% 173

5.18 BE Test Results of Sand at w = 20% 174

5.19 BE Test Results of Sand at w = 24% 175

5.20 BE Test Results of Clay at w = 13% 178

5.21 BE Test Results of Clay at w = 17% 179

5.22 BE Test Results of Clay at w = 20% 180

5.23 BE Test Results of Clay at w = 23% 181

5.24 BE Test Results of Clay at w = 27% 182

5.25 BE Test Result of Sand under K_0 Stress State at w = 0% 185

5.26 BE Test Result of Sand under K_0 Stress State at w = 5% 186

5.27 BE Test Result of Sand under K_0 Stress State at w = 10% 187

5.28 BE Test Result of Sand under K_0 Stress State at w = 15% 188

5.29 BE Test Result of Sand under K_0 Stress State at w = 20% 189

5.30 BE Test Result of Sand under K_0 Stress State at w = 24% 190

5.31 BE Test Result of Clay under K_0 Stress State at w = 13% 193

5.32 BE Test Result of Clay under K_0 Stress State at w = 17% 194

5.33 BE Test Result of Clay under K_0 Stress State at w = 20% 195

5.34 BE Test Result of Clay under K_0 Stress State at w = 23% 196

5.35 BE Test Result of Clay under K_0 Stress State at w = 27% 197
5.36 RC/BE Test Results of Sand at w = 0% 200
5.37 RC/BE Test Results of Sand at w = 5% 201
5.38 RC/BE Test Results of Sand at w = 10% 202
5.39 RC/BE Test Results of Sand at w = 15% 203
5.40 RC/BE Test Results of Sand at w = 20% 204
5.41 RC/BE Test Results of Sand at w = 24% 205
5.42 RC/BE Test Results of Clay at w = 13% 215
5.43 RC/BE Test Results of Clay at w = 17% 216
5.44 RC/BE Test Results of Clay at w = 20% 217
5.45 RC/BE Test Results of Clay at w = 23% 218
5.46 RC/BE Test Results of Clay at w = 27% 219
5.47 Strain-dependent BE Results of Sand at w = 0% 229
5.48 Strain-dependent BE Results of Sand at w = 5% 230
5.49 Strain-dependent BE Results of Sand at w = 10% 231
5.50 Strain-dependent BE Results of Sand at w = 15% 232
5.51 Strain-dependent BE Results of Sand at w = 20% 233
5.52 Strain-dependent BE Results of Sand at w = 24% 234
5.53 Strain-dependent BE Results of Clay at w = 13% 237
5.54 Strain-dependent BE Results of Clay at w = 17% 238
5.55 Strain-dependent BE Results of Clay at w = 20% 239
5.56 Strain-dependent BE Results of Clay at w = 23% 240
5.57 Strain-dependent BE Results of Clay at w = 27% 241
6.1 Soil-Water Characteristic Curve Best-Fit Parameters 248
6.2 Predicted Values of Matric Suction from Moisture Content 248

6.3 Constant Values for Prediction Model of Shear Modulus 253

6.4 Constant Values for Prediction Model of Damping Ratio 256

6.5 Constant Values of BE Correction Factor for Shear Modulus 260

6.6 Constant Values of BE Correction Factor for Damping Ratio 261

6.7 Constant Values for Prediction Model of Shear Modulus under K_0 Stress State 264

6.8 Constant Values for Prediction Model of Damping Ratio under K_0 Stress State 266

6.9 Constant Values for Prediction Model of Shear Modulus (K_0=1) 269

6.10 Constant Values of Correction Factor for Shear Modulus 269

6.11 Constant Values for Prediction Model of Damping Ratio (K_0=1) 270

6.12 Constant Values of Correction Factor for Damping Ratio 270

CHAPTER 1

INTRODUCTION

1.1 Background and Importance

In every state of the country, civil engineers face problems with road and railway embankments, riverbanks, earthdams, and shallow foundation materials that remain under partially saturated conditions throughout any given year. The lack of education and training among engineering graduates and practitioners to properly deal with unsaturated soil conditions has resulted in faulty or excessively conservative designs, construction delays, and deficient long-term performance of built infrastructure. Recently, the unsaturated soil mechanics discipline begun to receive increasing attention nationwide, providing better explanations for soil behavioral patterns than conventional saturated soil mechanics.

In the United States, various research efforts have been focused on field and laboratory measurements of soil suction, assessment of soil-water characteristic curve (SWCC), and analyses of swell-collapse behavior. However, very few efforts have been focused on small-strain response of unsaturated soils and their dynamic characterization at small strains. The critical role of soil stiffness at small strains in the design and analysis of geotechnical infrastructure (earthdams, embankments, foundations) is now widely accepted. As most soils involved in these structures are unsaturated and the real strains are small, there is a great need for a better understanding of the small-strain behavior of such soils. The present research work is partly motivated by these research needs.

In the unsaturated soil practice, a thorough understanding of the effects of season-dependent matric suction on small-strain stiffness properties of unsaturated soils, i.e., shear wave velocity (V_s), small-strain shear modulus (G_{max}), and material damping (D_{min}), is of critical importance. These are key subsoil parameters for an adequate design or analysis of unsaturated earth structures subject to non-static loading (Fig. 1.1). As the static/dynamic responses of unsaturated soils are known to largely depend on suction state, the lack of incorporation of suction effects in dynamic characterization of unsaturated soils may lead to erroneous property measurements and, ultimately, as stated earlier, faulty or excessively conservative designs of earth structures.

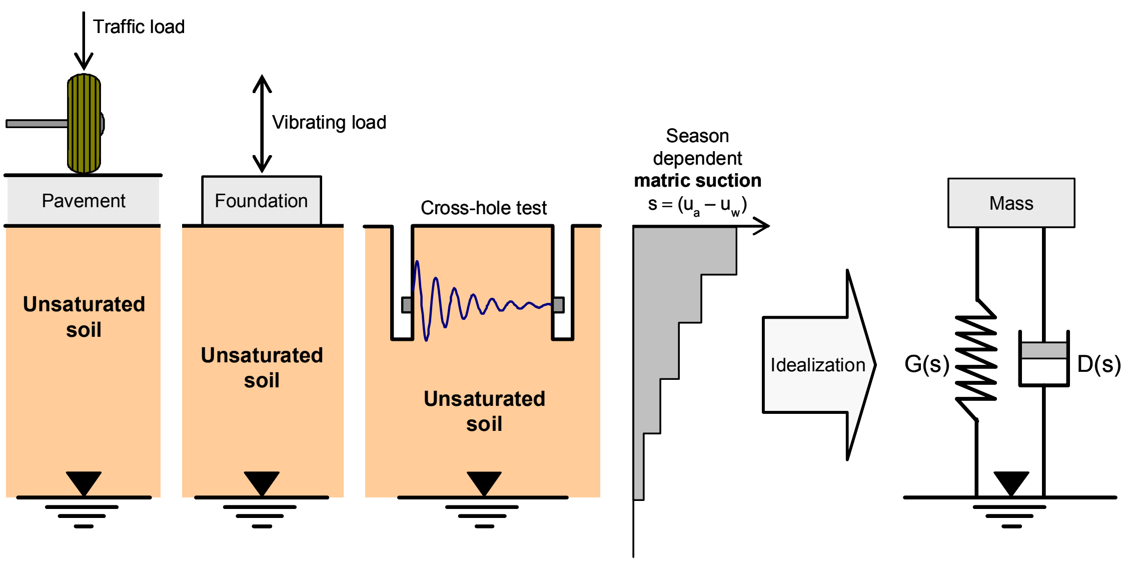

Figure 1.1 Idealization of Unsaturated Soil under Non-static Loading

Conventional geotechnical testing techniques cannot capture this small-strain behavior and, hence, vastly underestimate the true soil stiffness, mainly due to errors in small strain measurements. Bender element based techniques provide a viable way to investigate soil stiffness at very small strains, and they are starting to be used more widely for saturated soils. However, to date very limited use of bender element testing technique has been reported for unsaturated soils, and the results are very far from conclusive. There is, therefore, a great need for assessing the feasibility of bender element based techniques for unsaturated soils as compared to more reliable, fully standardized laboratory procedures such as simple shear and resonant column based methods. The present research work is also motivated in part by these research needs.

In the last four decades, the description of the stress-strain-strength behavior of unsaturated soils was closely linked with efforts to isolate the relevant effective stress fields governing unsaturated soil's mechanical response. Adopting matric suction, $(u_a - u_w)$, and the excess of total stress over air pressure, $(\sigma - u_a)$, as relevant stress state variables, various features of unsaturated soil behavior have been modeled via suction-controlled oedometer, triaxial, and direct shear tests using the axis-translation technique (Fredlund and Morgenstern 1977, Alonso et al. 1987, Toll 1990, Alonso et al. 1990, Wheeler and Sivakumar 1992, Fredlund and Rahardjo 1993).

During this same period, however, several semi-empirical procedures have been developed for estimating engineering properties of unsaturated soils using the soil-water characteristic curve (SWCC) as a predicting tool, which considerably reduces the time required in testing unsaturated soil behavior. There is a great potential to extend our present understanding of SWCC behavior to other critical geotechnical applications, such as the design of pavements and the analysis of shallow machine foundations, via small-strain stiffness parameters (Fig. 1.1).

The SWCC has become a readily available experimental means for estimating key engineering properties of unsaturated soils for a wide range of suction states, including hydraulic conductivity, volume change behavior, and shear strength parameters. Numerous laboratory techniques have been developed for accurately assessing the SWCC of unsaturated soils, from filter paper technique to the more sophisticated pressure plate extractor devices. However, the majority of these techniques and devices allow for the testing of unsaturated soils only under unknown or zero-confinement conditions, resulting in SWCC data that do not correspond to realistic in-situ stress states in the unsaturated soil mass; moreover, recent advances in SWCC testing using oedometer and triaxial setups may prove costly and very time consuming. In the present research work, an attempt has been made to develop a modified pressure plate extractor (MPPE) device for assessing the SWCC of unsaturated soils under anisotropic stress sates.

Results from the comprehensive series of pressure plate, filter paper, resonant column, and bender element tests undertaken in this research work have been used to devise empirical correlations between small-strain stiffness properties, such as shear modulus and material damping, and key environmental factors, such as compaction-induced matric suction and K_o stress state, for compacted sandy and clayey soils. The range of the experimental variables selected in this work, as well as the scope of the experimental program, has been intended to reproduce in situ stress states at different locations within a pavement or shallow foundation system that remains under partially saturated conditions throughout any given year.

The recent focus of the Departments of Transportation in the U.S. has been towards proposing pavement design procedures based on a mechanistic-empirical approach using resilient modulus as the primary soil parameter. However, a more rational procedure should be based on a thorough understanding of the effects of season-dependent matric suction (i.e., seasonal variations that include wet-dry and freeze-thaw cycles) on the small-strain stiffness properties of unsaturated soils. The present work is an attempt to contribute towards this goal.

1.2 Objective and Scope

The main objective of the present research work was to experimentally investigate the influence of key environmental factors, namely compaction moisture content, compaction-induced matric suction, confining pressure, and K_0 stress state, on small-strain stiffness properties of partially saturated soils using pressure plate, resonant column, and bender element testing techniques.

In order to accomplish this goal, a comprehensive series of resonant column (ASTM D 2325-68), bender element (ASTM C 778), pressure plate (ASTM D 4015-92), and filter paper (ASTM D 5298) tests were conducted on compacted specimens of poorly graded sand (SP) and high plasticity clay (CH) prepared at different compaction-induced matric suctions and subjected to different K_o stress states during testing. Compaction-induced matric suction in all test specimens was estimated prior to testing via a set of previously calibrated soil-water characteristic curves (SWCC) for each type of soil.

The research work was accomplished in six broad stages. During *Stage I*, a modified pressure plate extractor device was developed for assessing SWCC under anisotropic stress sates. Results from a series of SWCC tests on SP and CH specimens were used to assess the Fredlund and Xing's (1994) SWCC model parameters for each type of soil.

During *Stage II*, a comprehensive series of resonant column (RC) tests were conducted on SP and CH soil specimens, at different compaction-induced suctions and isotropic confinements, in order to devise correlations between small-strain stiffness properties, shear modulus (G_{max}) and material damping (D_{min}), and matric suction (ψ).

During *Stage III*, a comprehensive series of bender element (BE) tests were conducted on SP and CH soil specimens for the same experimental variables as in *Stage II*. Results were used to investigate the influence of suction on bender element performance as compared to resonant column testing. A correction factor for BE test results, on the basis of initial matric suction, was devised

During *Stage IV*, a comprehensive series of bender element (BE) tests were conducted on SP and CH soil specimens at different compaction-induced suctions and K_o stress states. Results were used to devise a correction factor for RC results, on the basis of initial compaction-induced suction, for any given K_o stress condition.

During *Stage V*, a series of RC and BE tests were conducted on SP and CH soil specimens using a resonant column device with self-contained bender elements. Results were used to further substantiate the experimental findings and correlations devised in *Stages II*, *III* and *IV*.

Finally, during *Stage VI*, bender element (BE) tests were conducted on SP and CH soil specimens sheared at different vertical strain levels in order to assess the influence of vertical strain level on suction loss and menisci regeneration patterns.

Figure 1.2 depicts schematically the multi-stage experimental and modeling investigations undertaken in the present work. The accomplished program, although offering plenty of room for further substantiation and corroboration, has a great potential to provide a framework that can be used in improving the design and construction of the next generation of pavements in the U.S. based on sound and rational principles instead of conventional empirical procedures.

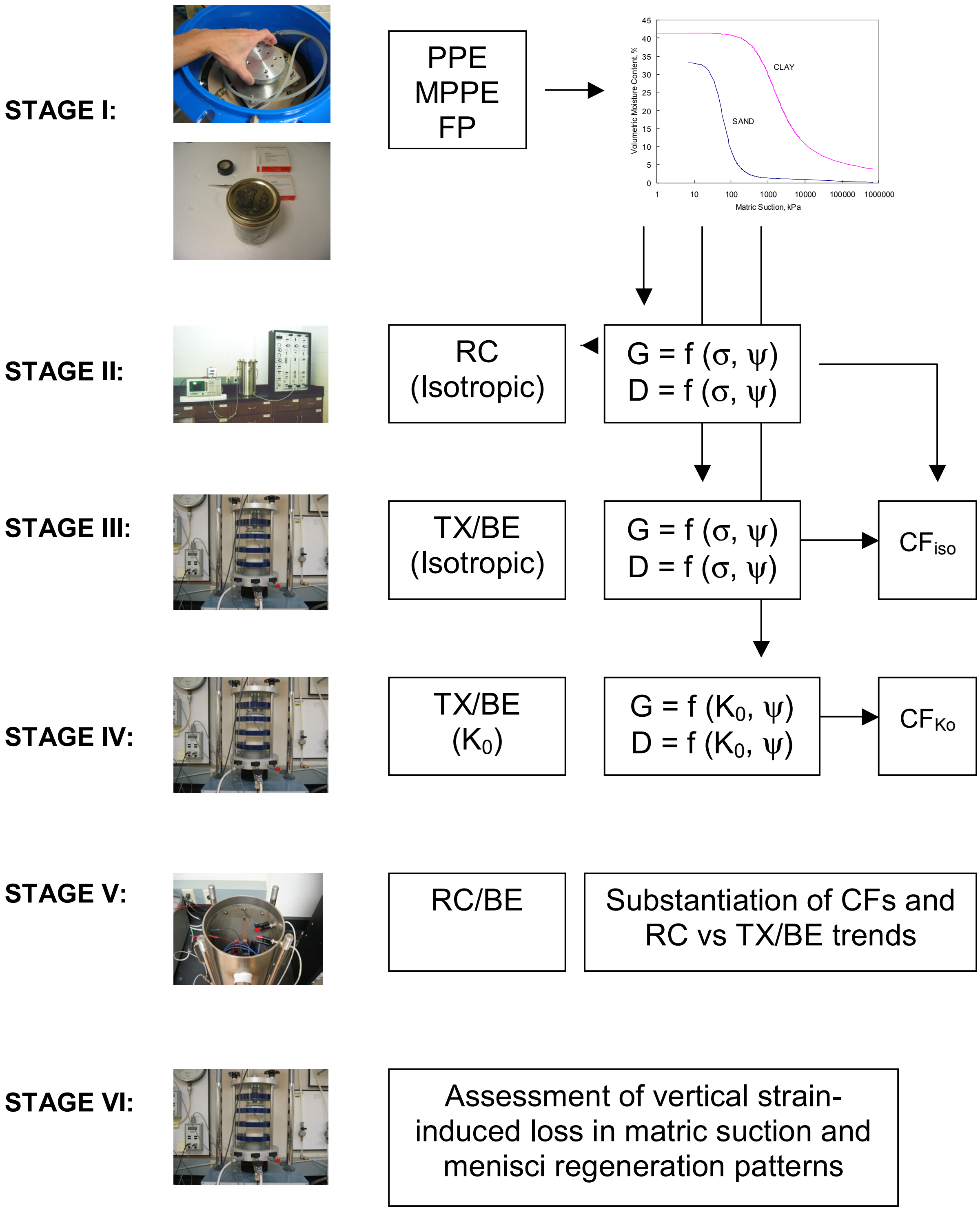

Figure 1.2 Experimental Program and Modeling Flow Chart

1.3 Organization

A brief summary of the chapters included in this dissertation is presented in the following paragraphs.

Chapter 2 presents a brief literature review on the importance of small-strain shear modulus in civil engineering practice, and the available methods for measuring the small-strain shear modulus in the field and laboratory. The chapter also describes some fundamentals of unsaturated soil mechanics, including key properties of unsaturated soils and the measurement of total suction and matric suction. Finally, a comprehensive literature review on previous studies is included.

Chapter 3 is devoted to describing the fundamentals of the resonant column (RC), bender element (BE), pressure plate (PP), and filter paper (FP) testing techniques, including main components of RC, BE, and PP devices, their step-by-step assembling processes, and the typical soil parameters obtained from these tests. The chapter also includes a complete description of the modified pressure plate extractor (MPPE) developed in this work for SWCC testing under controlled K_0 stress states.

Chapter 4 presents the basic engineering properties of the testing soils, along with a detailed description of all the experimental variables and soil specimen preparation procedures.

Chapter 5 describes the entire experimental program and procedures followed in this work, along with a comprehensive analysis of all test results, including the effect of each experimental variable on soil-water characteristic curve (SWCC), small-strain shear modulus (G), small-strain material damping (D), and the influence of vertical strain level on suction loss and menisci regeneration patterns.

Chapter 6 is devoted to describing all the empirical models devised herein for estimating small-strain shear modulus and damping ratio on the basis of compaction-induced matric suction, isotropic confinement, and K_0 stress state. Correction factors are also devised for G and D data from BE tests, on the basis on initial compaction-induced matric suction, for both isotropic and anisotropic stress states.

Chapter 7 includes a summary of the accomplished work, the main conclusions and some recommendations for future work.

CHAPTER 2

LITERATURE REVIEW

2.1 Introduction

In this chapter, an attempt is made to summarize the basic knowledge of small-strain stiffness properties of soils and the procedures available for measuring these properties in the field and the laboratory.

The first section describes a brief literature review on the significance of shear modulus as a material property and the available field and laboratory methods for assessing its magnitude. The chapter also includes the key fundamentals of unsaturated soil mechanics, including basic properties of unsaturated soils and the techniques available for measuring total suction and matric suction.

The chapter also focuses on a brief review of all previous works that have been reported related to this research. A brief explanation of the results from some of these previous works are presented in this section, as well as the empirical models to predict the small-strain shear modulus and damping ratio.

2.2 Significance of Shear Modulus as Material Property

A key material property necessary to evaluate the dynamic response of soil is shear modulus, G, which relates shear stresses to shear strains. Figure 2.1 shows the relationship between shear stresses and shear strains. At low strain amplitudes the shear modulus is high as the curve is linear in nature. This modulus is known as

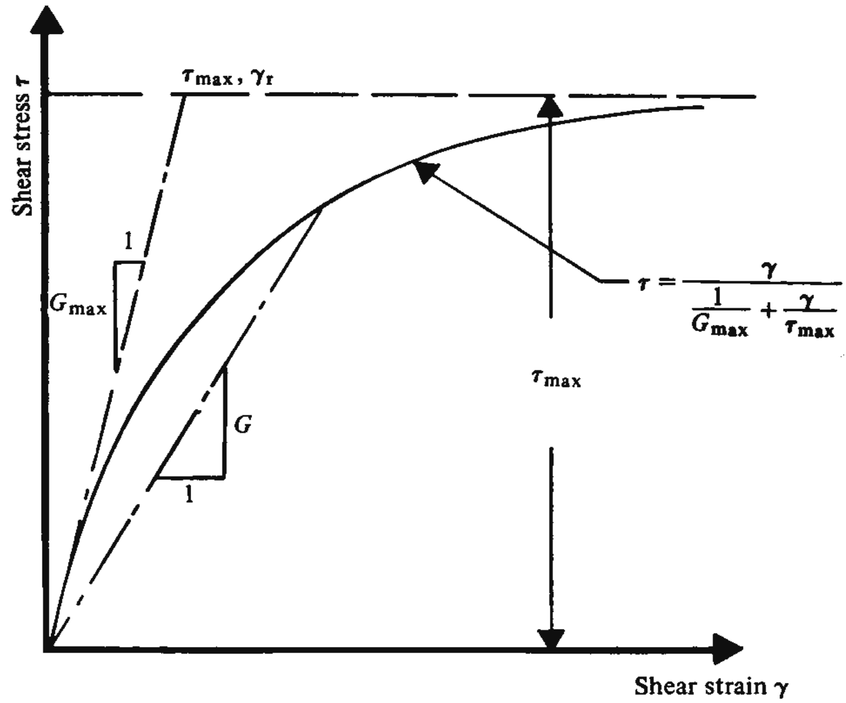

Figure 2.1 Variation of Shear Stress versus Shear Strain
(Hardin and Drnevich V. P, 1972)

the low-strain shear modulus (G_{max}). With an increase in strain, the curve becomes non-linear in nature, and the shear modulus related to these strains is known as the secant shear modulus (G). The shear modulus of soil can be simply related to the velocity of shear waves, hence measurements of shear wave velocity provide a convenient method for measuring soil stiffness (Viggiani and Atkinson, 1995a).

The dynamic response of a soil mass subjected to seismic excitation is the focus of much attention among engineers both in research studies and in the application of state-of-the-art technology to practical problems. Shear modulus is necessary to evaluate various types of geotechnical engineering problems including deformations in embankments, the stability of foundations for superstructures and deep foundation systems, dynamic soil structure interaction and machine foundation design (Dyvik and Madshus, 1985). Free-field dynamic response shear wave velocity has also been used to evaluate susceptibility of soils to liquefaction and to predict the ground surface and subsurface sub motions from outrunning ground shock produced by the detonation of high or nuclear explosives.

The shear modulus is essential for small strain cyclic situations such as those caused by wind or wave loading. It is equally important to predict soil behavior while designing highways, runways and their surrounding structures. The shear modulus may be used as an indirect indication of various soil parameters, as it correlates well to other soil properties such as density, fabric and liquefaction potential as well as sample disturbance.

The dynamic characteristics of soil deposits are of interest to civil engineers involved in the design or isolation of machine foundations, protection of structures against earthquakes, and the safety of offshore platforms and caissons during wave-storms (Gazetas, 1982). Current analysis procedures for soil dynamics problems generally require value of soil modulus. For many problems, this parameter adequately defines the stress-strain relation for the soil, when its dependence on strain level and state of effective stress is considered. Such analysis is essentially one-dimensional.

Most of the geotechnical research has been conducted by the engineers working in the area of static loading. A part of soil deformation under load is due to elastic deformation of the soil particles. This elastic deformation often constitutes only a small part of the total deformation of the soil. Elastic deformation is often obscured by deformation resulting from slippage, rearrangement, and crushing of particles. Classical elasto-plasticity assumes the elastic and plastic components of strain can be separated by loading and subsequent unloading. The recoverable strain is elastic. The total strain is the sum of the elastic strain and the plastic strain. However, in soils it is not usually possible to isolate the elastic strains simply by loading. When recovery of strain in soils is a result of stored elastic energy, the strains recovered are not always purely elastic. Slippage at particle contacts may accompany strain recovery. Sometimes elastic and plastic deformations are parallel to each other and one cannot be isolated from the other experimentally. Parallel elastic and slip deformation is one reason that recoverable strains in soils are not purely elastic. However, it appears that stress-strain relation for soils alone is purely elastic for small amplitude cyclic loading. Stricter definitions would probably require the strain amplitude to approach zero, but a more practical upper limit on strain is 0.001 percent. One of the best approaches to apply such loading and to isolate the purely elastic stress-strain relation is to study the propagation of small amplitude stress waves in soils.

Because the elastic stiffness is related to the wave propagation velocity, the relationship between different kind of stress increments and resulting elastic strain can be determined by measuring the wave propagation velocity. The differential shear stress-elastic strain relationship can be studied by propagating shear waves (S-waves). Wave propagation measurement is a very powerful way of isolating elastic strains. Elastic strains can be isolated in other static tests by applying small cyclic strains with amplitude less than 0.001 percent. The problem is that most conventional testing devices will not accurately measure such small strains. The shear modulus of a soil varies with the cyclic shear strain amplitude. At low strain amplitudes the modulus is high, and it decreases as the strain amplitude increases. Figure 2.2 is an idealization of soil stiffness over a large range of strains, from very small to large, and roughly distinguishes strain ranges. At very small strains, which are generally less than a yield strain of 0.001%, the shear modulus is nearly constant with strain. The shear modulus value corresponding to this strain is known as the limiting value G_0 (or G_{max}). For small strains which are generally less than an arbitrary limit of around 1%, the tangent shear modulus G is a non-linear function of strain. The large strain zone exceeds 1% and the shear stiffness is very small as the soil approaches failure.

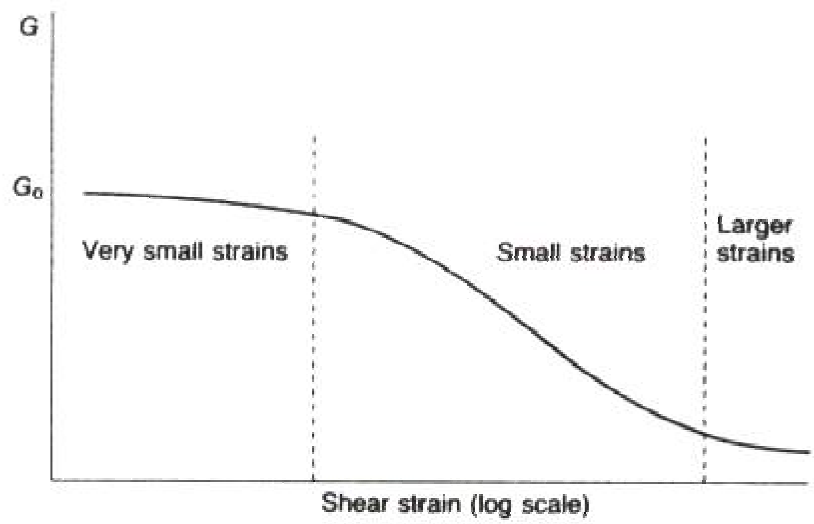

Figure 2.2 Variation of Soil Stiffness with Shear Strain
(Atkinson and Sallfors, 1991)

At strains exceeding about 1%, the stiffness is typically an order of magnitude less than the maximum, and it continues to decrease as the state approaches failure. In the intermediate small strain range the stiffness decreases smoothly with increasing strain. The maximum shear modulus, G_{max}, of a soil can be calculated from measured shear wave velocities. The measurement of soil stiffness at small strains is gaining greater importance in the study of soil mechanics and its application to geotechnical engineering design (Jovicic, 1997).

Routine estimations of stiffness have traditionally been made in a stress path triaxial apparatus using local displacement transducers fixed directly on the sample or using cyclic torsional shear test. However, recent research has brought importance to the development of dynamic methods for the measurement of soil stiffness at very small strains.

2.3 Nonlinear Soil Behavior

Once shearing strains exceed about 0.001% (referred to as the linear threshold), the stress-strain behavior of soils becomes increasingly nonlinear, and there is no unique way of defining shear modulus or damping. Therefore, any approach to characterize the soil for analyses of cyclic loading of larger intensity must account for the level of cyclic strain excursions.

When ground motions consist of vertically propagating shear waves and the residual soil displacements are small, the response can often be characterized in sufficient detail by the shear modulus and the damping characteristics of the soil under cyclic loading conditions. It is usual practice to express the nonlinear stress-strain behavior of the soil in terms of the secant shear modulus and the damping associated with the energy dissipated in one cycle of deformation. With reference to the hysteresis loop shown in figure 2.3, the secant modulus is usually defined as the ratio between maximum stress and maximum strain, while the damping factor is proportional to the area ΔE enclosed by the hysteresis loop, and corresponds to the energy dissipated in one cycle of motion. It is readily apparent that each of the aforementioned properties depends on the magnitude of the strain for which the hysteresis loop is determined; thus they are functions of the maximum cyclic strain.

The simplified response illustrated in figure 2.3 can be described through a backbone curve, corresponding to first loading, together with a set of rules for unloading and reloading, as proposed by Masing. Rheological models of this type can be represented by a set of elasto-plastic springs in parallel, with input parameters obtained by curve fitting the measured data.

When opting for an equivalent linear analysis, the characterization of the soil consists of three parts (figure 2.4):

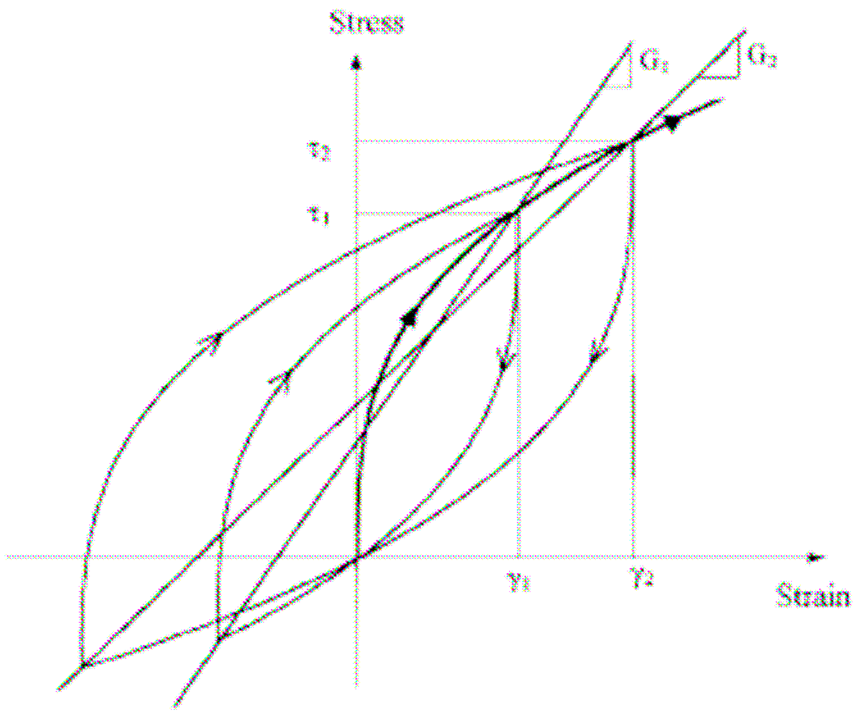

Figure 2.3 Loading-Unloading at Different Strain Amplitudes
(Assimaki and Kausel, 2000)

- The maximum shear modulus G_{max} in the very small strain linear region.
- The reduction curve for G/G_{max} versus maximum cyclic strain γ_c (referred to as modulus degradation curve), with G being the secant modulus.

- The fraction of hysteretic (or material) damping ξ versus the maximum cyclic strain γ_c. This parameter is defined as the area ΔE of the hysteresis loop normalized by the "elastic" strain energy through the following expression:

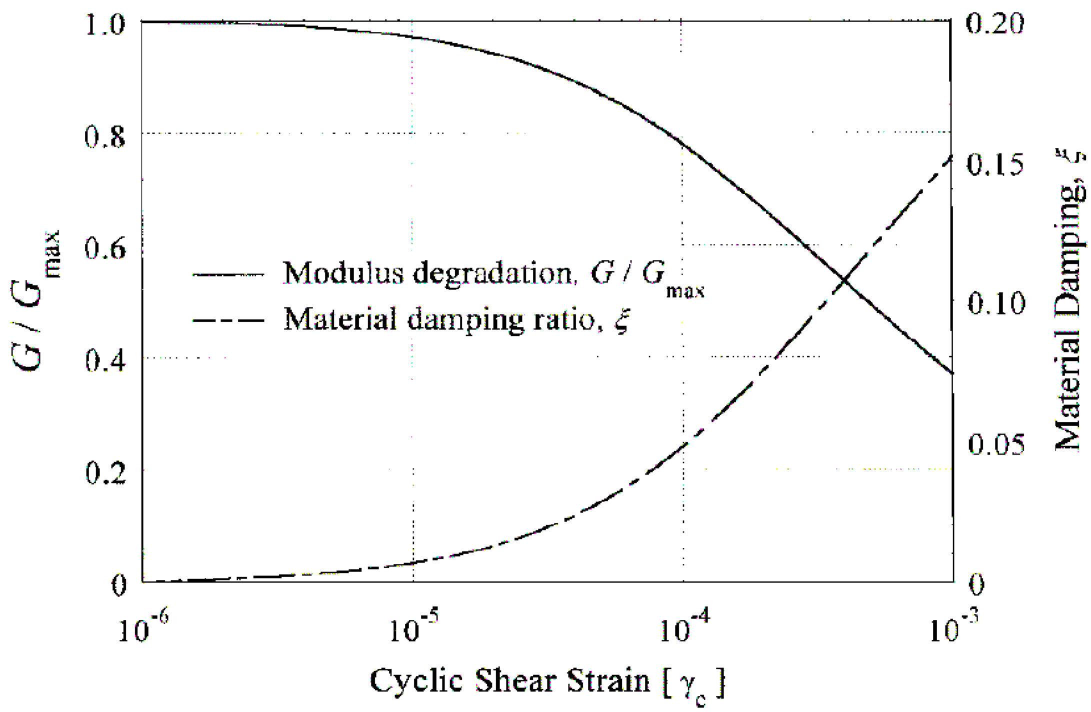

Figure 2.4 Secant Modulus and Material Damping Ratio as Function of Maximum Strain (Assimaki and Kausel, 2000)

$$\xi = \frac{1}{2\pi}\frac{\Delta E}{G\gamma_c^2} \tag{2.1}$$

In the case of dry cohesionless soils, the physical origin of the variation in modulus and damping with cyclic strain, as reflected in the shapes of the curves in figure 2.4, is now well understood. Both parameters are related to the frictional behavior at the interparticle contacts and the rearrangement of the grains during cyclic loading (Dobry et al., 1982, Ng and Dobry 1992, 1994). Therefore, even crude analytical models of particles can be used to mimic the degradation curves of G/G_{max}

and ξ versus γ_c, provided that they include friction and allow for particle rearrangements.

It should be noted however that reversible behavior is associated with minimal rearrangement of particle contacts and irrecoverable, plastic strains become significant only at strain levels $\gamma_c \geq 0.1\%$. Therefore, for smaller cyclic strain amplitudes dissipation of energy must be related to frictional behavior at contacts.

2.4 Methods to Measure Shear Modulus

There are various field methods as well as laboratory methods practically used to determine shear wave velocities of soils. Once velocities are determined, shear moduli of the soil are calculated. These moduli are used in dynamic soil-structure interaction analyses for small-strain problems such as machine foundations and as reference values for larger-strain problems such as earthquake shaking and blast loading. Field methods are in-situ techniques deployed to measure dynamic properties of soils. Field dynamic tests generally develop strains in the range of 10^{-3}-10^{-4} % and less. Field methods can be classified as direct and indirect field methods. The following describes various field and laboratory methods for measurement of shear modulus.

Direct Field Methods

(a) Seismic Reflection Method

(b) Seismic Refraction Method

(c) Seismic Cross-Hole Shear Wave Test

(d) Seismic Downhole, Uphole Method

(e) Spectrum Analysis of Surface Wave Technique (SASW)

(f) Seismic Flat Dilatometer Test

(g) Suspension Logger Method

Indirect Field Methods

(a) In Situ Measurement

(b) Hardin's Empirical Equation

Laboratory Methods

(a) Cyclic Triaxial Compression Test

(b) Resonant Column Test

(c) Bender Element Test

2.4.1 Direct Field Methods

2.4.1.1 Seismic Reflection Method

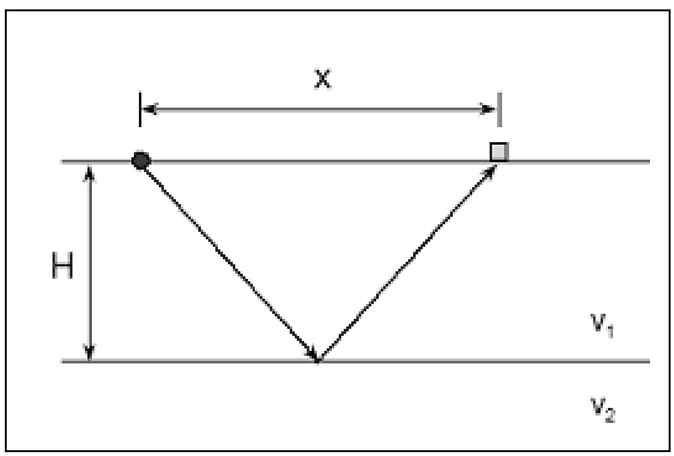

Figure 2.5 Seismic Reflection Method (Kramer, 1996)

The method works by reflecting sound waves off the boundaries between different types of soils (Kramer, 1996). As opposed to earthquake seismology, where the location and time of the source are unknown that needs to be solved for, seismic reflection profiling uses a controlled source to generate seismic waves. Using vibrators or dynamite as a source, seismic waves are generated and traces of shear waves are recorded by each geophone kept at known distances from the source. Figure 2.5 depicts seismic reflection method. Thus the measured shear wave velocity is used to evaluate the dynamic moduli of the soil.

2.4.1.2 Seismic Refraction Method

The technique used is similar to seismic reflection except the seismic refraction technique induces a sound wave into the subsurface and measures the velocity of sound at intervals along a traverse line to obtain depths and velocities of various subsurface strata. Figure 2.6 shows schematic representation of seismic refraction method.

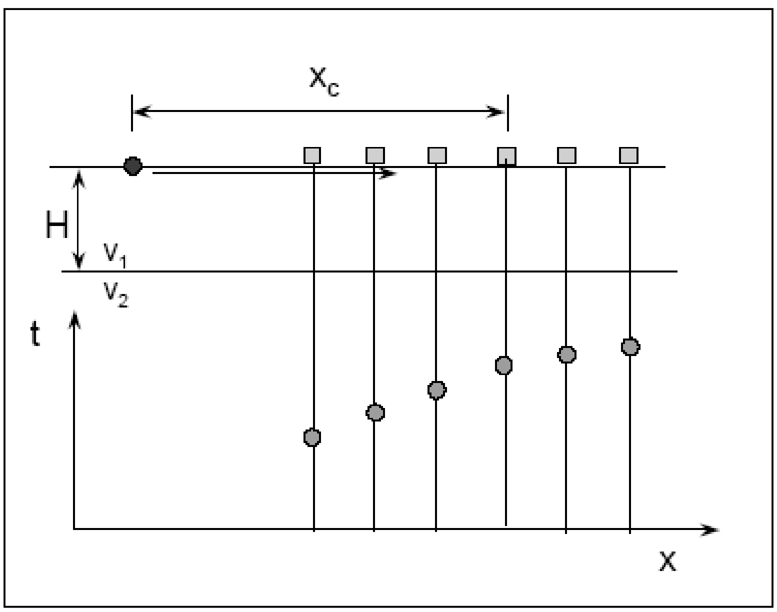

Figure 2.6 Seismic Refraction Method (Kramer, 1996)

By determining the arrival of the compression and shear wave, it is possible to calculate their propagation velocities. The method is typically used to characterize the elastic properties of subsurface materials for dynamic structural analysis.

2.4.1.3 Seismic Cross-Hole Shear Wave Test

The cross-hole shear wave apparatus is used to determine dynamic moduli of geologic materials and to locate water filled voids in soil and rock (ASTM D 4428M-91). In this method generally two or three holes are drilled, shear waves are generated in one of the holes at a given elevation and receivers are placed at the same elevation in each of the other borehole. Figure 2.7 represents schematic diagram of seismic cross-hole shear wave test.

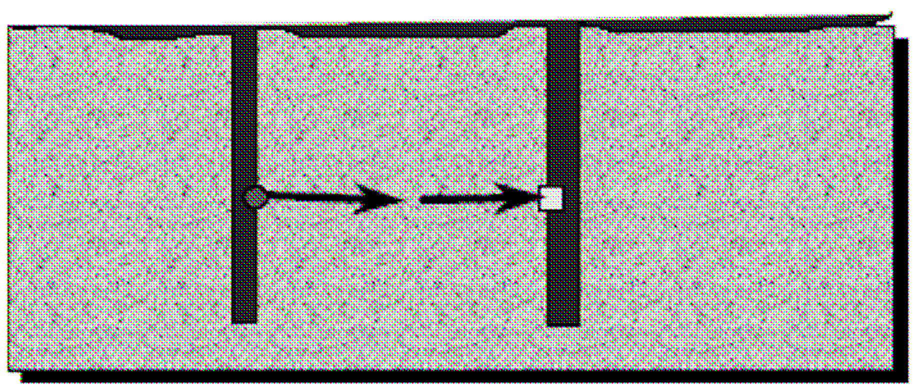

Figure 2.7 Seismic Cross-Hole Shear Wave Test (Kramer, 1996)

Travel time of these waves is measured in adjacent receiver holes at the corresponding elevation with the help of the geophones. The shear wave velocity is calculated based on the wave arrival time. This knowledge of the site-specific compression and shear wave velocities is used to determine the dynamic elastic moduli for the various layers.

2.4.1.4 Seismic Downhole/Uphole Method

In seismic downhole method, a seismic source such as explosives, vibroseis or other mechanical device is activated at or near the head of the borehole and receiver records the signal at fixed depths in the borehole.

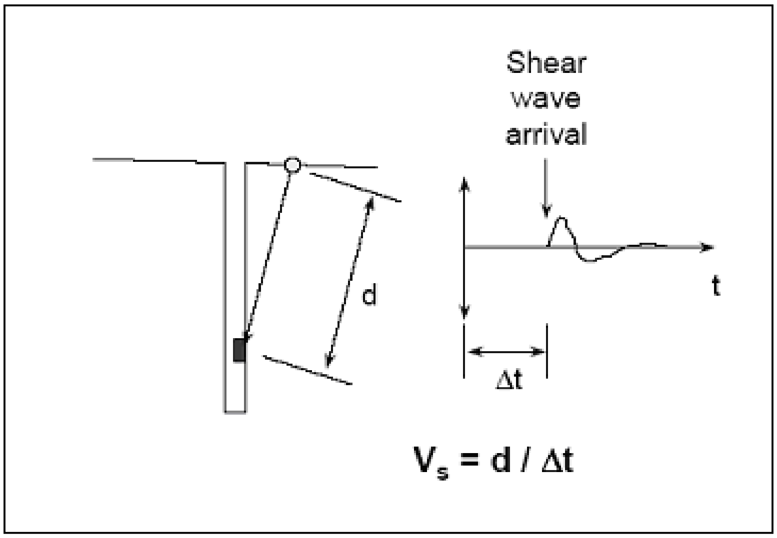

Figure 2.8 Seismic Down-Hole Method (Kramer, 1996)

A vibration sensor is installed in a borehole, or by pushing the sensor into the ground. A polarized shear (and/or compression) wave is generated at the ground surface and the time required for the wave to travel across the soil layers to a receiver is measured. Different methods of signal interpretation can be used to determine the first arrival time of the signal. From the known distance the wave propagation velocity (shear wave or compression wave) can be calculated. Down-hole tests are relatively easy to perform, as only one sensor must be installed in the ground.

2.4.1.5 Spectral Analysis Surface Wave Technique (SASW)

Spectral Analysis of Surface Wave Technique, SASW, is an increasingly popular seismic testing method. It uses a seismic source (impact or vibration generator) at the ground surface and at least two vibration transducers at the ground surface. The vertical transducers record the propagation of surface (Rayleigh) waves. By analyzing the phase information for each frequency contained in the wave train, the Rayleigh and shear wave velocity can be determined. The evaluation of SASW measurements is relatively complex and requires specially developed computer software. SASW measurements can determine wave velocity profiles to depth exceeding 20 m, which is sufficient for most foundation projects. The main advantage of SASW is that large soil volume can be investigated relatively rapidly.

2.4.1.6 Seismic Flat Dilatometer Test

The flat dilatometer test was formally introduced by Marchetti (1975) and has evolved into a robust, simple, and repeatable means for delineating soil engineering parameters.

Downhole shear wave velocity measurements have been incorporated within a “Marchetti” flat dilatometer by placing a velocity transducer in a connecting rod just above the blade. The hybrid of combining downhole seismic with flat dilatometer, termed the seismic dilatometer test (SDMT), has the superior advantages of determining both the routine estimates of soil properties and stratigraphic information, while also measuring the small-strain stiffness within a single sounding. The SDMT is rapid, simple, and cost effective, requiring essentially no more time than a conventional dilatometer sounding.

2.4.1.7 Suspension Logger Method

Suspension velocity logging is relatively new method of measuring seismic wave velocities in deep, uncased boreholes. The logging system contains a source and two receivers spaced one meter apart, suspended by a cable. The probe is lowered into the borehole to a specified depth where the source generates a pressure wave in the borehole fluid. The pressure wave is converted to a seismic wave (P and S) at the borehole wall. Along the wall at each receiver location, the P and S waves are converted back to pressure waves in the fluid and received by the geophones, which send the data to the recorder on the surface. The elapsed time between arrivals of the waves at the receivers is used to determine the average velocity of a one meter-high column of soil around the borehole.

2.4.2 Indirect Field Methods

2.4.2.1 In Situ Measurements

Although shear velocity can be obtained directly from field investigation or laboratory testing of soil samples of studied area, it is not always economical. Indeed, when direct measurement of shear wave velocity for soil layers is not available then the existing or developed correlation between N values of SPT or tip cone resistance (q_c) of CPT (CPTU) techniques can be used to measure shear moduli of soil layers. Following empirical formulae have been designed to fairly estimate shear modulus. Equation 2.2 is used for clayey soils.

$$V_S = 27 \cdot N^{0.73} \tag{2.2}$$

Shear modulus is related to SPT-N value with empirical correlations. Among these correlations, the following one proposed by Imai and Yoshimura is commonly used.

$$G = a \cdot N^b \cdot 100(kPa) \quad (2.3)$$

Where: G = shear modulus

a = constant (=100)

b = constant (0.78)

N = SPT value

Mayne and Rix (1993) have pointed out that G_{max} and q_c show similar dependence on the same parameters, namely mean effective stress and void ratio. According to their study, there exist a relationship between G_{max} and q_c

$$G_{max} = 49.2 \cdot {q_c}^{0.51} \quad (2.4)$$

The proposed relationship can be used to obtain preliminary G_{max} profiles of soils in the absence of direct measurements of shear wave velocity. Also from the ratio of average value of q_c and overburden pressure, the value of G_{max} can be determined.

2.4.2.2 Hardin's Empirical Equation

A more general expression was proposed by Hardin (1978) based on theoretical elastic stress-strain relationships by Rowe (1971) and empirical equations for initial tangent modulus by Janbu (1963) and Hardin and Black (1968). This can be written in the form:

$$G_{max} = S \cdot f(v) \cdot OCR^k \cdot {P_a}^{1-n} \cdot p'^n \quad (2.5)$$

Where: S = dimensionless coefficient which depends on the nature of the soil,

f (v) = a function of the specific volume, p' = mean effective stress,

P_a = the atmospheric pressure and

OCR = over consolidation ratio defined as the ratio of the maximum past stress to the present stress

2.4.3 Laboratory Methods

2.4.3.1 Cyclic Triaxial Test

Cyclic triaxial apparatus can be used to measure the cyclic properties of soils starting in the elastic strain range (lower than or equal to 0.001 percent) and extending into the plastic strain range (about 2 percent), provided highly specialized testing apparatus and techniques are used. The loading system should have the capability of applying cyclic sinusoidal loads and deformations varying between about 2 N (0.5 lbf) and 225 N (50 lbf) and 0.005 mm (0.0002 in.) and 2.5 mm (0.1 in.) respectively, at rates between about 0.1 Hz and 1 Hz. Such rates are typically used for wave loading and earthquake analysis, respectively. It should be noted that measured cyclic loads will be much greater than 225 N (50 lbf), frequently up to 4.5 kN (1000 lbf), and cyclic loads, not deformations, are typically applied at shear strain amplitudes less than about 0.01 percent. The basic parameters being measured and recorded during the test are changes in axial load, deformation and pore water pressure.

The shear strain amplitude is calculated from axial strain amplitude using the following equation:

$$\pm\gamma = \pm\varepsilon\cdot(1+\nu) = (\frac{\Delta L_{PP}}{2H_C})\times(1+\nu) = \pm 1.5\cdot\varepsilon \qquad (2.6)$$

Where: $\pm\gamma$ = shear strain amplitude (in. /in.)

$\pm\varepsilon$ = axial strain amplitude (in. /in.)

ΔL_{pp}= peak to peak axial deformation measured within a given loading cycle

H_c = height of specimen after consolidation

ν = Poisson's ratio, a value of 0.5 is typically used in all tests

The shear modulus is calculated using the following equation:

$$G = \frac{E}{2(1+\nu)} = \frac{(P_{PP} \times H_C)}{(3A_C \times \Delta L_{PP})} \tag{2.7}$$

Where: G = shear modulus

E = Young's modulus

P_{pp} = Peak to peak axial load measured within a given loading cycle.

A_c = Area of specimen after consolidation

Calculated values of shear strain amplitude and shear modulus are also corrected for equipment compliance using the following equations:

$$\pm\gamma_c = \pm\gamma \times CF \tag{2.8}$$

$$G_C = \frac{G}{CF} \tag{2.9}$$

Where: γ_c = shear strain amplitude corrected for equipment compliance

G_c = shear modulus corrected for equipment compliance

CF = equipment compliance factor

The maximum shear modulus, G_{max}, is estimated using the following equation:

$$G_{\max} = \frac{G_C(at\gamma_C = 10^{-3}\%)}{(O.95 \sim 0.98)} \tag{2.10}$$

The maximum shear modulus is determined by applying about three or more stages of sinusoidally varying cyclic load about an ambient load, at the prescribed frequency, and with about five loading cycles being applied in each stage. In the first stage, the initial cyclic load is about ± 0.5 lbf (2 N) or a value such that the resulting cyclic shear strain amplitude will be slightly less than $1x10^{-3}$ percent. The cyclic load applied in subsequent stages is adjusted to obtain a uniform distribution of shear moduli data, G, versus shear strain amplitude, γ, up to a γ of about $5x10^{-3}$ percent.

2.4.3.2 Resonant Column Test

The resonant column (RC) testing technique was first used to study dynamic properties of rock materials in the early 1930s, and has been continuously evolving since then for the dynamic characterization of a wide variety of geologic materials. During the late 1970s, Prof. Stokoe and his co-workers developed a new version of resonant column device which has been continuously refined in the last two decades. The stokoe RC testing method has been standardized by the American Society for Testing and Materials (ASTM D 4015-92), and is one of the most reliable and pragmatic test methods used for testing shear modulus (G) and material damping (D) of soils. Isenhower (1979) added a torsional shear device to the resonant column apparatus. In the torsional shear test the sample is subjected to a given number of low frequency cycles of torsional load and the soil stiffness is obtained directly from the torque-twist relationship.

The RC test essentially consists of a soil column which is in fixed-free end conditions is excited to vibrate in one of its natural modes. Once the frequency at resonance (f_r) is experimentally known, the shear wave velocity (V_s) and, hence, the shear modulus (G) of the soil can easily be determined. Damping ratio can be determined from decaying vibrations or by hystereses loop characteristics. The RC test is used to determine shear wave velocity, shear modulus and damping ratio of soil under different confining pressure, void ratios, and shear strain amplitude, number of cycles and time of confinement.

2.4.3.3 Bender Element Test

The bender element method, developed by Shirley and Hampton (1977), is a simple technique to obtain small strain shear modulus of a soil, G_{max}, by measuring the velocity of propagation of a shear wave through a sample. Bender element systems can be set up in most laboratory apparatus like oedometer or in direct simple shear (DSS) device, but are particularly versatile when used in the triaxial test as described by Dyvik and Madshus (1985). Shear waves in soils on laboratory samples can be transmitted and received using bender elements. A pair of bender elements are embedded into the opposing ends of each sample and wired in a transmitter-receiver configuration as recommended by Dyvik and Madshus (1985) to measure G_{max}, the maximum shear modulus. This is typically defined as the shear modulus measured at strain level below 0.001%.

2.5 Advantages of Laboratory Methods Over Field Methods

Structural anisotropy in the field is the inherent anisotropy in the soil skeleton which causes a difference in soil properties including wave velocities in different directions under isotropic loading. On the other hand, in laboratory, soil specimen can be subjected to design confined pressures. In field testing, large soil section is available for which the boundary conditions are uncontrollable whereas in the laboratory testing, soil skeleton of specific dimensions are tested under controlled boundary conditions.

The shear modulus of soil is simply related to the velocity of shear waves, so measurement of shear wave velocity provides a convenient method for measuring soil stiffness. Experiments related to measurement of shear wave velocity are convenient to carry out in laboratory rather than field testing which requires drilling equipments, and geophone setting. Laboratory tests such as resonant column or tests using bender elements are designed to be performed at very small strains ($<10^{-3}$ percent) whereas field tests are basically carried out at large strains. Hence, the low strain shear modulus calculated using laboratory methods is more accurate as well as more reliable than field methods. In addition to this, these methods are also non-destructive, hence can be performed several times on the same soil sample. Also it is possible to study the aging effects on shear moduli of soil samples which are subjected to different testing conditions. In the time crunch scenarios, laboratory tests can be done in short time under controlled conditions. Laboratory methods are reliable to get dynamic properties of the soils when field methods are not feasible to perform. Also real field problems involving traffic loading or shaking due to vibrations can be simulated in laboratory with more accuracy and precision.

Even in in-situ methods like CPT or SPT, q_c or N is measured at large deformations involving yielding and failure of soil surrounding the cone or split spoon sampler respectively whereas G_{max} measured by laboratory methods are at very small shear strain levels. A detailed description of the fundamentals of RC and BE testing is presented in chapter 3.

2.6 Fundamentals of Unsaturated Soil Mechanics

Saturated soil mechanics commonly related to effective stress, which influences both the strength and the volume change properties of saturated soils. However, in unsaturated soils, both soil suction and stresses contribute to the variations in strength and volume change properties of soils. The majority of stabilized soils in the field are under partial saturation soil conditions. In this section, parameters of importance in unsaturated soil mechanics, suction properties, and soil water characteristic curves are detailed.

Saturated soil mechanics has undergone significant changes in the past few decades. Some of these changes are related to increased attention given to the unsaturated soil zone (vadose zone), which is above the ground water table. However, the development of unsaturated soil mechanics has been relatively slow in comparison to saturated soil mechanics. It is interesting to note that the earlier form of the literature in 1936 had started focusing on unsaturated soil behavior (Fredlund and Rahardjo, 1993). Subsequently, the concepts for understanding unsaturated soil behavior are slowly established (Bishop, 1959). In the 1950's, most of the attention given to unsaturated soils was related to capillary flow (Black and Croney, 1957, Williams, 1957, Bishop et al. (1960), and Atchison, 1967). This research resulted in the proposal of several effective stress equations for unsaturated soils. In 1977, Fredlund and Morgenstern described the stress state for unsaturated soil by using two independent normal stress variables, which are net normal stress ($\sigma_{net} = \sigma - u_a$) and matric suction ($\psi = u_a - u_w$).

Basically, the water content in unsaturated soil is a function of the suction present in the soil. The relationship between the water content in soil and the suction can be expressed in a plot of volumetric water content versus suction curve that is well-known as the soil-water characteristic curve (SWCC). Both suction and SWCC profiles can be used to understand changes in void and saturation levels in unsaturated expansive soils that are subjected to soaking. Hence, an understanding of these principles will provide a better explanation of the mechanisms that lead to soil swelling and shrinking. Sections 2.6.1, 2.6.2, and 2.6.3 describe various properties of unsaturated soils, suction measurement techniques, and fundamentals of soil-water characteristic curve, respectively.

2.6.1 Properties of Unsaturated Soils

2.6.1.1 Unsaturated Soil Profile

The unsaturated zone can be divided into three subzones, the capillary, intermediate (or vadose), and soil water zones as shown in Figure 2.9. In coarse materials, the saturated zone is located below the ground water table. In fine-grained materials, the saturated zone can reach higher levels than the ground water table because of capillary forces (Bear, 1979). The extension of this so-called capillary zone depends on the soil stratigraphy, the grain size distribution, and the soil density. The unsaturated zone is located above the saturated part of the capillary zone (Bear, 1979).

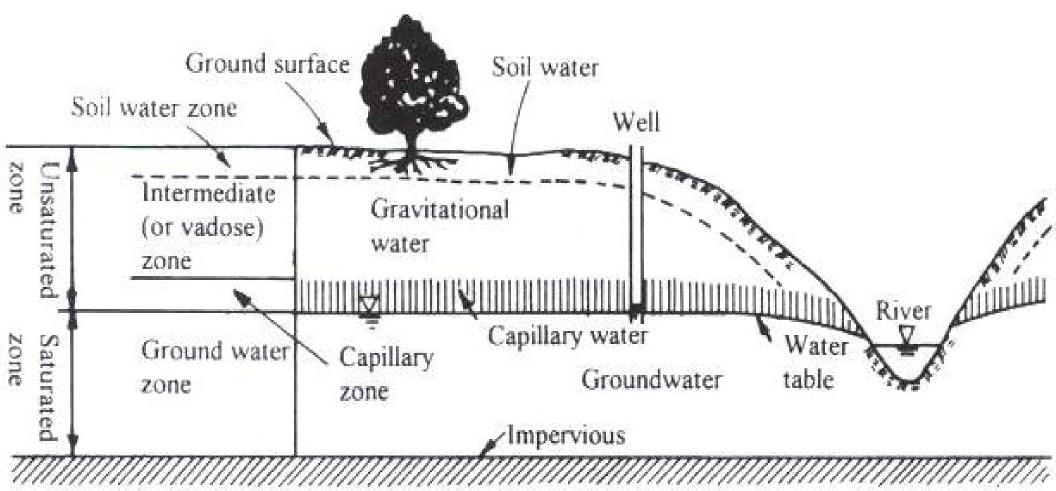

Figure 2.9 Unsaturated Soil Profile (Bear, 1979)

The zone situated closest to the ground surface is called the soil water zone. The water content in this zone depends heavily on climatic conditions. During periods with high precipitation, the pores may be filled with water and fully saturated, while during dry periods the pores may be almost completely filled with air. vaporation and transpiration as well as the root system of vegetation play an important role for how much of the precipitation that will infiltrate down to the ground water table.

Finally, the zone situated between the soil water zone and the capillary zone is called the intermediate zone. The water content in this zone depends on the percolation from the upper layer. The water is transported by gravitational forces down to the ground water.

2.6.1.2 Capillarity

The pores in the unsaturated zone are occupied by both water and air. At the interface between air and water, the difference between their inward attraction results in an interfacial tension, σ. The magnitude of this pressure depends on the curvature of the air-water interface and, consequently, on the degree of saturation. The difference in pressure just below the meniscus, called the capillary pressure p_c, can, according to Bear (1979), be written as

$$p_c = p_{air} - p_w \tag{2.11}$$

If the air pressure is equal to the atmospheric pressure, the capillary pressure becomes equal to the pressure in the water.

$$p_c = - p_w \tag{2.12}$$

Where p_w is lower than the atmospheric pressure, that is, a negative pressure exists.

Figure 2.10 shows a simple model, used to visualize the capillary phenomenon in a soil. If an air-filled capillary tube is placed in a water compartment, the adhesive forces between the glass tube and the water will cause the water to rise until equilibrium is reached between the capillary forces (directed upwards) and the gravitational forces (directed downwards), and a meniscus is created. The capillary rise of the water is in inverse proportion to the diameter of the tube.

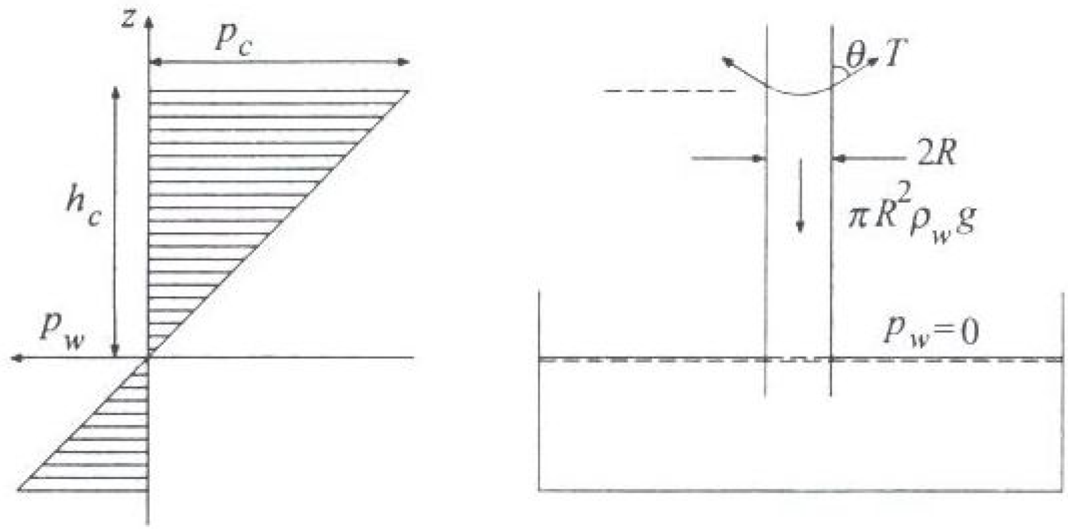

Figure 2.10 Water in a Capillary Tube (Bear, 1979)

The smaller the diameter, the higher the capillary rise. By analyzing the forces acting in the capillary tube, the following equation can be written (Bear, 1979)

$$h_c = \frac{2T\cos\theta}{R\rho_w g} \tag{2.13}$$

where T = surface tension of water

R = radius of the capillary tube

ρ_w = density of water

g = gravitational acceleration

θ = contact angle

h_c = capillary pressure head

Right below the meniscus in the capillary tube the water pressure is equal to $p_c = -p_w$ if $p_{air} = p_{atm}$.

2.6.1.3 Soil Suction

Soil suction is commonly referred to as the free energy state of soil water (Edlefsen and Anderson, 1943). The free energy of the soil water can be measured in terms of the partial vapor pressure of the soil water (Richards, 1965). According to Fredlund and Rahardjo (1988), the soil suction in terms of relative humidity is commonly called “total suction.” It has two components, namely, matric and osmotic suctions. The total suction is then described as

$$\psi_t = (u_a - u_w) + \pi \tag{2.14}$$

Where: ψ_t = total suction

ψ = $(u_a\text{-}u_w)$ = matric suction

u_a = pore-air pressure

u_w = pore-water pressure

π = osmotic suction

2.6.1.3.1 Matric Suction

By definition, matric suction can be defined as a capillary component of free energy. In suction terms, it is the equivalent suction derived from the measurement of the partial pressure of the water vapor in equilibrium with the soil water, relative to the partial pressure of the water vapor in equilibrium with a solution identical in composition with the soil water (Aitchison, 1965).

Matric suction is generally related to the surrounding environment. The matric suction may vary from time to time. Blight (1980) illustrated that the variations in the suction profile depend upon several factors such as ground surface condition, environmental conditions, vegetation, water table, and permeability of the soil profile. Figure 2.11 also shows the relative effects of the environment, the water table, and vegetation on the matric suction profiles.

Ground surface condition

The matric suction below an uncovered ground surface is affected by environmental changes. Dry and wet seasons cause variations in the suction, particularly near the ground surface. In real field conditions, suction beneath a covered ground surface is more constant with time than beneath an uncovered surface (Fredlund and Rahardjo, 1993).

Environmental conditions

The matric suction in the soil increases during dry seasons and decreases during wet seasons. Maximum changes in soil suctions occur near the ground surface (Fredlund and Rahardjo, 1993).

Vegetation

Vegetation on the ground surface has the ability to apply a tension to the pore-water of up to 1-2 MPa through the evapotranspiration process. Evapotranspiration results in the removal of water from the soil and an increase in the matric suction. However, the evapotranspiration rate is the function of climate, the type of vegetation, and the depth of the root zone (Fredlund and Rahardjo, 1993).

Water table

The depth of the water table influences the magnitude of the matric suction. The deeper the water table, the higher the possible matric suction (Fredlund and Rahardjo, 1993).

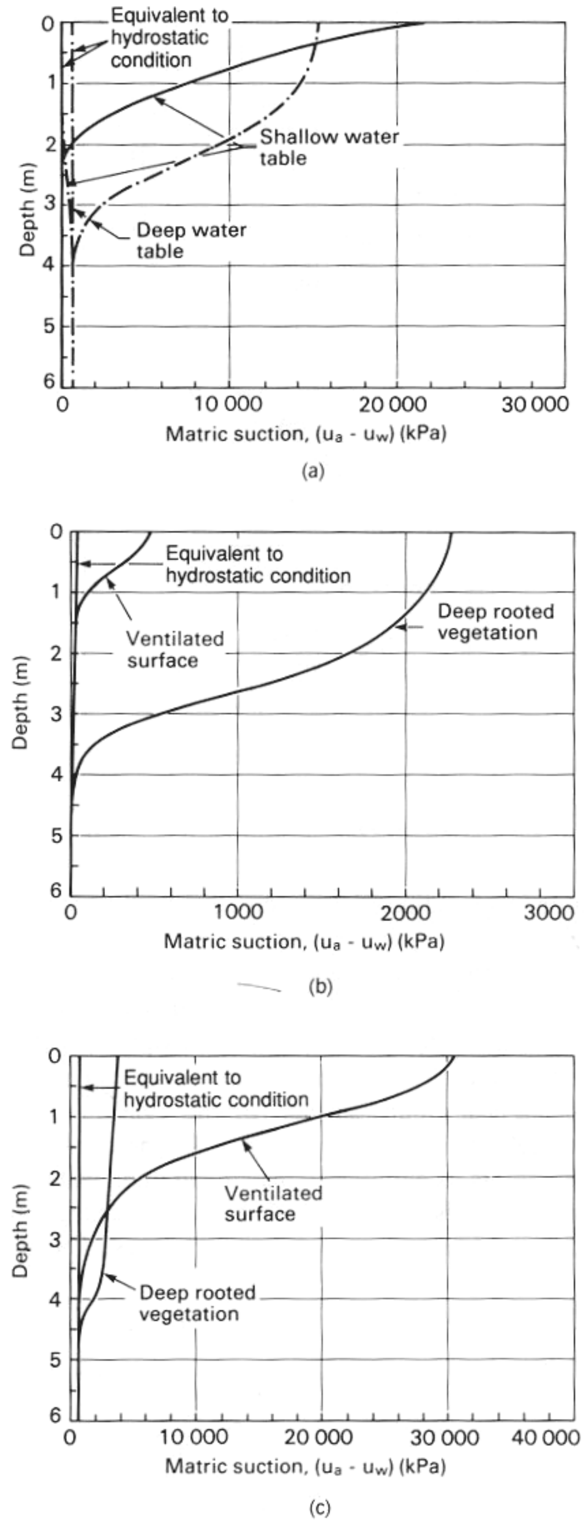

Figure 2.11 Typical Suction Profiles Below an Uncovered Ground Surface: (a) Seasonal Fluctuation; (b) Drying Influence on Shallow Water Table Condition; (c) Drying Influence on Deep Water Table Condition (Blight, 1980, Fredlund and Rahardjo, 1993)

Permeability of the soil profile

The permeability of soil represents its ability to transmit and drain water. This indicates the ability of the soil to change matric suction as the environment changes (Fredlund and Rahardjo, 1993).

2.6.1.3.2 Osmotic Suction

Osmotic suction is commonly related to the salt content in the pore-water, which is present in both saturated and unsaturated soils. Aitchison (1965) defined osmotic suction as follows (Aitchison, 1965a):

"*Osmotic (or solute) component of free energy is the equivalent suction derived from the measurement of the partial pressure of the water vapor in equilibrium with a solution identical in composition with the soil water, relative to the partial pressure of water vapor in equilibrium with free pure water.*"

The osmotic pressure has an effect on the mechanical behavior of the soil in both the saturated and unsaturated zones, but is normally neglected. Fredlund (1989, 1991) and Fredlund and Rahardjo (1993) discussed reasons for this practice. In most geotechnical problems, the change in osmotic suction can be neglected and the change in total suction is equal to the change in matric suction, as shown in Figure 2.12. Consequently, if the pore air pressure is equal to the atmospheric pressure, the total pressure becomes equal to the negative pore pressure. However, if salts are present in soils, then the osmotic component of suction must be taken into account.

2.6.1.4 Soil Water Characteristic Curve

According to Bear (1979), three different stages of saturation can be distinguished in a soil profile as shown in Figure 2.13. At low degrees of saturation

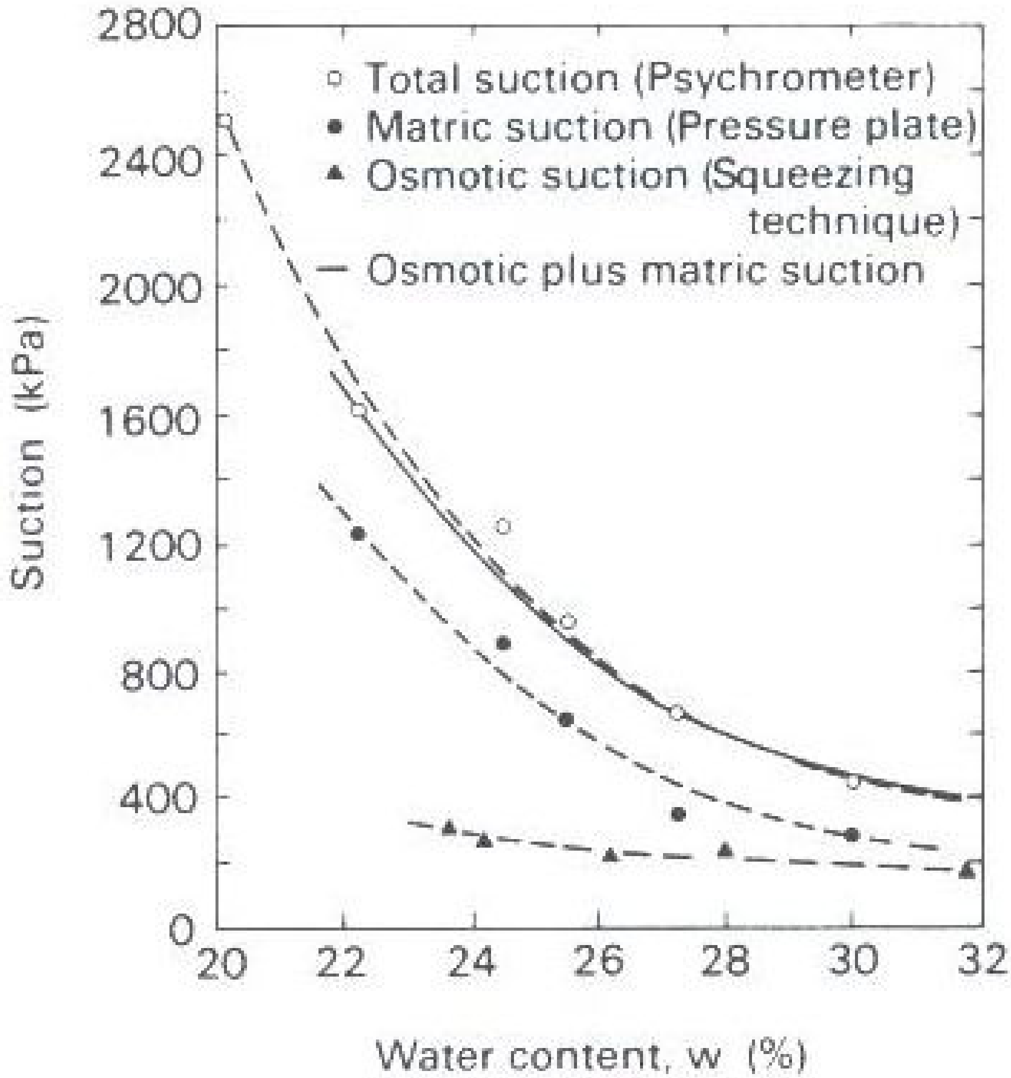

Figure 2.12 Total, Matric, and Osmotic Suction Measurements on Compacted Regina Clay (Fredlund and Rahardjo, 1993)

the water phase is not continuous except for the very thin film of water around the solids. This stage is called "*pendicular*" stage.

At higher degrees of saturation, both water and air phases are continuous and water flow is expected to occur. This stage is termed as '"Funicular" stage. As the degree of saturation increases, the air in the water turns into small bubbles and the air phase becomes discontinuous. The air bubbles can be transported along with the water, and the soil may reach full saturation, which is "Insular air" stage. As the water content changes in a soil profile, the pore pressure also changes. As the soil is drained, the total or matric suction will increase. Suction will reduce when soil is re-filled with water. By comparing the amount of drained water with the increase in suction, a relationship between the degree of saturation (or volumetric water content) and the matric suction of the soil can be established. This relationship is called the soil water characteristic curve of a soil.

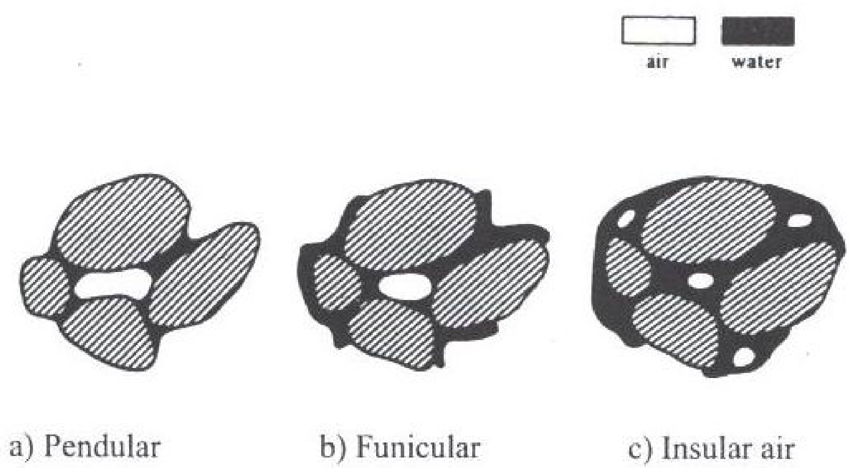

Figure 2.13 Possible Water Saturation Stages (Bear, 1979)

The soil-water characteristic curve can be obtained by performing tests using pressure plate device in the laboratory by following the axis-translation technique (Hilf, 1956). In the late 1950's, soil-water characteristic curve was commonly used to predict the coefficient of permeability at specific water content in terms of matric suction (Mashall, 1958, Millington and Quirk, 1961). This soil-water characteristic curve is also required in the determination of water volume changes in the soil respect to matric suction change. The coefficient of water volume change with respect to matric suction is given by the slope of the soil-water characteristic curve. For these applications, it is more useful if soil-water characteristic curve can be expressed as an equation. Over the last few decades, a number of equations have been suggested based on shape of the curve. These equations can be grouped into the number of curve-fit parameters that have to be determined (unknown parameters) as follows:

The two-parameter equations

Williams Model (1996):

$$\ln\psi = a + b\ln\theta_w \qquad \text{(unknowns: } a, b\text{)} \qquad (2.15)$$

where θ_w is volumetric water content and ψ is soil suction.

The three-parameter equations

Gardner Model (1956):

$$\theta_w = \theta_r + \left(\frac{\theta_s - \theta_r}{1 + a\psi^b}\right) \qquad \text{(unknowns: } \theta_r, a \text{ and } b\text{)} \qquad (2.16)$$

where θ_w is volumetric water content; θ_s is saturated volumetric water content; θ_r is residual volumetric water content; and ψ is soil suction.

Brooks and Corey Model (1964):

$$\theta_w = \theta_r + (\theta_s - \theta_r)\left(\frac{a}{\psi}\right)^b \qquad \text{(unknowns: } \theta_r, a \text{ and } b\text{)} \qquad (2.17)$$

where θ_w is volumetric water content; θ_s is saturated volumetric water content; θ_r is residual volumetric water content; and ψ is soil suction.

Note: equation 2.17 is valid for ψ greater than or equal to *a* (air-entry value). For ψ less than *a*, θ_w is equal to θ_s. For larger values of ψ, 2.17 will give similar values as 2.16.

McKee and Bumb Model (1984):

$$\theta_w = \theta_r + (\theta_s - \theta_r)\exp\left(\frac{a-\psi}{b}\right) \qquad \text{(unknowns: } \theta_r\text{, } a \text{ and } b\text{)} \qquad (2.18)$$

where θ_w is volumetric water content; θ_s is saturated volumetric water content; θ_r is residual volumetric water content; and ψ is soil suction.

McKee and Bumb Model (1984):

$$\theta_w = \theta_r + \frac{(\theta_s - \theta_r)}{1+\exp\left(\frac{\psi - a}{b}\right)} \qquad \text{(unknowns: } \theta_r\text{, } a \text{ and } b\text{)} \qquad (2.19)$$

where θ_w is volumetric water content; θ_s is saturated volumetric water content; θ_r is residual volumetric water content; and ψ is soil suction.

Fredlund and Xing Model (1994) with correction factor C(ψ) =1:

$$\theta_w = \frac{\theta_s}{\left[\ln\left[e + \left(\frac{\psi}{a}\right)^b\right]\right]^c} \qquad \text{(unknowns: } a\text{, } b \text{ and } c\text{)} \qquad (2.20)$$

where θ_w is volumetric water content; θ_s is saturated volumetric water content; θ_r is residual volumetric water content; ψ is soil suction; and *e* is void ratio.

Fredlund and Xing (1994) had mentioned that $C(\psi)$ is approximately equal to 1 at low suctions as the curve at the low suction range is not significantly affected by $C(\psi)$. With $C(\psi)$ =1, θ_w is not zero when ψ is 1,000,000 kPa.

The four-parameter equations

Van Genuchten Model (1980):

$$\theta_w = \theta_r + \frac{\theta_s - \theta_r}{\left(1 + a\psi^b\right)^c} \qquad \text{(unknowns: } \theta_r, a, b \text{ and } c\text{)} \qquad (2.21)$$

where θ_w is volumetric water content; θ_s is saturated volumetric water content; θ_r is residual volumetric water content; and ψ is soil suction.

Fredlund and Xing Model (1994):

$$\theta_w = \left[1 + \frac{\ln\left(1 + \frac{\psi}{\psi_r}\right)}{\ln\left(1 + \frac{1{,}000{,}000}{\psi_r}\right)}\right] \frac{\theta_s}{\left[\ln\left[e + \left(\frac{\psi}{a}\right)^b\right]\right]^c} \qquad (2.22)$$

(unknowns: θ_r, a, b and c)

where θ_w is volumetric water content; θ_s is saturated volumetric water content; ψ is soil suction; ψ_r is soil suction in residual condition that can be computed or assumed to be a value such as 15000 kPa or 3000 kPa; and e is void ratio

Fredlund and Xing Model (1994), if the residual water content θ_r is required:

$$\theta_w = \theta_r + \frac{\theta_s - \theta_r}{\left[\ln\left[e + \left(\frac{\psi}{a}\right)^b\right]\right]^c} \qquad \text{(unknowns: } \theta_r, a, b \text{ and } c\text{)} \qquad (2.23)$$

where θ_w is volumetric water content; θ_s is saturated volumetric water content; θ_r is residual volumetric water content; ψ is soil suction; and e is void ratio.

These equations have been developed to describe the soil-water characteristic curves of control samples. However, the variations in constant parameters can be used to explain void ratio distribution and particle size distribution in soils. A summary of the equations and applications of these equations are reported in Sillers et al. (2001). The equation 2.20 was proposed to be used in this research since it can easily provide the general soil suction properties effects of sandy and clayey soil samples.

In the present work, an attempt has been made to assess soil-water characteristic curves under two different K_0 stress state conditions: controlled radial confinement approach and controlled anisotropic stress state approach.

2.6.2 Measurement of Total Suction

Total suction or the free energy of the soil water can be determined by measuring the vapor pressure of the soil water or the relative humidity in the soil. The direct measurement of relative humidity in soil can be conducted using a device called a Psychrometer. The relative humidity in soil can be indirectly measured by using filter paper as a measuring sensor.

2.6.2.1 Psychrometer (Direct Measurement)

The thermocouple psychrometers can be used to measure the total suction of soil by measuring the relative humidity in the air phase of the soil pores or the region near the soil. Nowadays, the most commonly used instrument is the Wescor Dew Point Microvoltmeter. Figures 2.14 and 2.15 show the C-52 sample chamber with dew point microvoltmeter, which is used in the laboratory.

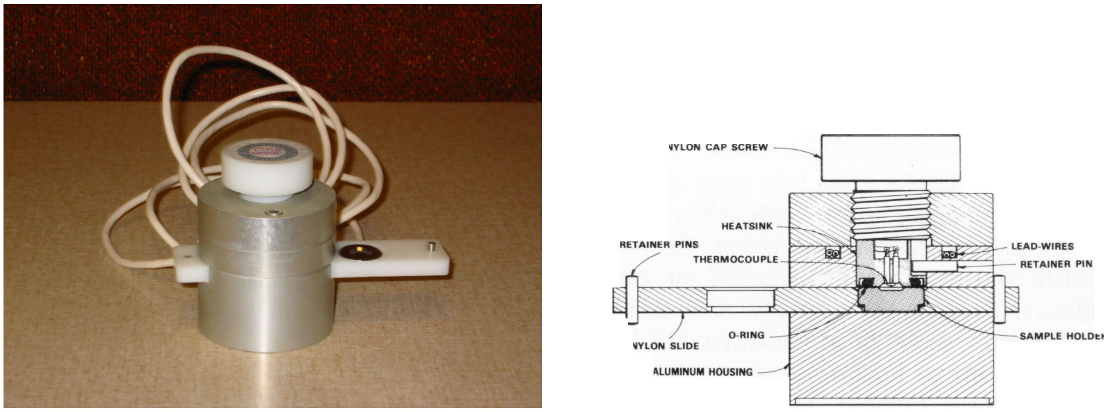

Figure 2.14 External and Internal C-52 Sample Chamber (Psychrometer Tests)

Figure 2.15 Wescor Dew Point Microvoltmeter (HR 33T) for Psychrometer Test

2.6.2.2 Filter Paper (Indirect Measurement)

Filter paper method is classified as an "indirect method" of measuring soil suction. It is based on the assumption that filter paper will come into equilibrium with the soil having a specific suction. Equilibrium can be reached by either liquid or vapor moisture exchange between the soil and the filter paper. After the filter paper reaches equilibrium, the water content of the filter paper was measured. As shown as in figure 2.16, there are two types of filter papers used in practice, which are contact and non-contact filter papers. The water content of contact paper corresponds to the matric suction, and the water content of non-contact filter paper corresponds the total suction of the soil.

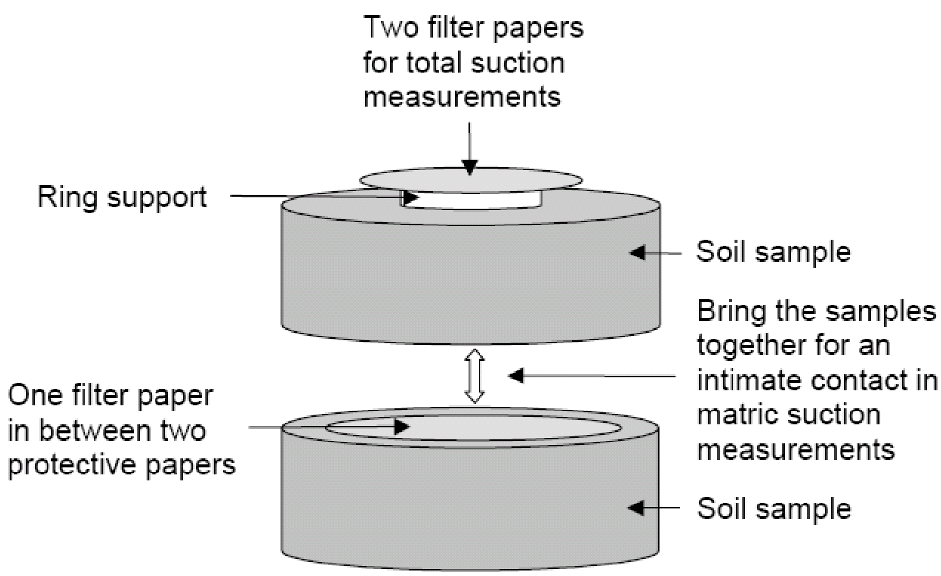

Figure 2.16 Contact and Noncontact Filter Paper Methods for Measuring Matric and Total Suction (Bulut et al., 2001)

2.6.3 Measurement of Matric Suction

Matric suction can be measured either in a direct or indirect manner. Tensiometer, piezometer, and the axis-translation apparatus are commonly used as a direct measurement. Indirect measurement of soil matric suction can be made using a standard porous block as the measuring sensor.

2.6.3.1 Direct Measurement Methods

2.6.3.1.1 Tensiometers

Tensiometer measures matric suctions in the field (Richards and Gardner, 1936, Fredlund and Rahardjo, 1993). The tensiometer consists of a high air entry porous cup connected to a measuring device through a narrow, very stiff plastic tube. The negative pressure measured in the tensiometer is equal to the matric suction (if $u_a = u_{atm}$) in the soil. The negative pressure in the tensiometer can be measured by the use of a mercury manometer, electrical pressure transducer, or vacuum gauge. The suction range of the tensiometer is limited due to cavitation in the system when the pressure approaches the vacuum. The upper limit is about 90 kPa. Problems with diffusion of air through the porous cup into the tensiometer constitute another limitation (Fredlund, 1989). Removal of the diffused air and the refilling of water on a regular basis is a method of reduce the problem (Fredlund and Rahardjo, 1993).

2.6.3.1.2 Piezometer

The piezometer, shown in figure 2.17, is the BAT-piezometer. This consists of a chamber closed at the top by a double rubber membrane and surrounded by a porous filter. A special ceramic high-air-entry filter is used in the measurements of the matric suction. The piezometer can be used to measure either a negative or positive pressure relative to the atmospheric pressure depending on whether the ground water table rises above the filter tip or not. This means that the transducer used must be calibrated for both positive and negative pressure ranges (Tremblay, 1995).

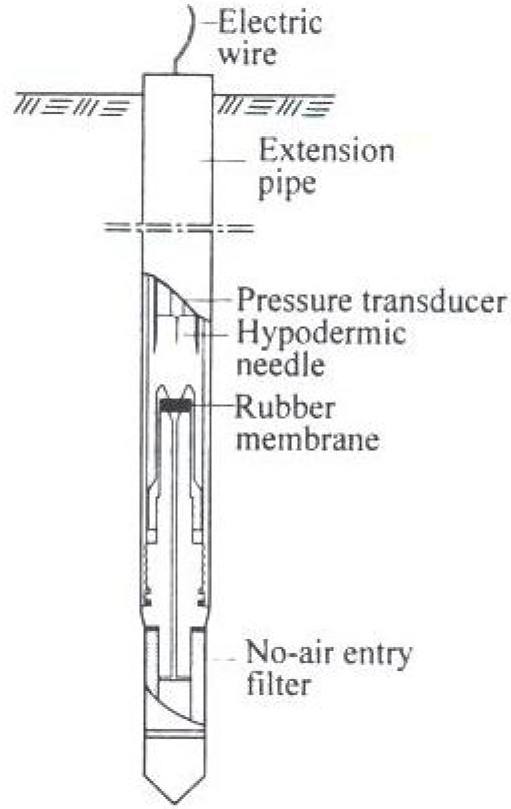

Figure 2.17 The BAT-Piezometer (Torstensson, 1984)

2.6.3.1.3 Null Type Pressure Plate

The null type pressure plate utilizes the axis translation technique (Hilf, 1956) to measure matric suction in soil specimens over a wide pressure range in the laboratory. As shown in figure 2.18, a soil specimen is placed on a saturated high-air-entry porous disc, and the air-tight chamber is pressurized to a desired matric suction. Matric suction is measured versus various different degrees of saturation states of soil sample. This device can measure or induce the suctions in the range of 0 to 100 bars.

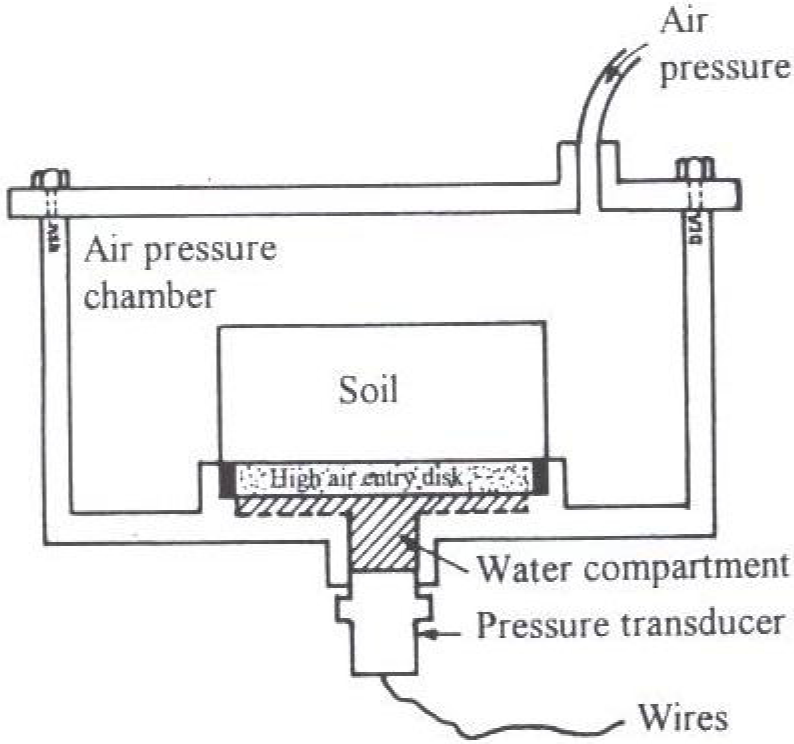

Figure 2.18 Schematic of a Null Type Pressure Plate
(Fredlund and Rahardjo, 1993)

2.6.3.2 Indirect Measurement Methods

Several types of porous sensors are used for performing indirect measurements of the matric suction. A measurement of electrical or thermal properties of the sensor indicates the matric suction both in the sensor and in the surrounding soil (Fredlund and Rahardjo, 1993).

Osmotic suction measurement methods are not presented since that suction is expected to be small and insignificant for expansive soil heave movements. In the present research, various magnitudes of total suctions are applied to soil specimen by using pressure plate device method, and moisture contents were measured at these states when soil sample reached equilibrium states.

2.7 Review Previous Studies

The importance of accurate suction measurements for a better understanding of unsaturated soil behavior has been widely recognized by the scientific and practicing geotechnical society in the last decades. Currently, the requirement of considering suction as a separate variable has been commonly accepted. Efforts have been devoted to better understanding the general rules governing unsaturated soil behavior, proposing state relationships for deformation and failure problems (Fredlund, 1998), as well as for the development of elasto-plastic frameworks capable of predicting the main features of the experimentally observed behavior (Alonso et al., 1990). Although many researchers (e.g., Vanapalli et al., 1996, and many others) have conducted experimental investigations on shear strength behavior with respect to suction and have proposed various models for prediction of shear strength properties from suction, studies on dynamic properties of unsaturated soil are still scarce. Moreover, engineers have long been aware of the potential detrimental effects on unsaturated soil behavior from seismic events (earthquakes). Therefore, there is a great need for a better understanding of the dynamic properties (shear modulus, G, and damping ratio, D) and response of unsaturated soils.

Brull (1980) reported a linear relationship between initial shear stiffness, G_0 and suction for compacted silt and compacted sand, in the range 0-80 kPa of suction. Wu et al. (1985) performed resonant column tests on a silt without controlling suction, but assessing the degree of saturation immediately after measuring stiffness. Their testing procedure consisted in applying a confining pressure on unsaturated specimen under drained conditions and measuring G_0 after 1000 minutes. Finally, they extracted the specimen from the cell to measure S_r. The obtained G_0 and S_r function, for a certain confining stress, shows a distinct peak, corresponding to S_r near 10-20%. The ratio between the maximum shear modulus and the saturated value decreases as the confining pressure increases.

Qian et al. (1991) studied the influence of capillary effects on dynamic shear modulus of partially saturated sands. A Hall-type resonant column apparatus was used to perform the experiments. They reported that capillary stresses can significantly increase shear modulus of unsaturated sands. The void ratio, confining pressure, degree of saturation, grain shape, and grain-size distribution were identified as the primary factors affecting the shear modulus of partially saturated sands.

The experiments described above, nonetheless, was unable to control all the stress variables affecting soil behavior (not performed under controlled suction conditions). Hence the interpretation of their results is not simple, as usually the observed trends of stiffness versus suction hide unknown variations of other factors. Even more difficult is the case when either water content or degree of saturation, rather than suction, is measured (Vassallo and Mancuso, 2006).

Other studies were conducted more recently under controlled suction conditions, but at null (σ-u_a). Marinho et al. (1995) performed bender elements measurements on London Clay specimens assessing suction with the filter paper technique. Their results indicate a maximum in the G_0:(u_a-u_w) relation, in the range Sr = 75-85%. Picornell and Nazarian (1998) reported some results obtained on silt and clay reconstituted samples, using bender elements inside a suction plate. The authors show that a power law can fit G_0 values versus suction and that the moduli tent to a constant value when moving towards residual water content.

Cabarkapa et al. (1999) used the bender elements technique in a triaxial cell and controlled suction via axis translation. The conclusion is that, for normally consolidated quartz silt, and unsaturated G_0 value can be obtained by multiplying the saturated G_0 value pertaining to the same $(p-u_a)$ by a factor depending only on (u_a-u_w). As a matter of fact, every $G_0:(p-u_a)$ curve pertaining to a constant suction level is fitted by a power law with the same exponent. This implies that the ratio between two G_0 values at a certain $(p-u_a)$ but at different suctions, such as the ratio between unsaturated and saturated values, is independent of $(p-u_a)$ level. In the other words "normalized" $G_0/G_{0,sat}:(u_a-u_w)$ curves should plot in a single trend.

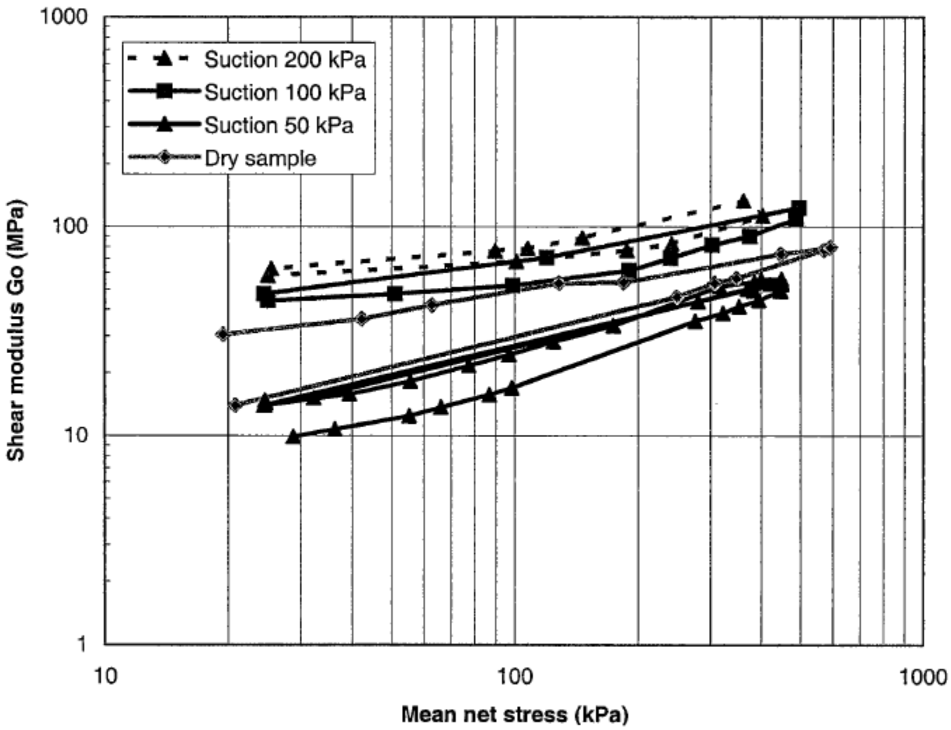

Figure 2.19 Variation of Shear Modulus and Mean Net Stress (Cabarkapa, 1999)

At this period of time most experimental evidence about effects of suction on shear stiffness concerns the triaxial conditions and large strains. Understanding of small and medium strain behavior of unsaturated soils is of greater importance for many engineering applications (Vinale et al., 1999). Lack of experimental evidence on this aspect is probably due to the difficulties that are encountered in developing and working with devices which really allow controlling soil suction. Consequently, data concerning the precise form of the relationship between shear stiffness and suction are rather insufficient and contradictory (Vassallo and Mancuso, 2006).

Santamarina et al. (2001) performed a series of bender element based experiments to gain further insight into behavior of unsaturated particulate materials, with emphasis on pendular menisci stage (figure 2.18). Small strain stiffness was continuously measured on specimens subjected to drying, and changes in stiffness were related to changes in interparticle forces. Microscale experiments were also performed to assess the strain at menisci failure in multiple deformation modes, indicating that the lower the degree of saturation S_r, the lower the strain required to eliminate the effects of capillarity. Hence, while capillary forces affect small-strain stiffness, they may not contribute to large-strain stiffness or strength.

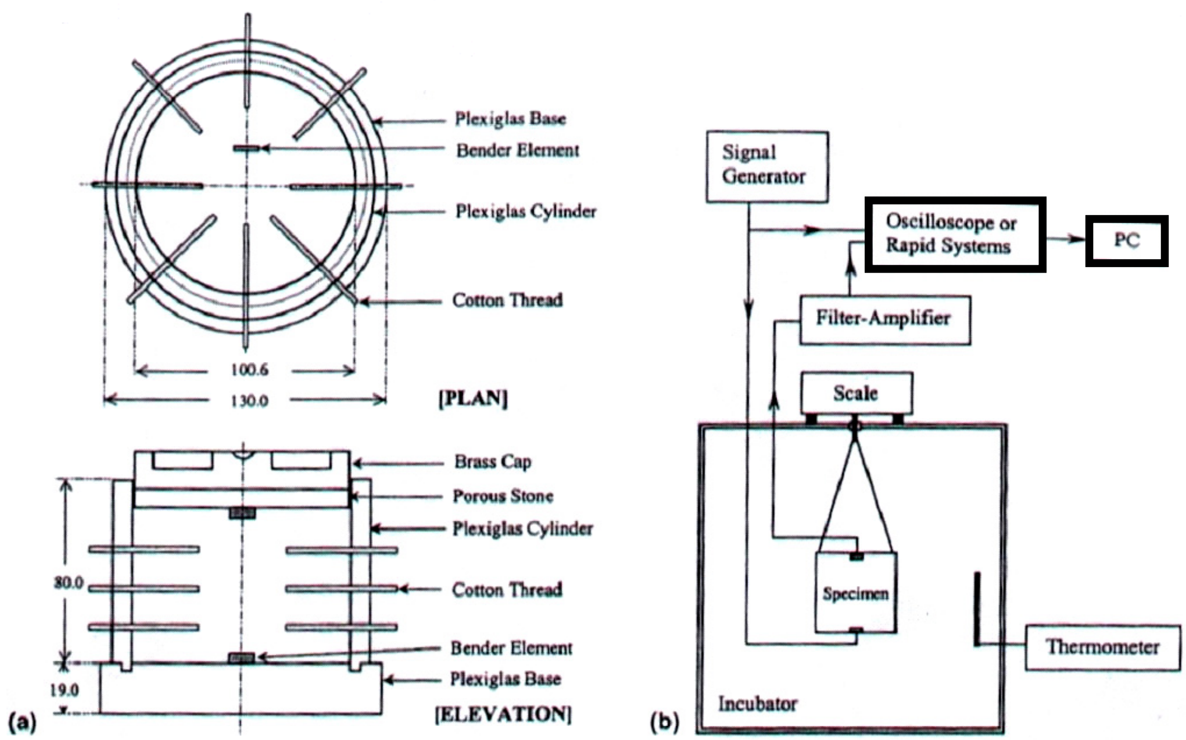

Figure 2.20 (a) Schematic Cell Design; (b) Experimental Setup (Santamarina, 2001)

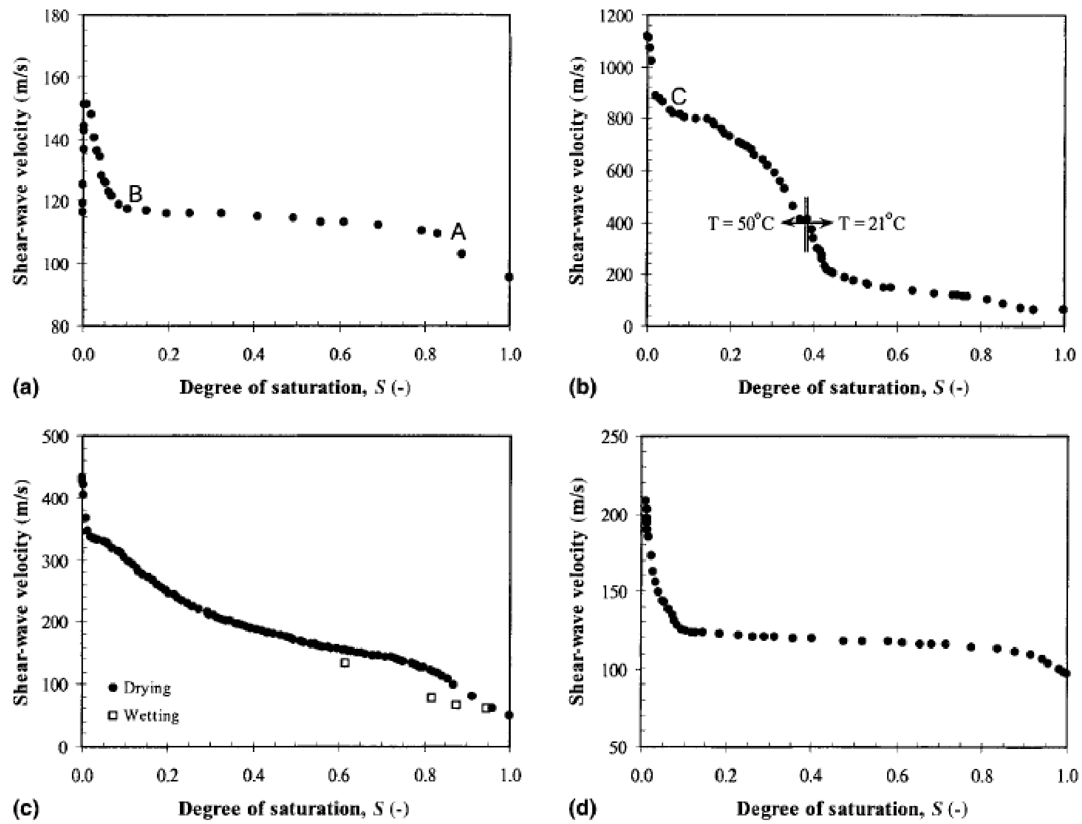

Figure 2.21 Shear-Wave Velocity versus Degree of Saturation for Different Materials: (a) Clean Glass Beads (Deionized Water); (b) Mixture of Kaolinite and Glass Beads; (c) Granite Powder; (d) Sandboil Sand (Santamarina, 2001)

Figure 2.21 shows the results from previous work of shear wave velocity versus degree of saturation for different materials (Santamarina, 2001). It can be noticed that the shear wave velocity decreases when degree of saturation increases.

As demonstrated by this brief bibliography, important efforts have been accomplished in the US since the early 1980's to study the influence of capillarity and degree of saturation on dynamic and stiffness properties of unsaturated soils using either resonant column or bender element testing technique. Even though these works have made a paramount contribution in this area, virtually none has directly dealt with resonant column testing of unsaturated soils under suction-controlled conditions, which would allow for the determination of not only shear moduli (G) and stiffness but also material damping ratio (D).

Only until very recently, Vassallo and Mancuso (2006) performed a series of suction-controlled resonant column and torsional shear tests on unsaturated silty sand using an RC/TS apparatus developed at the University of Napoli, Naples, Italy (Vinale et al., 1999). Matrix suction $\psi = (u_a - u_w)$ was applied via axis-translation technique, and torque was progressively increased to study dynamic response at small-, mid-, and high-shear strain amplitude levels. Results within the small-strain range were similar to those reported by Cabarkapa et al. (1999) using bender element technique, and no attempt was made to study effects of suction on material damping (D) of the silty sand.

Table 2.1 Existing Models from Previous Studies

Dyamic Parameter Model	Author and Year
$G_{max} = S(u_a - u_w)p_a\left(\frac{p - u_a}{p_a}\right)^n f(e)$	(Cabarkapa 1999)
$G_{max} = 87.296\frac{(2.17 - e)^2}{1 + e}(\sigma'_m)^{0.553}$ (MPa)	(Chien and Oh 2002)
$G_{max} = 1000K_{2,max}(\sigma'_m)^{0.5}$	(Seed and Idriss 1970b)
$G_{max} = 49.2q_c^{0.51}$ (MPa)	(Mayne and Rix 1993)
$G_{max} = 32.9q_c^{0.48}e^{-1.23}$ (MPa)	(Jamiolkowski 1994)
$G_{max} = 321\frac{(2.97 - e)^2}{1 + e}(p_a)(OCR)^{0.3}(\frac{\sigma'_c}{p_a})^{0.5}$	(Drnevich 1978)
$G_{max} = 900\frac{(2.17 - e)^2}{1 + e}(p')^{0.4}(p_a)^{0.6}$ (kPa)	(Hardin 1978)
$G_{max} = \frac{s_m}{F(e)}(\sigma'_o)^n(P_a)^{1-n}$ (MPa)	(Hardin and Black 1966)
$G_{max} = 1.64\,\text{MPa}\,\frac{(2.97 - e)^2}{1 + e}(\frac{a_{pr}}{1m})^{0.1}(\frac{p_{pr}}{1kPa})^{0.5}$	(Park and Gobert 1991)
$G_{max} = 3.23\frac{(2.973 - e)^2}{1 + e}(\frac{\sigma'_m}{1kPa})^{0.5}(OCR)^k$ (MPa)	(Hardin and Black 1969)
$D = 6350\gamma^2 + 50\gamma + 1.5$ (%)	(Chien and Oh 2002)
$D = 20.4\left(\frac{G}{G_{max}} - 1\right)^2 + 3.1$ (%)	(Hardin and Drnevich 1972)

Bender element (BE) technique has provided a viable way to investigate soil stiffness at very small strains, and they are starting to be used more widely for saturated soils. However, to date very limited use of the BE technique has been reported for unsaturated soils, and the results are very far from conclusive. There is, therefore, a great need for assessing the feasibility of BE technique for unsaturated soils as compared to more reliable, fully standardized laboratory procedures. The present research work is partly motivated by these research needs. Table 2.1 summarizes some of the empirical models previously proposed for assessing the dynamic properties of soils based on other basic engineering properties.

The following chapter describes the fundamentals of resonant column, bender element, pressure plate, and filter paper testing techniques used in the present research work, including their step-by-step assembling processes.

CHAPTER 3

FUNDAMENTALS OF RESONANT COLUMN, BENDER ELEMENT, PRESSURE PLATE, AND FILTER PAPER TESTING TECHNIQUES

3.1 Introduction

This chapter is devoted to describing the fundamentals of the Resonant Column (RC), Bender Element (TX/BE), Pressure Plate (PP), and Filter Paper (FP) tests and the main components of RC, TX/BE, PP, and RC/BE devices; the step-by-step assembly processes followed in the present work; and the typical soil parameters obtained from these tests. Considerable attention is devoted to the description and fundamentals of the RC, TX/BE, and PP testing techniques.

The Resonant Column device originally developed at UT-Austin is known as the Stokoe torsional shear/resonant column device (TS/RC), and has been continuously refined in the last three decades. The TS/RC testing method is one of the most reliable, efficient, and pragmatic laboratory test methods used nowadays for testing shear modulus (G) and material damping (D) of soils.

In this work, an attempt was made to assess the soil-water characteristic curves (SWCCs) of clay and sand specimens subject to controlled radial confinement and K_o stress states during SWCC testing. A conventional pressure plate extractor was modified to this end.

The series of PP Tests (ASTM D2325-68), TX/BE Tests (ASTM C 778), and RC Tests (ASTM D 4015-92) were conducted on several identically prepared specimens of high plasticity clay and poorly graded sand to assess the reliability of BE results, as compared to RC results, for different suction states in the soil.

3.2 RC Testing

3.2.1 Basic RC Test Configuration

The Stokoe torsional shear/resonant column (TS/RC) testing apparatus can be idealized as the fixed-free system shown in figure 3.1. The test specimen is in the shape of a circular cylinder (solid or hollow). The bottom of the specimen rests on a rough, rigidly fixed surface, and both the top cap and torsional drive plate are securely attached onto the top of the specimen. During RC testing, the drive plate is allowed to rotate freely so that a torsional excitation can be applied at the top end of the soil specimen. The added mass of the top cap and drive plate on top of the soil specimen has the beneficial effect of making the peak torsional displacement nearly linear from top to bottom, that is, induced shearing strains do not vary in the vertical direction.

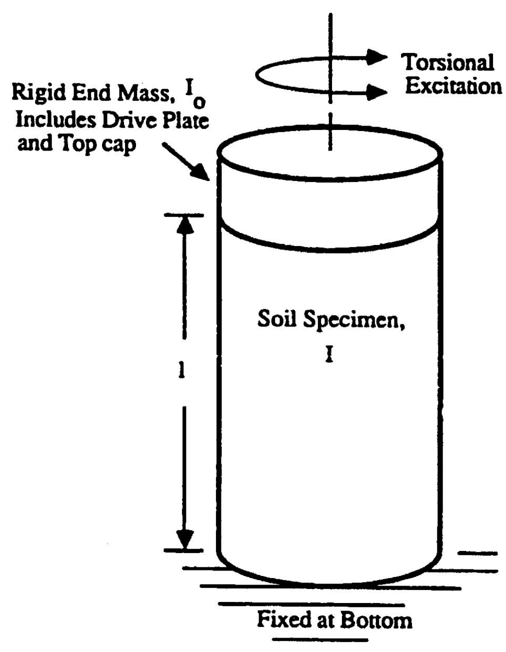

Figure 3.1 Idealization of a Fixed-Free RC Device (Huoo-Ni, 1987)

The above testing description corresponds to a cyclic torque of constant amplitude and varying frequency being applied to the top of the specimen. Variations of the peak torsional displacement with frequency are recorded in order to obtain the frequency response curve. The peak torsional displacements are captured via an accelerometer securely attached to the drive plate.

A typical frequency response curve obtained in this research work is shown in figure 3.2. The resonant frequency (f_r), corresponding to the peak of the curve, is then obtained. Typical values of resonant frequency for soil specimens range from 6 to 150 Hz (Stokoe and Huoo-Ni, 1985). Dynamic soil properties such as G and D are then determined from f_r and the frequency response curve, as described in the following sections.

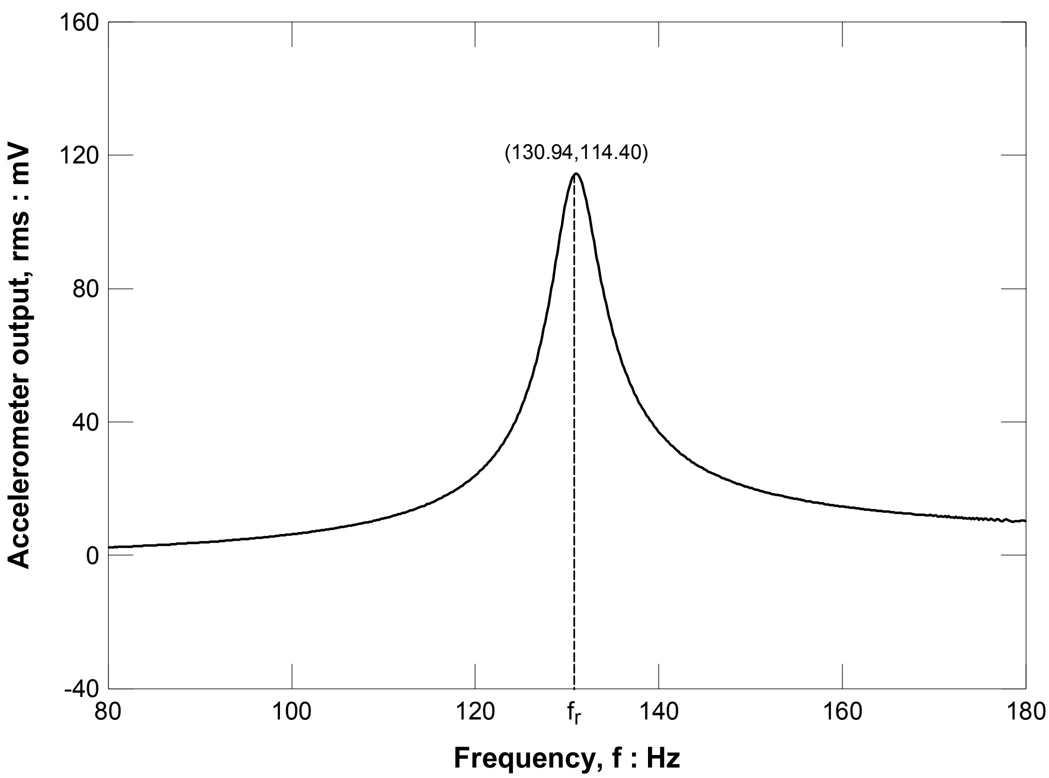

Figure 3.2 Typical Frequency Response Curve from a RC Test

3.2.2 Shear Modulus (G)

For a system undergoing linear vibration, the behavior of the material is linear elastic. In other words, parameters such as stiffness or viscous damping, used to describe the system, are assumed to be constant and independent of frequency and amplitude. For the case of a soil column under torsional vibration, linear vibration theory can be used as long as the peak shearing strain amplitude is less than a threshold limit. Dynamic soil properties below this threshold limit are then considered to be strain independent.

The frequency equation of motion of a fixed-free elastic soil column subjected to harmonic torque at the top can be devised as follows:

$$\frac{\sum I}{I_o} = \frac{\omega_n l}{V_s} \tan\left(\frac{\omega_n l}{V_s}\right) \tag{3.1}$$

where,

$\sum I = I_s + I_m + I_w + \ldots\ldots$

and,

I_s = mass moment of inertia of soil column,

I_m = mass moment of inertia of latex membrane,

I_w = mass moment of inertia of central wire (for hollow specimens),

I_o = mass moment of inertia of top rigid mass (top cap + spider),

V_s = composite shear wave velocity in soil column,

ω_n = natural frequency of soil column (rad/sec), and,

l = length of soil column.

A detailed analytical derivation of equation (3.1), based on second Newton's law, is presented by Huoo-Ni (1987). In practice, the natural frequency (ω_n) of the soil column is replaced by its resonant frequency (ω_r). Nevertheless, using resonant frequency (ω_r) in equation (3.1), instead of natural frequency (ω_n), is only valid for those systems presenting no damping. The relationship between natural and resonant frequencies is given by,

$$\omega_r = \omega_n \sqrt{1-2D^2} \tag{3.2}$$

where D is the material damping ratio. Reviewing equation (3.2), as damping increases, the difference between ω_r and ω_n also increases, which yields to an increasing error being introduced by substituting ω_r for ω_n. Yet, fortunately enough, the damping ratio of most soils is less than 20%, which results in a difference of less than 4.5% between ω_r and ω_n (Huoo-Ni, 1987). In this study, experimental values obtained for material damping D are far less than 20% (from 3% to 8%), hence, it is reasonable to substitute resonant frequency (ω_r) for natural frequency (ω_n) in determining shear wave velocity (V_s) from equation (3.1).

The small-strain shear modulus (G_{max}) of the soil can now be related to shear wave velocity (V_s), using theory of elasticity, as follows:

$$G = \rho (V_s)^2 \tag{3.3}$$

where ρ is the total mass density of the soil (i.e., unit weight divided by gravitational acceleration), $\rho = \gamma/g$. Richart (1975) suggested a simplified method for calculating the shear modulus (G) using the resonant frequency (f_r), obtained from the frequency response curve (figure 3.2), and the geometric characteristics of the soil column and the top cap-driver system. The method can be summarized as follows:

Once the system is under resonance, equation (3.1) can be rewritten in terms of resonant frequency (ω_r) as,

$$\frac{\sum I}{I_o} = \frac{\omega_r l}{V_s} \tan\left(\frac{\omega_r l}{V_s}\right) \quad (3.4)$$

where,

$$\omega_r = 2\pi f_r \quad (3.5)$$

Now, for most cases,

$$\frac{\sum I}{I_o} << 1$$

Therefore, from equations (3.8), (3.9) and (3.10), the shear modulus (G) can finally be expressed as,

$$G = \rho(2\pi L)^2 \left[\frac{f_r}{F_r}\right]^2 \quad (3.6)$$

where F_r is a constant known as the dimensionless frequency factor, and defined as,

$$F_r = \sqrt{\frac{I_s}{I_o}} \quad (3.7)$$

Equations (3.6) and (3.7) were used in the present study for calculating linear (low-amplitude) shear moduli (G). Further details of the RC calibration process is presented by Hoyos (1993) and Chainuwat (2001).

3.2.3 Material Damping Ratio (D)

In the present work, the half-power bandwidth method was used to determine material damping ratio (Richart et al., 1970). This half-power bandwidth approach is based on measuring the width of the frequency response curve near resonance.

Frequencies above and below resonance (f_1 and f_2), corresponding to response amplitude that is 0.707 times the resonant amplitude, are referred to as the half-power points (figure 3.3). Material damping (D) can now be determined as,

$$D(\%) = \frac{1}{2}\frac{f_2 - f_1}{f_r} \tag{3.8}$$

where, f_r is the resonant frequency (Hz). Equation (3.8) was used in the present work for calculating linear (low-amplitude) material damping ratios (D).

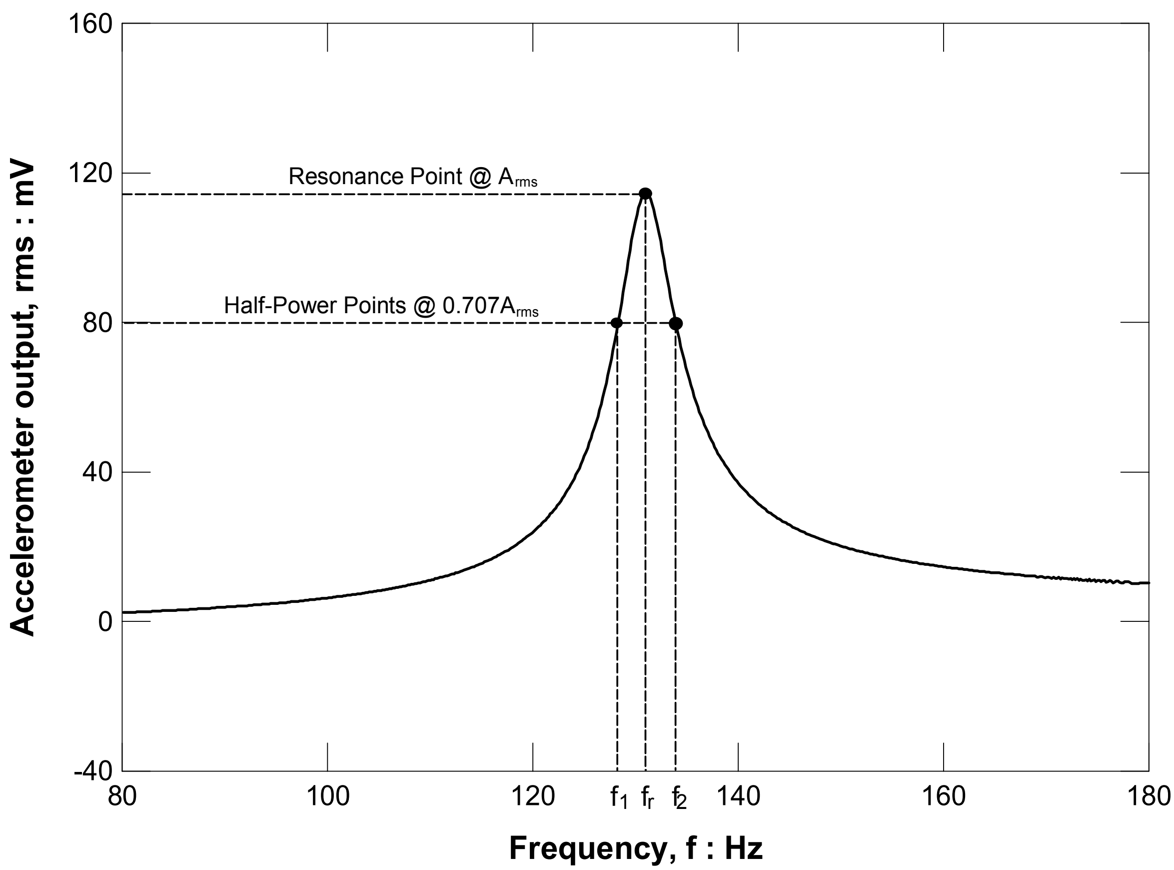

Figure 3.3 Bandwidth Method for Determination of Material Damping Ratio, D

3.2.4 Shearing Strain (γ)

When the top of the soil column is subjected to a torsional displacement, the shearing strain (γ) at any given point within the soil column depends on the distance between this point and the center of the soil column. As depicted schematically in figure 3.4, the shearing strain in a fixed-free hollowed specimen subject to a torque can be determined as $\gamma(r) = r\,\theta_{max}/l$, where r is the radial distance from the central vertical axis of the soil column to the point at which the shearing strain (γ) is being calculated. The shearing strain (γ) increases linearly from 0, at $r = 0$, to a maximum of $r_o\,\theta_{max}/l$, at $r = r_o$, where r_o is the radius of the soil column (Huoo-Ni, 1987).

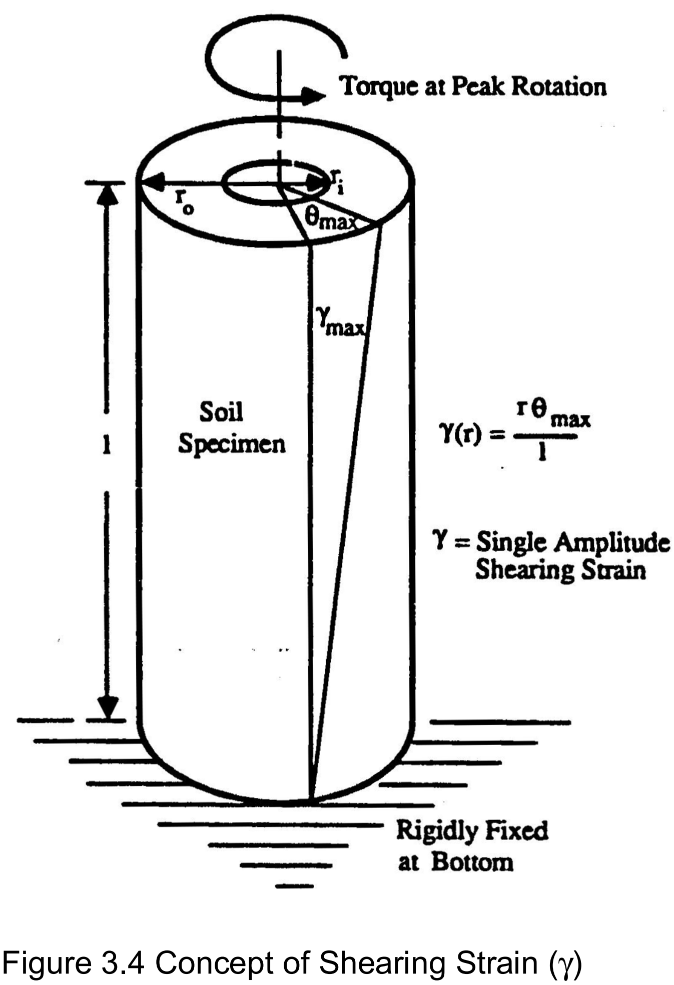

Figure 3.4 Concept of Shearing Strain (γ)

Since shearing strain (γ) is not constant at every point in the soil specimen, an equivalent shearing strain (γ_{eq}) ought to be chosen, which may be represented as $\gamma_{eq}(r) = r_{eq}.\theta_{max}/l$, where r_{eq} is the equivalent radius of a solid specimen utilized in an actual RC test. In the present work, all resonant column (RC) tests were conducted on solid specimens of sulfate-rich clay, and shearing strains (γ) were calculated at a distance of $0.707(r_o)$ from the central vertical axis of the RC test specimen, where r_o is the radius of the specimen. A detailed explanation of how the shearing strains (γ) were calculated from the accelerometer response (Volt) is presented in Hoyos (1993).

3.2.5 Resilient Modulus (M_r)

Resilient modulus (M_r) is the key subsoil stiffness parameter recommended by the American Association of State Highway and Transportation Officials (AASHTO) for pavement design. Resilient modulus (M_r) is used as the basic material property in the design of multi-layered flexible, rigid, or composite pavements, and also as an indication of roughness and potential cracking, rutting, or faulting (AASHTO, 1993).

For practical purposes, the resilient modulus (M_r) is considered to be equal to the elastic Young's modulus (E). Therefore, the resilient modulus (M_r) can be related to the elastic shear modulus (G), using theory of elasticity, as follows:

$$M_r = E = 2G(1+\mu) \tag{3.9}$$

where G is obtained from the resonant column (RC) test, and μ is the Poisson's ratio of the soil. The following sections describe the basic components of the RC device.

3.2.6 Basic Components of RC Testing Device

The resonant column (RC) testing device used in this work is composed of three basic modules or components: confining chamber, torsional drive mechanism, and torsional motion monitoring system. A detailed description of these three basic modules is presented in the following sections.

3.2.6.1 Confining Chamber

The RC confining chamber is composed of a thin-wall hollow cylinder, a base plate, a cover plate, and four guide rods used to secure the base and cover plates to the hollow cylinder. All components are made of stainless steel. The thin-wall hollow cylinder has an outside diameter of 8.5 in (21.6 cm), a wall thickness of 0.25 in (0.64 cm), and a height of 18 in (45.7 cm). Photographs of the base plate and the fully assembled chamber are shown in figure 3.5.

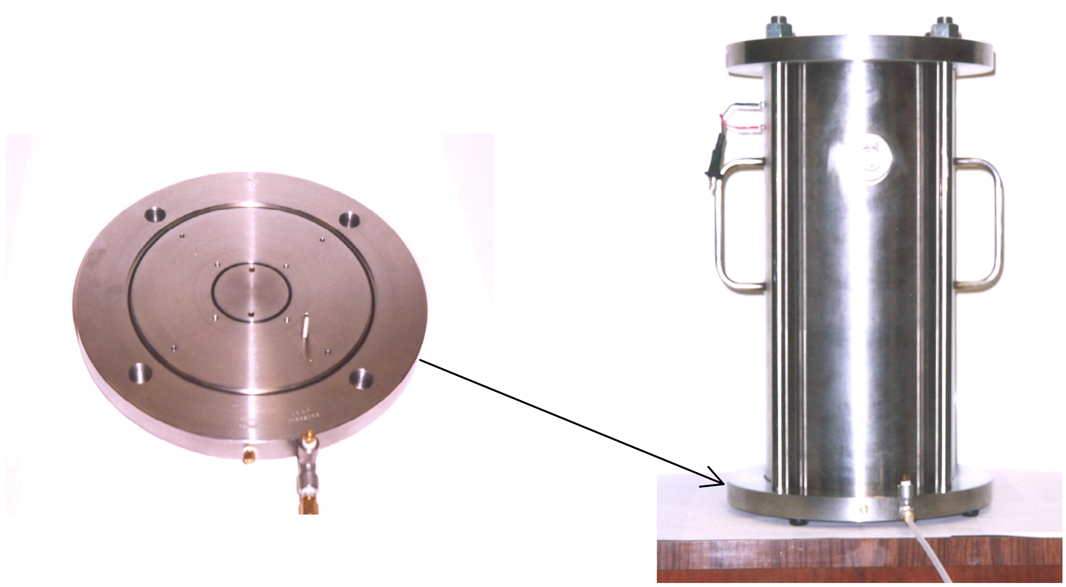

Figure 3.5 Base Plate and Fully Assembled Confining Chamber

Prior to RC testing, the soil specimen, along with the remaining components of the RC device, are placed inside the confining chamber and pressurized with air at the desired isotropic confining pressure. Air pressure is supplied to the chamber via an inlet air-pressure port located at the base plate (figure 3.5). The chamber has been designed to withstand a maximum air pressure of 600 psi (4,173 kPa).

Inside the confining chamber, the RC specimen is seated on a base pedestal. The top surface of the pedestal is extremely roughed to avoid slippage between the soil specimen and the pedestal during torsional vibration. A photograph of the base pedestal tightly secured onto the base plate is shown in figure 3.6.

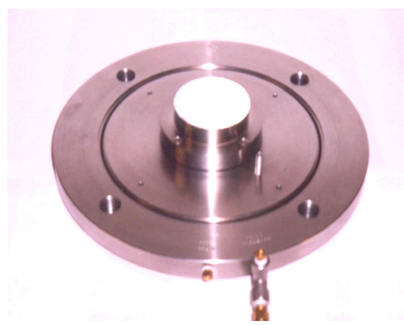

Figure 3.6 Base Pedestal Tightly
Secured Onto Base Plate

3.2.6.2 Torsional Drive Mechanism

The torsional drive mechanism (driver) includes a flat aluminum four-armed plate (spider), with a cubical magnet encircled by a pair of drive coils at each end, and an input signal current connection. The magnets are securely attached to the four ends of the spider, which allow the magnets to move during soil consolidation. Photographs of top and side views of the torsional drive mechanism (driver) are shown in figure 3.7.

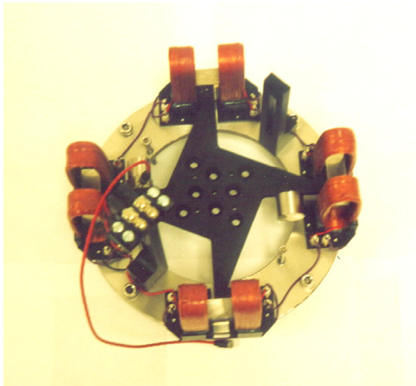

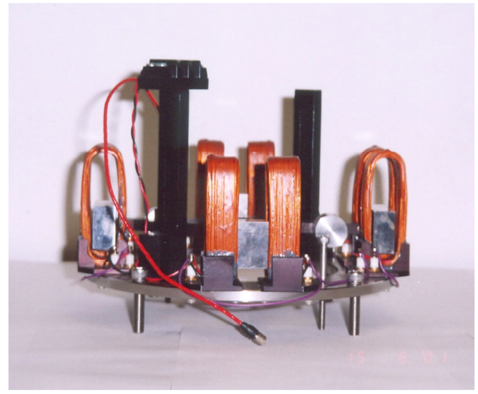

Figure 3.7 Top and Side Views of the Torsional Drive Mechanism (Driver)

The spider and drive coils form a torsional motor that excites the specimen in torsional motion. During RC testing, the spider is fixed to the top cap resting on top of the specimen. The top cap has a rough surface on the side making contact with the specimen to insure that no slippage occurs between the specimen and the driver during torsional excitation. The set of eight drive coils is fixed to a cylindrical cage that is securely attached to the base plate of the chamber, as shown in figure 3.8.

Figure 3.8 Cylindrical Cage Supporting
Set of Drive Coils

3.2.6.3 Torsional Motion Monitoring System

The torsional motion monitoring system is used to capture the frequency response of the soil column during RC testing, and includes an accelerometer rigidly attached to one of the arms of the spider, and an associated counterweight installed on the opposite side of the four-armed spider (figure 3.7). The voltage response of the accelerometer is sent to a charge amplifier and then recorded by a dynamic signal analyzer, as explained in the following section.

3.2.7 Frequency Response Measurement System

The frequency response measurement system used in this work includes a dynamic signal analyzer, a charge amplifier box, and a PC-based computer terminal. The analyzer is a dual-channel SR785-model dynamic signal analyzer acquired from Stanford Research Systems, Inc. The amplifier is a 4102M-model charge amplifier box acquired from Columbia Research Laboratories. Photographs of analyzer and charge amplifier box (resting on top of the analyzer) are shown in figure 3.9.

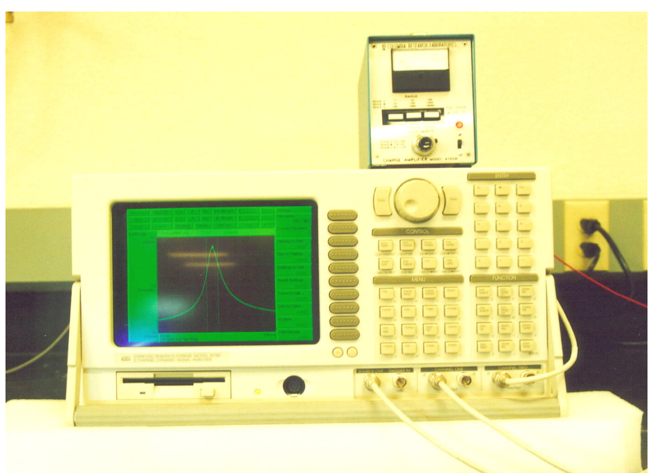

Figure 3.9 SR785 Dynamic Signal Analyzer and
4102 Charge Amplifier Box

From the dynamic signal analyzer, a constant-amplitude sinusoidal current is sent to the driver fixed on top of the soil column (figure 3.7). The sinusoidal current travels along a coaxial cable that transmits the signal, via microdot connectors on the thin wall of the confining chamber, to the driver's input current connection. The signal is distributed among the drive coils of the driver system inducing a sinusoidal torsional excitation on the specimen via the reacting magnets of the spider.

The amplitude of vibration is captured by the accelerometer rigidly attached to one of the arms of the spider, and sent to the charge amplifier box in the form of output voltage response. The amplified signal from the charge amplifier is sent back to the dynamic signal analyzer. A frequency response curve is then obtained by sweeping the entire preset frequency scale in the analyzer, and it can be displayed on the screen of the SR785 analyzer (figure 3.9).

The SR785 analyzer allows for storage and graphic display of the captured data in a PC-based computer terminal. A photograph of the dynamic analyzer and charge amplifier interacting with the RC device is shown in figure 3.10.

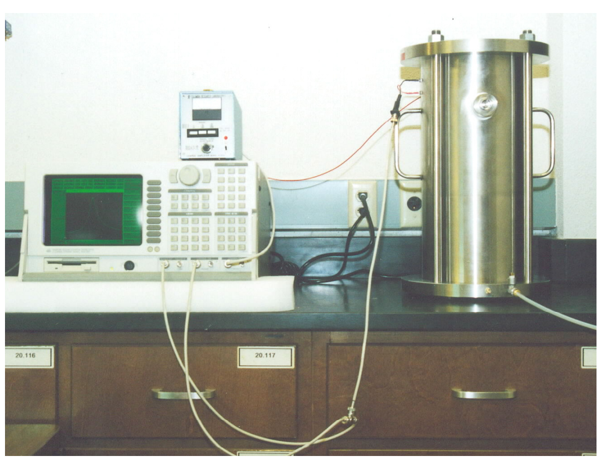

Figure 3.10 Dynamic Analyzer and Charge Amplifier Interacting With RC Device

3.2.8 Apparatus Assembly

A detailed, illustrated description of the step-by-step assembling process of the resonant column (RC) testing device, interacting with the frequency response measurement system, is presented in the following paragraphs.

1. **<u>Specimen placement:</u>** Once the soil specimen has been fully compacted at the desired moisture content, it is carefully placed on the rough-surface base pedestal, with the top cap resting on top of the specimen. A latex membrane is then rolled downward over the specimen and two O-rings are gently placed at the base pedestal and the top cap (figure 3.11).

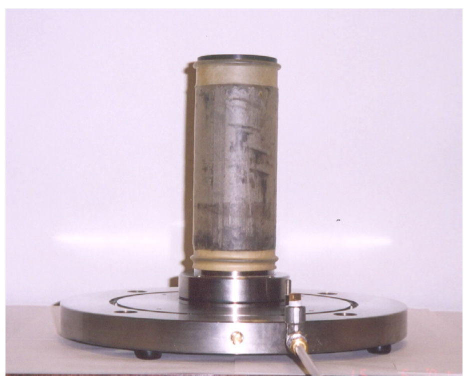

Figure 3.11 Specimen With Membrane
and O-rings Resting on Base Pedestal

2. **<u>Water-bath application:</u>** An inner water-bath acrylic cylinder is placed over the soil specimen and securely fitted into the slip O-ring of the base pedestal until it makes full contact with the base plate (figure 3.12). The space gap between the acrylic cylinder and the specimen is filled with water in order to minimize extrusion of the latex membrane and/or air migration through the specimen upon application of confining pressure (figure 3.13).

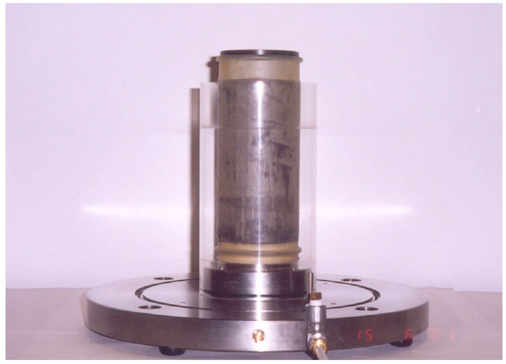

Figure 3.12 Inner Water-Bath Acrylic Cylinder
Fitted Into the Base Pedestal

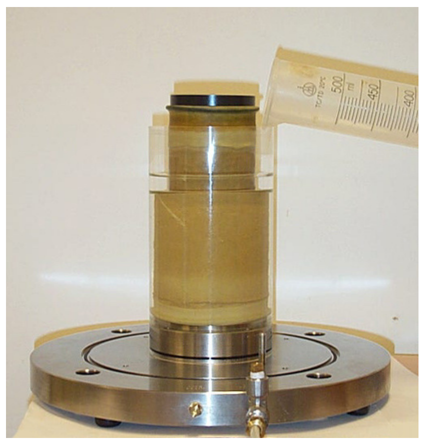

Figure 3.13 Application of Water Bath Between
Acrylic Cylinder and Soil Specimen

3. <u>Torsional driver setup:</u> The stainless steel cylindrical cage is fitted over the specimen and the acrylic cylinder and securely attached to the base plate (figure 3.14). The torsional driver (coils and spider) is then assembled onto the top cap. The spider is attached to the top cap by means of four flat-head screws. The set of drive coils is accommodated such that each magnet is encircled by a pair of coils without contact. The set of coils is finally secured to the cylindrical cage (figures 3.8 and 3.15).

Figure 3.14 Stainless Steel Cylindrical
Cage Attached to Base Plate

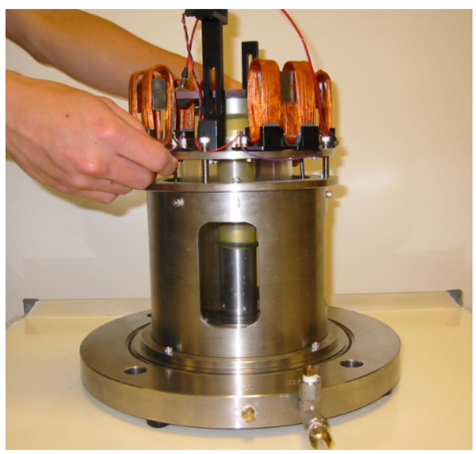

Figure 3.15 Assembling of Torsional Drive
Mechanism (Driver)

4. <u>Confining pressure application:</u> The thin-wall cylinder of the confining chamber is fitted onto the O-ring groove of the base plate. The electrical wiring is then connected to the corresponding microdot connectors on the inner side of the thin-wall cylinder, that is, the input signal current wire and the accelerometer output wire. The cover plate is placed over the top of the vessel and bolted tightly with the four guide rods. Then, the soil specimen, along with the remaining components of the RC device, is pressurized with air at the desired isotropic confining pressure (σ_o). Air pressure is supplied by a HM-4150-model pressure control panel (Humboldt Manufacturing Co.) via an inlet air-pressure port located at the base plate of the confining chamber (figures 3.15 and 3.16). This step concludes the assembly of the RC device prior to RC testing.

Figure 3.16 Application of Isotropic Confining
Air-Pressure From HM-4150 Panel

5. **<u>Frequency response measurement system setup:</u>** The electrical wiring of the SR785 dynamic signal analyzer and the 4102M charge amplifier box is then connected to the corresponding microdot connectors on the outer side of the thin-walled cylinder, that is, the input signal coaxial wire and the accelerometer input wire. The analyzer is then configured at the desired test settings, including amplitude of sinusoidal signal, range of frequency scale, swept-sine testing mode, and number of data points to be recorded (figures 3.17 and 3.18).

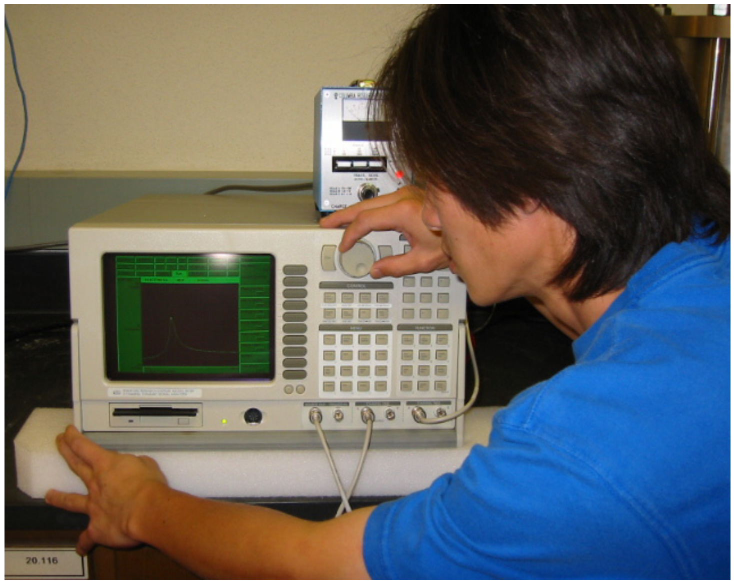

Figure 3.17 Pre-setting of the SR785 Dynamic
Signal Analyzer Prior to RC Testing

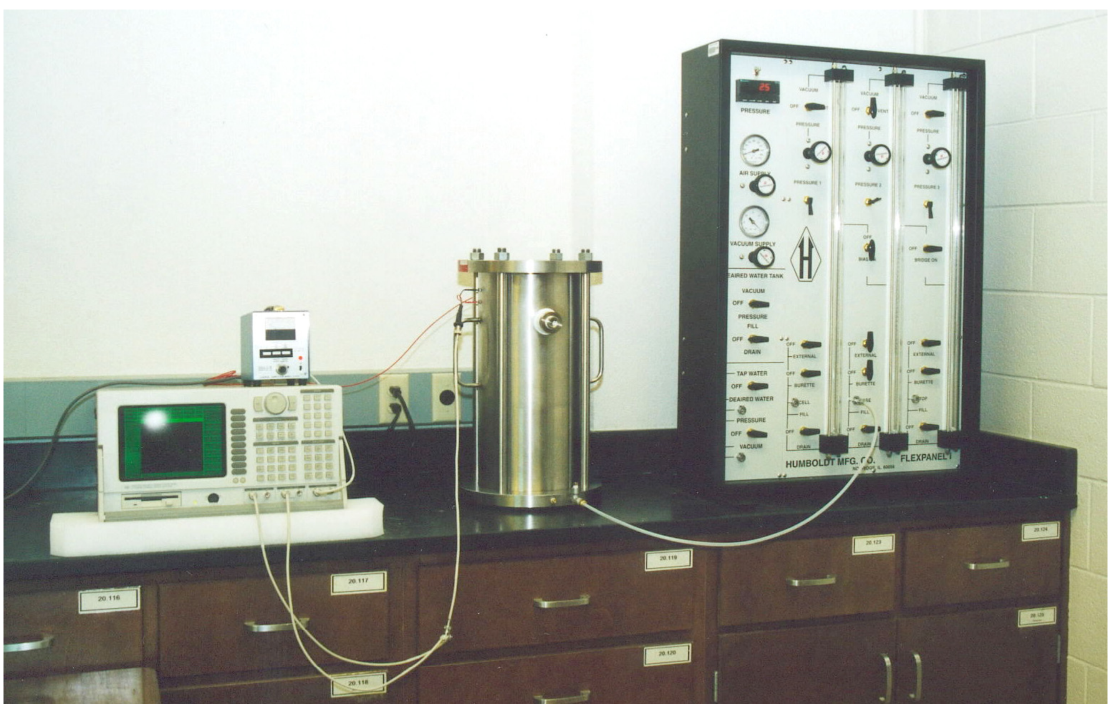

Figure 3.18 Analyzer, Amplifier and Panel Interacting with RC Device

6. Frequency response data capturing and storage: Once the swept-sine mode RC test has been completed, the frequency response curve and captured test data are transferred to the CPU of the PC-based computer terminal for future data processing using software such as Excel, Grapher, and Statistica. A photograph of the dynamic analyzer interacting with the computer terminal is shown in figure 3.19.

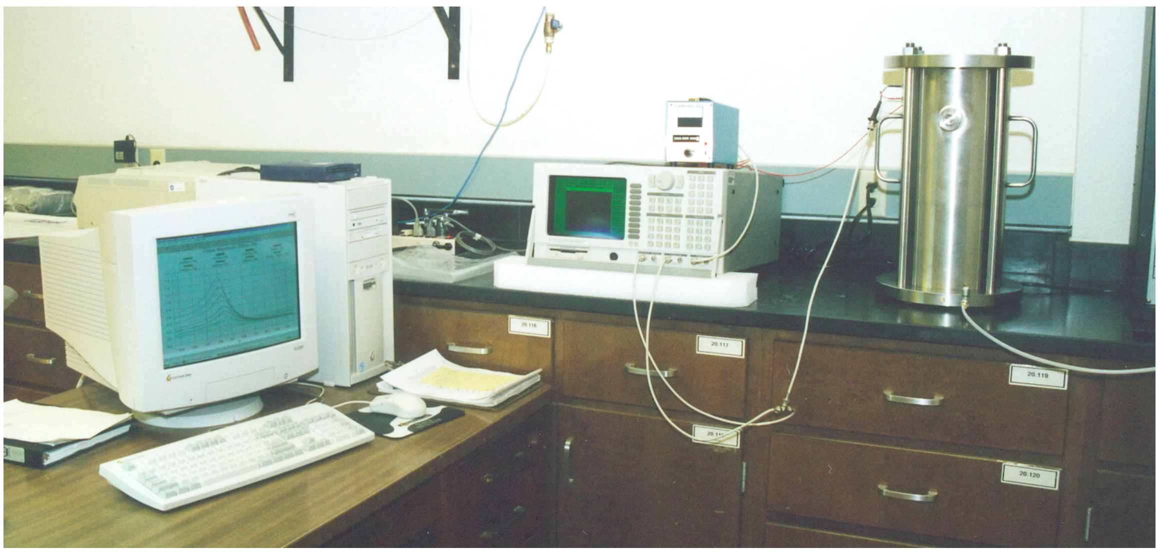

Figure 3.19 Dynamic Analyzer Interacting With PC-Based Computer Terminal

3.3 BE Testing

3.3.1 Introduction

A bender element is a thin piezoceramic element made of two transversely poled plates bonded together with surface electrodes coating it. Bender element systems can be set up in most laboratory apparatus, however, are particularly versatile when used in the triaxial test as described by Dyvik and Madshus (1985). Piezoceramic plates, or 'bender elements', are embedded in the base pedestal and the top platen of the triaxial apparatus (Jovicic et al., 1995). Base pedestal and the top platen can be of different sizes those specified by ASTM. The cantilevering length of bender elements can also be variable. Generally available sizes are 3 mm, 5 mm and 9 mm. The cantilevering length of the bender elements at the transmitting as well as receiving end should be the same.

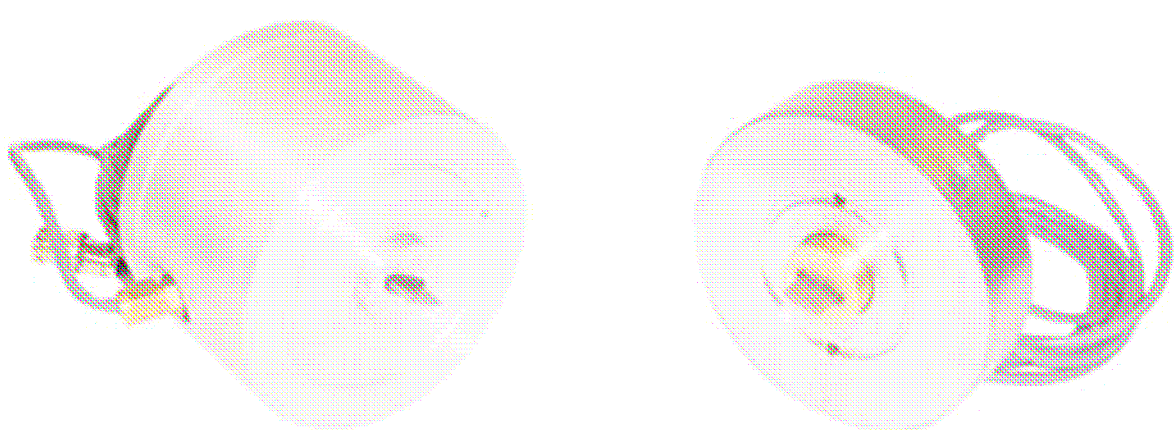

Figure 3.20 A Typical Set of Transmitter and Receiver Bender Elements

A pulse generator and a function generator feed the transmitter element with a waveform voltage, typically of 20 V, causing it to bend so that shear pulse is sent through the sample. The piezoelectric plates are reversible in their function so that the motion of the receiver element caused by the arrival of the pulse generates a small voltage, typically of 0.1-5 mV. The transmitted and received waves are captured and displayed by a digital oscilloscope which is connected parallel to personal computer, and the value of G_{max} is calculated from the velocity of the shear wave, V_s, as it travels through the sample.

Typically a square wave was used as a transmitting wave, but the complexity arises from the fact that a square wave is composed of a spectrum of different frequencies. Viggiani and Atkinson (1995) attempted to reduce the degree of subjectivity in the interpretation, and to avoid the difficulty in interpreting the square wave response, they suggested a sine pulse as the input signal. Being mainly of one frequency, the output wave was generally of a similar shape, which allowed them to apply numerical techniques to reduce the uncertainty in the arrival time to around ±7%. A substantial improvement in the quality of the received trace which is made by carefully shielding the cables to the elements so that neither external amplification of the signal prior to the oscilloscope is needed, nor any filtering or averaging of the data.

3.3.2 Advantages of Bender Elements over Other Laboratory Methods

Most of the ground surrounding structures experience shears strains of magnitude less than 0.1%. Hence, under working conditions, the soil behavior is controlled by its properties at small strain levels (Simpson et al., 1979, Jardine et al., 1986, Burland, 1989).

The resulting stress-strain relationships obtained using triaxial tests are highly non-linear even at small strain levels (from 0.01% to 0.1%) for a wide range of soil types (Jardine et al., 1984). Resonant column device is based on torsional excitations at very small strains, sweeping the frequency around the resonance peak. The resonant column test can be used to evaluate the stiffness of soils at shearing strains ranging from 0.00001% to 1%. However, since analysis of resonant column tests are based on the assumption that the behavior of the soil is linear and elastic; analysis of the test data is strictly valid only in the region of very small strain (Isenhower, 1979). The difficulty with the resonant column test is that both driving apparatus used for the excitation of the soil specimen and motion monitoring instruments must be attached to the soil specimen. This alters the specimen boundary conditions so that the interpretation of the test is based on the assumption that the attachments are lumped into a mass which oscillates with the soil specimen. Using bender elements, the instantaneous shear wave velocity and small strain shear modulus can be obtained at very small strains. Strains in the soil skeleton in both methods are less than 10^{-5} percent. Bender elements can be installed in many devices such that the need for parallel resonant column test may be eliminated. Measurement and calculation of G_{max} is much faster and easier than in the resonant column device, and shear modulus at small and large strains can be compared directly on the same specimen.

In bender element method, strains are not constant throughout the sample because of both material and geometric damping. Bender element is a compatible technique for evaluation of variations of low strain shear moduli against elapsed time. This non-destructive technique is a simple way to measure low strain shear moduli of soils and can be carried out several times to verify the test results.

3.3.3 Working Mechanism

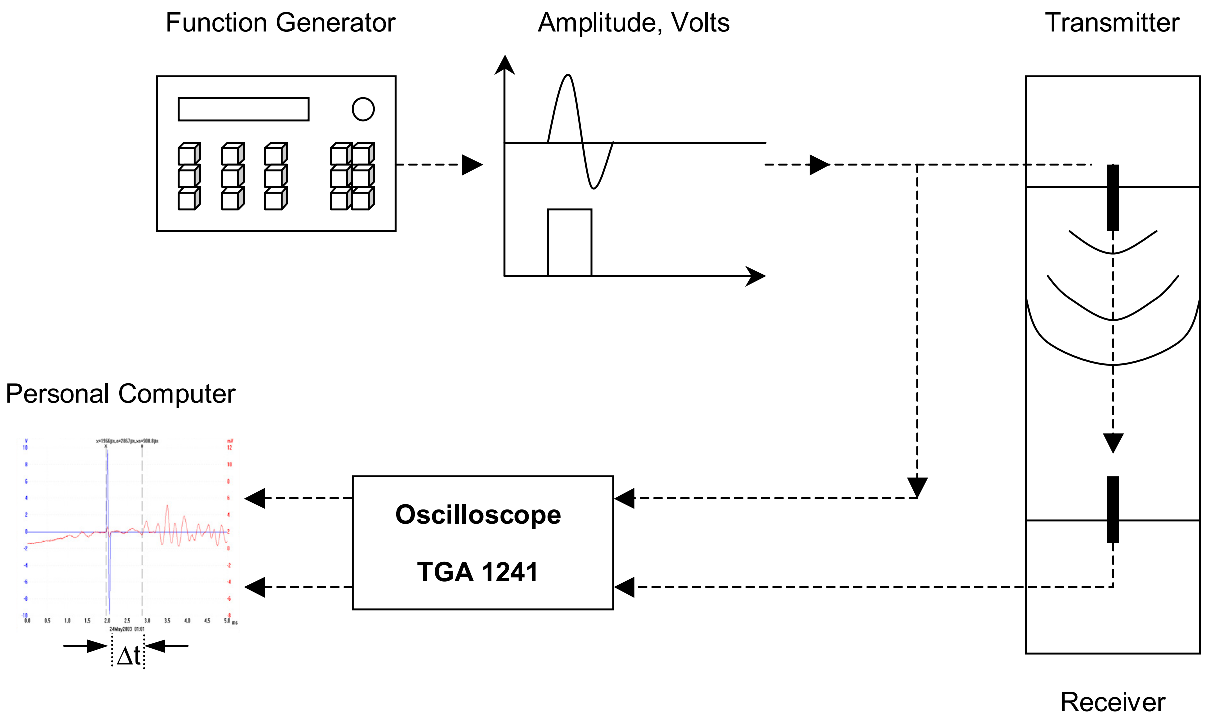

Figure 3.21 Schematic Representation of Principle of Bender Elements

Shear waves can be generated and measured by small pieces of piezoceramic called bender elements, which can be installed in the end caps of the specimens. Piezoceramics have the ability to convert electrical impulses to mechanical impulses and vice versa. When a voltage impulse is applied across a single sheet of piezoceramic, it will either shorten or lengthen with a corresponding increase or decrease in thickness. If two piezoceramic sheets are mounted together with their respective polarities opposite to each other, an electrical impulse will cause one side to lengthen and the other side to shorten. The net result of this will be a bending of the two sheets, hence the name bender elements.

Thus, if an electrical impulse is sent to a bender element mounted in the top cap of a specimen, the bender element will produce a small “wiggle” and generate a shear wave that will propagate down through the soil. When the shear wave reaches the bottom of the specimen it will cause the bender element mounted in the bottom cap to vibrate slightly, thus creating an electrical impulse. Using a parallel connection between personal computer and an oscilloscope, one can observe both the impulse that is sent to the top bender element (transmitter) and the impulse that is generated by the bottom bender element (receiver), the time it took the wave to propagate can be measured directly, and is called arrival time.

3.3.4 Equipment Details

The equipment required to operate the bender elements is shown schematically in figure 3.21. There are four important components for a good bender element setup: the oscilloscope, signal generator, bender elements and the personal computer.

The important aspects of an oscilloscope for the study of shear waves through soils include the sampling rate, resolution, and storage capabilities. Bringoli et al. (1996) suggest that a minimum sampling rate of 20 x 10^6 samples per second is necessary for accurate shear wave velocity measurement. Typical sampling rates for new digital oscilloscopes are 50 x 10^6 samples per second and are sufficient for testing soil at frequencies less than 100 kHz.

The resolution of the oscilloscope, meaning the smallest voltage signal that can be accurately observed, is extremely important. The received signal of the shear wave velocity is very small, usually between 0.1 and 5 mV. Using an oscilloscope with good resolution can remove the need for complicated post-processing techniques such as stacking (adding signals to increase the voltage of the received signal) or using amplifiers on the received signal.

The signal generator TGA1241 used with the bender elements produces user defined pulsed signals to the bender receiver. Different types of wave shapes, frequencies and amplitudes can be set depending on the application for which it is to be used. The synthesized programmable arbitrary waveform generator has 40MHz sampling frequency and 12 bit vertical resolution. With the signal generator, it is possible to send a number of different input signals to the transmitting bender element, including square waves, sine waves, halve sine and high frequency pulses, etc. The maximum voltage that could be outputted from the signal generator or signal could be supplied to the transmitter is 20 V. In general, a larger input signal results in a larger received signal, which usually makes interpretation of the signal easier. Larger received signals can be obtained using amplifiers if the received signals are very weak which makes their interpretation difficult. During the tests, the frequency of the driving signal is adjusted to get the received signal of optimal amplitude and shape.

Because the amplitude of the received signal is very small, it is critical that electrical noise be minimized. For this reason, the wiring of the bender elements is very important and 3.18 mm coaxial cable was used. Dyvik and Madshus (1985) identified two different possible wiring setups for bender elements: a series connection and a parallel connection. These are shown in figure 3.22. The series connection has a positive and negative lead attached to either piezoceramic sheet. The parallel connection has two positive leads attached to the piezoceramic sheets with the negative lead attached to the steel shim mounted in between. This is significantly more difficult to fabricate because a portion of the piezoceramic material must be ground away to access the steel shim. With a parallel connection the available voltage is applied to each ceramic plate and is not divided between them

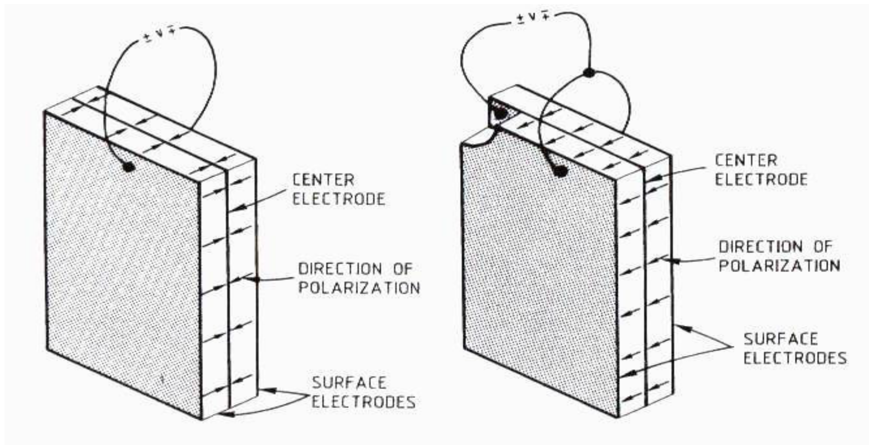

Figure 3.22 Series and Parallel Connected Piezoceramic Bender Elements
(Dyvik and Madshus, 1985)

as in the series connection. An element with parallel-connected electrodes will provide twice as displacement as one with a series connection and is therefore preferred to transmit the energy of movement to the soil.

Dyvik and Madshus (1985) reported that the parallel connection was more effective for transferring electrical impulses to mechanical impulses, and the series connection was more effective converting mechanical energy to electrical signals. Thus the parallel connection is reported to be better for a transmitting bender element, while the series connection is better for a receiver.

The bender elements are placed in a vacuum top cap and base pedestal. The top and base pedestals of standard sizes like 70, 100 or 150 mm are available in the market. Because the bender elements operate by creating a voltage drop across the two piezoceramic sheets, the presence of water will short circuit the system. It is thus imperative to coat bender elements with a good waterproofing material, especially for long term tests. The coated bender elements were set into 3 mm wide slots that were cut into the top caps and the base pedestal.

3.3.5 Near-field Effects

Theoretical studies by Sahnero et al. (1986) show that the first deflection of the signal may not correspond to the arrival of the shear wave but to the arrival of the so-called near-field component which travels with the velocity of a compression wave. Evidence for the existence of near field components in bender element tests was found by Brignoli and Gotti (1992). Parametric studies of the propagation of elastic waves in an elastic medium by Mancuso and Vinale (1988) show that the near-field effect may mask the arrival of the shear wave when the distance between the source and the receiver is in the range ¼-4 wavelengths, which can be estimated from $\lambda = V_s/f$ where f is the mean frequency of the received signal. Inverting the polarity of the source wave inverts the polarity of all the components of the shear wave, including the near-field components, and therefore does not positively identify it (Viggiani and Atkinson, 1995a).

Bender elements are like antennas which tend to pick up every little electrical noise. Due to electrical short, transmitting wave is followed by the immediate response from the receiving wave. So cables should be insulated and grounded properly in order to get rid of the noise.

Near-field effects in bender element tests have been recognized by previous investigators (Brignoli and Gotti, 1992, Viggiani and Atkinson, 1995, Jovicic et al., 1996) with references made to the findings of Sanchez-Salinero et al. (1986). However "near-field" effects are potentially more complicated in triaxial specimen than in the unbounded 3-D space considered by Sanchez-Salinero et al. (1986) because:

(1) interpretation methods that use the input signal are similar using d_1/λ of zero (where d_1 is the distance from the source to first receiver), and so near-field waves will be stronger than were considered in many of their analyses.

(2) the spherically spreading wave fronts that are generated by transmitting bender can reflect from the boundaries and therefore travel between benders by indirect paths and

(3) the transmitting bender is not a point source. Consequently, the assumption of planar wave fronts moving one-dimensionally between the caps will introduce errors that are in addition to the near-field effects identified by Sanchez-Salinero et al. (1986). Furthermore the transfer functions relating the physical waveform to the measured electrical signals introduce significant phase or time lags that are different at the transmitting and receiving benders (Arulnathan et al., 1998).

3.3.6 Time of Flight

The principal problem with bender elements method has always been the subjectivity of the determination of the arrival time used to measure shear wave velocity. Researchers have faced considerably greater difficulty in establishing a procedure for accurately evaluating the travel time of the shear wave. The shape of the arriving wave can vary substantially depending on the geometry and fabrication of the apparatus, the specimen properties, and the nature of the transmitted pulse, making a precise interpretation of the travel time difficult.

3.3.6.1 Travel Time of First Direct Arrival in the Output Signals

Travel time of an impulse wave between two points in space may be taken as the time between the first direct arrival of the wave at each point. This method of interpretation assumes plane wave fronts and the absence of any reflected or refracted waves (Arulnathan et al., 1998).

In applying this approach to bender element tests, travel time has been estimated as the time between the start of voltage pulse input to be transmitting bender and the deflection in the output signal from the receiving bender.

3.3.6.2 Travel Time between Characteristic Peaks off Input and Output Signals

Travel Time of an impulse wave between two points in space may be taken as the time between characteristic points in the signals recorded at these two points, again based on the assumption of plane wave fronts and the absence of any reflected or refracted waves. The most commonly used characteristic points are the 'first peak', 'first trough', or 'zero crossings' of the input and output signals.

3.3.6.3 Travel Time by Cross-Correlation of Input to Output Signals

Travel time of an impulse wave between two points in space may be taken as the time shift that produces the peak cross-correlation between signals recorded at these two points, again based on the assumption of plane wave fronts and the absence of any reflected or refracted waves. For an impulse wave that has been recorded at two spaced points will reach maximum value for the time shift τ that equals the travel time of the impulse between two points.

It is convenient to calculate cross-correlation in the frequency domain using the Fast Fourier Transform (FFT). The calculations take only a few steps in commercial mathematics program and are no longer of onerous task.

3.3.6.4 Travel Time Using the Second Arrival in the Output Signals

An improved method of measuring the shear wave velocity of soil specimens using piezoceramic bender elements is proposed using reflections of a transmitted shear wave having a carefully controlled waveform which relies solely on data obtained by the receiving element. By relying only on multiple responses at the receiving element, the technique circumvents uncertainties associated with identifying the initial arrival of the shear wave. The second arrival is just the input wave after it reflects from the receiver cap (first arrival), travels back to the transmitter cap where it reflects again, and then returns to the receiver cap a second time. Assuming plane wave propagation, the time between the first and second arrivals in the output signal is equal to twice the travel time of the wave from cap to cap (Riemer et al., 1998). To obtain useful data, it is important not only to generate a sufficiently strong wave to detect the reflections, but the shapes of the subsequent reflections must be sufficiently similar to identify equivalent points on them.

For the cross-correlation method it was useful to decompose the output signal into two dummy signals, both being modified copies of the original output signal. The first dummy signal is modified by setting the signals equal to zero outside the time window that contains the first arrival. The second dummy signal is modified by setting the signal equal to zero outside the time window that contains the second arrival. Then these two dummy signals can be cross-correlated to obtain the travel time for twice the cap-to-cap distance.

Analytical solutions for the body waves generated by point sources in a 3-D elastic space were used to show that the wave fronts spread in a spherical manner and involved coupling between waves that exhibited the same particle motion but propagated at different velocities (compression or shear wave velocity) and attenuated at different rates. The coupling of these waves was shown to obscure the first direct arrival of shear waves and to affect travel times calculated using characteristic peaks, cross-correlation, or phase velocity methods at locations near the source. The cross-correlation method was shown to be accurate for determining shear wave velocities for cases where the distance from the source to the first receiver (d_1) was greater than one shear wavelength (λ) and the distance from the source to second receiver (d_2) was twice d_1. The phase velocity method was shown to develop significant errors for a typical receiver spacing of $d_1/d_2 = 2$ when the ratio of d_1/λ was less than 1.

The frequency of the input signal is commonly selected by manually varying it to visually optimize the strength and clarity of the output signal. Experience from bender element tests in a variety of soils suggests that the optimum range of input signal frequencies often corresponds to λ/l_b ratios of about 8 to 16. (l_b is the length of the bender element). This range of frequencies appear to balance the following competing factors: (1) the transmitting bender may appear most like a "point source" for λ/l_b values much larger than 4; (2) the system of waves generated by the transmitting bender can be more complex a λ/l_b values near 4 and decreases as λ/l_b increases, (3) the distortion of the output signal due to wave interference theoretically increases as λ/l_b increases, and (4) minimizing the near-field effect requires maximizing the value of L_{tt}/λ and hence minimizing λ/l_b (where L_{tt} is the tip to tip distance between bender elements) (Arulnathan et al., 1998).

It is recommended that several excitation frequencies and interpretation methods to be used for at least the first set of cantilever-type bender element tests on a given soil in a given device for the first time. The results can be used to identify cases where the choice of interpretation method and input signal frequency are of practical importance and provide insight for arriving at final estimate of V_s. Further experimental and analytical research is needed to provide more structures guidelines for the interpretation of cantilever-type bender element tests and to evaluate alternative configurations of piezoceramic sensors. In practice, first significant inversion of received signal represents true arrival of shear wave velocity. In this research study, the first significant inversion of received signal is considered as the arrival time of shear wave.

3.3.7 Small Strain Shear Modulus Measurements Using Bender Element

In recent years, a technique using bender elements was developed to investigate the small strain shear modulus, G_{max}, (Dyvik and Madshus, 1985, Thomann and Hryciw, 1990, Jovicic et al., 1996, Viggiani and Atkinson, 1995). The small strain shear modulus, G_{max}, is an important parameter for many geotechnical analyses in earthquake engineering and soil dynamics. The value of G depends on a number of parameters, including void ratio, confining stress, soil structure, degree of saturation, temperature, stress history, and time. The stiffness of soils is often measured by the tangent shear modulus obtained from stress-strain relationships. At strains within the elastic range, typically 10^{-4}% or less, the stiffness is represented by the small strain shear modulus, G_{max}. This parameter is very important in soil structure interaction problems and earthquake engineering where it is necessary to know how the shear modulus degrades from its small strain value as the level of shear strain increases.

The small strain shear modulus can be determined from the theory of elasticity, and can be written as (Baxter, 1999)

$$G = \rho \times v_s^2 \tag{3.10}$$

where

G = small strain shear modulus

ρ = mass, or total, density

v_s = shear wave velocity

A shear wave is an elastic body wave, meaning it is a wave that travels within an elastic medium, whose direction of propagation is perpendicular to its direction of particle displacement. A compression wave is another type of elastic body wave, however, its direction of propagation is parallel to its direction of particle displacement.

Although both types of body waves can propagate through soils, the shear wave exhibits some properties that make it more applicable for studying soils. First, in a saturated soil (a two-phase porous medium), shear waves propagate only through the solid phase, because water cannot support shear stresses. However, water can support compressive stresses and, for fully saturated undrained conditions, the soil can be considered to be incompressible. Thus, compression waves propagating through a soil travel through both the solid and water phase. This means that the compression wave velocity is heavily dependent on the water in the pores of the soil. In fact, for fully saturated conditions, the water is incompressible compared to the soil skeleton, and the compression waves travel almost exclusively through the water phase. The resulting compression wave velocity in this case equals the compression wave velocity of water.

One method for determining the small strain shear modulus of soils in the laboratory is to propagate a shear wave through a specimen, measure its velocity, and calculate the small strain shear modulus using equation 3.10. Shear waves can be generated and measured by small pieces of piezoceramic called bender elements, which can be installed in the end caps of specimens. Piezoceramics have the ability to convert electrical impulses to mechanical impulses and vice versa. When a voltage impulse is applied across a single sheet of piezoceramic, it will either shorten or lengthen with a corresponding increase or decrease in thickness, as demonstrated in figure 3.23(a). If two piezoceramic sheets are mounted together with their respective polarities opposite to each other, as shown in figure 3.23(b), an electrical impulse will cause one side to lengthen and the other side to shorten. The net result of this will be a bending of the two sheets, hence the name bender elements.

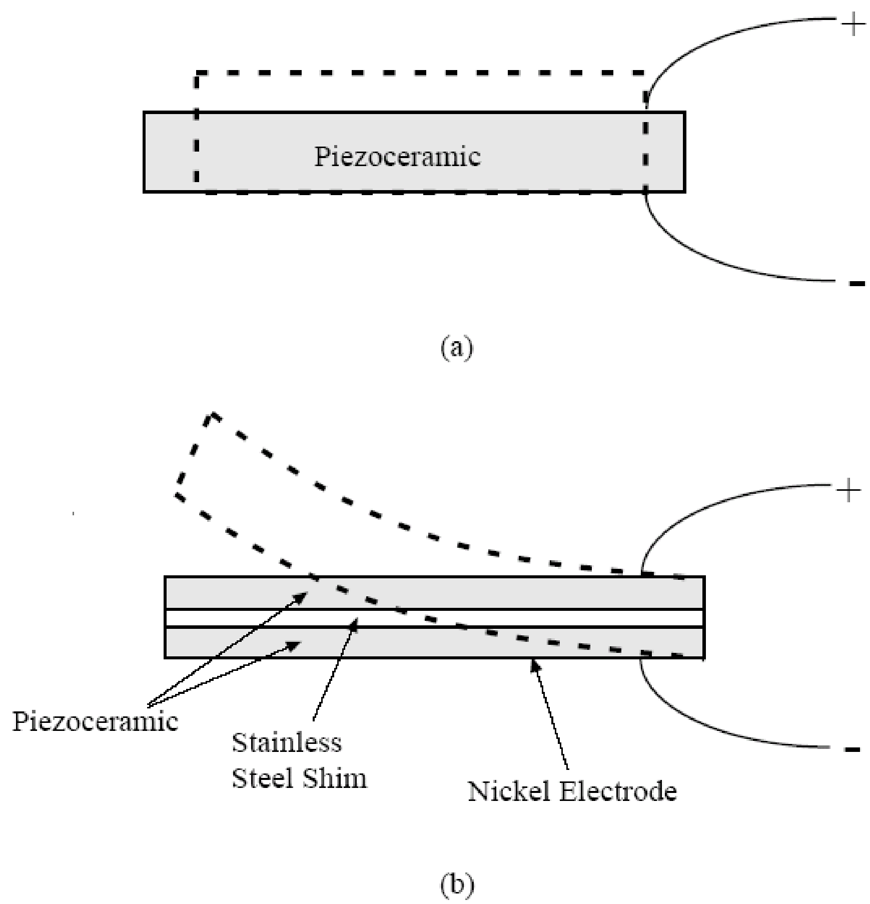

Figure 3.23 Schematic of Piezoceramic (a) Single Sheet and (b) Double Sheet “Bender Element” (Baxter, 1999)

Thus, if an electrical impulse is sent to a bender element mounted in the top cap of a specimen, the bender element will produce a small “wiggle” and generate a shear wave that will propagate down through the soil. When the shear wave reaches the bottom of the specimen it will cause the bender element mounted in the bottom cap to vibrate slightly, thus creating an electrical impulse. If an oscilloscope is used to observe both the impulse that was sent to the top bender (transmitter) and the impulse that was generated by the bottom bender element (receiver), the time that it took the wave to propagate can be measured directly, and is called the arrival time. A schematic of this is shown in figure 3.24. If the length the wave traveled, usually considered to be the length of the sample minus the length of the bender elements (tip-to-tip distance), the shear wave velocity can be calculated by dividing this length (L) by travel time (Δt), using equation 3.11, or

$$v_s = L / \Delta t \tag{3.11}$$

The travel length is taken as the bender element tip to tip distance within the soil specimen i.e. total specimen height minus the protrusion of the transmitter and receiver bender elements into the specimen. Because the bender elements protrude into the soil from the surface of the end caps, it is not intuitively apparent whether the travel path length is the full specimen height, the distance between the tips of the bender elements, or some intermediate “effective” length. Dyvik and Madshus (1985) showed that using the distance between the tips of the bender elements as the travel path length of the shear wave gave the best agreement with the other measurements of the modulus. Viggiani and Atkinson (1995) performed a series of bender element tests on specimens of varying heights, and reached the same conclusion. As a result of these studies, it is standard practice to adopt the tip-to-tip distance between the elements as the effective length of the travel path.

As the specimen height is much greater than the bender element protrusion, the net G_{max} value is relatively unchanged even if the total height of the specimen is considered as a travel length for the shear wave. Also near-field effects should be taken into account for determining correct arrival time of the shear wave.

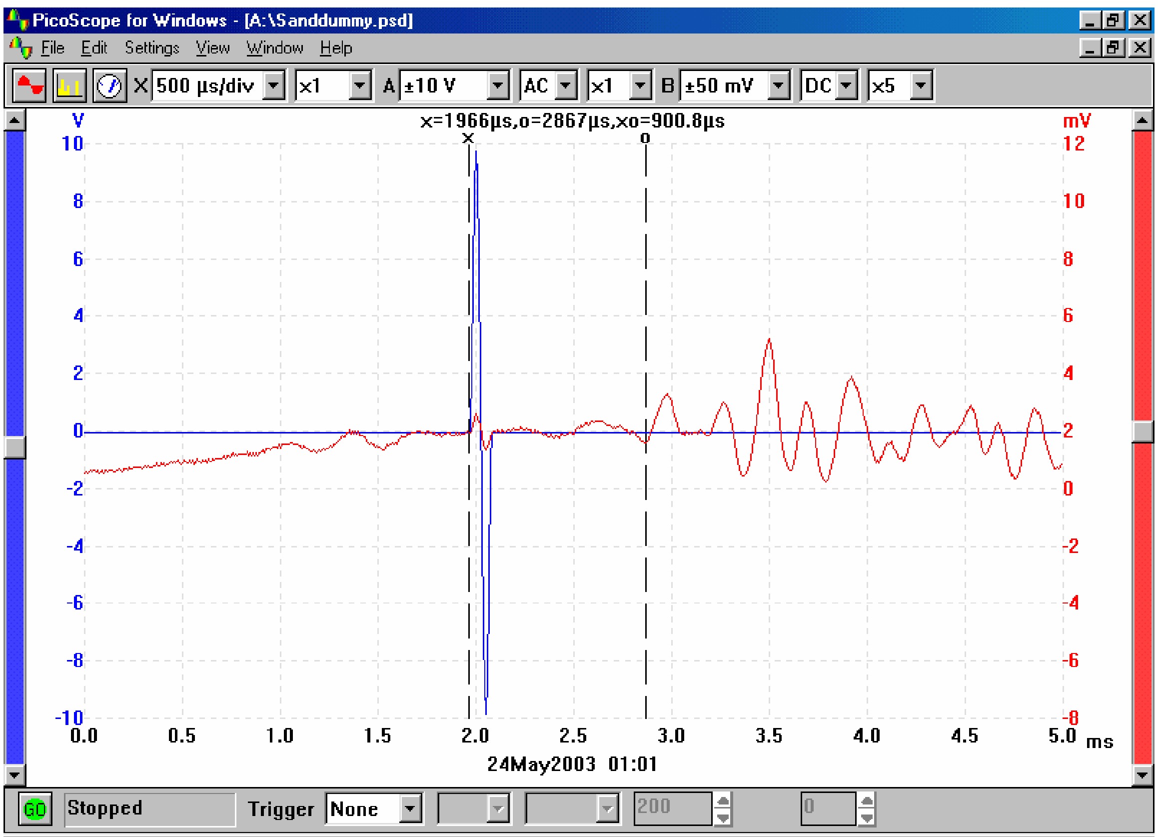

Figure 3.24 Typical Transmitted and Received Signals from Monitor

3.3.8 Damping Ratio Measurements Using Bender Element

Bender element consists of two thin piezoceramic plates rigidly bonded to a central metallic plate. Two thin conductive layers, electrodes, are glued externally to the bender. The polarization of the ceramic material in each plate and the electrical connections are such that when a driving voltage is applied to the element, one plate elongates and the other shortens. The net result is a bending displacement (Pyl and Degrande, 2000). On the other hand, when an element is forced to bend an electrical signal can be measured through the wires leading to the element. A transmitter element and a receiver element are respectively placed in the bottom and top cap of a triaxial cell.

The basis for the analysis of the frequency response of the soil sample is the identification of different modes of vibration at resonance. The damping ratio D is calculated at these points of the response spectrum in the neighborhood of a resonance peak. The bender element is excited with a steady sine signal of constant voltage and amplitude is measured at the receiver element. To make this value independent from the source amplitude it is normalized by this amplitude. This process is repeated at different frequencies until the whole spectrum of soil sample is defined. The damping ratio is estimated at the points of the curve around the natural frequency of the shear mode. For this purpose different techniques are available such as the half-power and circle-fit method.

3.3.8.1 Half-Power Method

The most common method of measuring damping uses the relative width of the response spectrum. The application of latter expression is usually called the half-power method. This measurement need use the continue sine waveform to produce the vibration to the receiver bender element. Then, the peak-to-peak amplitude from received signal is collected at different frequency near the highest amplitude. The typical signal and measurement from the received signal have shown in figure 3.25.

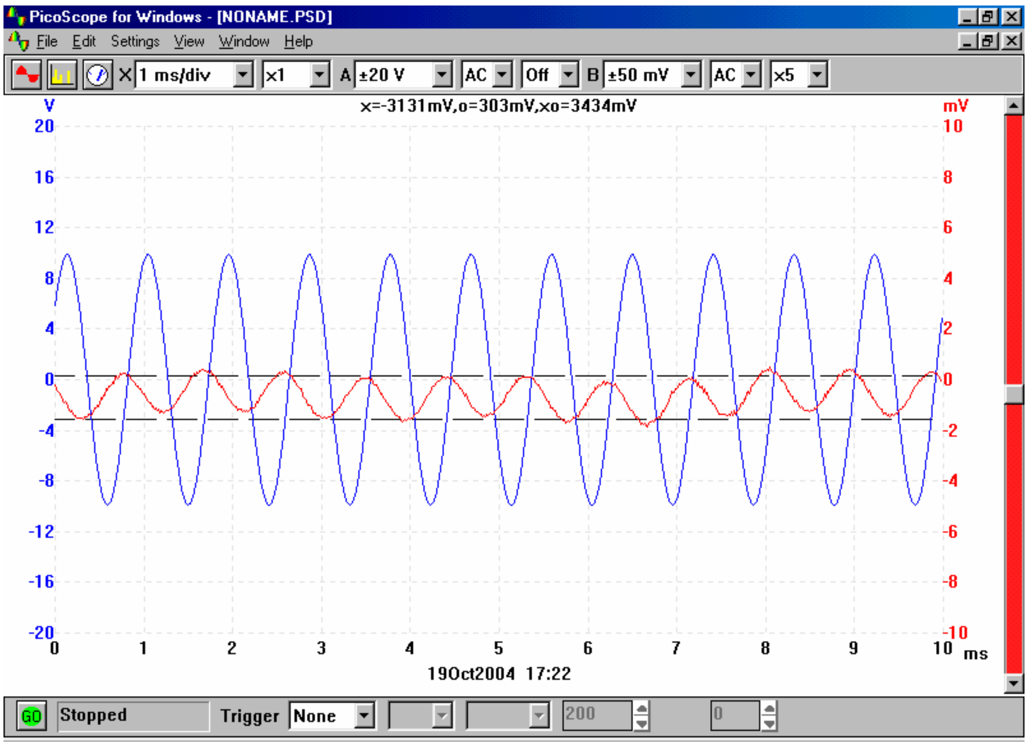

Figure 3.25 Typical Amplitude Measurement from BE Test

The figure 3.26 has shown the typical frequency and amplitude result from the bender element test. After creating the resonant frequency curve, the half-power method is performed to calculate the damping ration, D from equation 3.12:

$$D(\%) = \frac{1}{2}\frac{f_2 - f_1}{f_r} \tag{3.12}$$

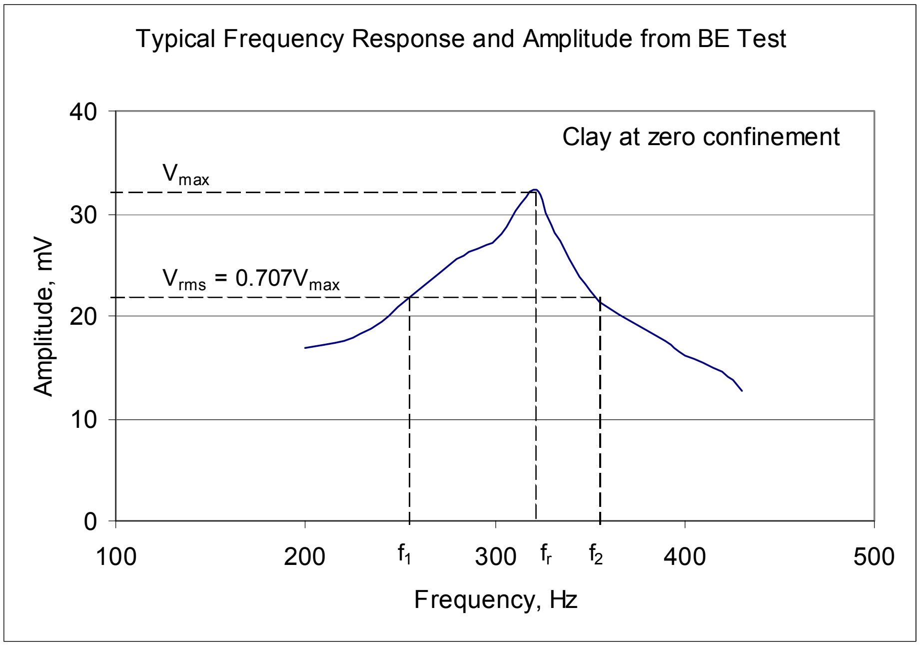

Figure 3.26 Typical Resonant Curve with Variables for Half-Power Method

3.3.8.2 Circle-Fit Method

The circle-fit method, described in Ewins (1988) is able to calculate the damping ratio with very few points around the resonance peak and the amplitude of the peak has only little influence on the result. This is an advantage in cases were different modes have frequencies close to each other.

The Nyquist plot of the response spectrum of a single degree of freedom system leads to a circle as shown in figure 3.27. Even though the sample is not such a system it behaves for selected frequency sections in the same way. The material damping can be calculated from points close to that corresponding to the maximum amplitude using the following expression (equation 3.13):

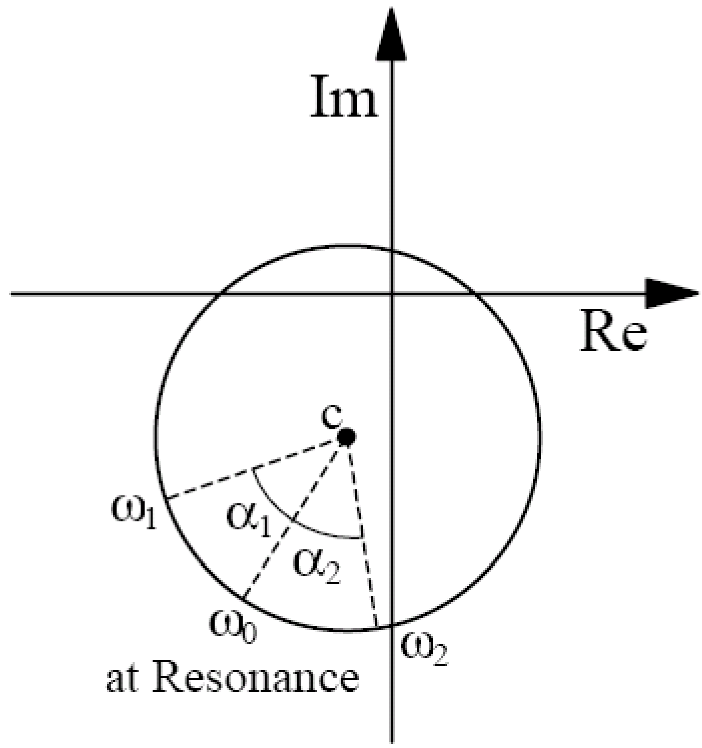

Figure 3.27 Nyquist Plot Used in the Circle-Fit Method

$$D = \frac{\omega_2^2 - \omega_1^2}{2\omega_0\left[\omega_2 \tan\frac{\alpha_2}{2} + \omega_1 \tan\frac{\alpha_1}{2}\right]} \tag{3.13}$$

where:

ω_0 = angular frequency corresponding to the maximum

angular sweep velocity

ω_1, ω_2 = angular frequencies

α_1, α_2 = angles at both sides of ω_0

A circle is fitted to the points of the response curve close to the resonant frequency to find the center. Knowing this point makes it possible to determine the necessary angles α (Pyl and Degrande, 2000).

3.3.9 Basic Components of BE Testing Device

Basically the bender element test has two major components which are triaxial cell and bender elements. Nevertheless, the other equipments required to operate are performed in the bender element test. There are five important components for a working bender element test setup, which are the oscilloscope, receiving signal converter, bender element, triaxial pressure cell, and personal computer. The bender element setup in this research (shown in figure 3.28) was purchased from the Wykeham Farrance in the United Kingdom. The description of five components is mentioned individually in the following section in brief.

Figure 3.28 Triaxial and Bender Element Setup

1. <u>Oscilloscope:</u> The oscilloscope used in this research is called the Arbitrary Waveform Generator Model TGA 1241(figure 3.29). This oscilloscope can generate any waveform signal at different frequency vary from 1 to 40MHz and the maximum amplitude is 20 Volts peak-to-peak. However, the frequencies, used in this research, range from 2 to 15 kHz for clay and sand specimens. And, the amplitude was applied at 20 Volts peak-to-peak which is the maximum amplitude available for this oscilloscope, so the received signal can be observed readily and obviously on the computer by not using the amplifier. The main function of this oscilloscope not only performs a waveform signal to the top bender element, but also sends the wave form to the receiving signal converter.

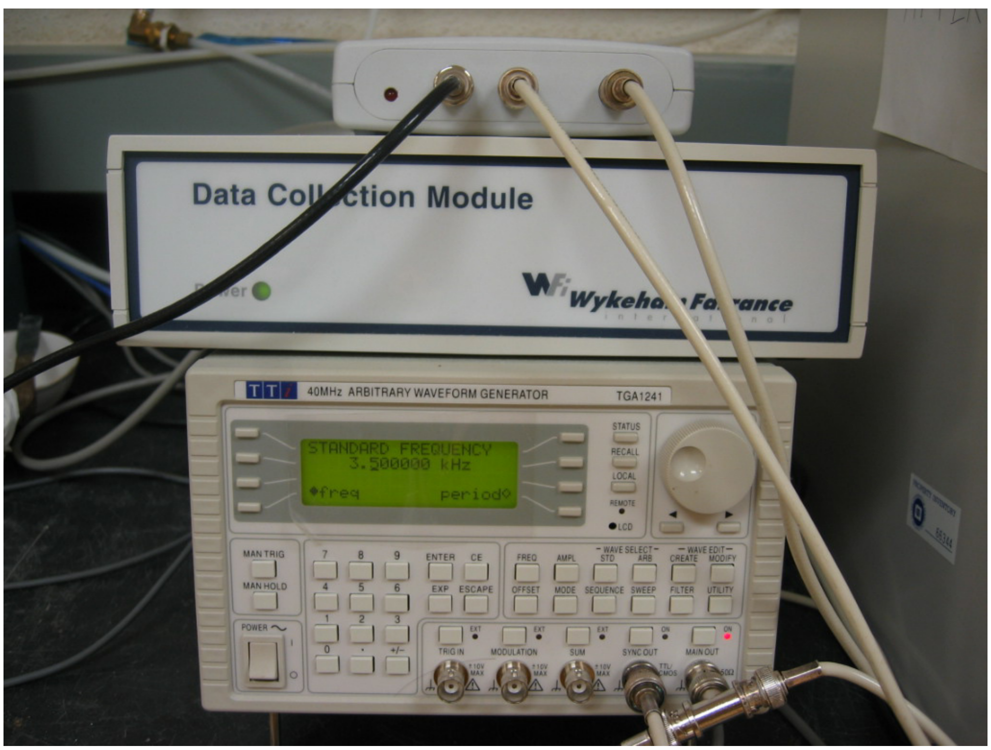

Figure 3.29 Arbitrary Waveform Generator and Receiving Signal Converter

2. Receiving signal converter: Figure 3.29 also shows the receiving signal converter put on the top of the oscilloscope. The major role of the signal converter is to convert the voltage signals from both top and bottom bender elements into digital signals and then the digital signals was sent to the personal computer that has been installed the Picowave program to view the waveform generated from oscilloscope.

3. Bender element: Bender element set with wires shown on figure 3.30 is used to perform the horizontal vibration through the soil specimen from top to bottom as described in previous. In the other word, the top bender element vibrates when received the signal from the oscilloscope, and then the vibration expands through the soil specimen so that the bottom bender element receives the vibration. Consequently, the elapse time between the transmitted signal and received signal are measured and calculated.

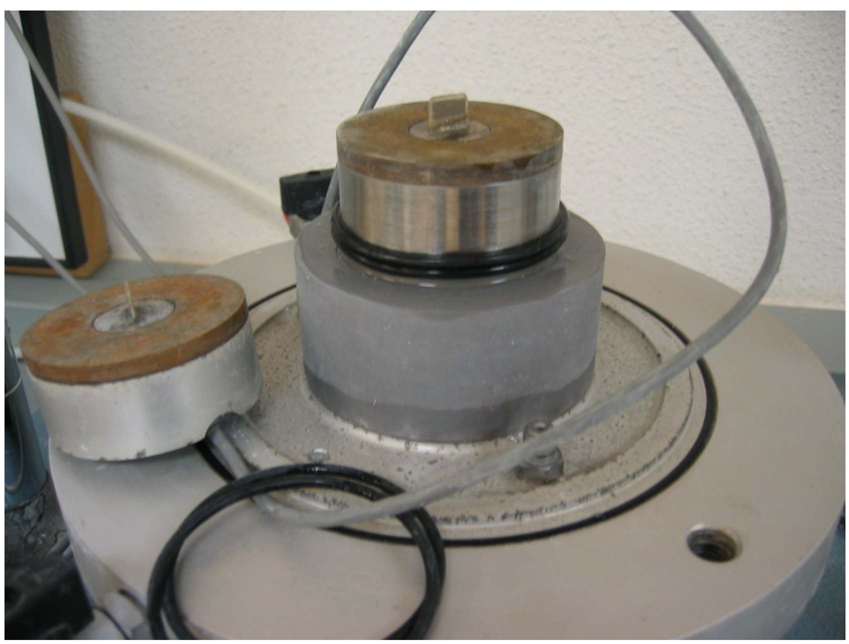

Figure 3.30 Bender Element on the Triaxial Cell Base

4. Triaxial cell: For the reason that a specimen is subjected to be applied a certain confining pressure and other applications, the triaxial pressure cell (figure 3.31) is needed to success in this research. The size of cylindrical specimen performed in the bender test is 2.8 inches in diameter and 5.6 inches in height.

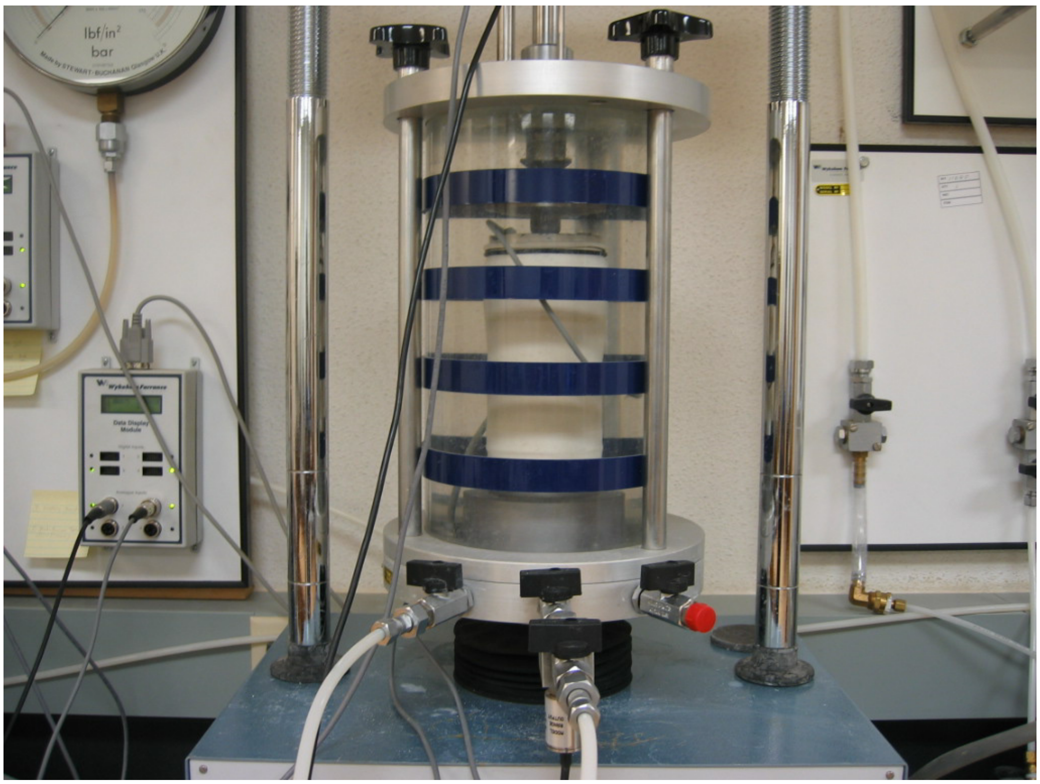

Figure 3.31 Triaxial Pressure Cell with Bender Element

5. Personal computer: During the bender element test, signals from the converter are sent to the personal computer in order to visualize both transmitted and received signal on the monitor. The Picowave program is also required in order to capture, save, and collect data. Eventually, the shear wave velocity is determined by measuring the elapse time between the transmitted and received signal normally represented by blue and red lines respectively as shown on figure 3.25 and 3.26.

3.3.10 Apparatus Assembly

An illustrated description of the step-by-step assembling process of the bender element (BE) testing device is presented in the following paragraphs.

1. <u>Chiseling specimen:</u> Once the soil specimen has been fully compacted and retrieved for a compaction mold (2.8 inches in diameter and 5.6 inches in height) at desired moisture content, it is cautiously chiseled at the top and bottom of the specimen at the same size as a piece of piezoceramic bender element in order to keep away from breaking the bender element because sometimes at low moisture content specimens are unable to put the piece of bender element inside. Figure 3.32 shows the chiseled specimen.

Figure 3.32 Chiseled Sample Surfaces

2. <u>Specimen placement:</u> After the specimen was chiseled, it is carefully placed on the base pedestal with bender element. A latex membrane is then rolled downward by stretcher over the specimen and two O-rings are gently placed at the base pedestal. And the top cap with bender element is rested on top of the specimen then placed another two O-rings at the top cap (figure 3.33).

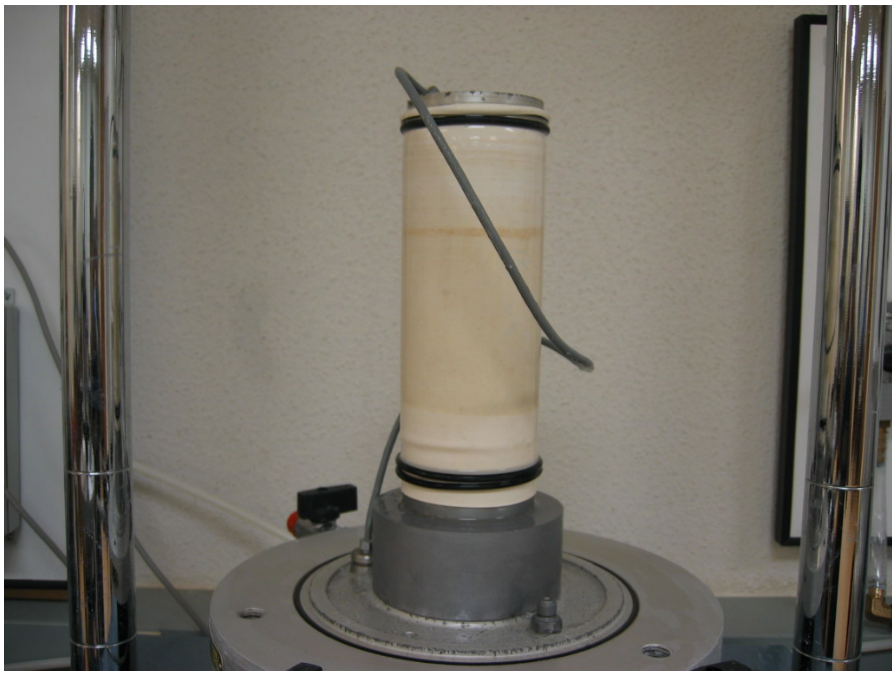

Figure 3.33 Specimen with Membrane
and O-rings Resting on Base Pedestal

3. <u>Water pressure application:</u> A triaxial cylindrical chamber is placed over the soil specimen and securely fitted the base in which the sample is subjected to an isotropic confining pressure. A wire leads from the bender element in the base pedestal exit the cell directly through a vertical hole. In the top cap, the wire leads are run through a diagonal hole from the base of the slot to the top corner of the cap. These wires then exit the cell through a pressure-proof fitting in the cell base and connected to the oscilloscope and receiving signal converter. After that, the triaxial cell is filled with water with the top small hole opened in order to let the air bubble out from chamber. When triaxial chamber is completely filled with water confining pressure is applied with the pressure regulator at desired pressure (figure 3.34).

Figure 3.34 Triaxial Chamber Filled Up with Water

4. <u>Elapse time measurement setup:</u> As mentioned before, the elapse time between transmitted and received signal is enable to visualize and measure by using the triaxial cell with bender element setup as shown in figure 3.28 and described in the previous section. Then the shear wave velocity can be calculated from the travel time of shear wave through the soil specimen. This setup also can collect a measurement of travel time in the personal computer.

3.4 RC/BE Testing in RC Chamber

In this research, another interesting part is to perform the resonant column test (RC) and bender element (BE) in the air confining chamber in order to simulate the identical isotropic condition during both RC and BE tests simultaneously. Consequently, the comparison of the results from both method can be determined accurately The reason that the air confinement needs to be performed on, 2.8 inches (7.2 cm) in diameter and 5.6 inches (14.4 cm) in height, clay and sand specimen instead of water confining pressure because a wire needs to be connected with the piezoceramic bender elements on the top cap and bottom pedestal (figure 3.35). As a result, the water-bath application mentioned in RC test section cannot be applied.

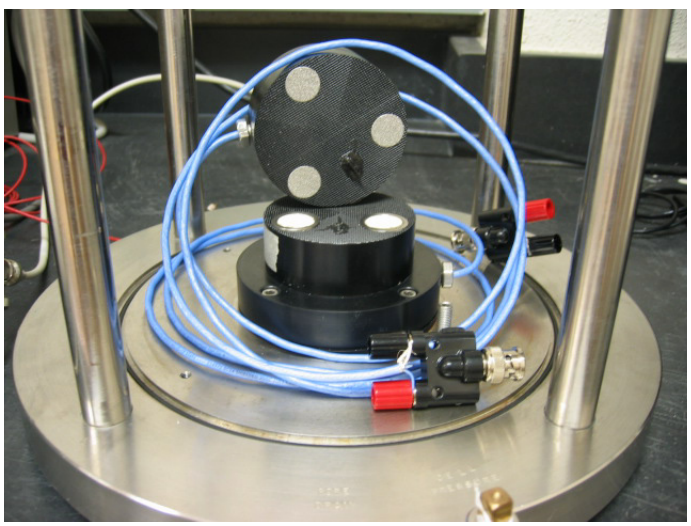

Figure 3.35 Couple Bender Elements for RC/BE Testing

The conventional resonant column was modified to make a connection of both top and bottom bender element wires connected with the oscilloscope between confining chamber wall the RC/BE test by drilling two small hole and replacing the sealed 50 psi bulkhead BNC connector to prevent any air leak during running the

RC/BE test as shown in figure 3.36. RC/BE measurement methods of shear modulus (G) and damping ratio (D) are the same concepts as mentioned from previous sections. The RC/BE setup (figure 3.37) is the combination of conventional resonant column and bender element tests.

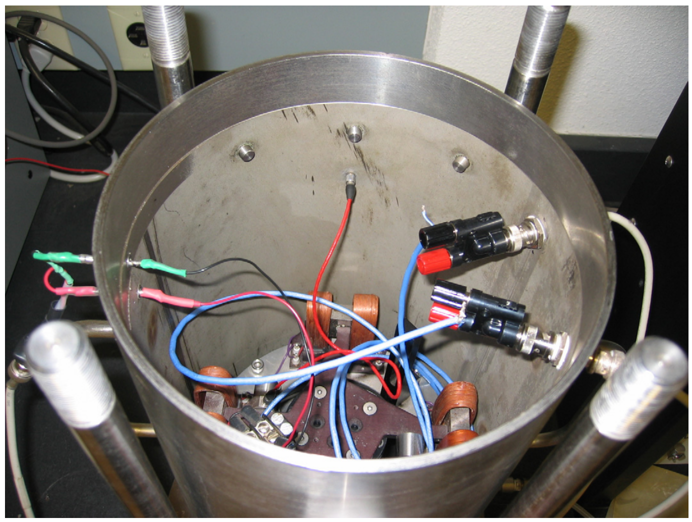

Figure 3.36 Sealed 50 Psi Bulkhead Connectors

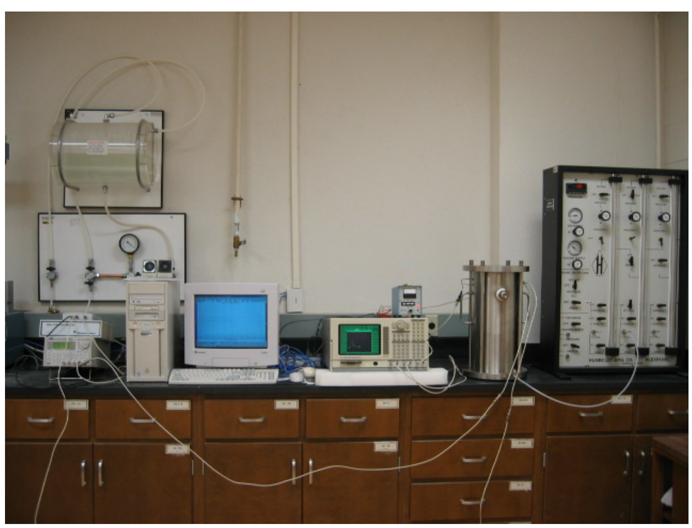

Figure 3.37 RC/BE Device Setup

An illustrated description of the step-by-step assembling process of the RC/BE testing device is presented in the following paragraphs.

1. Chiseling specimen: After the soil specimen has been fully compacted and retrieved for a compaction mold (2.8 inches in diameter and 5.6 inches in height) at desired moisture content, it is cautiously chiseled at the top and bottom of the specimen at the same size and position as a piece of piezoceramic bender element (shown in figure 3.38) in order to keep away from breaking the bender element because sometimes at low moisture content specimens are unable to put the piece of bender element inside.

Figure 3.38 Chiseled Sample Surfaces for RC/BE Test

2. Specimen placement: After the specimen was chiseled, it is carefully placed on the base pedestal with bender element (figure 3.39). A latex membrane is then rolled downward by stretcher over the specimen and two O-rings are gently placed at the base pedestal. And the top cap with bender element is rested on top of the specimen then placed another two O-rings at the top cap (figure 3.40).

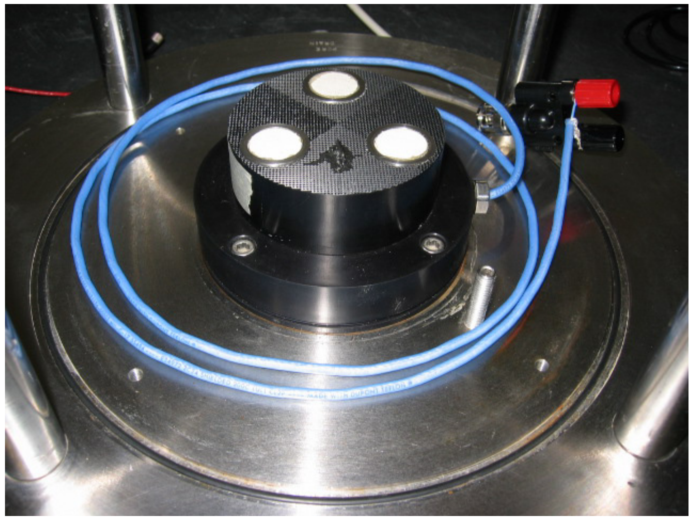

Figure 3.39 Base Pedestal with Bender Element

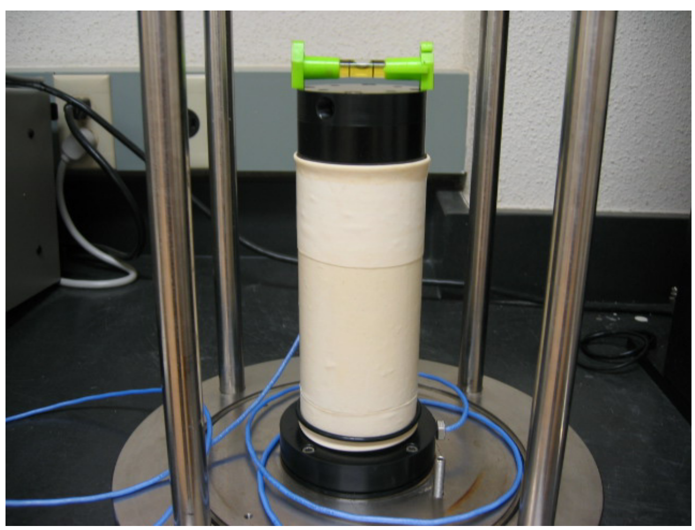

Figure 3.40 Specimen and O-rings Resting on Base Pedestal

3. Torsional driver setup: The stainless steel cylindrical cage is fitted over the specimen and securely attached to the base plate. The torsional driver (coils and spider) is then assembled onto the top cap. The spider is attached to the top cap by means of four flat-head screws. The set of drive coils is accommodated such that each magnet is encircled by a pair of coils without contact. The set of coils is finally secured to the cylindrical cage (figures 3.41).

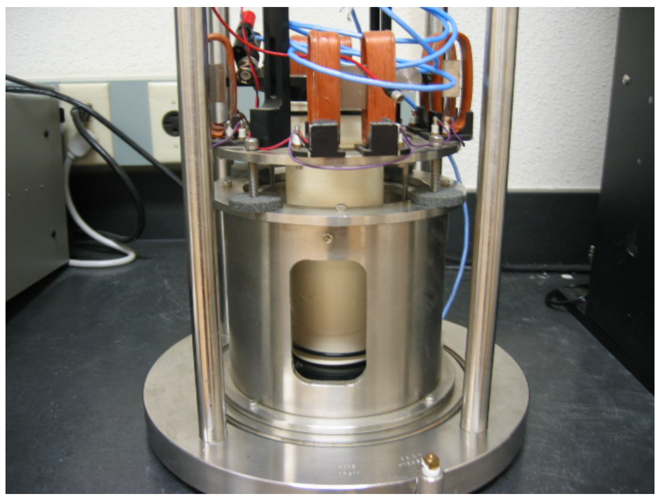

Figure 3.41 Torsional Driver over Cylindrical Cage

4. Plugging in the Connection: A stainless steel cylindrical chamber is placed over the soil specimen and securely fitted the base in which the sample is subjected to an isotropic confining pressure. Both wires lead from the bender elements in the base pedestal and top cap exit the cell directly through the connection on the side of the chamber. These wires then exit the cell through a pressure-proof fitting connection on the side of the chamber and connected to the oscilloscope and receiving signal converter. For RC testing, all cables need to be connected from the driver mechanism as described in conventional resonant column section. When chamber is completely sealed with a circular top plate, confining pressure is applied with the pressure regulator at desired pressure. Figures 3.42 and 3.43 show all wires and connections inside and outside the confining chamber.

Figure 3.42 Wires and Connections in Confining Chamber

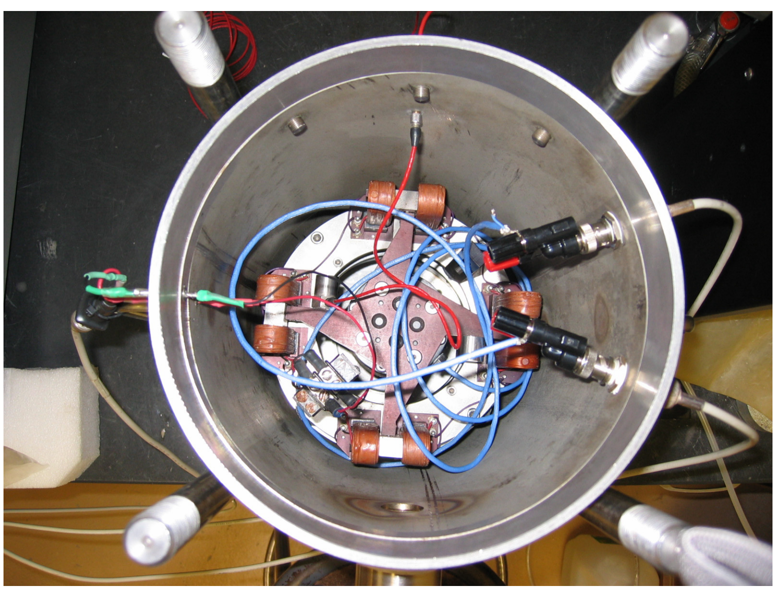

Figure 3.43 Top View of RC/BE Chamber

5. Measurement setup: The electrical wiring of the SR785 dynamic signal analyzer and the 4102M charge amplifier box is then connected to the corresponding microdot connectors on the outer side of the thin-walled cylinder, that is, the input signal coaxial wire and the accelerometer input wire. The analyzer is then configured at the desired test settings, including amplitude of sinusoidal signal, range of frequency scale, swept-sine testing mode, and number of data points to be recorded.

As mentioned before, the elapse time between transmitted and received signal is enable to visualize and measure by using bender element and resonant column setup as shown in figure 3.44 and described in the previous section. Then the shear wave velocity can be calculated from the travel time of shear wave through the soil specimen. This setup also can collect a measurement of travel time in the personal computer.

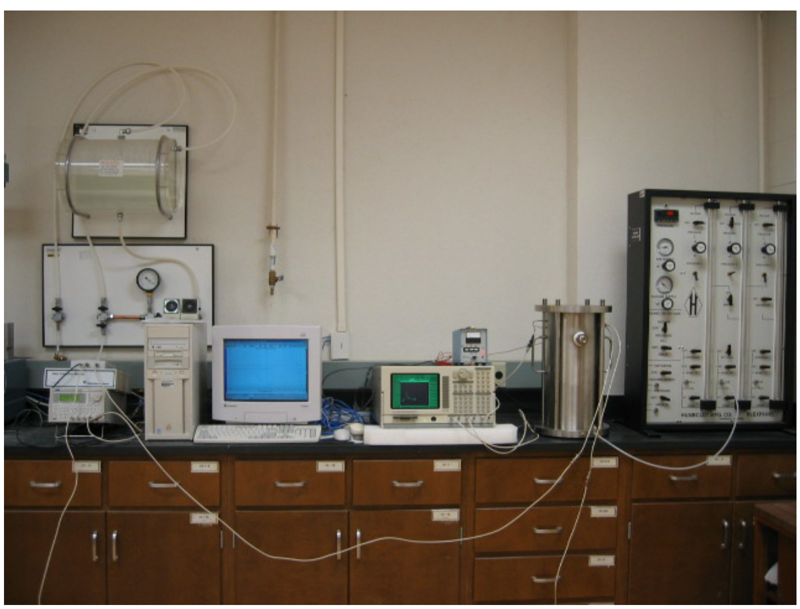

Figure 3.44 Resonant Column with Bender Element Setup

3.5 PPE Testing with Radial Confinement

3.5.1 Introduction

The soil-water characteristic curve (SWCC) is one of the most readily available experimental means for estimating fundamental engineering properties of unsaturated soils for a wide range of matric suction states. Numerous laboratory techniques have been developed for the accurate assessment of the SWCC, from filter paper technique to the more sophisticated pressure plate extractor devices. The majority of these methods, however, allow for the testing of unsaturated soils under unknown or zero-confinement conditions, resulting in SWCC data that do not correspond to realistic in-situ stress states in soils well above the ground water table.

On the other hand, advances in SWCC testing using oedometer or triaxial setups may also prove costly and very time consuming. In this work, an attempt has been made to develop a modified pressure plate extractor (MPPE) device for assessing the SWCC of unsaturated soils under anisotropic stress states. The MPPE features independent control of net radial confinement ($\sigma_r - u_a$) and vertical pressure ($\sigma_v - u_a$).

With the developed MPPE device, a series of SWCC tests were conducted on poorly-graded sand (SP) and low-plasticity clay (CL), for different values of K_o ratio, that is, the ($\sigma_r - u_a$) to ($\sigma_v - u_a$) ratio. Results show a paramount influence of the net radial confinement ($\sigma_r - u_a$), and hence the initial K_o condition, on soil's air-entry value (ψ_a) and residual volumetric water content (θ_r).

3.5.2 Conventional PPE Device

Fredlund and Rahardjo (1993) provide a comprehensive review of the types of extractors in use today, their ranges of applicability, and their advantages and disadvantages. A PPE device has two basic components: (1) A porous plate with air-entry value higher than the maximum matric suction to be applied during SWCC test, and (2) A sealed pressure cell or vessel. The porous plate is usually made of ceramic material, although polymeric membranes are used when considerably high suctions are to be applied (more than 1500 kPa or 150 m of water). Pore water pressure (u_w) in the soil specimen is maintained at zero because the pore water is exposed to atmospheric pressure at the outflow end of specimen. Air pressure (u_a) inside the pressure cell or vessel is elevated to induce the desired matric suction state (ψ) via axis-translation technique, that is, $\psi = (u_a\text{-}u_w)$ (Fredlund and Rahardjo, 1993).

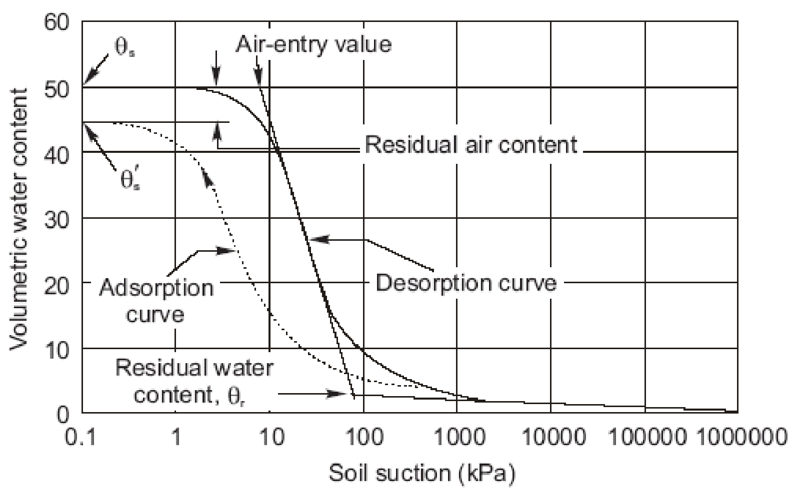

Figure 3.45 Typical SWCC for Silt with Suction Parameters (Fredlund and Xing, 1993)

The desorption (drying) soil water characteristic curve SWCC (figure 3.45) is measured by first saturating the specimen and then applying u_a in a series of increments to attain different values of matric suction ψ. Each increment in u_a causes the pore water to be expelled from the specimen until an equilibrium state is reached for the pre-established value of ψ. Additional increments in u_a are applied only after outflow from the specimen has stopped. The volume of water expelled during each increment of u_a is measured (volumetrically and/or gravimetrically) to define the gravimetric water content (w), the volumetric water content (θ_w), or the degree of saturation (S_r) corresponding to each matric suction ψ.

A conventional Model 1500 15-Bar PPE device (Soilmoisture Equipment Corp.) was used for assessment of water-holding characteristics of poorly-graded sand and low-plasticity clay using flexible sample retaining rings, that is , for zero net stress or $(\sigma - u_a) = 0$. The pressure vessel is 4 in (10 cm) deep with an inside diameter of 12 in (30 cm). Up to three ceramic plates can be accommodated at one time, thus allowing approximately 36 samples (2-1/4 in diameter each) to be analyzed simultaneously. The Model 1500 consists of a pressure vessel and lid, clamping bolts, O-ring seals, and outflow tube assemblies, as shown in figure 3.46. The existing PPE device shown in figure 3.46 was slightly modified to accommodate a custom made confining ring seating on the 15-bar ceramic, as described in the following section.

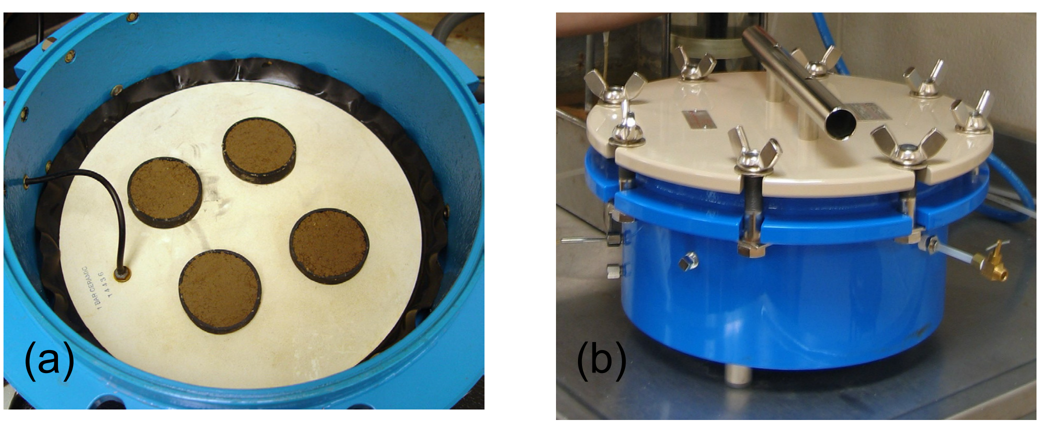

Figure 3.46 Model 1500 15-Bar PPE Device:
(a) Sample retaining rings, (b) Sealed vessel

3.5.3 Modified PPE Device

Conventional PPE devices like the one shown in figure 3.46 are suitable for measuring SWCCs for surficial soil conditions, that is , for low in situ overburden pressures. For deeper soils, a normal stress must be applied to properly reproduce in situ stress states (Vanapalli et al., 1999, Ng and Pang, 2000, Wang and Benson, 2004). In the latter cans, the so-called *Tempe Cells* are commonly used. Tempe Pressure Plate Cells are used to determine the water-holding characteristics of a soil sample in the 0 to 1 bar pressure range. The cell accepts an undisturbed soil sample contained in a 2-1/4 in (5.7 cm) or 3-1/2 in (8.8 cm) outside diameter brass cylinder, and it features top and bottom Plexiglass plates, a porous ceramic plate, a brass cylinder, and sealing and connecting hardware. An external pressure source is connected to the Tempe cell using Neoprene tubing (Fredlund and Rahardjo, 1993). The cell, however, does not allow simulation of in situ axisymmetric stress states (K_0 conditions), given the difficulties in measuring lateral stresses on the specimen inside the brass confining cylinder upon application of normal loads. The present work is a preliminary attempt to overcome these limitations using the well known Model 1500 15-Bar PPE device.

In this work, the existing Model 1500 15-Bar PPE device (figure 3.46) was slightly modified to accommodate a custom made, 2.8 in (7.2 cm) diameter, 1 in (2.5 cm) height, stainless steel, confining ring, as shown in figure 3.47. The assembled ring surrounded by latex membrane seats on the top of the 15-bar Plate, as in figure 3.47 (a). A coarse porous stone, tightly secured onto the top of edge of the ring with the stainless steel plate as shown in figure 3.47 (b), facilitates the flow of air pressure u_a in the vessel toward the soil pores. A latex membrane between the wall of the ring and the specimen can be accommodated to allow application of radial confinement σ_r during testing and a set of heavy weigh metal was placed onto top of assembled ring setup to prevent a horizontal and vertical movement, as show in figure3.47 (c). The latex is tightly secured onto the outer wall of the ring via a full set of burst-resistant O-rings. Radial confinement σ_r is supplied from the exterior via nylon tubing across the wall of the vessel. Assembling of the modified PPE device, as shown in figure 3.47 (d), is similar to that of conventional devices.

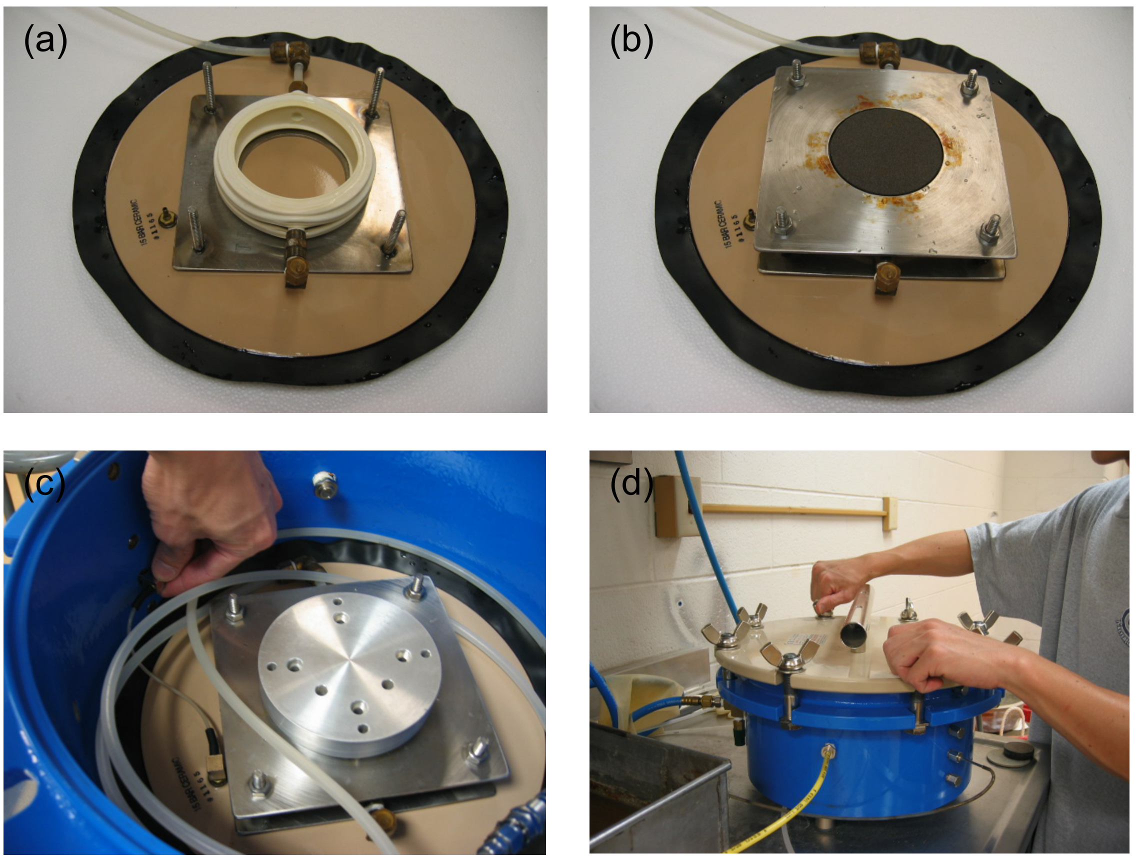

Figure 3.47 Modified 15-Bar PPE Device: (a) Confining Ring,
(b) Assembled Ring, (c) Ring Inside PPE Vessel, (d) Sealed Vessel

External pressure is generated from a Model HM-414 Humbodt pressure panel via a Model HM-4151 bladder air/water cylinder. De-aired potable water is used as pressurizing fluid. The space between the inner wall of the ring and the latex

(a) (b)

Figure3.48 SWCC Testing: (a) Air Pressure Application,
(b) Radial Confinement Application

membrane is fully saturated with water prior to testing. During desorption (drying) SWCC testing, air pressure u_a is applied in a series of increments to achieve different values of matric suction ψ. Each increment in u_a is followed by an increase in σ_r in order to keep constant the pre-established value of net radial confinement (σ_r – u_a), as shown in figure 3.48. Continuous adjustments to σ_r within the first half hour upon an increase in u_a may be necessary to attain full equilibrium state in the specimen. The volume of water expelled during each increment of u_a is then measured (volumetrically and/or gravimetrically) and plotted against the corresponding matric suction ψ. Figure 3.49 shows the SWCCs measured from conventional and modified PPE devices. As it can be seen from figure 3.49, the SWCC position is greatly affected by the boundary conditions (rigid or flexible) imposed on the specimen by the type of confining ring used. The repeatability of poorly graded sand from modified PPE device is shown on figure 3.50.

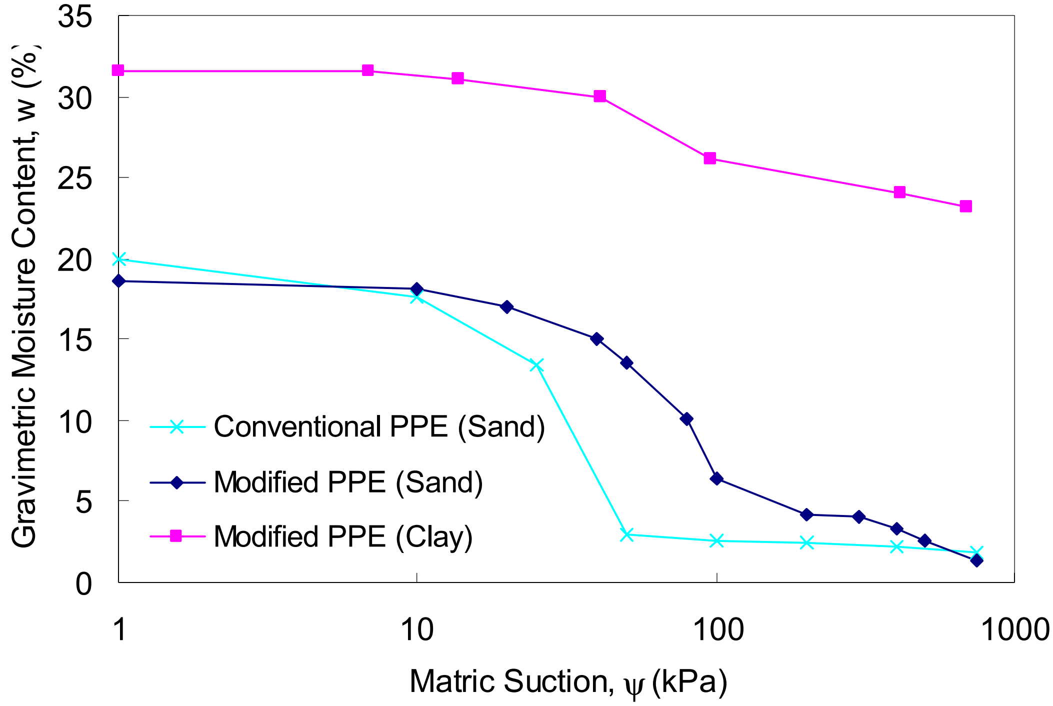

Figure 3.49 SWCCs Measured from Conventional and Modified PPE Devices

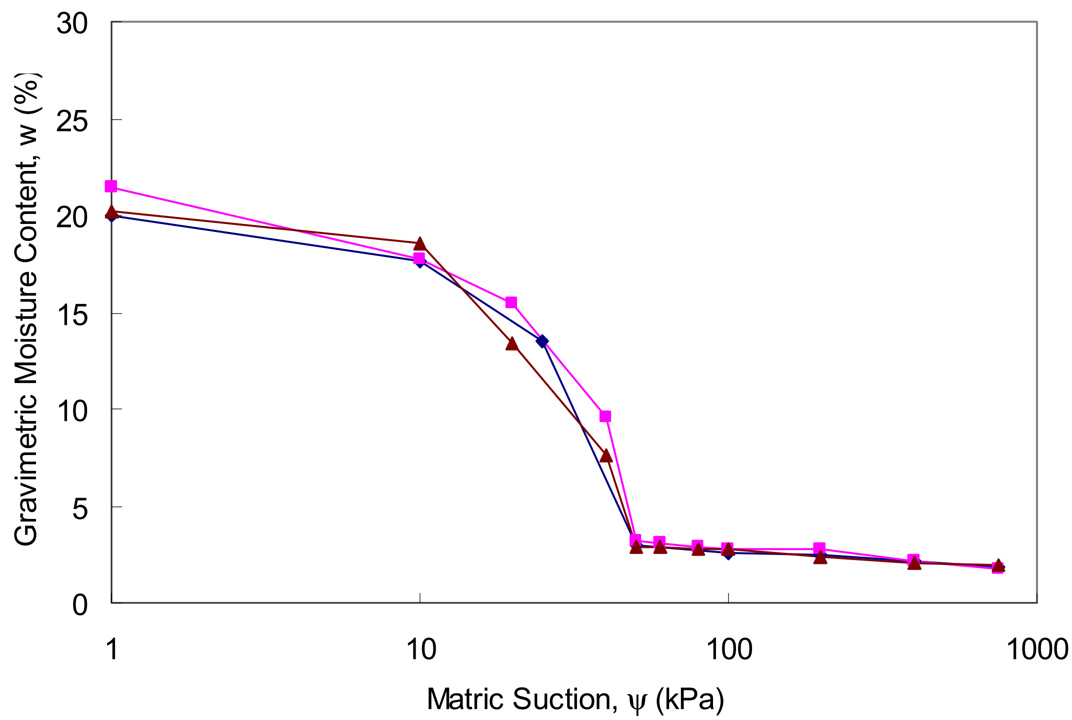

Figure 3.50 The Repeatability of SWCCs from Modified PPE

The modified PPE device consists mainly of five major components: (1) modified pressure plate vessel, (2) air pressure compressor, (3) air pressure application controller, (4) radial confinement application controller, and (5) bladder air/water cylinder. The schematic of modified PPE device setup is shown on figure 3.51.

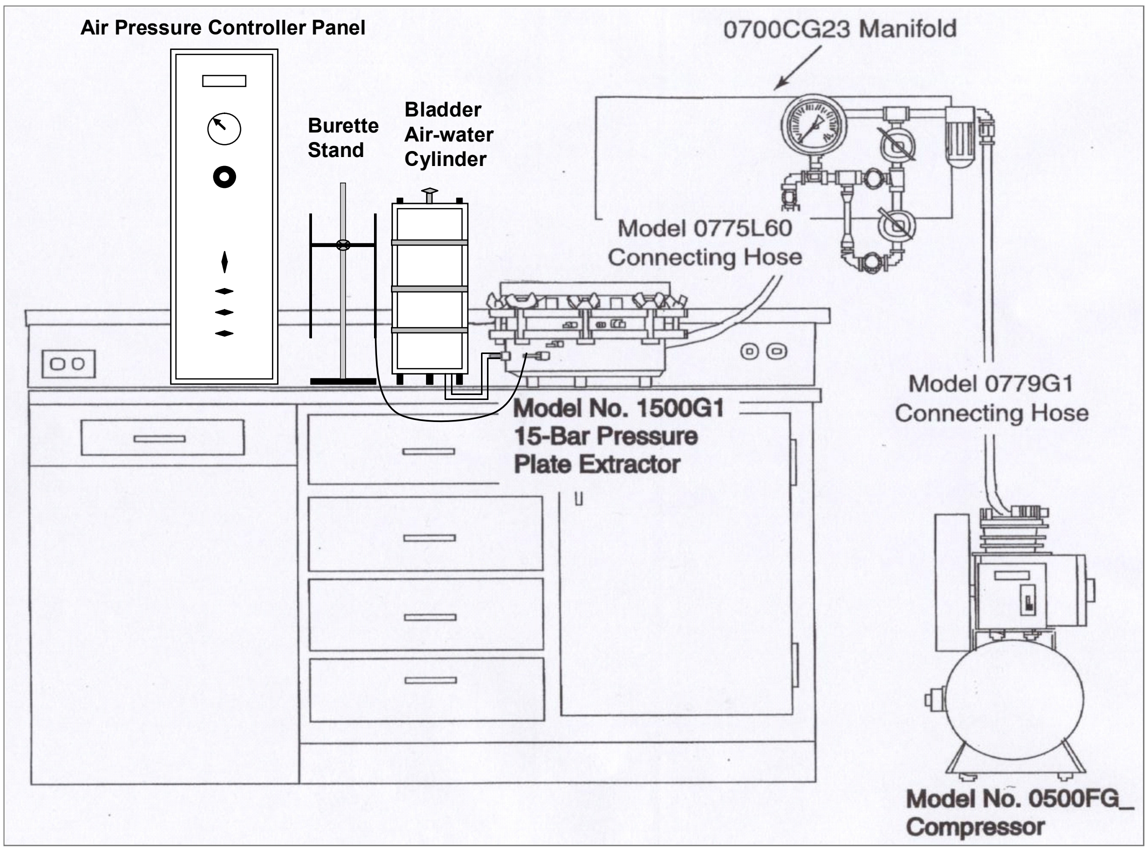

Figure 3.51 Schematic of Modified PPE Device Setup

3.6 FP Testing

The filter paper method has long been used in soil science and engineering practice and it has recently been accepted as an adaptable test method for soil suction measurements because of its advantages over other suction measurement devices. Fundamentally, the filter paper comes to equilibrium with the soil either through vapor (total suction measurement) or liquid (matric suction measurement) flow. At equilibrium, the suction value of the filter paper and the soil will be equal. After equilibrium is established between the filter paper and the soil, the water content of the filter paper disc is measured. Then, by using filter paper water content versus suction calibration curve, the corresponding suction value is found from the curve. This is the basic approach suggested by ASTM Standard Test Method for Measurement of Soil Potential (Suction) Using Filter Paper (ASTM D 5298). In other words, ASTM D 5298 employs a single calibration curve that has been used to infer both total and matric suction measurements. The ASTM D 5298 calibration curve is a combination of both wetting and drying curves (Bulat et al., 2001).

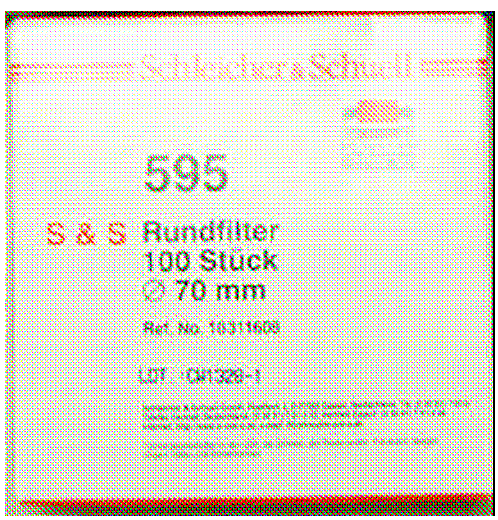

Figure 3.52 The Schleicher & Schuell No. 589-WH Filter Paper

For this research, filter paper testing technique was used for soil suction measurement of clay at high suction in order to complete the SWCC for clay. The Schleicher & Schuell No. 589-WH filter paper (figure 3.52) was used for soil suction measurement along with the filter paper wetting calibration curve as shown in figure 3.53 (Bulat et al., 2001).

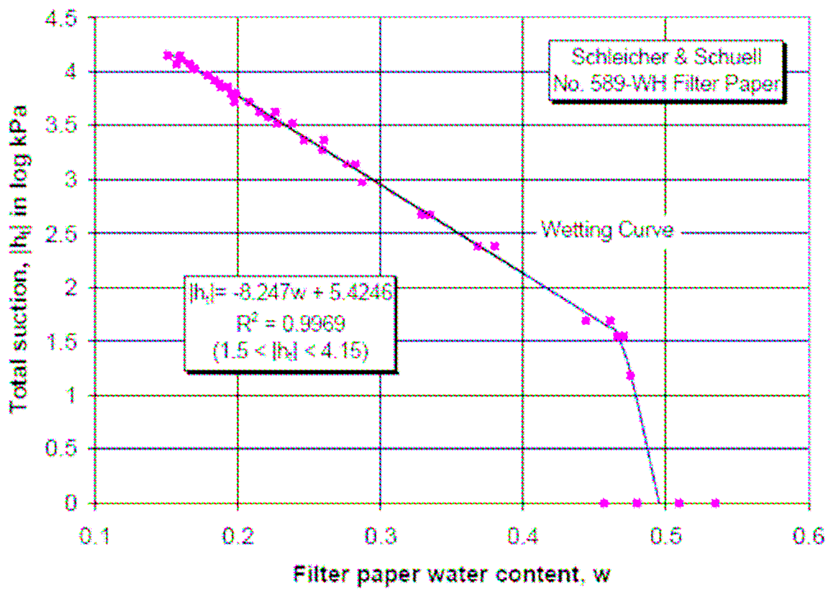

Figure 3.53 Filter Paper Wetting Calibration Curve
(Bulat et al., 2001)

The filter paper wetting calibration curve (figure 3.53) was used to interpret the filter paper water content to soil suction. The following chapter was included step by step procedure for soil suction measurement by using filter paper method.

The next chapter describes all the experimental variables and procedures, including basic engineering properties and compaction curves for the poorly graded sand and high plasticity clay soils used in this present research.

CHAPTER 4

EXPERIMENTAL VARIABLES AND PROCEDURES

4.1 Introduction

The experimental program accomplished in this work was designed to assess the influence of key in-situ factors on small-strain stiffness properties of unsaturated soils using bender element and resonant column testing techniques. Several identically prepared specimens of poorly graded sand and high plasticity clay from Arlington, Texas, were tested with bender element, resonant column, and pressure plate extractor devices as described in Chapter 3. Specimens were prepared at different compaction moisture contents, which are to induce different initial soil suction states, and tested at different confinements (0, 1, 2.5, and 5 psi or 0, 6.9, 14.25, and 34.5 kPa) via bender element and resonant column. SWCCs were determined by using the modified pressure plate extractor for three different conditions, which are (1) controlled radial confinement condition, (2) constant K_o stress state condition, and (3) variable K_o stress state condition. Filter paper technique was then used to assess the remaining SWCC trends of clay at high suction states (ψ>100 psi or 690 kPa).

The following sections provide the basic engineering properties of the testing soils used in this study, along with a detailed description of all the experimental variables and specimen preparation procedures.

4.2 Properties of Testing Soil

4.2.1 Clay

The clayey soil used in this investigation was sampled from the east side of South Cooper Estate Village in southeast Arlington. This clayey soil is a high-plasticity, low sulfate clay, dark brown in color, with natural moisture content (w_n) of 3%, standard Proctor optimum moisture content (w_{opt}) of 20%, specific gravity (G_s) of 2.75, liquid limit (LL) of 62%, plasticity index (PI) of 37%, and soluble sulfate content of 62 ppm. The soil classifies as A-7-6 and CH according to the AASHTO and USCS, respectively. The basic engineering properties of the testing soil are summarized in table 4.1. And, grain size distribution for clay is shown in figure 4.1.

Table 4.1 Basic Engineering Properties of Testing Clay

Properties	Result
Color	Dark brown
Natural moisture content, w_n (%)	3
Passing No. 200 sieve (%)	71
Clay fraction, CF (%)	25
Specific gravity, G_S (-)	2.75
Liquid limit, LL (%)	62
Plasticity index, PI (%)	37
Standard Proctor maximum dry unit weight, $\gamma_{d\text{-}max}$ (kN/m^3)	15.98
Standard Proctor optimum moisture content, w_{opt} (%)	20
Soluble sulfate content (ppm)	62
AASHTO classification	A-7-6
USCS classification	CH

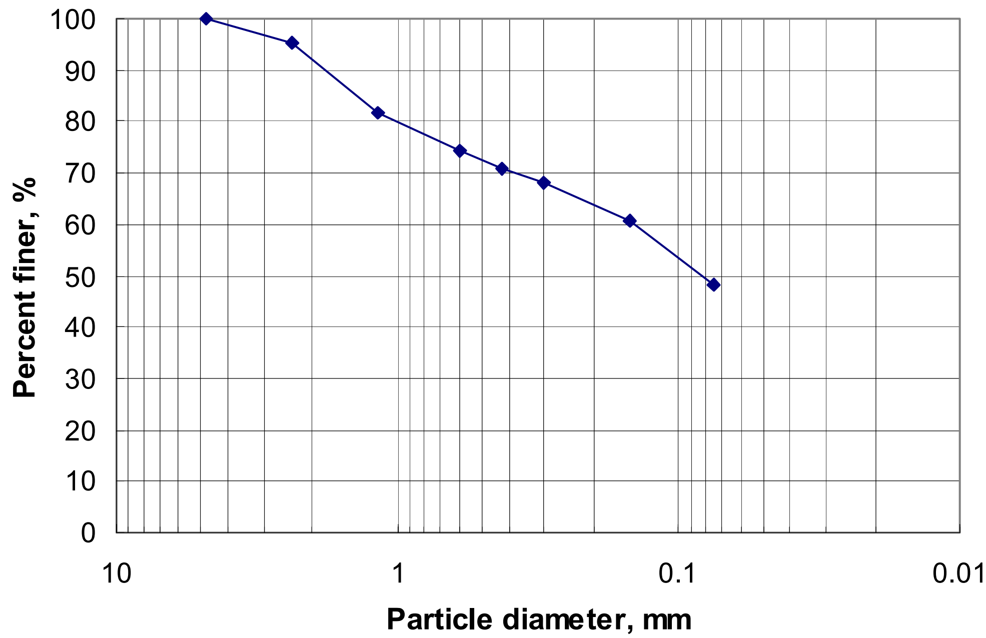

Figure 4.1 Grain Size Distribution for Clay

4.2.2 Sand

Clean sand used in this research is a locally available soil with similar properties as the Ottawa sand. This sand appears as a yellow white crystalline material. Several physical tests including specific gravity, particle size studies and Atterberg limit tests were first conducted to determine physical soil properties. This sand is poorly graded sand, with natural moisture content (w_n) of 2%, standard Proctor optimum moisture content (w_{opt}) of 18%, specific gravity (G_s) of 2.65, and liquid limit (LL) of 24%. The soil classifies as A-3 and SP (poorly graded sand) according to the AASHTO and USCS, respectively. The basic engineering properties of the testing sandy soil are summarized in table 4.2. Figure 4.2 shows the grain size distribution for sand.

Table 4.2 Basic Engineering Properties of Testing Sand

Properties	Result
Color	Yellow white
Natural moisture content, w_n (%)	2
Passing No. 200 sieve (%)	2
Clay fraction, CF (%)	N/A
Specific gravity, G_S (-)	2.65
Liquid limit, LL (%)	N/A
Plasticity index, PI (%)	N/A
Standard Proctor maximum dry unit weight, $\gamma_{d\text{-}max}$ (kN/m^3)	15.35
Standard Proctor optimum moisture content, w_{opt} (%)	18
Soluble sulfate content (ppm)	N/A
AASHTO classification	A-3
USCS classification	SP

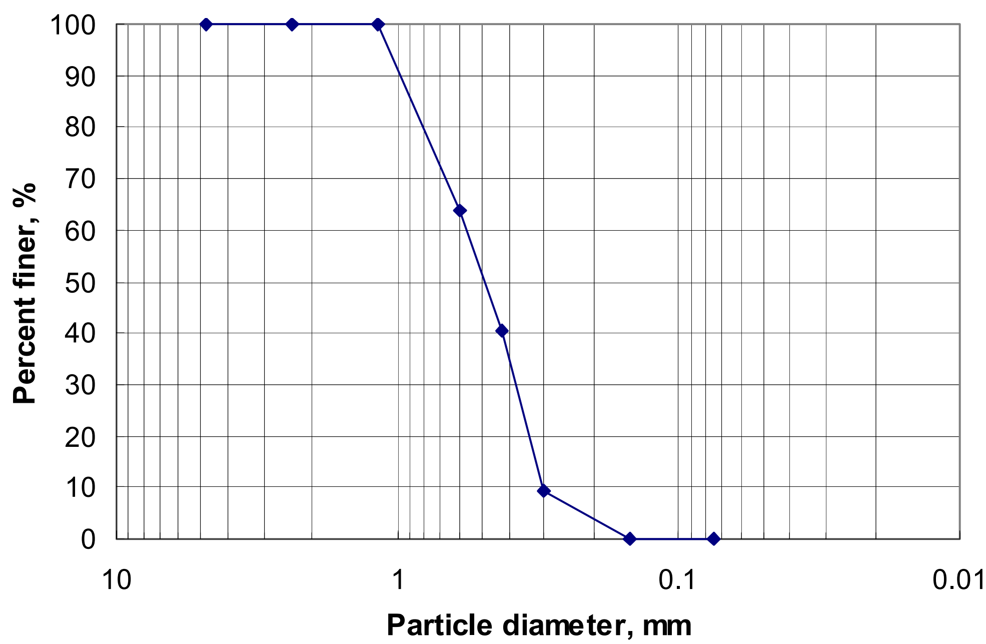

Figure 4.2 Grain Size Distribution for Sand

4.3 Experimental Variables

In this thesis work, several clay and sand specimens were tested in the RC, TX/BE, RC/BE, and PP testing devices at four confinements (0, 1, 2.5, and 5 psi, or 0, 6.9, 17.25, and 34.5 kPa) reproducing typical tress state conditions under shallow foundations and pavement subgrades. Clay specimens were compacted at five different moisture contents (optimum, and 90% and 95% of optimum dry unit weight on both dry and wet sides of optimum from standard proctor compaction curve). Sand specimens were compacted in place at six different moisture contents (0, 5, 10, 15, 20, and 24% by weight). All specimens were then subject to RC, TX/BE, and RC/BE tests under constant isotropic confining pressure as described above. The reason for compacting soil specimens at different moisture contents was to attain different matric suction states, assessed via SWCCs from pressure plate extractor and filter paper, prior to RC, TX/BE and RC/BE testing. Four K_o stress states ($K_o = (\sigma_n - u_a)/(\sigma_v - u_a)$ = 0, 0.25, 0.625, and 1.25) were achieved during TX/BE testing.

Furthermore, tests in the modified pressure plate extractor were performed at a given range of net radial confinement, ($\sigma_{net} = \sigma_r - u_a$) = 0, 1, 2.5, and 5 psi or 0, 6.9, 17.25, and 34.5 kPa, to assess the SWCCs for clay and sand under three conditions: (1) controlled radial confinement condition, (2) constant K_o stress state condition, and (3) variable K_o stress state condition.

Figure 4.3 shows the schematic of a specimen under the controlled radial confinement condition. A porous stone is placed directly on top of a thin-wall, stainless steel confining ring; the specimen is secured in place with a hollow steel plate that allows passage of air pressure (matric suction, u_a) through the porous stone. The net radial confinement ($\sigma_{net} = \sigma_r - u_a$) was kept constant under a certain net radial confinement throughout the SWCC test.

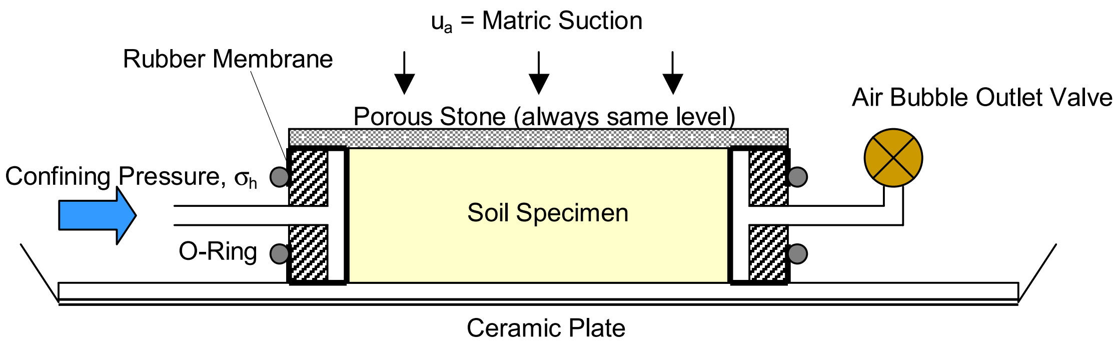

Figure 4.3 Schematic of PPE under Controlled Radial Confinement Condition

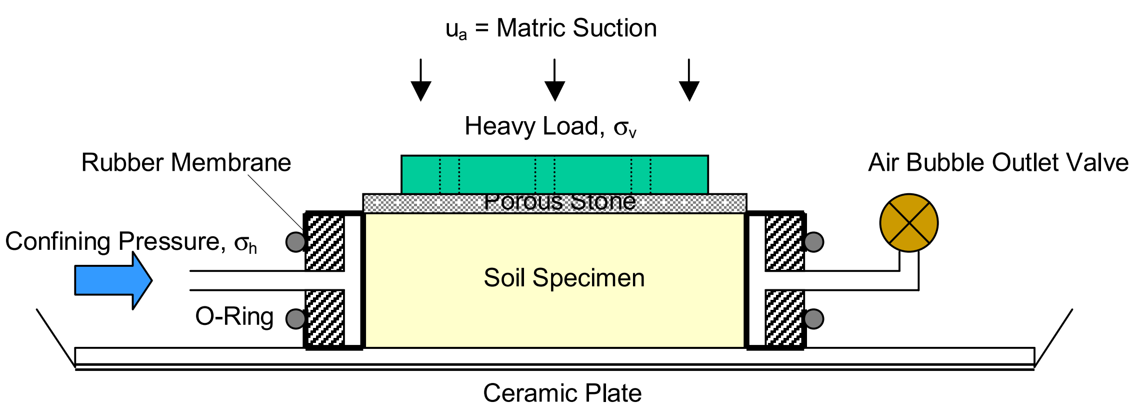

Figure 4.4 Schematic of PPE under Constant K_o Stress State
and Variable K_o Stress State Condition

Figure 4.4 shows the schematic of *constant* K_o stress state approach and the *variable* K_o stress state approach. A porous stone, 2.8-inch in diameter, is placed directly on top of the soil specimen while a stainless steel weight seats on the porous stone in order to keep a constant vertical pressure on the specimen, as shown in figure 4.5. By knowing the magnitude of the seating weight, the desired K_o

stress state (K_o = 0, 0.25, 0.625, and 1.25) was applied by supplying the necessary external confinement via the latex membrane. The vertical pressure of 4 psi (27.6 kPa) was kept constant under either approach, but the difference is the way the external water confining pressure (σ_r) is applied during SWCC testing. For *constant* K_o stress state condition, the net radial confinement ($\sigma_{net} = \sigma_r - u_a$) was kept constant, so the desired K_o value ($(\sigma_r - u_a)/\sigma_v$) does not change throughout the SWCC test while increasing the matric suction (u_a). For *variable* K_o stress state condition, the external water confining pressure (σ_r) was initially set at the desired value to attain the intended K_o stress state prior to SWCC testing. Upon an increase in matric suction (u_a), the external water confining pressure (σ_r) was kept constant at the initial value, therefore yielding a variable K_o value throughout the test.

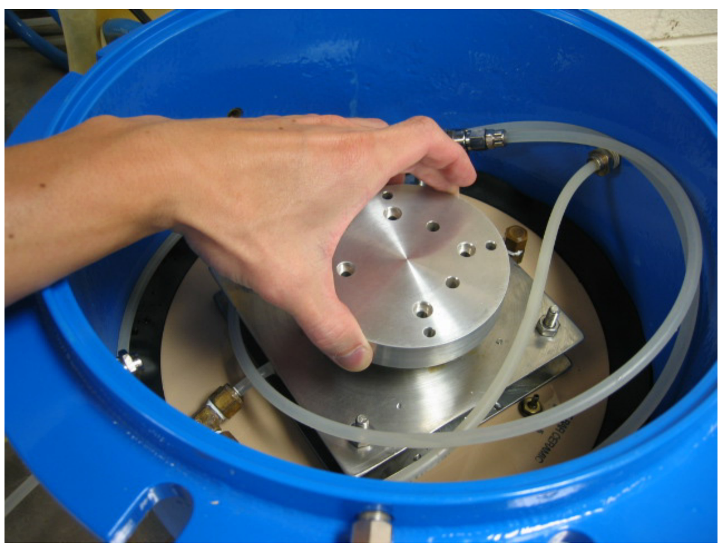

Figure 4.5 A Piece of Heavy Steel Resting of Top of Porous Stone

Table 4.3 summarizes the experimental variables used in this research work for Resonant Column (RC), Triaxial Cell with Bender Element (TX/BE), Resonant Column with Bender Element (RC/BE), and Pressure Plate Extractor (PPE) testing.

Table 4.3 Experimental Variables Used for RC, BE, RC/BE, and PPE Testing

Description	**Number of variables**
Soil type	**1**. Poorly graded sand (SP) **2**. High plasticity clay (CH)
Compaction moisture content for clay	**1**. w = 13% (90% dry), S_r = 42% **2**. w = 17% (95% dry), S_r = 55% **3**. w = 20% (optimum), S_r = 65% **4**. w = 23% (95% wet), S_r = 74% **5**. w = 27% (90% wet), S_r = 87%
Compaction moisture content for sand	**1**. w = 0%, S_r = 0% **2**. w = 5%, S_r = 22% **3**. w = 10%, S_r = 44% **4**. w = 15%, S_r = 66% **5**. w = 20%, S_r = 88% **6**. w = 24%, S_r = 100%
Radial confinement (RC, TX/BE, RC/BE)	**1**. 0 psi (0 kPa) **2**. 1 psi (6.9 kPa) **3**. 2.5 psi (17.25 kPa) **4**. 5 psi (34.5 kPa)
PPE condition	**1**. Controlled radial confinement condition **2**. Constant K_o stress state condition **3**. Variable K_o stress state condition
Number of repeated specimens	**1**. 5 for RC, TX/BE, RC/BE tests

4.4 Standard Proctor Compaction Curves

Figure 4.6 shows the standard Proctor compaction curves obtained for clay and sand to determine the graphic relationships between dry unit weight (γ_d) and compaction moisture content (w).

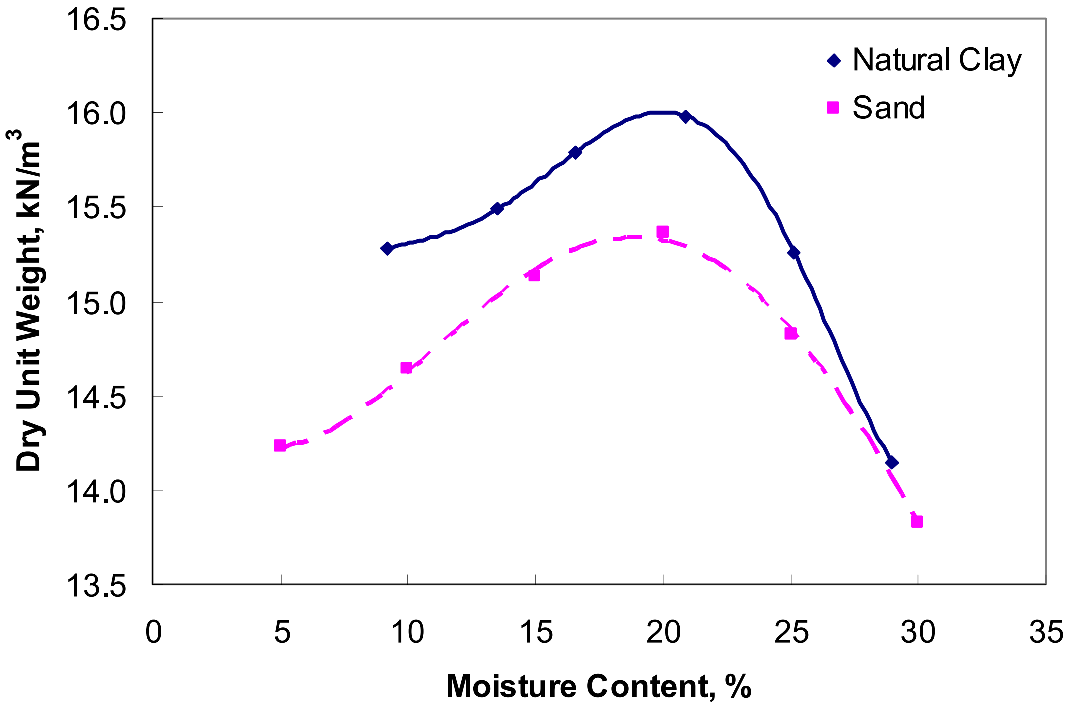

Figure 4.6 Standard Proctor Compaction Curves for Clay and Sand

To obtain the compaction moisture content and dry unit weight relationships, soil compaction tests were conducted on both clay and sand as per ASTM D-3551 method. Compaction test results were also used to establish 90 and 95 percent of optimum dry unit weight conditions on both dry and wet sides of the Proctor curve for clay. Subsequently, compaction moisture contents and dry unit weight levels were used in the soil specimen preparation.

4.5 Specimen Preparation Method

4.5.1 RC, BE, and RC/BE Specimen Preparation

Specimen preparations for this research were separated into two methods, one is preparing cohesive soil specimens outside and then transfer into the chamber, and the other is to prepare granular soil specimens inside the triaxial chamber and resonant column chamber. During specimen preparation, the necessary amounts of water, by dry weight of soil, were calculated from the desired compaction moisture content in tables 4.3. Dry soil was first thoroughly mixed with the required amount of water until ensuring homogeneity, and then this soil mix was compacted by following impact compaction method. Specimens were compacted in three equal layers into a 2.875-in diameter, 5.75-in height split miter box reinforced with two clamps (figure 4.7). Each layer was compacted using a 5.5-lb, 12-in drop, U.S. Army Corps hammer with 25 uniformly distributed blows (figure 4.8) and the soil specimens were then extruded and transferred into the triaxial cell. In case of granular soils, the soil was compacted inside the triaxial cell and resonant column chamber after applying vacuum to hold the membrane that surrounds soil specimen.

Figure 4.7 Split Miter Box with Clamps Used for Compaction

Figure 4.8 Compaction of Specimen Using U.S. Army Corps Hammer

4.5.2 Saturation of Ceramic Plate and PPE Specimen Preparation

Saturation of the 15-bar ceramic plate is initiated by soaking the plate in a pan with de-aired potable water having less than 2 mg/L of dissolved oxygen concentration. After soaking for at least 24 h, the ceramic plate is transferred to a sealed chamber containing de-aired water with a small headspace above the water. A vacuum exceeding 90 kPa is applied to the head space for 2 h. After 2 h, the vacuum is completely removed and the plate allowed to sit submerged for ½ h. The vacuum is then immediately increased to 90 kPa and held for another 2 h. While under vacuum, the plate is inspected intermittently for escaping air bubbles. This process is repeated until no air bubbles are observed for at least two consecutive applications of vacuum. The PPE device developed herein can be used to test undisturbed specimens or specimens that are compacted or reconstituted.

For *clay*, compaction tools, hammer, and a custom-made compaction ring (figure 4.9) were needed. The necessary amounts of water, by dry weight of soil, were calculated to attain optimum moisture content (w = 20%). Dry soil was first thoroughly mixed with the required amount of water until ensuring homogeneity, and then this soil mix was compacted into the 2.8-in diameter, 1-in height steel ring. Specimens were compacted in two equal layers with 16 uniformly distributed blows of a 2-lb, 12-in drop, hammer (figure 4.10). Then the soil specimens (figure 4.11) were extruded and transferred into the confining ring over the ceramic plate.

Figure 4.9 Clayey Specimen Compaction Tools for PPE Testing

Figure 4.10 Compaction of Clayey Specimen for PPE Testing

Figure 4.11 Compacted Clayey Specimen for PPE Testing

For *sand*, specimens were prepared directly into the custom-made confining ring. During compaction, the confining ring remains seated on top of the saturated 15-bar ceramic plate. A known mass of soil corresponding to optimum gravimetric moisture content is placed in the confining ring and compacted in three lifts using in-place tamping compaction, as shown in figure 4.13. The number of blows is also adjusted so that the desired unit weight is achieved.

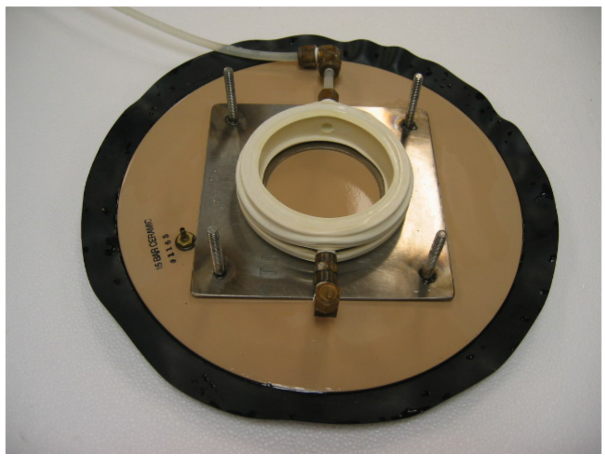

Figure 4.12 Confining Ring Seated on the Ceramic Plate

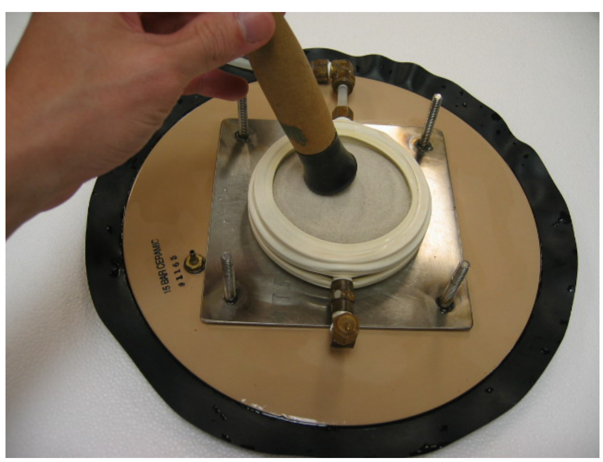

Figure 4.13 Tamping Compaction for Sand

After either compaction method is completed, saturation of the specimen is immediately initiated by placing a coarse porous stone on top of the ring and soaking the full arrangement of ceramic plate, ring, specimen, and stone was submerged in a pan of de-aired potable water. A thin hollow stainless steel plate was placed on top of the porous stone to prevent the loss of soil during soaking as shown in figure 4.14. Soaking is allowed for 24 h in sandy soils and 48 h in clayey soils. After saturation of specimen is complete, the confining ring is fully assembled into the PPE vessel.

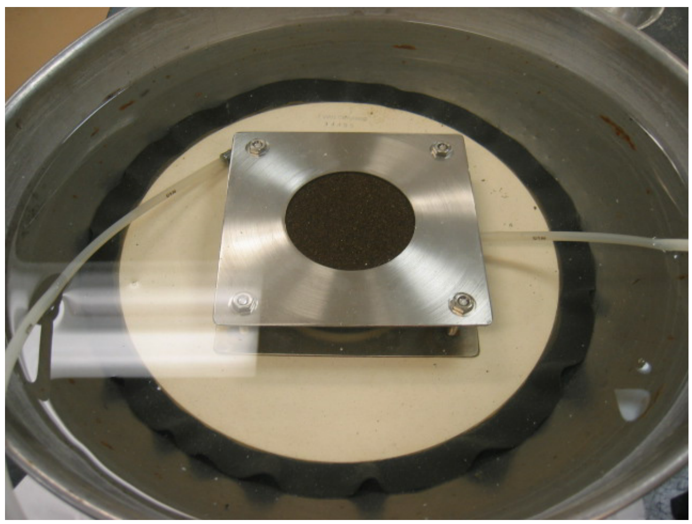

Figure 4.14 A Full Soaking Arrangement with Stainless Steel Setup

4.6 Filter Paper Testing Measurement

Specimens compacted at 20% moisture content and used for RC and BE tests, were cut in two halves for matric suction measurement with filter paper. The specimens were trimmed to easily fit into a clean glass jar making sure that the surfaces of the sample are smooth and flat enough to establish an intimate contact with the filter paper for accurate matric suction measurement. Figure 4.15 shows the specimen cut in two halves with filter paper supplies.

In order to get soil suction values at low moisture contents (high suction), however, the specimens were left air-drying in opened glass jars at room temperature (25°C), to allow for some moisture to evaporate at the same dry density. After a moisture content was reached at the approximately desired amount of water (3% ≤ w ≤ 15%), then suction measurement was initiated via filter paper.

Figure 4.15 Two Halves Soil Specimens with Filter Paper Apparatus

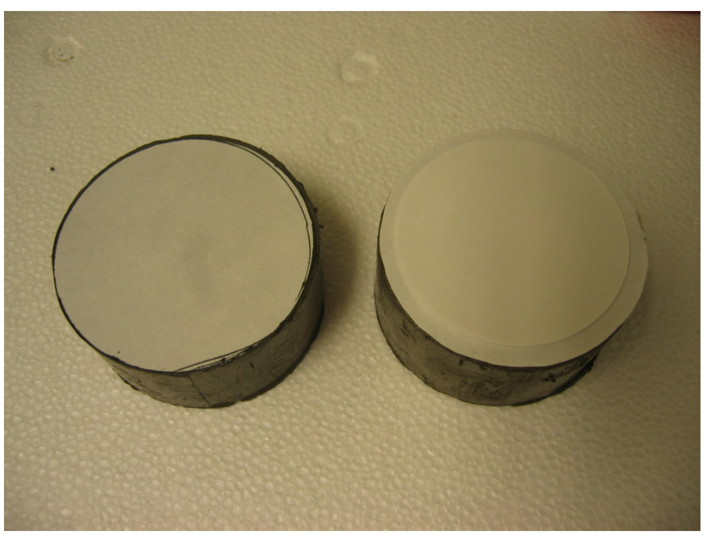

Figure 4.16 Schleicher&Schuell No. 589-WH Filter Paper
in between Two Larger Protective Filter Papers

For matric suction measurements, a single Schleicher&Schuell No. 589-WH filter paper was inserted in between two protective filter papers larger in diameter (figure 4.16). After that, the other half of the soil sample was put on top, keeping the sandwiched filter papers in between and in intimate contact with the soil samples. The two pieces of soil were then taped together, as shown in figure 4.17.

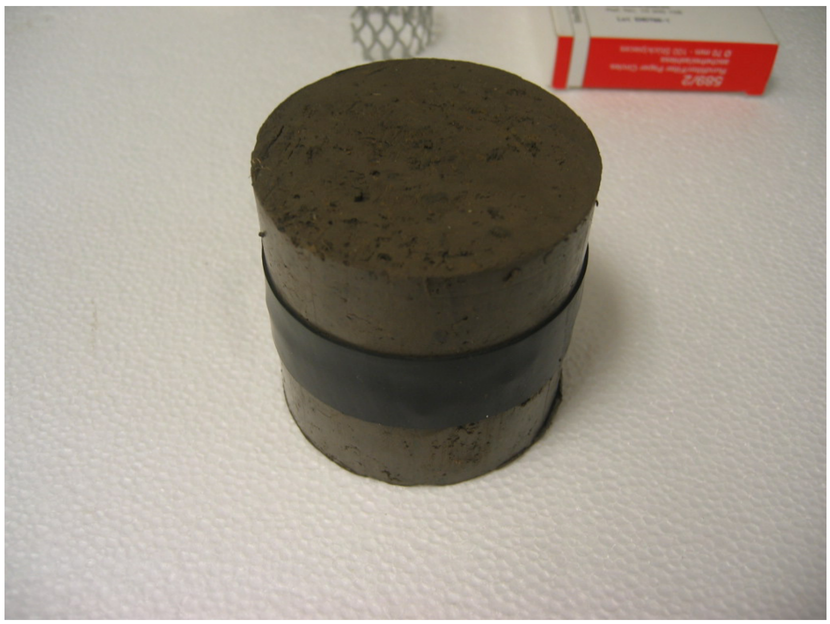

Figure 4.17 Two Pieces of Soil Samples Taped Together

For total suction measurements, after the two halves of the soil specimens were carefully put in the glass jar, a piece of rolled stainless steel net was placed on top of the specimen, as shown in figure 4.18. Then, dry filter paper, 5.5-cm diameter, was removed from the box using tweezers and placed on top of a piece of rolled stainless steel net that has the sharp edge facing up in order to minimize the contact area (figure 4.19). Next, the lid was closed and secured tightly in order to prevent any moisture exchange between the air inside and the air outside of the glass jar (figure 4.20). The jar was then left in a controlled temperature room for 3 weeks.

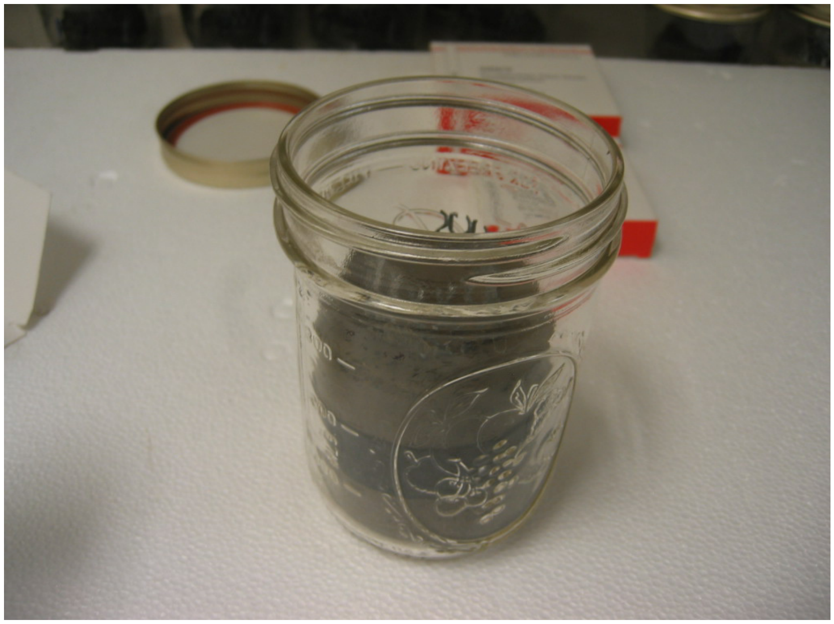

Figure 4.18 Soil Specimen in Glass Jar with Rolled Stainless Steel Net on Top

Figure 4.19 Filter Paper Resting on Top of Rolled Stainless Steel Net Using Tweezers

Figure 4.20 Glass Jar Secured Tightly with Lid

After the three-week equilibrium period, the glass jar is opened and the filter paper quickly and gently carried with a pair of tweezers (figure 4.21) in less than a few seconds. Subsequently, filter paper was directly put on a moisture tin and the weight measured with a balance to the nearest 0.0001 gram accuracy (figure 4.22).

Figure 4.21 Filter Paper Removed from Glass Jar Using Tweezers

Figure 4.22 A tin with Wet Filter Paper inside Small Scale Balance

Then, the tin with the wet filter paper was transferred to a hot oven and left in the oven for at least 10 hours. After that, the weight of the fully dry filter paper was measured using the same balance. Soil moisture and the moisture content of each filter paper were then calculated. Suction values were obtained accordingly from the appropriate calibration curve, as shown in figure 3.49.

Chapter 5 describes the experimental program followed in this work and a comprehensive analysis of all test results.

CHAPTER 5

EXPERIMENTAL PROGRAM AND TEST RESULTS

5.1 Introduction

In this thesis, a total of 220 resonant column (RC) tests, 495 bender element (TX/BE) tests in the triaxial cell, 220 resonant column with bender element (RC/BE) tests, and 336 pressure plate extractor tests were performed on 1,171 specimens of clay and sand combining all the experimental variables described in Chapter 4.

The present chapter describes the experimental program and procedures followed in this work, and presents a comprehensive analysis of all test results, including effects of all test variables on soil's small-strain shear modulus (G_{max}) and material damping (D_{min}).

5.2 Specimen Notation

A simple notation for specimen identification was adopted in order to facilitate the reading of all variables intervening in the fabrication/compaction of a specific specimen, particularly those variables referred to soil types, compacted moisture contents, and confinements. Table 5.1 shows the notation symbols used in this work.

For instance, a specimen identified as **"S-05-00-2"** indicates that this is a specimen made of **S**and mixed with water at **05**%-by-weight, subjected to **0.0**-psi confinement, and labeled as trial specimen number **2**. Table 5.2 summarizes compaction moisture conditions and dry unit weight for each compaction for both clay and sand.

Table 5.1 Notation Symbols Used for Identification of all Test Specimens

Symbol	Description
S	Specimen made of **S**and
C	Specimen made of **C**lay
00	Sand compacted at **00**% moisture content
05	Sand compacted at **05**% moisture content
10	Sand compacted at **10**% moisture content
15	Sand compacted at **15**% moisture content
20	Sand compacted at **20**% moisture content
24	Sand compacted at **24**% moisture content
90D	Clay compacted at **90**% of optimum on **D**ry side
95D	Clay compacted at **95**% of optimum on **D**ry side
OPT	Clay compacted at **OPT**imum moisture content
95W	Clay compacted at **95**% of optimum on **W**et side
90W	Clay compacted at **90**% of optimum on **W**et side
00-1	**0.0** psi confinement applied to trial specimen **1**
10-1	**1.0** psi confinement applied to trial specimen **1**
25-1	**2.5** psi confinement applied to trial specimen **1**
50-1	**5.0** psi confinement applied to trial specimen **1**

Table 5.2 Dry Unit Weights and Compaction Moisture Contents

Soil Specimen	Dry Unit Weight, γ_d (kN/m^3)	Moisture Content, w (%)
S-00	14.28	0
S-05	14.39	5
S-10	14.63	10
S-15	15.07	15
S-20	15.38	20
S-24	14.83	24
C-90D	14.76	13
C-95D	15.56	17
C-OPT	16.33	20
C-95W	15.51	23
C-90W	14.71	27

5.3 Experimental Program and Procedure

After the sand and clay specimens were compacted at desired dimensions and moisture contents, five specimens for each moisture content were tested in the RC, TX/BE, and RC/BE testing devices at four confinement (0, 1, 2.5, and 5 psi, or 0, 6.9, 17.25, and 34.5 kPa), which are aimed at reproducing stress conditions in shallow foundation and subgrade soils. Additionally, PPE test was performed in three condition as described in chapter 4, (1) fixed-boundary condition, (2) constant K_o stress state condition, and (3) variable K_o stress state condition, in order to determine the SWCCs for three stress state conditions.

All RC tests were performed by sending a 250-mV peak-to-peak sinusoidal signal from the Dynamic Signal Analyzer (DSA) to the torsional driver fixed on top of specimen (chapter 3). The frequency of the signal was incrementally changed by sweeping the frequency scale in the DSA until the resonant frequency (f_r) of the soil-driver system was found and the complete frequency response curve was obtained.

This low-amplitude signal induces a linear response in the specimen and allows for the determination of the low-amplitude values of G_{max} and D_{min}.

TX/BE tests were achieved by sending the pulse signal from the oscilloscope to the transmitter, and then the shear wave generated from top bender element was traveling through the specimen to the receiver, the bottom bender element. Subsequently, the travel time of shear wave along the height of the specimen was measured from Picowave program on computer monitor, after that shear wave velocity was calculated. At last, the shear modulus (G) was determined using the equation as described in chapter 3. Moreover, the damping ratio (D) was measured by sending the continuous sine waveform at different frequency and creating the plot of frequency and amplitude of receiving signal until find the peak. Then, damping ratio (D) was calculated using the half power method as shown in chapter 3.

RC/BE also was performed at sand and clay specimens to find out the shear modulus (G) and damping ratio (D) of the specimen under four confinements (0, 1, 2.5, and 5 psi, or 0, 6.9, 17.25, and 34.5 kPa) and compare the result from both RC method and TX/BE method in the same air confinement chamber.

Besides, modified PPE was used to create the soil water characteristic curves (SWCC) of three stress state conditions: (1) controlled radial confinement, (2) constant K_o stress state condition, and (3) variable suction dependent K_o stress state condition for sand and clay as described in chapter 4. Additionally, in order to complete the SWCC for clay at high suctions, filter paper technique was presented to measure the matric suctions for clay that modified PPE was incapable to reach the air pressure (u_a) more than 100 psi (690 kPa).

5.4 SWCCs from Modified PPE

5.4.1 Controlled Radial Confinement Condition

5.4.1.1 SWCC for Sand

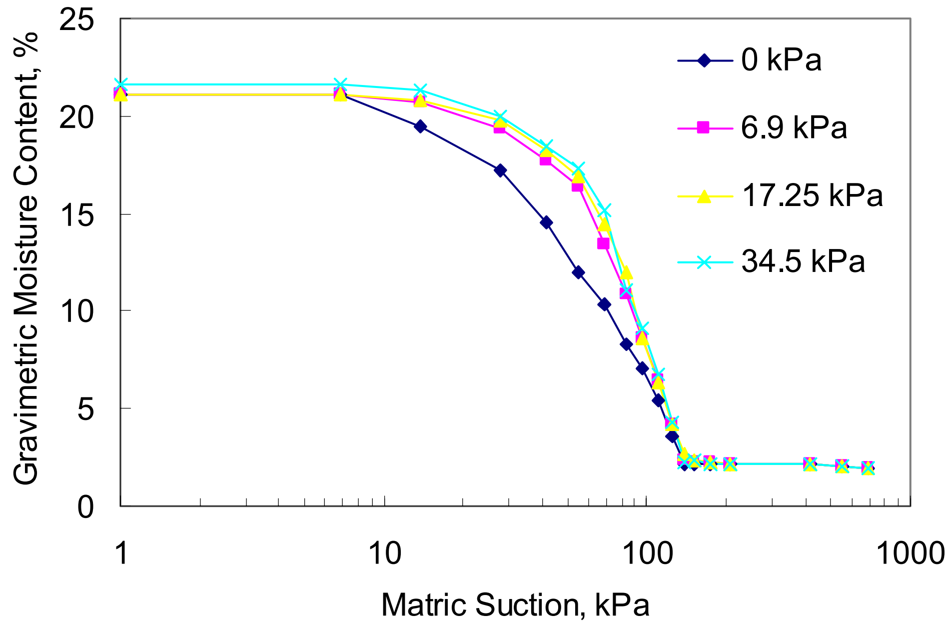

Figure 5.1 SWCC at Different Net Radial Confinement under Controlled Radial Confinement for Sand

Figure 5.1 shows a series of four SWCC tests performed on poorly-graded sand (SP) in the modified PPE device at fixed-boundary condition. Each test was performed at a different net radial confinement (N.R.C.), that is, $(\sigma_r - u_a)$ = 0, 1, 2.5, or 5 psi (0, 6.9, 17.25, or 34.5 kPa, respectively). It can be noticed the significant influence of N.R.C. on the shape and position of the SWCC. The SWCC is shifted rightward at higher net confinements. This can be attributed to a decrease in the average pore size (void ratio) of the soil mass as the N.R.C. is increased, despite the fact that all specimens featured similar moisture content and density prior to SWCC testing.

5.4.1.2 SWCC for Clay

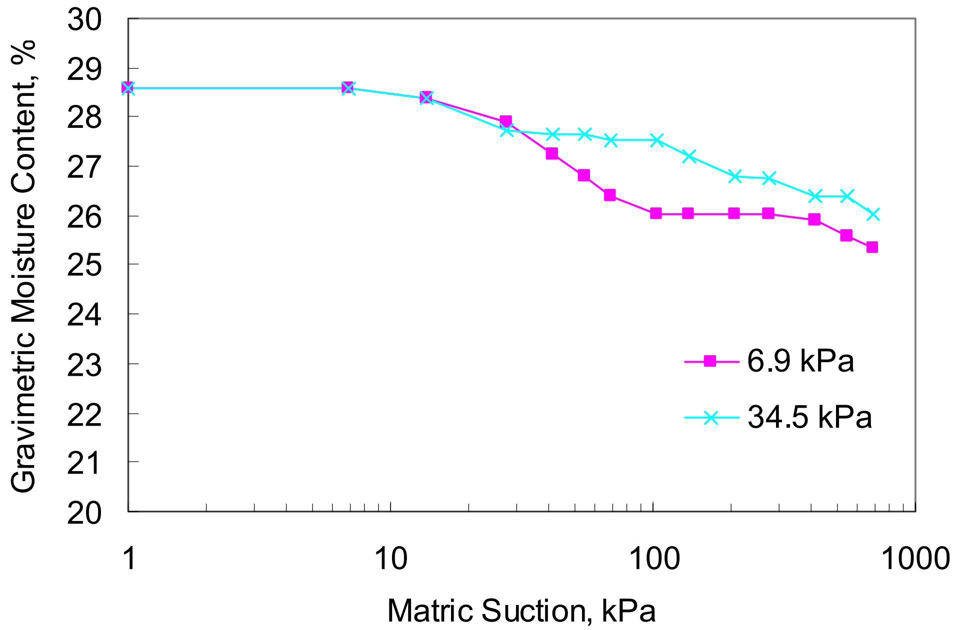

Figure 5.2 SWCC at Different Net Radial Confinement under Controlled Radial Confinement for Clay

Figure 5.2 shows a series of two SWCC tests performed on high plasticity clay (CH) in the modified PPE device at fixed-boundary condition. Each test was performed at a different net radial confinement (N.R.C.), that is, $(\sigma_r - u_a)$ = 1 or 5 psi (6.9 or 34.5 kPa, respectively). It can be noticed the significant influence of N.R.C. on the shape and position of the SWCC. The initial SWCCs were started at similar moisture content. It can be stated that N.R.C. has no effect of saturation moisture content. The SWCC is shifted rightward at higher net confinements. This also can be attributed to a decrease in void ratio of the soil mass as the N.R.C. is increased, despite the fact that all specimens featured similar moisture content and density prior to SWCC testing.

5.4.2 Constant K_0 Stress State Condition

5.4.2.1 SWCC for Sand

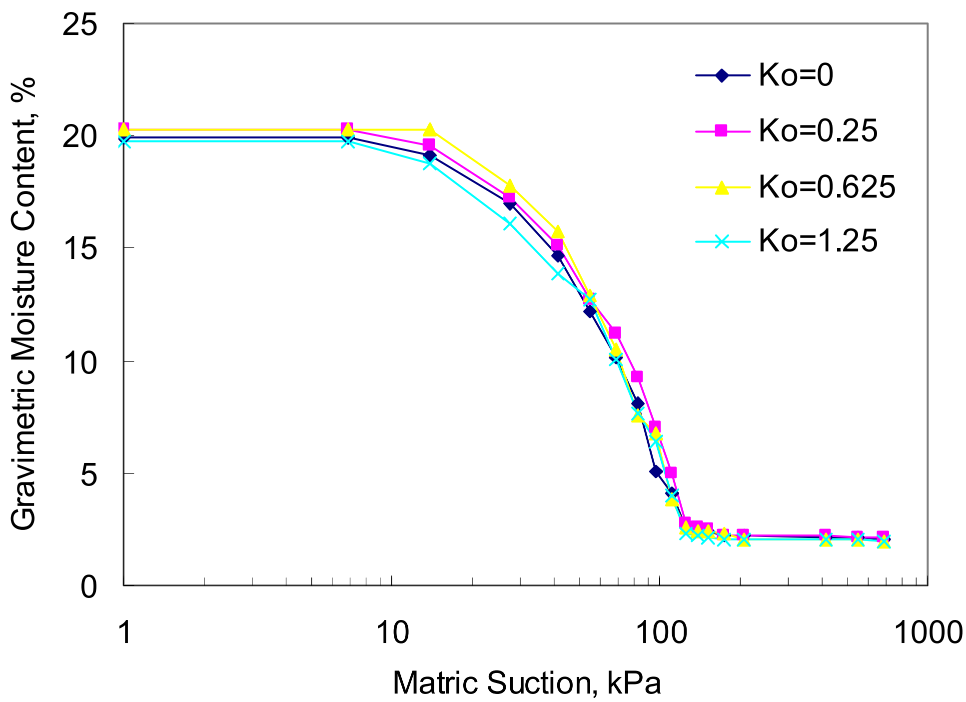

Figure 5.3 SWCC at Different K_0 under Constant K_0 Condition for Sand

Figure 5.3 shows a series of four SWCC tests performed on poorly-graded sand (SP) in the modified PPE device at constant K_0 condition. Each test was performed at a different constant K_0, that is, $(\sigma_r - u_a)/\sigma_v$ = 0, 0.25, 0.625, and 1.25. It can be noticed that the influence of K_0 on the shape and position of the SWCC is almost negligible. In this work, the selected range of the experimental variables was intended to reproduce in-situ stress states within a pavement or shallow foundation system (less than 5-psi confinement). Therefore, it is expected that higher levels of stress (more than 10-psi confinement) will have a considerable effect on the SWCC response of SP soils.

5.4.2.2 SWCC for Clay

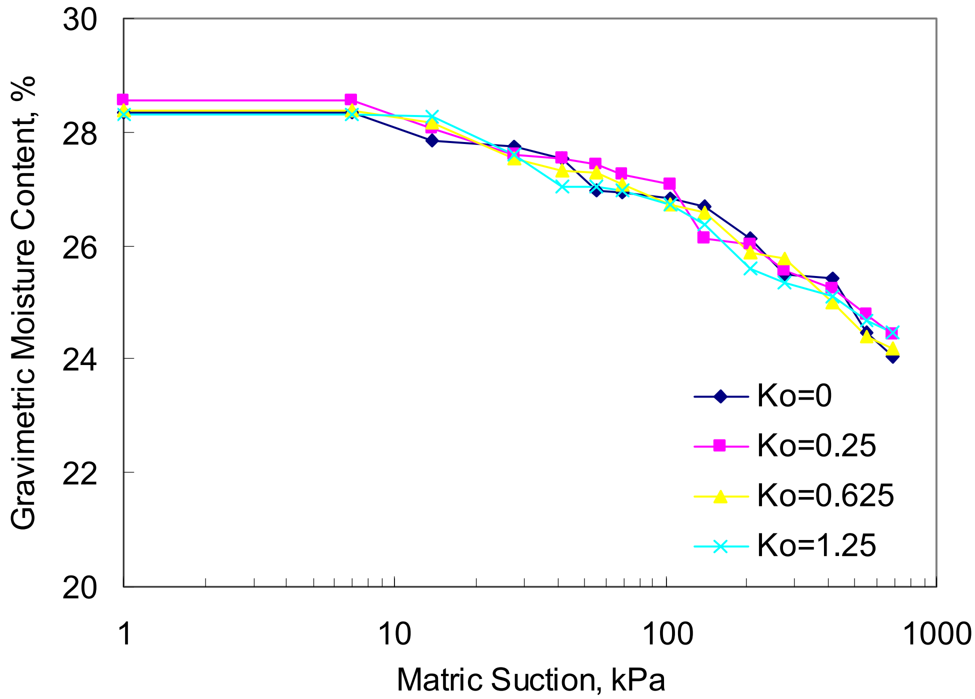

Figure 5.4 SWCC at Different K_0 under Constant K_0 Condition for Clay

Figure 5.4 shows a series of four SWCC tests performed on high plasticity clay (CH) in the modified PPE device at constant K_0 condition. Each test was performed at a different constant K_0, that is, $(\sigma_r - u_a)/\sigma_v$ = 0, 0.25, 0.625, and 1.25. It can be noticed that the considerable influence of K_0 on the shape and position of the SWCC is negligible.

Again, the selected range of the experimental variables was intended to reproduce in-situ stress states within a pavement or shallow foundation system (less than 5-psi confinement). It is expected that higher levels of stress (more than 10-psi confinement) will have a considerable effect on the SWCC response of CH soils.

5.4.3 Variable K_0 Stress State Condition

5.4.3.1 SWCC for Sand

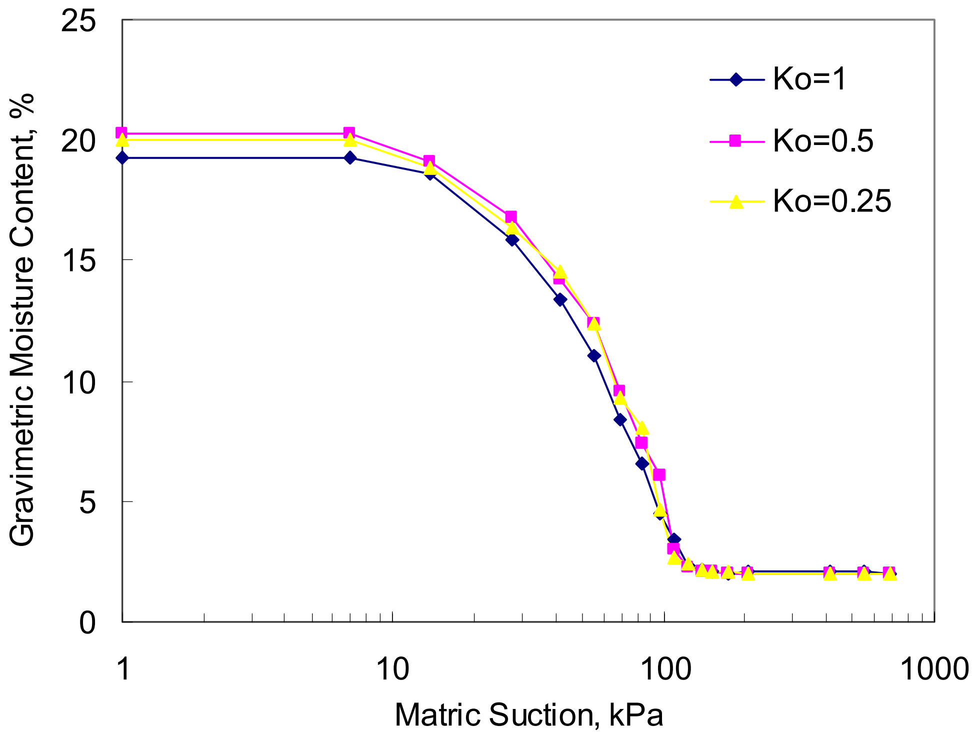

Figure 5.5 SWCC at Different Initial K_0 Stress State under Variable Suction Dependent K_0 Condition for Sand

Figure 5.5 shows a series of four SWCC tests performed on poorly-graded sand (SP) in the modified PPE device under variable suction dependent K_0 stress state condition. Each test was performed at different three initial K_0 stress states, that is, $(\sigma_r - u_a)/\sigma_v$ = 0, 0.5, and 1. Likewise, the suction-dependent (variable) K_0 stress state was found to exert no significant influence on the SWCC response of SP soils under controlled K_0 stress state condition. This can be explained by the possible fact that the average pore size (void ratio) of the soil mass, for the range of stress levels applied, did not experience major variations during SWCC testing.

5.4.3.2 SWCC for Clay

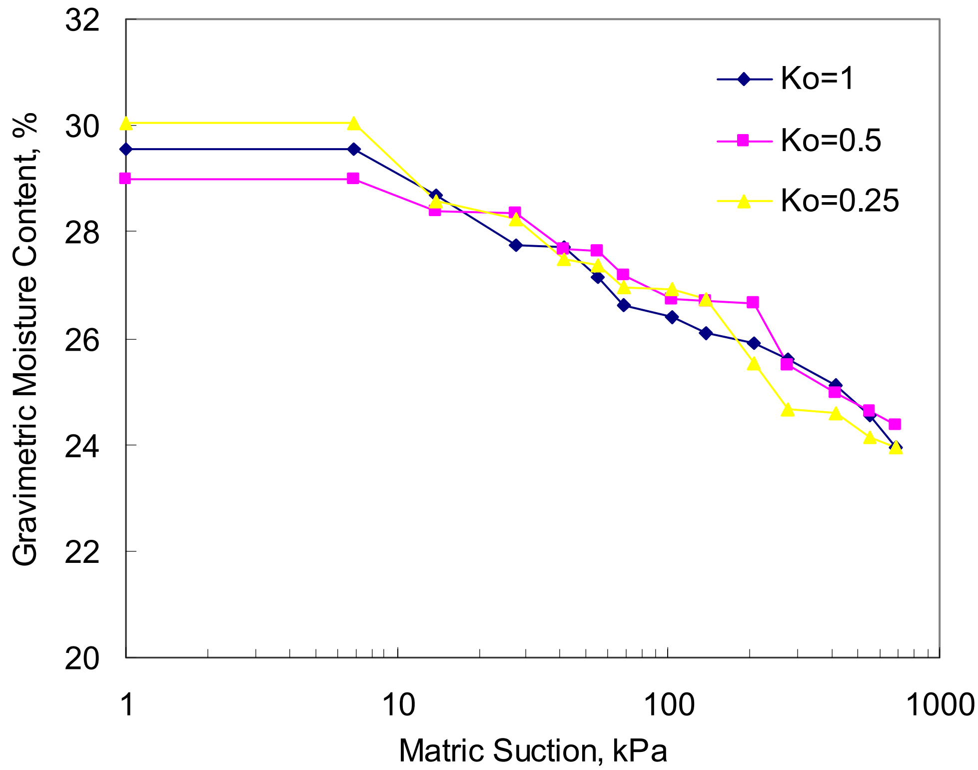

Figure 5.6 SWCC at Different Initial K_0 Stress State under Variable Suction Dependent K_0 Condition for Clay

Figure 5.6 shows a series of four SWCC tests performed on high plasticity clay (CH) in the modified PPE device under variable suction dependent K_0 condition. Each test was performed at different initial K_0 stress state, that is, $(\sigma_r - u_a)/\sigma_v = 0$, 0.5, and 1. Again, suction-dependent (variable) K_0 stress state was found to exert no significant influence on the SWCC response of CH soils under controlled K_0 stress state condition. This can also be explained by the possible fact that the average pore size of the soil mass, for the range of stress levels applied, did not experience major variations during SWCC testing.

5.5 RC Response

5.5.1 Typical RC Test Result

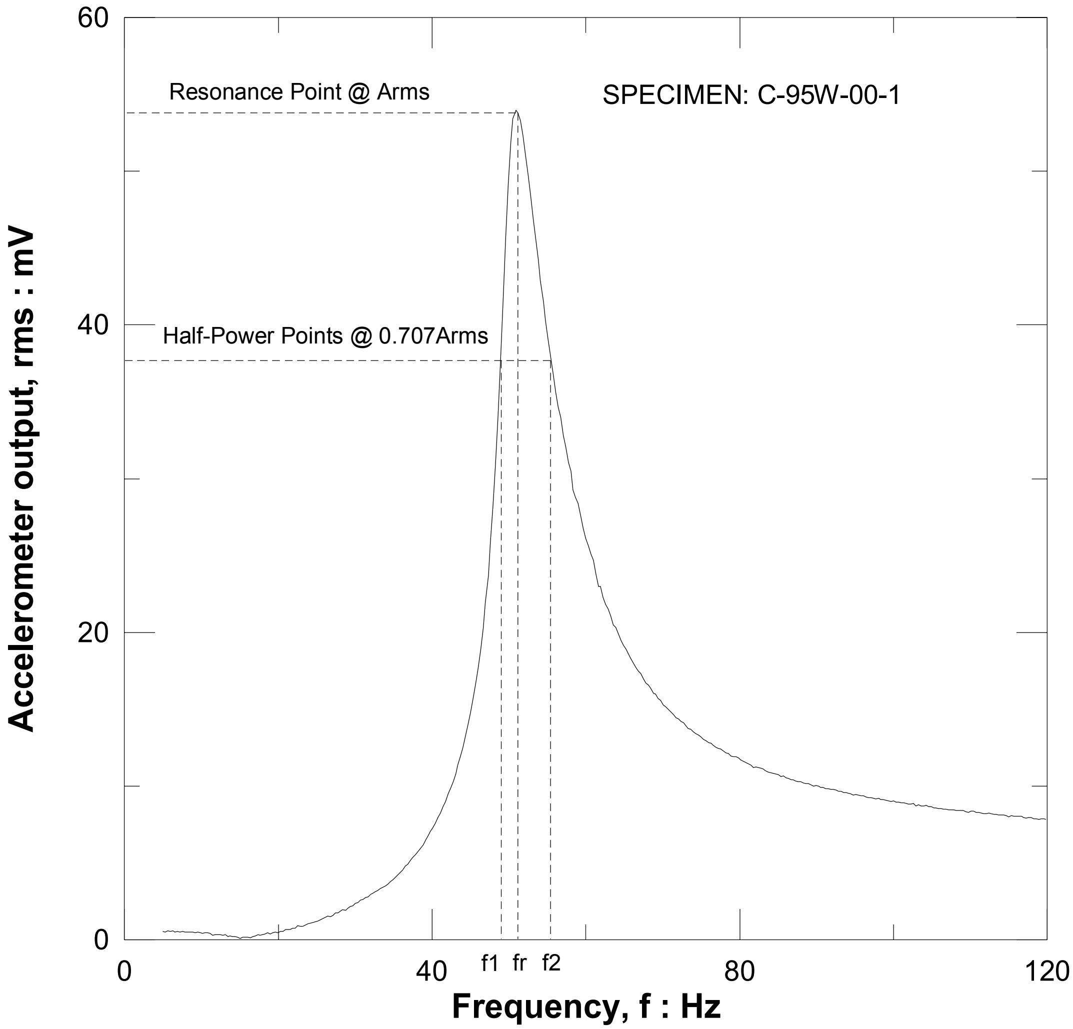

Figure 5.7 Typical Response at Low-Amplitude Shearing Strain Level

Figure 5.7 shows a typical stress and strain curve obtained for specimen C-95W-00-1 under 0-psi (0 kPa) isotopic confinement and low-amplitude excitation. The resonant frequency, (f_r), corresponding to the peak of the frequency response curve and the half power points (f_1 and f_2), is used to determine small-strain stiffness properties (G_{max} and D_{min}) for this particular specimen as described in chapter 3. Tables 5.3 through 5.13 show shear modulus (G) and damping ratio (D) values of sand and clay, respectively, in different moisture contents.

5.5.2 Sand

A series of resonant column (RC) tests were conducted on several specimens of sand compacted at six moisture contents, 0%, 5%, 10%, 15%, 20%, and 24% in order to determine relationships between small-strain shear modulus (G_{max}) and small-strain damping ratio (D_{min}) with isotropic confining pressure (σ_0).

Tables 5.3 through 5.8 present the results of small-strain shear modulus (G_{max}), small-strain damping ratio (D_{min}), and the average values of shear modulus and damping ratio of specimens under the same isotropic confining pressure (σ_0).

Figures 5.8 and 5.9 show the variation of small-strain shear modulus (G_{max}) and damping ratio (D_{min}) for sand at six moisture contents with confining pressure (σ_0). It can be seen that G_{max} increases and D_{min} decreases with confinement σ_0. This can be explained by the fact that the higher the confinement level, the more the specimen consolidates, and hence the stiffer it becomes.

It can be observed from these figures that the specimen prepared at 0% moisture content give the highest values of G_{max} and also give the lowest value of D_{min} as compared to any other specimen at any confinement. Moreover, it can be noted that the shear modulus (G_{max}) decreases and damping ratio (D_{min}) increases with an increase in the amount of moisture content.

Consequently, knowing that as the moisture content increases the soil suction decreases, it can be stated that the shear modulus (G_{max}) increases and damping ratio (D_{min}) decreases with soil suction (ψ).

Table 5.3 RC Test Results of Sand at w = 0% ($\psi \rightarrow \infty$)

Specimen	f_r (Hz)	V_{rms} (mV)	G_{max} (MPa)	D_{min} (%)	Avg G_{max} (MPa)	Avg D_{min} (%)
S-00-00-1	46.72	63.27	19.69	4.224	18.74 (SD* = 1.232)	4.373 (SD = 0.521)
S-00-00-2	43.13	62.84	16.74	4.325		
S-00-00-3	44.87	63.49	18.12	4.654		
S-00-00-4	45.85	64.35	18.93	3.540		
S-00-00-5	47.46	64.54	20.27	5.120		
S-00-10-1	76.11	195.70	52.15	1.973	53.90 (SD = 1.576)	2.459 (SD = 0.396)
S-00-10-2	77.06	191.91	53.46	2.301		
S-00-10-3	76.41	195.73	52.56	2.245		
S-00-10-4	78.12	196.26	54.94	3.120		
S-00-10-5	79.15	194.26	56.40	2.654		
S-00-25-1	91.84	246.81	75.93	1.682	74.58 (SD = 1.894)	1.786 (SD = 0.338)
S-00-25-2	91.76	254.20	75.81	1.542		
S-00-25-3	90.16	249.26	73.17	1.354		
S-00-25-4	92.15	253.15	76.45	2.097		
S-00-25-5	89.16	251.36	71.56	2.254		
S-00-50-1	106.03	317.70	101.21	0.660	102.37 (SD = 2.257)	0.903 (SD = 0.228)
S-00-50-2	106.09	320.10	101.33	0.893		
S-00-50-3	107.12	321.32	103.31	1.325		
S-00-50-4	108.65	319.15	106.28	0.880		
S-00-50-5	105.26	318.21	99.74	0.756		

* SD = Standard Deviation

Table 5.4 RC Test Results of Sand at w = 5% (ψ = 111.99 kPa)

Specimen	f_r (Hz)	V_{rms} (mV)	G_{max} (MPa)	D_{min} (%)	Avg G_{max} (MPa)	Avg D_{min} (%)
S-05-00-1	45.82	43.68	19.84	5.857	19.09 (SD = 0.685)	5.568 (SD = 0.431)
S-05-00-2	45.67	55.20	19.71	5.362		
S-05-00-3	44.65	47.91	18.84	5.451		
S-05-00-4	44.99	49.35	19.12	4.956		
S-05-00-5	43.56	52.12	17.93	6.213		
S-05-10-1	70.64	114.40	47.14	2.301	48.81 (SD = 1.329)	2.576 (SD = 0.377)
S-05-10-2	71.35	115.36	48.10	2.546		
S-05-10-3	71.58	115.45	48.42	2.846		
S-05-10-4	72.25	114.26	49.33	3.124		
S-05-10-5	73.52	116.23	51.07	2.065		
S-05-25-1	85.86	138.60	69.65	1.893	70.29 (SD = 2.334)	1.994 (SD = 0.228)
S-05-25-2	85.46	139.36	69.00	1.638		
S-05-25-3	87.25	137.65	71.93	2.136		
S-05-25-4	88.37	140.26	73.78	2.314		
S-05-25-5	84.26	137.65	67.08	1.987		
S-05-50-1	92.28	149.70	80.45	1.788	84.41 (SD = 2.575)	1.640 (SD = 0.224)
S-05-50-2	94.66	149.99	84.65	1.685		
S-05-50-3	93.57	147.91	82.72	1.895		
S-05-50-4	96.08	148.19	87.22	1.623		
S-05-50-5	95.95	149.64	86.99	1.236		

Table 5.5 RC Test Results of Sand at w = 10% (ψ = 68.72 kPa)

Specimen	f_r (Hz)	V_{rms} (mV)	G_{max} (MPa)	D_{min} (%)	Avg G_{max} (MPa)	Avg D_{min} (%)
S-10-00-1	45.91	66.29	19.91	4.357	18.80 (SD = 2.148)	4.383 (SD = 0.205)
S-10-00-2	39.88	63.26	15.03	4.678		
S-10-00-3	45.93	65.84	19.93	4.248		
S-10-00-4	47.33	60.37	21.17	4.098		
S-10-00-5	43.60	60.55	17.96	4.536		
S-10-10-1	68.26	70.37	44.02	4.944	45.84 (SD = 1.296)	4.347 (SD = 0.383)
S-10-10-2	68.76	70.52	44.67	4.376		
S-10-10-3	70.40	70.93	46.83	4.438		
S-10-10-4	70.88	71.47	47.46	3.756		
S-10-10-5	69.92	69.17	46.20	4.219		
S-10-25-1	81.58	71.13	62.88	4.933	60.81 (SD = 1.948)	4.425 (SD = 0.420)
S-10-25-2	81.34	73.75	62.51	4.876		
S-10-25-3	78.01	73.74	57.50	4.376		
S-10-25-4	80.49	72.07	61.20	4.019		
S-10-25-5	79.67	72.56	59.98	3.921		
S-10-50-1	94.18	71.31	83.80	4.619	77.49 (SD = 3.810)	4.292 (SD = 0.332)
S-10-50-2	91.34	75.14	78.82	3.805		
S-10-50-3	88.01	73.45	73.18	3.987		
S-10-50-4	88.49	73.52	73.98	4.573		
S-10-50-5	90.67	74.20	77.68	4.476		

Table 5.6 RC Test Results of Sand at w = 15% (ψ = 42.50 kPa)

Specimen	f_r (Hz)	V_{rms} (mV)	G_{max} (MPa)	D_{min} (%)	Avg G_{max} (MPa)	Avg D_{min} (%)
S-15-00-1	45.67	62.79	19.71	5.474	17.36 (SD = 1.311)	5.328 (SD = 0.200)
S-15-00-2	42.52	63.75	17.08	5.378		
S-15-00-3	43.29	63.36	17.70	5.284		
S-15-00-4	41.24	63.16	16.07	4.967		
S-15-00-5	41.47	62.69	16.25	5.536		
S-15-10-1	65.64	70.02	40.71	4.761	41.51 (SD = 1.868)	4.642 (SD = 0.173)
S-15-10-2	68.75	71.14	44.66	4.875		
S-15-10-3	65.99	70.31	41.14	4.635		
S-15-10-4	66.75	70.83	42.09	4.573		
S-15-10-5	64.22	71.85	38.97	4.367		
S-15-25-1	75.87	70.89	54.39	4.765	53.02 (SD = 0.987)	4.481 (SD = 0.168)
S-15-25-2	74.93	70.51	53.05	4.437		
S-15-25-3	75.41	70.46	53.72	4.521		
S-15-25-4	73.88	70.41	51.57	4.437		
S-15-25-5	74.46	70.47	52.38	4.247		
S-15-50-1	78.72	70.99	58.55	4.509	65.94 (SD = 5.648)	4.313 (SD = 0.183)
S-15-50-2	81.21	71.09	62.31	4.432		
S-15-50-3	88.97	71.14	74.79	4.378		
S-15-50-4	85.69	7/.35	69.37	4.261		
S-15-50-5	82.74	7/.98	64.67	3.984		

Table 5.7 RC Test Results of Sand at w = 20% (ψ = 7.04 kPa)

Specimen	f_r (Hz)	V_{rms} (mV)	G_{max} (MPa)	D_{min} (%)	Avg G_{max} (MPa)	Avg D_{min} (%)
S-20-00-1	43.79	60.13	18.12	5.823	16.24 (SD = 1.198)	5.725 (SD = 0.172)
S-20-00-2	42.35	56.46	16.94	5.794		
S-20-00-3	39.58	56.17	14.80	5.932		
S-20-00-4	40.11	57.02	15.20	5.638		
S-20-00-5	41.35	56.96	16.15	5.438		
S-20-10-1	64.07	69.92	38.78	4.917	36.85 (SD = 1.512)	4.925 (SD = 0.170)
S-20-10-2	60.34	68.31	34.40	4.675		
S-20-10-3	63.10	69.17	37.62	4.836		
S-20-10-4	61.72	66.49	35.99	5.013		
S-20-10-5	62.96	67.86	37.45	5.183		
S-20-25-1	74.66	69.92	52.66	4.492	50.70 (SD = 1.109)	4.687 (SD = 0.224)
S-20-25-2	72.71	65.03	49.95	4.873		
S-20-25-3	72.33	62.74	49.43	4.426		
S-20-25-4	73.09	64.45	50.48	5.013		
S-20-25-5	73.47	62.97	51.00	4.632		
S-20-50-1	84.81	71.32	67.95	4.227	61.16 (SD = 3.788)	4.213 (SD = 0.172)
S-20-50-2	80.23	48.79	60.81	4.362		
S-20-50-3	77.80	47.39	57.19	4.071		
S-20-50-4	80.85	48.32	61.76	3.974		
S-20-50-5	78.42	48.35	58.10	4.432		

Table 5.8 RC Test Results of Sand at w = 24% (ψ = 0.64 kPa)

Specimen	f_r (Hz)	V_{rms} (mV)	G_{max} (MPa)	D_{min} (%)	Avg G_{max} (MPa)	Avg D_{min} (%)
S-24-00-1	36.11	56.55	12.32	5.539	13.44 (SD = 0.750)	5.450 (SD = 0.152)
S-24-00-2	37.35	56.46	13.18	5.433		
S-24-00-3	38.58	56.17	14.07	5.218		
S-24-00-4	39.11	57.02	14.45	5.673		
S-24-00-5	37.35	56.96	13.18	5.385		
S-24-10-1	60.46	68.81	34.54	4.424	32.80 (SD = 0.966)	4.516 (SD = 0.146)
S-24-10-2	58.34	68.31	32.16	4.368		
S-24-10-3	59.10	69.17	33.00	4.457		
S-24-10-4	58.72	66.49	32.58	4.546		
S-24-10-5	57.96	67.86	31.74	4.783		
S-24-25-1	70.32	69.66	46.72	4.431	43.96 (SD = 2.488)	4.278 (SD = 0.166)
S-24-25-2	66.71	65.03	42.05	4.473		
S-24-25-3	70.33	62.74	46.74	4.278		
S-24-25-4	68.09	64.45	43.81	4.192		
S-24-25-5	65.47	62.97	40.50	4.016		
S-24-50-1	82.37	69.76	64.10	4.737	59.19 (SD = 2.496)	4.367 (SD = 0.275)
S-24-50-2	78.23	48.79	57.82	4.633		
S-24-50-3	78.80	47.39	58.67	4.281		
S-24-50-4	77.85	48.32	57.26	4.162		
S-24-50-5	78.42	48.35	58.10	4.021		

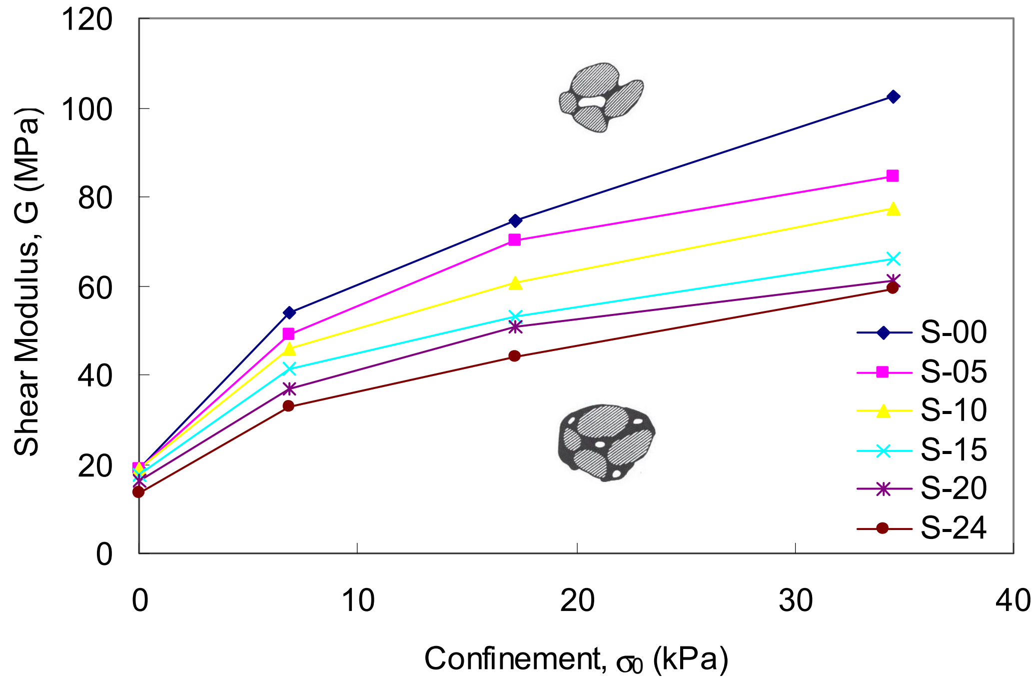

Figure 5.8 Variation of Average Shear Modulus with Confinement for Sand (RC)

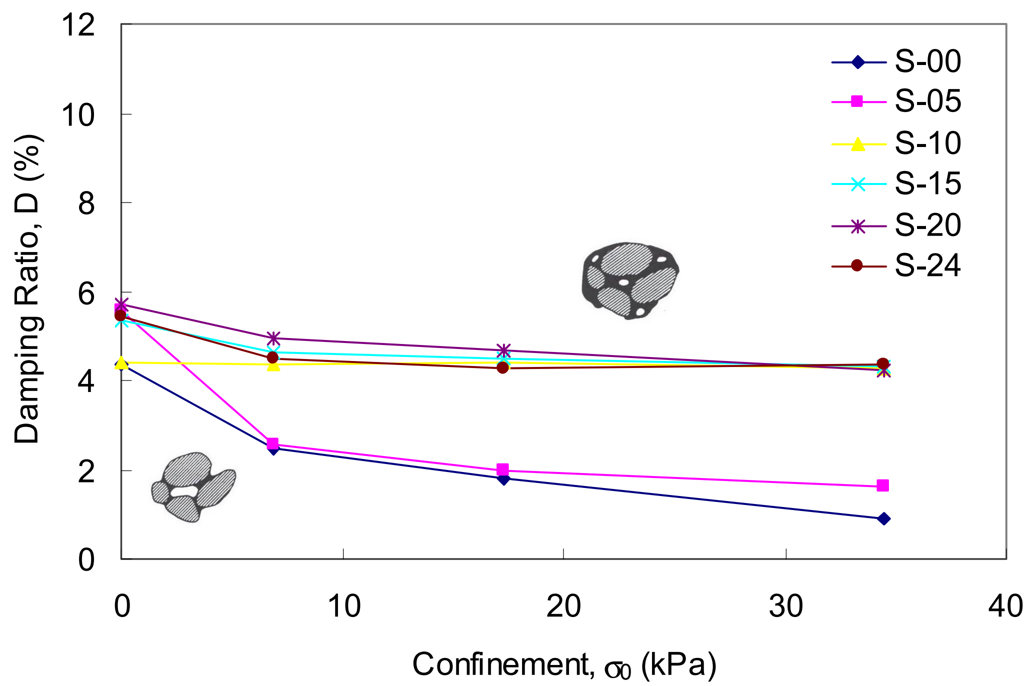

Figure 5.9 Variation of Average Damping Ratio with Confinement for Sand (RC)

5.5.3 Clay

A series of resonant column (RC) tests were conducted on several specimens of clay compacted at 90% dry, 95% dry, optimum, 95% wet, and 90% wet of $\gamma_{d\text{-}max}$ (13%, 17%, 20%, 23%, and 27% moisture contents, respectively) in order to determine relationships between small-strain shear modulus (G_{max}) and small-strain damping ratio (D_{min}) with isotropic confining pressure (σ_0).

Tables 5.9 through 5.13 present the results of small-strain shear modulus (G_{max}), small-strain damping ratio (D_{min}), and the average values of shear modulus and damping ratio of specimens under the same isotropic confining pressure (σ_0).

Figures 5.10 and 5.11 show the variation of small-strain shear modulus (G_{max}) and damping ratio (D_{min}) for clay at five moisture contents with confining pressure (σ_0). It can be seen that G_{max} increases and D_{min} decreases with confinement σ_0. This can be explained by the fact that the higher the confinement level, the more the specimen consolidates, and hence the stiffer it becomes.

It can be observed from these figures that the specimen prepared at 13% moisture content give the highest values of G_{max} as compared to any other specimen at any confinement. Moreover, it can be noted that the shear modulus (G_{max}) decreases with amount of moisture content.

Thus, knowing that the moisture content increases, the soil suction decreases, it can be stated that the shear modulus (G_{max}) increases and damping ratio (D_{min}) decreases with soil suction (ψ).

Table 5.9 RC Test Results of Clay at w = 13% (ψ = 2346 kPa)

Specimen	f_r (Hz)	V_{rms} (mV)	G_{max} (MPa)	D_{min} (%)	Avg G_{max} (MPa)	Avg D_{min} (%)
C-90D-00-1	107.02	42.63	103.11	6.867	102.66 (SD = 0.639)	6.650 (SD = 0.230)
C-90D-00-2	107.26	42.63	103.57	6.362		
C-90D-00-3	106.55	42.52	102.19	6.451		
C-90D-00-4	106.78	42.55	102.65	6.956		
C-90D-00-5	106.32	42.36	101.77	6.613		
C-90D-10-1	106.55	43.05	102.19	6.301	103.39 (SD = 0.851)	6.376 (SD = 0.288)
C-90D-10-2	106.78	43.03	102.65	6.546		
C-90D-10-3	107.50	42.85	104.03	6.846		
C-90D-10-4	107.73	44.08	104.49	6.124		
C-90D-10-5	107.26	43.54	103.57	6.065		
C-90D-25-1	114.63	43.99	118.29	5.889	116.57 (SD = 2.789)	5.793 (SD = 0.289)
C-90D-25-2	111.11	43.41	111.14	5.638		
C-90D-25-3	113.92	44.01	116.83	6.136		
C-90D-25-4	114.39	44.02	117.80	5.314		
C-90D-255	114.87	43.98	118.78	5.987		
C-90D-50-1	117.72	43.99	124.76	5.649	125.67 (SD = 0.671)	5.592 (SD = 0.212)
C-90D-50-2	118.20	43.91	125.77	5.558		
C-90D-50-3	118.67	44.03	126.78	5.895		
C-90D-50-4	117.96	43.93	125.26	5.623		
C-90D-50-5	118.20	43.85	125.77	5.236		

Table 5.10 RC Test Results of Clay at w = 17% (ψ = 1380 kPa)

Specimen	f_r (Hz)	V_{rms} (mV)	G_{max} (MPa)	D_{min} (%)	Avg G_{max} (MPa)	Avg D_{min} (%)
C-95D-00-1	76.58	41.25	55.41	6.364	63.48 (SD = 4.870)	6.265 (SD = 0.252)
C-95D-00-2	81.81	44.42	63.24	6.678		
C-95D-00-3	84.91	46.20	68.11	6.248		
C-95D-00-4	80.86	43.96	61.78	6.098		
C-95D-00-5	85.38	46.08	68.88	5.936		
C-95D-10-1	88.24	47.27	73.56	5.667	73.58 (SD = 0.599)	5.491 (SD = 0.196)
C-95D-10-2	88.47	47.44	73.95	5.376		
C-95D-10-3	88.00	47.45	73.16	5.438		
C-95D-10-4	87.76	47.13	72.77	5.756		
C-95D-10-5	88.79	48.32	74.48	5.219		
C-95D-25-1	91.56	48.15	79.21	5.624	80.37 (SD = 0.885)	5.363 (SD = 0.359)
C-95D-25-2	91.80	48.15	79.63	5.876		
C-95D-25-3	92.52	46.44	80.87	5.376		
C-95D-25-4	92.28	46.71	80.45	5.019		
C-95D-25-5	92.99	48.44	81.70	4.921		
C-95D-50-1	96.80	48.51	88.52	5.166	85.11 (SD = 4.237)	5.001 (SD = 0.308)
C-95D-50-2	94.66	47.81	84.65	4.805		
C-95D-50-3	96.56	47.91	88.09	4.987		
C-95D-50-4	96.08	48.19	87.22	4.573		
C-95D-50-5	90.32	49.64	77.08	5.476		

Table 5.11 RC Test Results of Clay at w = 20% (ψ = 953 kPa)

Specimen	f_r (Hz)	V_{rms} (mV)	G_{max} (MPa)	D_{min} (%)	Avg G_{max} (MPa)	Avg D_{min} (%)
C-OPT-00-1	64.22	46.25	38.96	5.532	42.06 (SD = 2.695)	5.339 (SD = 0.209)
C-OPT-00-2	65.88	47.53	41.01	5.378		
C-OPT-00-3	64.93	47.19	39.83	5.284		
C-OPT-00-4	68.97	50.37	44.95	4.967		
C-OPT-00-5	69.45	50.55	45.57	5.536		
C-OPT -0-1	71.35	51.49	48.10	4.984	47.27 (SD = 0.684)	4.927 (SD = 0.248)
C-OPT-10-2	71.11	51.19	47.78	4.875		
C-OPT-10-3	70.40	50.93	46.83	4.635		
C-OPT-10-4	70.88	51.47	47.46	4.773		
C-OPT-10-5	69.92	49.17	46.20	5.367		
C-OPT-25-1	75.63	53.59	54.05	5.008	54.46 (SD = 1.001)	4.870 (SD = 0.092)
C-OPT-25-2	75.16	53.75	53.37	4.937		
C-OPT-25-3	75.39	53.74	53.71	4.821		
C-OPT-25-4	76.35	52.07	55.07	4.837		
C-OPT-25-5	77.59	52.56	56.10	4.747		
C-OPT-50-1	77.30	53.99	56.45	5.151	58.93 (SD = 2.128)	4.881 (SD = 0.323)
C-OPT-50-2	81.34	55.14	62.51	4.432		
C-OPT-50-3	78.01	53.45	57.50	4.578		
C-OPT-50-4	78.49	53.52	58.20	5.261		
C-OPT-50-5	79.67	54.20	59.98	4.984		

Table 5.12 RC Test Results of Clay at w = 23% (ψ = 635 kPa)

Specimen	f_r (Hz)	V_{rms} (mV)	G_{max} (MPa)	D_{min} (%)	Avg G_{max} (MPa)	Avg D_{min} (%)
C-95W-00-1	48.76	36.79	22.46	8.408	22.55 (SD = 0.408)	7.442 (SD = 0.688)
C-95W-00-2	48.53	36.75	22.25	7.794		
C-95W-00-3	48.29	36.36	22.03	6.932		
C-95W-00-4	49.24	38.16	22.90	7.638		
C-95W-00-5	49.47	36.69	23.13	6.438		
C-95W-10-1	58.51	54.37	32.35	5.127	32.71 (SD = 0.270)	5.167 (SD = 0.280)
C-95W-10-2	58.75	52.14	32.61	5.675		
C-95W-10-3	58.99	52.31	32.87	4.836		
C-95W-10-4	58.75	52.83	32.61	5.013		
C-95W-10-5	59.22	52.85	33.14	5.183		
C-95W-25-1	65.17	59.92	40.13	4.757	40.13 (SD = 0.586)	4.740 (SD = 0.201)
C-95W-25-2	64.93	59.51	39.83	4.873		
C-95W-25-3	65.41	59.46	40.42	4.426		
C-95W-25-4	65.88	58.41	41.01	5.013		
C-95W-25-5	64.46	58.47	39.25	4.632		
C-95W-50-1	68.97	61.35	44.95	4.857	45.13 (SD = 0.422)	4.739 (SD = 0.288)
C-95W-50-2	69.21	61.09	45.26	4.362		
C-95W-50-3	68.97	61.14	44.95	5.071		
C-95W-50-4	69.69	60.35	45.88	4.974		
C-95W-50-5	68.74	60.98	44.64	4.432		

Table 5.13 RC Test Results of Clay at w = 27% (ψ = 235 kPa)

Specimen	f_r (Hz)	V_{rms} (mV)	G_{max} (MPa)	D_{min} (%)	Avg G_{max} (MPa)	Avg D_{min} (%)
C-90W-00-1	37.11	55.94	13.01	5.794	13.14 (SD = 0.126)	5.501 (SD = 0.207)
C-90W-00-2	37.35	56.46	13.18	5.433		
C-90W-00-3	37.58	56.17	13.35	5.218		
C-90W-00-4	37.11	57.02	13.01	5.673		
C-90W-00-5	37.35	56.96	13.18	5.385		
C-90W-10-1	38.15	58.24	13.75	4.194	13.97 (SD = 0.298)	4.870 (SD = 0.482)
C-90W-10-2	38.34	58.31	13.89	5.368		
C-90W-10-3	39.10	59.17	14.44	5.457		
C-90W-10-4	39.72	56.49	14.16	4.546		
C-90W-10-5	37.96	57.86	13.61	4.783		
C-90W-25-1	42.90	55.78	17.39	5.361	17.39 (SD = 0.308)	5.064 (SD = 0.317)
C-90W-25-2	42.71	55.03	17.24	4.473		
C-90W-25-3	42.33	52.74	16.93	5.278		
C-90W-25-4	43.09	54.45	17.55	5.192		
C-90W-25-5	43.47	52.97	17.86	5.016		
C-90W-50-1	48.04	48.58	21.80	3.737	22.01 (SD = 0.299)	3.967 (SD = 0.247)
C-90W-50-2	48.23	48.79	27.98	3.633		
C-90W-50-3	48.80	47.39	22.50	4.281		
C-90W-50-4	47.85	48.32	21.63	4.162		
C-90W-50-5	48.42	48.35	22.15	4.021		

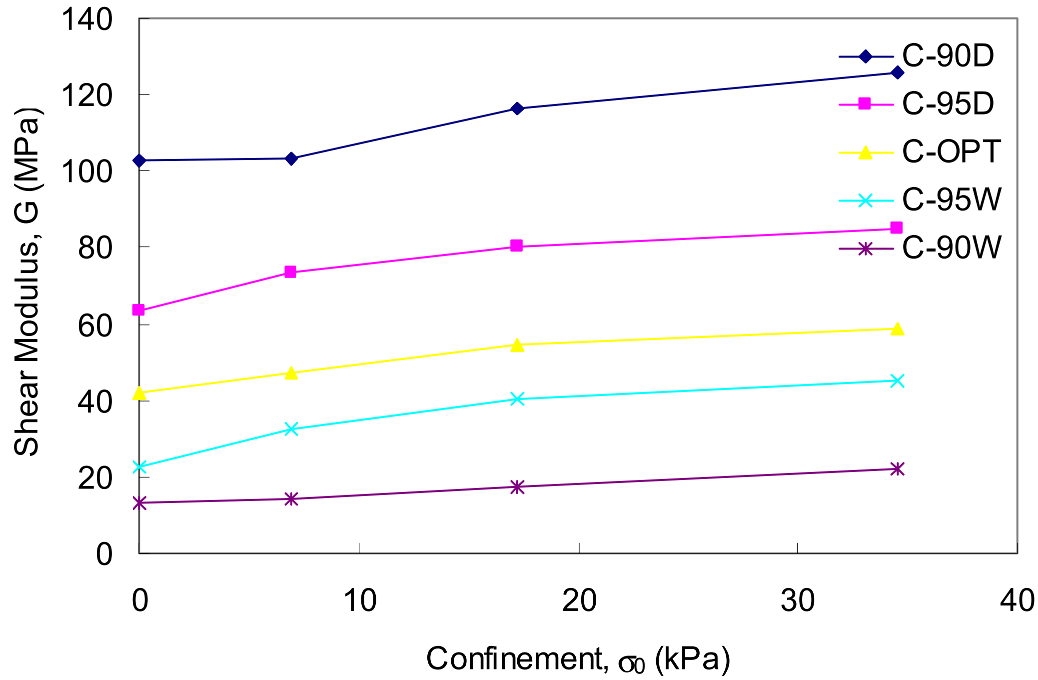

Figure 5.10 Variation of Average Shear Modulus with Confinement for Clay (RC)

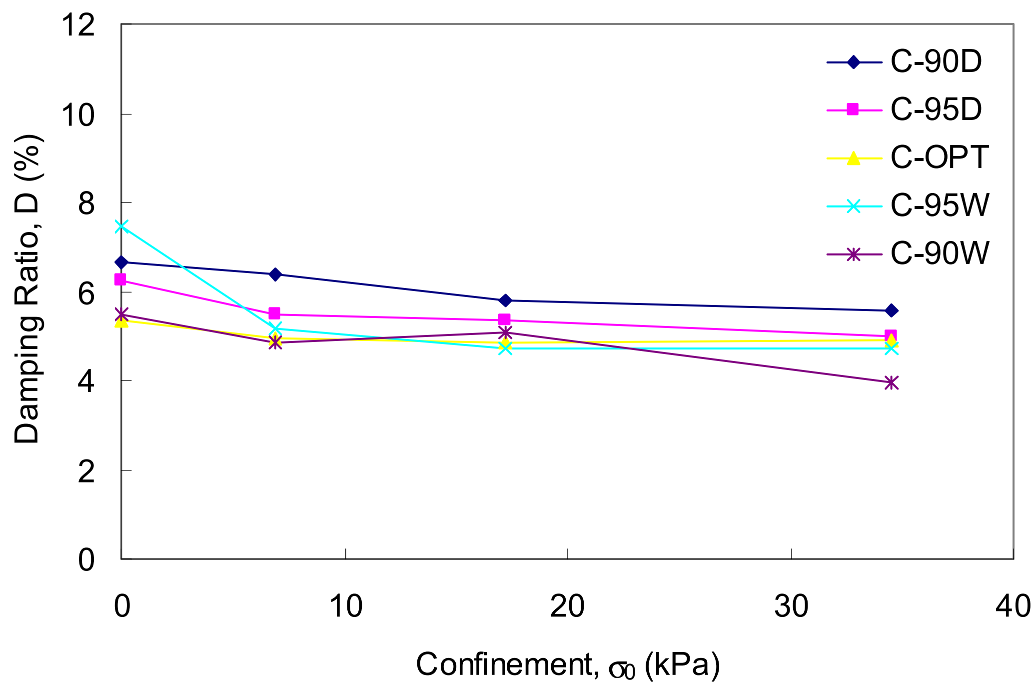

Figure 5.11 Variation of Average Damping Ratio with Confinement for Clay (RC)

5.6 BE Response

5.6.1 Typical BE Test Result

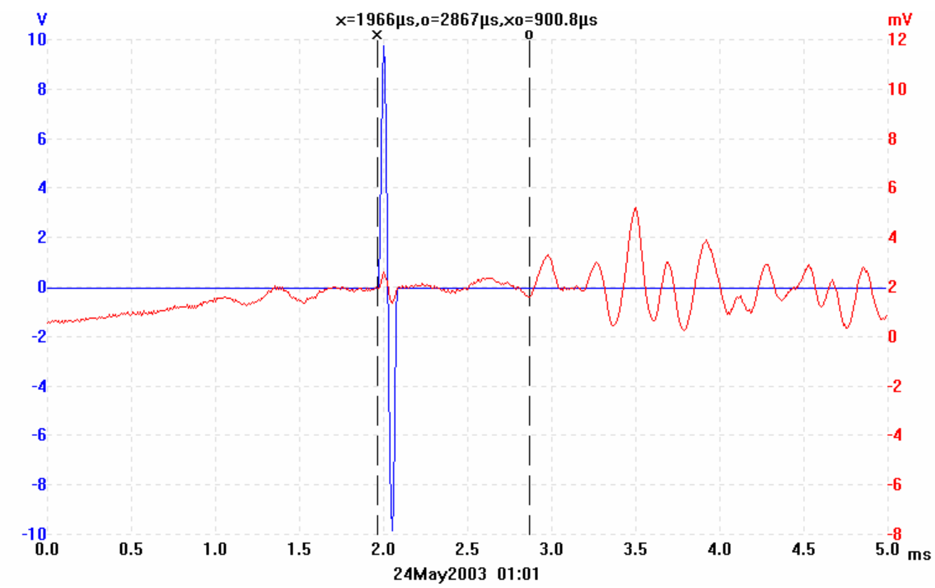

Figure 5.12 Typical BE Test Result for Shear Modulus Determination

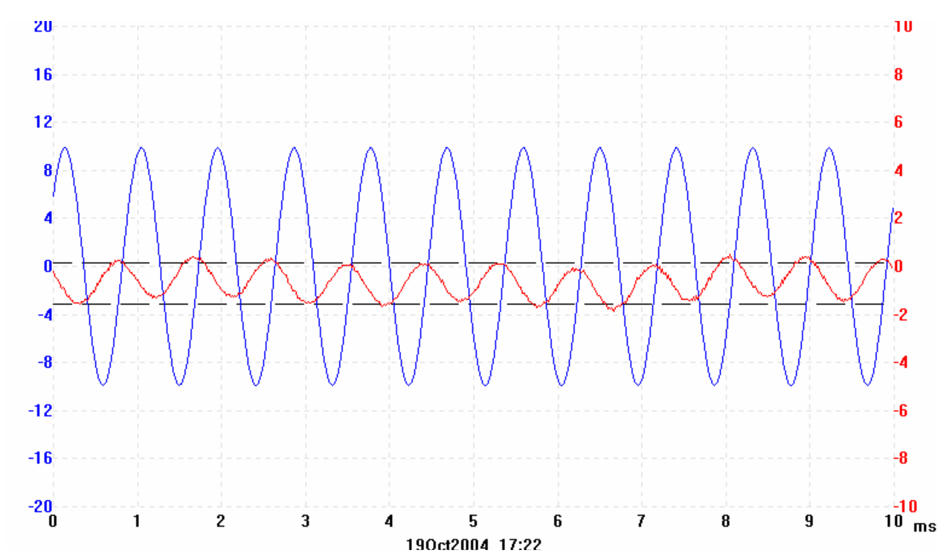

Figure 5.13 Typical BE Test Result for Damping Ratio Determination

Figures 5.12 and 5.13 show the typical response from BE test for specimen SA-10-00-5 under 0-psi isotropic confinement. Travel time of shear wave was measured from the result of figure 5.12 in order to determine the shear wave velocity (v_s) traveling through specimen and then calculate the shear modulus (G_{max}) as described in chapter 3. Also, the result from figure 5.13 was used to create a frequency and amplitude curve in order to determine the damping ratio (D_{min}) by using the half power points method as illustrated in chapter 3.

5.6.2 Isotropic Condition

5.6.2.1 Sand

A series of bender element (TX/BE) tests were conducted on several specimens of sand compacted at six moisture contents, 0%, 5%, 10%, 15%, 20%, and 24% in order to determine relationships between small-strain shear modulus (G_{max}) and small-strain damping ratio (D_{min}) with isotropic confining pressure (σ_0).

Tables 5.14 through 5.19 demonstrate the results of small-strain shear modulus (G_{max}) and damping ratio (D_{min}), and the average values of shear modulus and damping ratio of specimens under the same isotropic confining pressure (σ_0).

Figures 5.14 and 5.15 show the variation of small-strain shear modulus (G_{max}) and damping ratio (D_{min}) for sand at six moisture contents with confining pressure (σ_0). It can be seen that G_{max} increases and D_{min} decreases with confinement σ_0. This can be explained by the fact that the higher the confinement level, the more the specimen consolidates, and hence the stiffer it becomes.

It can be observed from these figures that the specimen prepared at 0% moisture content give the highest values of G_{max} and also give the lowest value of D_{min} as compared to any other specimen at any confinement. Moreover, it can be noted that the shear modulus (G_{max}) decreases and damping ratio (D_{min}) increases with the amount of moisture content. As a result, the shear modulus (G_{max}) increases and damping ratio (D_{min}) decreases with soil suction (ψ).

Table 5.14 BE Test Results of Sand at w = 0% ($\psi \rightarrow \infty$)

Specimen	Vs (m/s)	G_{max} (MPa)	D_{min} (%)	Avg G_{max} (MPa)	Avg D_{min} (%)
S-00-00-1	197.55	66.69	2.866	62.93 (SD = 2.710)	4.101 (SD = 0.804)
S-00-00-2	187.66	60.18	4.325		
S-00-00-3	186.95	59.73	4.654		
S-00-00-4	195.19	65.11	3.540		
S-00-00-5	191.92	62.95	5.120		
S-00-10-1	206.74	73.04	4.973	75.62 (SD = 1.704)	3.559 (SD = 0.987)
S-00-10-2	209.43	74.95	2.301		
S-00-10-3	211.22	76.24	4.245		
S-00-10-4	214.02	78.28	3.620		
S-00-10-5	210.32	75.59	2.654		
S-00-25-1	272.61	127.00	2.682	121.87 (SD = 7.745)	3.366 (SD = 0.856)
S-00-25-2	278.80	132.84	3.242		
S-00-25-3	259.54	115.12	4.554		
S-00-25-4	255.47	111.54	4.097		
S-00-25-5	268.12	122.86	2.254		
S-00-50-1	292.20	145.91	2.660	145.48 (SD = 8.193)	3.343 (SD = 0.810)
S-00-50-2	285.35	139.15	3.893		
S-00-50-3	303.06	156.96	2.325		
S-00-50-4	280.11	134.09	3.280		
S-00-50-5	297.53	151.29	4.556		

Table 5.15 BE Test Results of Sand at w = 5% (ψ = 111.99 kPa)

Specimen	Vs (m/s)	G_{max} (MPa)	D_{min} (%)	Avg G_{max} (MPa)	Avg D_{min} (%)
S-05-00-1	167.09	50.08	5.857	50.93 (SD = 3.219)	4.768 (SD = 0.851)
S-05-00-2	173.64	54.08	5.362		
S-05-00-3	162.11	47.13	3.451		
S-05-00-4	175.51	55.25	4.956		
S-05-00-5	163.74	48.09	4.213		
S-05-10-1	181.39	59.01	5.301	61.60 (SD = 2.149)	4.376 (SD = 1.383)
S-05-10-2	182.06	59.45	4.546		
S-05-10-3	185.52	61.73	3.846		
S-05-10-4	187.66	63.16	6.124		
S-05-10-5	189.87	64.66	2.065		
S-05-25-1	208.52	77.98	4.493	82.09 (SD = 3.172)	4.114 (SD = 0.785)
S-05-25-2	214.02	82.15	3.638		
S-05-25-3	216.87	84.35	4.136		
S-05-25-4	210.32	79.34	5.314		
S-05-25-5	219.79	86.64	2.987		
S-05-50-1	242.77	105.71	4.788	111.38 (SD = 5.728)	4.040 (SD = 1.082)
S-05-50-2	251.53	113.48	5.658		
S-05-50-3	254.12	115.82	3.895		
S-05-50-4	240.37	103.63	2.623		
S-05-50-5	256.80	118.28	3.236		

Table 5.16 BE Test Results of Sand at w = 10% (ψ = 68.72 kPa)

Specimen	Vs (m/s)	G_{max} (MPa)	D_{min} (%)	Avg G_{max} (MPa)	Avg D_{min} (%)
S-10-00-1	155.93	43.61	8.875	46.20 (SD = 1.722)	6.887 (SD = 1.147)
S-10-00-2	159.98	45.90	6.678		
S-10-00-3	163.18	47.76	7.248		
S-10-00-4	164.28	48.41	6.098		
S-10-00-5	159.00	45.34	5.536		
S-10-10-1	176.14	55.64	7.083	54.72 (SD = 1.115)	6.774 (SD = 0.909)
S-10-10-2	174.89	54.86	6.376		
S-10-10-3	171.82	52.95	5.438		
S-10-10-4	176.79	56.06	6.756		
S-10-10-5	173.64	54.08	8.219		
S-10-25-1	199.97	71.72	6.818	72.81 (SD = 1.284)	6.202 (SD = 0.586)
S-10-25-2	199.16	71.15	5.876		
S-10-25-3	202.45	73.51	5.376		
S-10-25-4	204.15	74.75	6.019		
S-10-25-5	201.63	72.92	6.921		
S-10-50-1	250.22	112.29	5.619	119.38 (SD = 7.600)	5.892 (SD = 0.659)
S-10-50-2	248.96	111.17	6.805		
S-10-50-3	256.80	118.28	4.987		
S-10-50-4	271.06	131.78	5.573		
S-10-50-5	262.29	123.39	6.476		

Table 5.17 BE Test Results of Sand at w = 15% (ψ = 42.50 kPa)

Specimen	Vs (m/s)	G_{max} (MPa)	D_{min} (%)	Avg G_{max} (MPa)	Avg D_{min} (%)
S-15-00-1	130.45	30.52	8.474	30.37 (SD = 1.770)	7.728 (SD = 0.834)
S-15-00-2	131.89	31.20	7.378		
S-15-00-3	128.13	29.44	6.284		
S-15-00-4	124.24	27.69	7.967		
S-15-00-5	135.63	33.00	8.536		
S-15-10-1	146.52	38.50	7.761	40.11 (SD = 1.442)	6.842 (SD = 0.728)
S-15-10-2	153.92	42.49	6.875		
S-15-10-3	148.75	36.69	5.635		
S-15-10-4	151.05	40.92	6.573		
S-15-10-5	147.41	38.97	7.367		
S-15-25-1	171.20	52.57	6.765	56.45 (SD = 3.465)	6.481 (SD = 0.654)
S-15-25-2	174.26	54.46	7.437		
S-15-25--3	175.51	55.25	6.521		
S-15-25-4	178.73	57.29	5.437		
S-15-25-5	186.95	62.68	6.247		
S-15-50-1	199.97	71.72	6.509	76.70 (SD = 4.026)	6.313 (SD = 0.604)
S-15-50-2	203.32	74.14	5.432		
S-15-50-3	204.15	74.75	6.378		
S-15-50-4	212.15	80.73	7.261		
S-15-50-5	214.02	82.15	5.984		

Table 5.18 BE Test Results of Sand at w = 20% (ψ = 7.04 kPa)

Specimen	Vs (m/s)	G_{max} (MPa)	D_{min} (%)	Avg G_{max} (MPa)	Avg D_{min} (%)
S-20-00-1	105.90	20.12	8.823	19.72 (SD = 0.557)	8.325 (SD = 0.970)
S-20-00-2	106.77	20.45	8.794		
S-20-00-3	105.21	19.85	7.932		
S-20-00-4	103.61	19.25	6.638		
S-20-00-5	102.72	18.92	9.438		
S-20-10-1	115.63	23.98	7.917	23.46 (SD = 0.437)	8.125 (SD = 0.792)
S-20-10-2	112.73	22.79	8.675		
S-20-10-3	115.08	23.75	6.836		
S-20-10-4	114.80	23.64	8.013		
S-20-10-5	113.53	23.12	9.183		
S-20-25-1	130.22	30.41	8.492	30.64 (SD = 1.397)	7.887 (SD = 0.876)
S-20-25-2	127.10	28.98	7.873		
S-20-25-3	135.63	32.99	6.426		
S-20-25-4	128.47	29.60	9.013		
S-20-25-5	131.89	31.20	7.632		
S-20-50-1	170.00	51.84	8.227	51.28 (SD = 1.177)	7.813 (SD = 0.891)
S-20-50-2	169.40	51.47	9.362		
S-20-50-3	171.82	52.95	7.071		
S-20-50-4	165.95	49.40	6.974		
S-20-50-5	168.25	50.77	7.432		

Table 5.19 BE Test Results of Sand at w = 24% (ψ = 0.64 kPa)

Specimen	Vs (m/s)	G_{max} (MPa)	D_{min} (%)	Avg G_{max} (MPa)	Avg D_{min} (%)
S-24-00-1	92.28	15.27	10.539	15.53 (SD = 0.531)	10.050 (SD = 1.009)
S-24-00-2	92.94	15.49	11.433		
S-24-00-3	95.48	16.35	10.218		
S-24-00-4	93.85	15.80	9.673		
S-24-00-5	90.71	14.76	8.385		
S-24-10-1	105.21	19.85	10.424	20.37 (SD = 0.680)	9.826 (SD = 0.964)
S-24-10-2	106.53	20.36	9.368		
S-24-10-3	108.96	21.29	8.457		
S-24-10-4	107.98	20.91	9.546		
S-24-10-5	104.06	19.42	11.283		
S-24-25-1	118.79	25.31	9.431	25.29 (SD = 0.579)	9.278 (SD = 1.446)
S-24-25-2	116.76	24.45	8.473		
S-24-25-3	117.92	24.94	10.278		
S-24-25-4	119.38	25.56	11.192		
S-24-25-5	120.79	26.17	7.016		
S-24-50-1	143.21	36.79	9.737	40.01 (SD = 1.809)	9.167 (SD = 0.796)
S-24-50-2	152.95	41.96	8.633		
S-24-50-3	149.67	40.18	10.281		
S-24-50-4	148.75	39.69	9.162		
S-24-50-5	152.00	41.44	8.021		

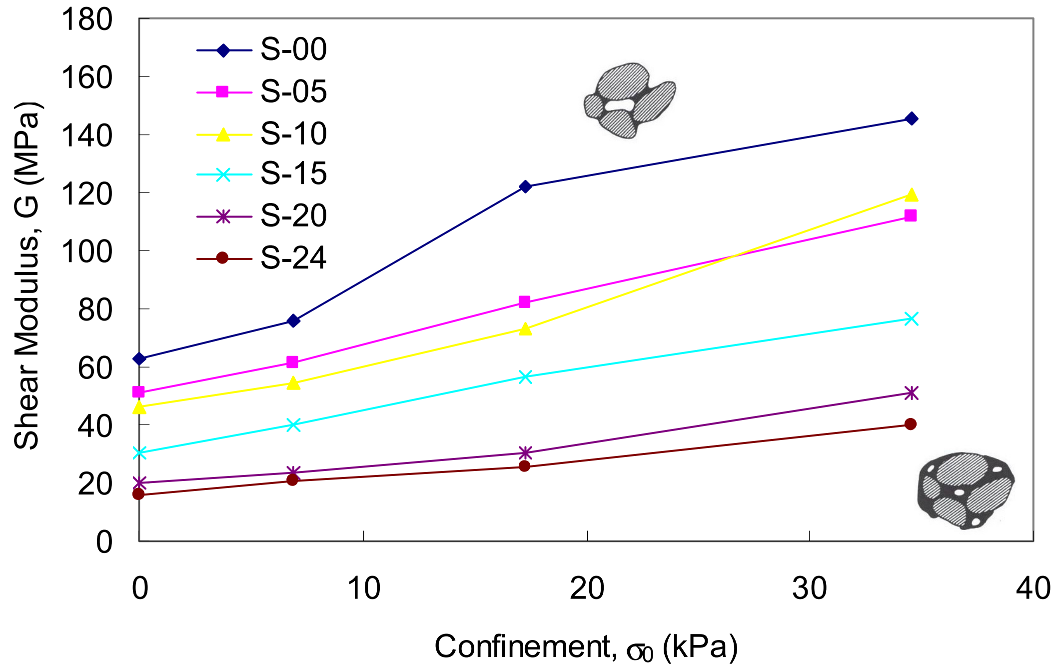

Figure 5.14 Variation of Average Shear Modulus with Confinement for Sand (TX/BE)

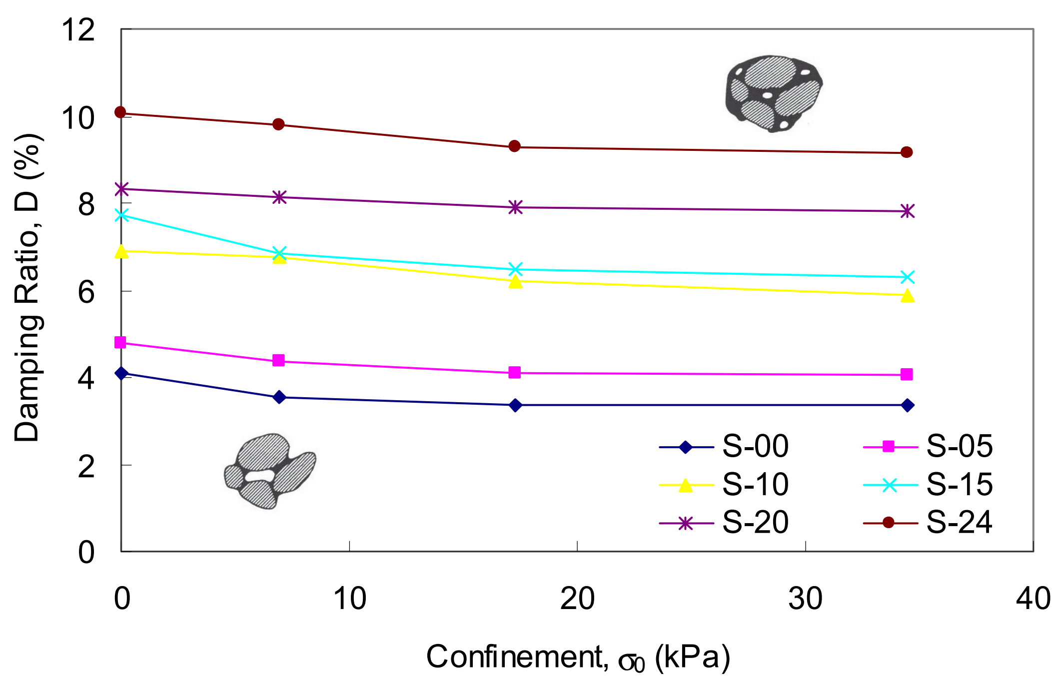

Figure 5.15 Variation of Average Damping Ratio with Confinement for Sand (TX/BE)

5.6.2.2 Clay

A series of bender element (TX/BE) tests were conducted on several specimens of clay compacted at 90% dry, 95% dry, optimum, 95% wet, and 90% wet of $\gamma_{d\text{-}max}$ (13%, 17%, 20%, 23%, and 27% moisture contents, respectively) in order to determine relationships between small-strain shear modulus (G_{max}) and small-strain damping ratio (D_{min}) with isotropic confining pressure (σ_0).

Tables 5.20 through 5.24 present the results of small-strain shear modulus (G_{max}), small-strain damping ratio (D_{min}), and the average values of small-strain shear modulus and damping ratio of specimens under the same isotropic confining pressure (σ_0).

Figures 5.16 and 5.17 show the variation of small-strain shear modulus (G_{max}) and damping ratio (D_{min}) for clay at five moisture contents with confining pressure (σ_0). It can be seen that G_{max} increases and D_{min} decreases with confinement σ_0. This can be explained by the fact that the higher the confinement level, the more the specimen consolidates, and hence the stiffer it becomes.

It can be observed from these figures that the specimen prepared at 13% moisture content give the highest values of G_{max} and also give the lowest value of D_{min} as compared to any other specimen at any confinement. Additionally, it can be noted that the shear modulus (G_{max}) decreases and damping ratio (D_{min}) increases with the amount of moisture content.

Therefore, knowing that the moisture content increases, the soil suction decreases, it can be stated that the shear modulus (G_{max}) increases and damping ratio (D_{min}) decreases with soil suction (ψ).

Table 5.20 BE Test Results of Clay at w = 13% (ψ = 2346 kPa)

Specimen	Vs (m/s)	G_{max} (MPa)	D_{min} (%)	Avg G_{max} (MPa)	Avg D_{min} (%)
C-90D-00-1	282.04	135.94	9.861	142.21 (SD = 4.292)	10.569 (SD = 1.008)
C-90D-00-2	285.34	139.15	10.362		
C-90D-00-3	292.20	145.91	11.451		
C-90D-00-4	293.94	147.65	11.956		
C-90D-00-5	288.67	142.41	9.213		
C-90D-10-1	293.94	147.65	10.301	147.70 (SD = 2.524)	10.016 (SD = 0.768)
C-90D-10-2	290.43	144.15	9.546		
C-90D-10-3	295.75	149.48	9.846		
C-90D-10-4	297.53	151.29	11.324		
C-90D-10-5	292.20	145.91	9.065		
C-90D-25-1	301.22	155.06	10.893	154.05 (SD = 1.900)	10.034 (SD = 0.990)
C-90D-25-2	299.33	153.12	8.638		
C-90D-25-3	297.53	151.29	9.136		
C-90D-25-4	300.02	153.83	10.314		
C-90D-25-5	303.06	156.96	11.187		
C-90D-50-1	303.06	156.96	8.788	157.00 (SD = 2.747)	9.240 (SD = 0.906)
C-90D-50-2	304.99	158.97	9.658		
C-90D-50-3	301.22	155.06	7.895		
C-90D-50-4	306.82	160.88	10.623		
C-90D-50-5	299.33	153.12	9.236		

Table 5.21 BE Test Results of Clay at w = 17% (ψ = 1380 kPa)

Specimen	Vs (m/s)	G_{max} (MPa)	D_{min} (%)	Avg G_{max} (MPa)	Avg D_{min} (%)
C-95D-00-1	176.14	55.64	13.218	57.32 (SD = 1.338)	12.356 (SD = 1.486)
C-95D-00-2	177.42	56.46	14.678		
C-95D-00-3	178.08	56.88	12.248		
C-95D-00-4	180.05	58.14	11.098		
C-95D-00-5	182.06	59.45	10.536		
C-95D-10-1	182.06	59.45	11.944	59.10 (SD = 0.753)	12.147 (SD = 0.808)
C-95D-10-2	180.03	58.13	12.376		
C-95D-10-3	180.71	58.57	12.438		
C-95D-10-4	181.39	59.01	10.756		
C-95D-10-5	183.39	60.32	13.219		
C-95D-25-1	186.95	62.68	11.933	62.90 (SD = 1.169)	11.225 (SD = 0.836)
C-95D-25-2	186.24	62.21	10.876		
C-95D-25-3	188.39	63.66	12.376		
C-95D-25-4	189.87	64.66	10.019		
C-95D-25-5	184.83	61.27	10.921		
C-95D-50-1	208.52	77.98	9.619	77.24 (SD = 2.430)	11.192 (SD = 0.965)
C-95D-50-2	213.07	81.42	10.805		
C-95D-50-3	206.74	76.66	11.987		
C-95D-50-4	205.85	76.00	12.373		
C-95D-50-5	203.32	74.14	11.176		

Table 5.22 BE Test Results of Clay at w = 20% (ψ = 953 kPa)

Specimen	Vs (m/s)	G_{max} (MPa)	D_{min} (%)	Avg G_{max} (MPa)	Avg D_{min} (%)
C-OPT-00-1	162.11	47.13	14.375	50.35 (SD = 2.074)	13.708 (SD = 0.859)
C-OPT-00-2	167.09	50.08	13.378		
C-OPT-00-3	170.61	52.21	13.284		
C-OPT-00-4	165.95	49.40	14.967		
C-OPT-00-5	171.82	52.95	12.536		
C-OPT-10-1	174.00	54.30	13.761	54.74 (SD = 1.322)	13.042 (SD = 0.949)
C-OPT-10-2	173.41	53.94	12.875		
C-OPT-10-3	171.82	52.95	11.635		
C-OPT-10-4	176.79	56.06	12.573		
C-OPT-10-5	177.42	56.46	14.367		
C-OPT-25-1	188.39	63.66	13.765	63.67 (SD = 1.196)	12.881 (SD = 1.079)
C-OPT-25-2	189.11	64.15	14.437		
C-OPT-25-3	191.31	65.64	12.521		
C-OPT-25-4	187.00	62.72	11.437		
C-OPT-25-5	186.24	62.21	12.247		
C-OPT-50-1	195.96	68.87	11.509	70.69 (SD = 1.327)	12.813 (SD = 0.960)
C-OPT-50-2	200.78	72.31	12.432		
C-OPT-50-3	199.17	71.15	14.378		
C-OPT-50-4	196.74	69.42	13.261		
C-OPT-50-5	199.97	71.72	12.484		

Table 5.23 BE Test Results of Clay at w = 23% (ψ = 635 kPa)

Specimen	Vs (m/s)	G_{max} (MPa)	D_{min} (%)	Avg G_{max} (MPa)	Avg D_{min} (%)
C-95W-00-1	145.21	37.82	13.823	35.46 (SD = 2.991)	13.925 (SD = 0.733)
C-95W-00-2	132.62	31.55	14.794		
C-95W-00-3	133.73	32.08	13.932		
C-95W-00-4	144.79	37.60	12.638		
C-95W-00-5	146.06	38.26	14.438		
C-95W-10-1	154.40	42.76	13.917	41.42 (SD = 3.479)	13.325 (SD = 0.706)
C-95W-10-2	156.88	44.14	13.675		
C-95W-10-3	141.52	35.92	12.836		
C-95W-10-4	158.93	45.30	14.013		
C-95W-10-5	147.41	38.97	12.183		
C-95W-25-1	159.44	45.60	14.492	45.11 (SD = 1.316)	13.687 (SD = 0.690)
C-95W-25-2	158.93	45.30	13.873		
C-95W-25-3	159.98	45.90	12.426		
C-95W-25-4	160.50	46.20	14.013		
C-95W-25-5	154.02	42.55	13.632		
C-95W-50-1	167.80	50.50	11.227	48.12 (SD = 1.406)	12.813 (SD = 1.077)
C-95W-50-2	160.50	46.20	12.362		
C-95W-50-3	163.74	48.09	14.071		
C-95W-50-4	162.64	47.44	13.974		
C-95W-50-5	164.26	48.39	12.432		

Table 5.24 BE Test Results of Clay at w = 27% (ψ = 235 kPa)

Specimen	Vs (m/s)	G_{max} (MPa)	D_{min} (%)	Avg G_{max} (MPa)	Avg D_{min} (%)
C-90W-00-1	108.47	21.10	13.539	22.27 (SD = 0.680)	13.970 (SD = 0.332)
C-90W-00-2	112.46	22.68	14.433		
C-90W-00-3	113.53	23.12	14.218		
C-90W-00-4	111.67	22.37	13.673		
C-90W-00-5	110.90	22.06	13.985		
C-90W-10-1	119.58	25.65	13.824	26.18 (SD = 1.071)	13.856 (SD = 0.337)
C-90W-10-2	122.34	26.84	14.368		
C-90W-10-3	123.28	27.26	13.457		
C-90W-10-4	122.34	26.84	13.546		
C-90W-10-5	116.48	24.33	14.083		
C-90W-25-1	122.65	26.98	13.431	27.54 (SD = 0.419)	13.818 (SD = 0.265)
C-90W-25-2	124.24	27.69	13.773		
C-90W-25-3	123.28	27.26	13.678		
C-90W-25-4	123.92	27.54	14.192		
C-90W-25-5	125.44	28.22	14.016		
C-90W-50-1	132.26	31.37	13.737	31.82 (SD = 0.850)	12.967 (SD = 0.539)
C-90W-50-2	134.49	32.44	12.633		
C-90W-50-3	133.74	32.08	13.281		
C-90W-50-4	130.22	30.41	13.162		
C-90W-50-5	135.25	32.81	13.021		

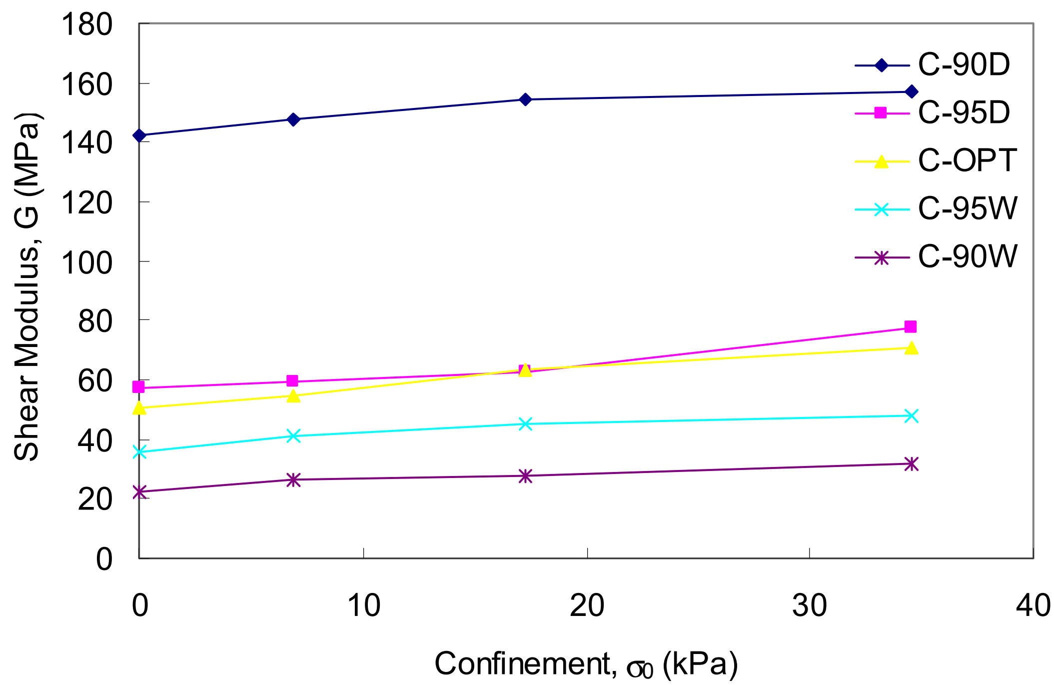

Figure 5.16 Variation of Average Shear Modulus with Confinement for Clay (TX/BE)

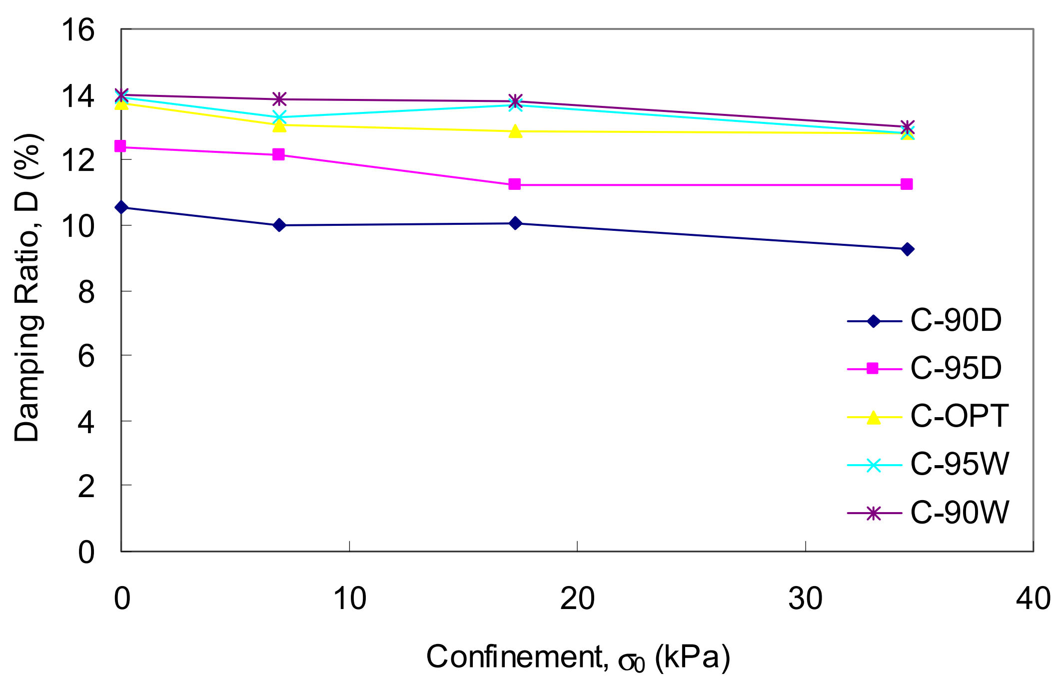

Figure 5.17 Variation of Average Damping Ratio with Confinement for Clay (TX/BE)

5.6.3 K_0 Stress State Condition

5.6.3.1 Sand

A series of bender element (TX/BE) tests were conducted on several specimens of sand compacted at six moisture contents, 0%, 5%, 10%, 15%, 20%, and 24% in order to determine relationships between small-strain shear modulus (G_{max}) and small-strain damping ratio (D_{min}) with K_0 stress state

Tables 5.25 through 5.30 demonstrate the results of small-strain shear modulus (G_{max}), small-strain damping ratio (D_{min}), and the average values of small-strain shear modulus and damping ratio of specimens under the same K_0 stress state condition.

Figures 5.18 and 5.19 show the variation of small-strain shear modulus (G_{max}) and damping ratio (D_{min}) for sand at six moisture contents with K_0 stress state. It can be seen that G_{max} increases and D_{min} decreases with K_0 stress state. This can be explained by the fact that the higher the K_0 stress value, the more the specimen consolidates, and hence the stiffer it becomes.

It can be observed from these figures that the specimen prepared at 0% moisture content give the highest values of G_{max} and also give the lowest value of D_{min} as compared to any other specimen at any confinement. Furthermore, it can be noted that the shear modulus (G_{max}) decreases and damping ratio (D_{min}) increases with amount of moisture content.

Subsequently, knowing that the moisture content increases, the soil suction decreases, it can be stated that the shear modulus (G_{max}) increases and damping ratio (D_{min}) decreases with soil suction (ψ).

Table 5.25 BE Test Results of Sand under K_0 Stress State at w = 0% ($\psi \rightarrow \infty$)

Specimen	K_0	Vs (m/s)	G_{max} (MPa)	D_{min} (%)	Avg G_{max} (MPa)	Avg D_{min} (%)
S-00-00-1	0.0	177.42	53.80	3.866	55.91 (SD = 1.258)	3.701 (SD = 0.273)
S-00-00-2		183.43	57.50	3.325		
S-00-00-3		181.39	56.23	3.654		
S-00-00-4		182.06	56.65	3.540		
S-00-00-5		180.05	55.40	4.120		
S-00-10-1	0.25	234.59	94.05	3.973	90.24 (SD = 2.556)	3.801 (SD = 0.322)
S-00-10-2		231.27	91.40	4.301		
S-00-10-3		224.85	86.40	3.345		
S-00-10-4		230.15	90.52	3.630		
S-00-10-5		227.99	88.83	3.754		
S-00-25-1	0.625	248.96	105.92	4.882	105.14 (SD = 3.537)	3.646 (SD = 0.635)
S-00-25-2		243.96	101.71	3.342		
S-00-25-3		242.77	100.72	3.554		
S-00-25-4		250.22	107.00	3.097		
S-00-25-5		254.12	110.36	3.354		
S-00-50-1	1.25	271.83	126.28	3.560	123.00 (SD = 2.115)	3.703 (SD = 0.411)
S-00-50-2		269.58	124.20	3.793		
S-00-50-3		266.63	121.49	4.425		
S-00-50-4		265.20	120.19	3.180		
S-00-50-5		268.12	122.86	3.556		

$K_0 = (\sigma_h - u_a)/(\sigma_v - u_a)$; σ_v = constant = 4 psi

Table 5.26 BE Test Results of Sand under K_0 Stress State at w = 5% (ψ = 112 kPa)

Specimen	K_0	Vs (m/s)	G_{max} (MPa)	D_{min} (%)	Avg G_{max} (MPa)	Avg D_{min} (%)
S-05-00-1	0.0	146.97	38.74	4.827	37.80 (SD = 0.635)	4.518 (SD = 0.252)
S-05-00-2		144.79	37.60	4.342		
S-05-00-3		143.21	36.79	4.151		
S-05-00-4		145.66	38.05	4.756		
S-05-00-5		145.21	37.82	4.513		
S-05-10-1	0.25	154.90	43.04	4.311	41.76 (SD = 0.820)	4.332 (SD = 0.254)
S-05-10-2		153.44	42.23	4.646		
S-05-10-3		152.48	41.70	3.946		
S-05-10-4		150.59	40.67	4.194		
S-05-10-5		151.53	41.18	4.565		
S-05-25-1	0.625	181.39	59.01	4.393	58.00 (SD = 1.219)	4.352 (SD = 0.397)
S-05-25-2		180.05	58.14	3.738		
S-05-25-3		178.73	57.29	4.236		
S-05-25-4		176.79	56.06	4.414		
S-05-25-5		182.06	59.45	4.977		
S-05-50-1	1.25	211.28	80.06	4.488	76.98 (SD = 2.148)	4.278 (SD = 0.532)
S-05-50-2		206.74	76.66	4.648		
S-05-50-3		205.00	75.37	3.795		
S-05-50-4		203.32	74.14	3.523		
S-05-50-5		209.43	78.67	4.936		

$K_0 = (\sigma_h - u_a)/(\sigma_v - u_a)$; σ_v = constant = 4 psi

Table 5.27 BE Test Results of Sand under K_0 Stress State at w = 10%
(ψ = 68.7 kPa)

Specimen	K_0	Vs (m/s)	G_{max} (MPa)	D_{min} (%)	Avg G_{max} (MPa)	Avg D_{min} (%)
S-10-00-1	0.0	141.10	35.71	6.875	34.69 (SD = 0.744)	6.917 (SD = 0.362)
S-10-00-2		140.27	35.29	6.978		
S-10-00-3		139.05	34.68	7.548		
S-10-00-4		137.85	34.08	6.448		
S-10-00-5		137.06	33.69	6.736		
S-10-10-1	0.25	151.53	41.18	7.183	40.14 (SD = 0.768)	6.694 (SD = 0.336)
S-10-10-2		150.59	40.67	6.776		
S-10-10-3		149.67	40.18	6.438		
S-10-10-4		148.75	39.69	6.856		
S-10-10-5		147.41	38.97	6.219		
S-10-25-1	0.625	171.82	52.95	6.518	51.07 (SD = 1.257)	6.340 (SD = 0.347)
S-10-25-2		170.00	51.84	5.766		
S-10-25-3		168.82	51.12	6.676		
S-10-25-4		167.09	50.08	6.119		
S-10-25-5		165.95	49.40	6.621		
S-10-50-1	1.25	199.97	71.72	5.419	69.34 (SD = 1.742)	5.872 (SD = 0.255)
S-10-50-2		198.34	70.56	5.805		
S-10-50-3		195.16	68.31	5.987		
S-10-50-4		192.85	66.70	5.973		
S-10-50-5		196.74	69.42	6.176		

$K_0 = (\sigma_h - u_a)/(\sigma_v - u_a)$; σ_v = constant = 4 psi

Table 5.28 BE Test Results of Sand under K_0 Stress State at w = 15%
(ψ = 42.5 kPa)

Specimen	K_0	Vs (m/s)	G_{max} (MPa)	D_{min} (%)	Avg G_{max} (MPa)	Avg D_{min} (%)
S-15-00-1	0.0	139.46	34.88	7.474	33.95 (SD = 0.673)	7.408 (SD = 0.496)
S-15-00-2		138.65	34.48	7.778		
S-15-00-3		137.45	33.89	7.284		
S-15-00-4		136.67	33.50	7.967		
S-15-00-5		135.63	33.00	6.536		
S-15-10-1	0.25	147.41	38.97	7.761	37.76 (SD = 0.839)	7.642 (SD = 0.744)
S-15-10-2		146.07	38.27	6.675		
S-15-10-3		145.21	37.82	8.935		
S-15-10-4		143.93	37.16	7.573		
S-15-10-5		142.79	36.57	7.267		
S-15-25-1	0.625	167.68	50.43	6.665	48.69 (SD = 1.216)	6.620 (SD = 0.393)
S-15-25-2		165.95	49.40	7.327		
S-15-25-3		161.56	46.82	6.423		
S-15-25-4		164.85	48.74	6.537		
S-15-25-5		163.74	48.09	6.147		
S-15-50-1	1.25	193.63	67.25	6.409	64.60 (SD = 1.992)	6.259 (SD = 0.299)
S-15-50-2		192.10	66.19	5.922		
S-15-50-3		189.87	64.66	6.738		
S-15-50-4		187.66	63.16	6.251		
S-15-50-5		185.52	61.73	5.974		

$K_0 = (\sigma_h - u_a)/(\sigma_v - u_a)$; σ_v = constant = 4 psi

Table 5.29 BE Test Results of Sand under K_0 Stress State at w = 20%
(ψ = 7.04 kPa)

Specimen	K_0	Vs (m/s)	G_{max} (MPa)	D_{min} (%)	Avg G_{max} (MPa)	Avg D_{min} (%)
S-20-00-1	0.0	126.10	28.52	8.623	27.82 (SD = 0.513)	8.123 (SD = 1.030)
S-20-00-2		125.44	28.22	8.974		
S-20-00-3		124.57	27.83	7.292		
S-20-00-4		123.60	27.40	6.538		
S-20-00-5		122.96	27.12	9.186		
S-20-10-1	0.25	142.79	36.57	7.817	35.55 (SD = 0.741)	8.027 (SD = 0.924)
S-20-10-2		141.94	36.13	8.765		
S-20-10-3		140.69	35.50	6.386		
S-20-10-4		139.86	35.09	9.013		
S-20-10-5		138.65	34.48	8.154		
S-20-25-1	0.625	163.18	47.76	8.292	46.40 (SD = 1.046)	7.643 (SD = 0.661)
S-20-25-2		162.11	47.13	7.683		
S-20-25-3		161.04	46.51	6.386		
S-20-25-4		159.98	45.90	8.023		
S-20-25-5		157.90	44.72	7.832		
S-20-50-1	1.25	184.12	60.80	8.333	58.60 (SD = 1.600)	7.569 (SD = 0.667)
S-20-50-2		182.73	59.89	8.062		
S-20-50-3		180.71	58.57	7.771		
S-20-50-4		178.73	57.29	6.457		
S-20-50-5		177.42	56.46	7.223		

$K_0 = (\sigma_h - u_a)/(\sigma_v - u_a)$; σ_v = constant = 4 psi

Table 5.30 BE Test Results of Sand under K_0 Stress State at w = 24%
(ψ = 0.64 kPa)

Specimen	K_0	Vs (m/s)	G_{max} (MPa)	D_{min} (%)	Avg G_{max} (MPa)	Avg D_{min} (%)
S-24-00-1	0.0	105.90	20.12	10.339	20.51 (SD = 0.805)	9.910 (SD = 0.834)
S-24-00-2		106.77	20.45	11.123		
S-24-00-3		110.13	21.75	10.032		
S-24-00-4		107.98	20.91	8.673		
S-24-00-5		103.84	19.34	9.385		
S-24-10-1	0.25	123.28	27.26	10.172	28.10 (SD = 1.102)	9.687 (SD = 0.876)
S-24-10-2		125.11	28.07	9.457		
S-24-10-3		128.47	29.60	8.336		
S-24-10-4		127.10	28.98	9.485		
S-24-10-5		121.71	26.57	10.983		
S-24-25-1	0.625	143.93	37.16	9.413	37.19 (SD = 0.947)	9.426 (SD = 1.013)
S-24-25-2		146.52	38.50	8.673		
S-24-25-3		141.10	35.71	10.078		
S-24-25-4		143.21	36.79	10.920		
S-24-25-5		145.21	37.82	8.046		
S-24-50-1	1.25	157.40	44.43	9.377	42.06 (SD = 1.388)	9.374 (SD = 0.838)
S-24-50-2		152.95	41.96	8.743		
S-24-50-3		149.67	40.18	10.668		
S-24-50-4		153.53	42.27	8.262		
S-24-50-5		152.00	41.44	9.821		

$K_0 = (\sigma_h - u_a)/(\sigma_v - u_a)$; σ_v = constant = 4 psi

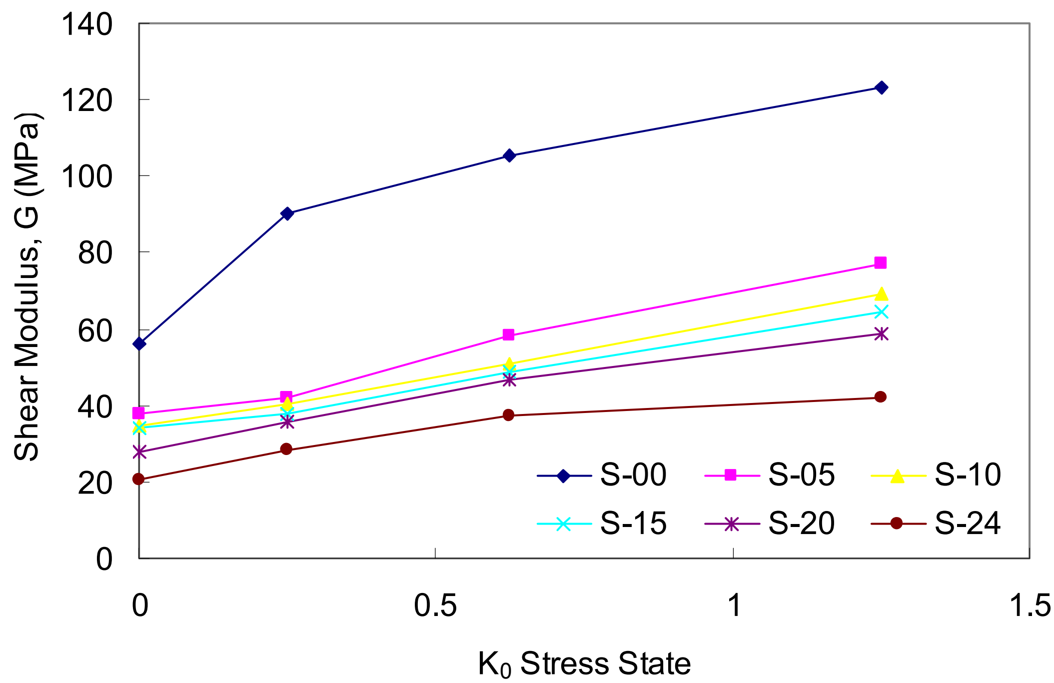

Figure 5.18 Variation of Average G with K_0 Stress State for Sand (TX/BE)

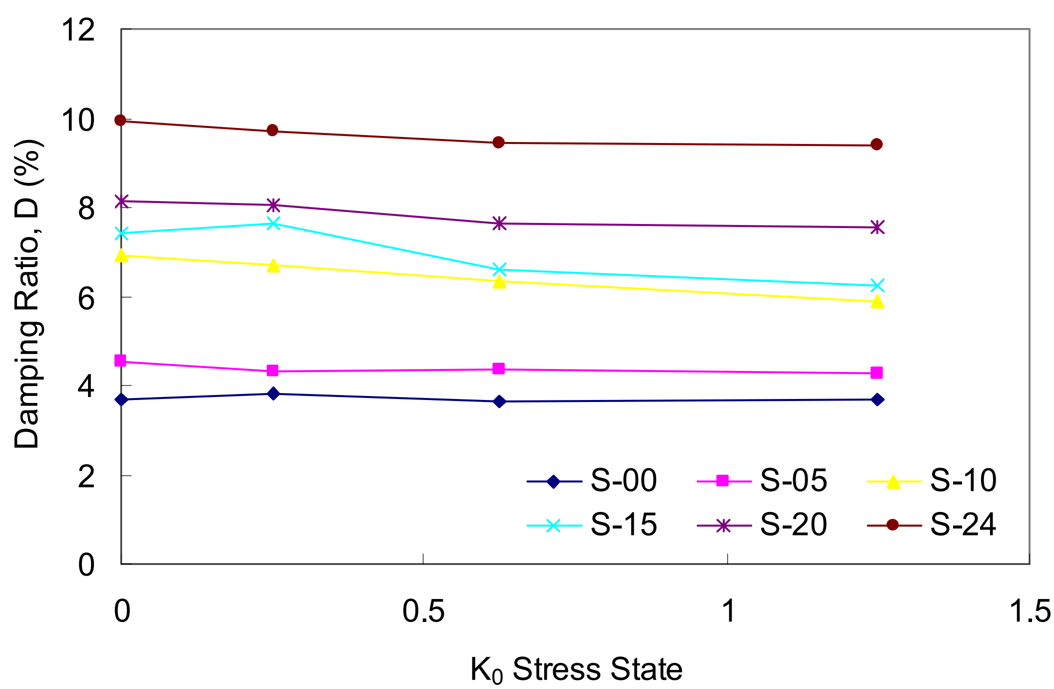

Figure 5.19 Variation of Average D with K_0 Stress State for Sand (TX/BE)

5.6.3.2 Clay

A series of bender element (TX/BE) tests were conducted on several specimens of clay compacted at 90% dry, 95% dry, optimum, 95% wet, and 90% wet of $\gamma_{d\text{-}max}$ (13%, 17%, 20%, 23%, and 27% moisture contents, respectively) in order to determine relationships between small-strain shear modulus (G_{max}) and small-strain damping ratio (D_{min}) with K_0 stress state.

Tables 5.31 through 5.35 present the results of small-strain shear modulus (G_{max}), small-strain damping ratio (D_{min}), and the average values of small-strain shear modulus and damping ratio of specimens under the same K_0 stress state.

Figures 5.20 and 5.21 show the variation of small-strain shear modulus (G_{max}) and damping ratio (D_{min}) for clay at five moisture contents with K_0 stress state. It can be seen that G_{max} increases and D_{min} decreases with K_0 stress state. This can be explained by the fact that the higher the K_0 stress value, the more the specimen consolidates, and hence the stiffer it becomes.

It can be observed from these figures that the specimen prepared at 13% moisture content give the highest values of G_{max} and also give the lowest value of D_{min} as compared to any other specimen at any confinement. Moreover, it can be noted that the shear modulus (G_{max}) decreases and damping ratio (D_{min}) increases with the amount of moisture content.

When moisture content decreases, soil suction increases. Then, it can be stated that the shear modulus (G_{max}) increases and damping ratio (D_{min}) decreases with soil suction (ψ).

Table 5.31 BE Test Results of Clay under K_0 Stress State at w = 13%
(ψ = 2346 kPa)

Specimen	K_0	Vs (m/s)	G_{max} (MPa)	D_{min} (%)	Avg G_{max} (MPa)	Avg D_{min} (%)
C-90D-00-1	0.0	256.80	112.70	10.761	115.03 (SD = 4.904)	10.938 (SD = 0.409)
C-90D-00-2		250.22	106.99	10.362		
C-90D-00-3		262.34	117.61	11.431		
C-90D-00-4		266.63	121.49	10.756		
C-90D-00-5		260.96	116.38	11.381		
C-90D-10-1	0.25	282.04	135.94	10.101	132.96 (SD = 4.291)	9.888 (SD = 0.281)
C-90D-10-2		278.80	132.84	9.635		
C-90D-10-3		275.70	129.89	9.786		
C-90D-10-4		272.61	127.00	10.324		
C-90D-10-5		285.35	139.15	9.567		
C-90D-25-1	0.625	295.75	149.48	10.593	150.29 (SD = 4.433)	9.869 (SD = 0.591)
C-90D-25-2		293.94	147.65	8.904		
C-90D-25-3		290.43	144.15	9.536		
C-90D-25-4		299.40	153.19	10.071		
C-90D-25-5		303.06	156.96	10.239		
C-90D-50-1	1.25	341.26	199.02	8.989	196.96 (SD = 6.671)	9.487 (SD = 0.577)
C-90D-50-2		336.54	193.55	9.754		
C-90D-50-3		343.63	201.80	8.895		
C-90D-50-4		329.73	185.80	10.472		
C-90D-50-5		346.03	204.63	9.326		

$K_0 = (\sigma_h - u_a)/(\sigma_v - u_a)$; σ_v = constant = 4 psi

Table 5.32 BE Test Results of Clay under K_0 Stress State at w = 17%
(ψ = 1380 kPa)

Specimen	K_0	Vs (m/s)	G_{max} (MPa)	D_{min} (%)	Avg G_{max} (MPa)	Avg D_{min} (%)
C-95D-00-1	0.0	233.45	97.74	13.128	101.68 (SD = 3.169)	12.103 (SD = 0.798)
C-95D-00-2		235.71	99.65	12.578		
C-95D-00-3		236.88	100.64	12.248		
C-95D-00-4		240.37	103.63	11.798		
C-95D-00-5		243.95	106.75	10.764		
C-95D-10-1	0.25	243.96	106.75	11.644	105.91 (SD = 1.810)	11.801 (SD = 0.659)
C-95D-10-2		240.33	103.59	12.216		
C-95D-10-3		241.54	104.64	12.348		
C-95D-10-4		242.77	105.71	10.576		
C-95D-10-5		246.35	108.85	12.219		
C-95D-25-1	0.625	252.82	114.64	11.493	115.18 (SD = 2.899)	11.069 (SD = 0.388)
C-95D-25-2		251.53	113.48	10.546		
C-95D-25-3		255.47	117.06	11.356		
C-95D-25-4		258.19	119.56	10.659		
C-95D-25-5		248.96	111.17	11.291		
C-95D-50-1	1.25	293.94	154.96	11.169	152.96 (SD = 6.805)	11.218 (SD = 0.418)
C-95D-50-2		303.06	164.73	10.606		
C-95D-50-3		290.43	151.28	11.897		
C-95D-50-4		288.67	149.46	11.343		
C-95D-50-5		283.71	144.36	11.075		

$K_0 = (\sigma_h - u_a)/(\sigma_v - u_a)$; σ_v = constant = 4 psi

Table 5.33 BE Test Results of Clay under K_0 Stress State at w = 20% (ψ = 953 kPa)

Specimen	K_0	Vs (m/s)	G_{max} (MPa)	D_{min} (%)	Avg G_{max} (MPa)	Avg D_{min} (%)
C-OPT-00-1	0.0	218.82	85.88	13.355	80.20 (SD = 4.325)	13.314 (SD = 0.440)
C-OPT-00-2		216.87	84.35	13.438		
C-OPT-00-3		203.32	74.14	13.252		
C-OPT-00-4		209.40	78.64	13.947		
C-OPT-00-5		208.52	77.98	12.576		
C-OPT-10-1	0.25	215.89	83.59	13.707	86.88 (SD = 2.983)	13.135 (SD = 0.555)
C-OPT-10-2		218.82	85.88	12.375		
C-OPT-10-3		225.91	91.54	13.653		
C-OPT-10-4		222.79	89.02	12.573		
C-OPT-10-5		216.87	84.35	13.367		
C-OPT-25-1	0.625	239.17	102.59	13.745	96.82 (SD = 4.840)	12.814 (SD = 0.785)
C-OPT-25-2		236.84	100.60	13.454		
C-OPT-25-3		234.59	98.71	12.621		
C-OPT-25-4		225.88	91.51	11.487		
C-OPT-25-5		224.85	90.68	12.765		
C-OPT-50-1	1.25	255.47	117.06	11.490	111.35 (SD = 5.375)	12.843 (SD = 0.828)
C-OPT-50-2		252.82	114.64	12.562		
C-OPT-50-3		251.49	113.44	13.358		
C-OPT-50-4		247.67	110.02	13.961		
C-OPT-50-5		238.02	101.61	12.844		

$K_0 = (\sigma_h - u_a)/(\sigma_v - u_a)$; σ_v = constant = 4 psi

Table 5.34 BE Test Results of Clay under K_0 Stress State at w = 23% (ψ = 635 kPa)

Specimen	K_0	Vs (m/s)	G_{max} (MPa)	D_{min} (%)	Avg G_{max} (MPa)	Avg D_{min} (%)
C-95W-00-1	0.0	161.56	46.82	13.623	43.61 (SD = 4.064)	13.759 (SD = 0.667)
C-95W-00-2		146.13	38.30	14.394		
C-95W-00-3		147.48	39.01	13.872		
C-95W-00-4		161.04	46.51	12.558		
C-95W-00-5		162.61	47.42	14.348		
C-95W-10-1	0.25	173.02	53.69	13.196	51.85 (SD = 4.850)	13.265 (SD = 0.498)
C-95W-10-2		176.14	55.64	13.465		
C-95W-10-3		157.00	44.21	12.676		
C-95W-10-4		178.73	57.29	14.103		
C-95W-10-5		164.28	48.41	12.883		
C-95W-25-1	0.625	179.38	57.71	14.443	57.02 (SD = 1.864)	13.783 (SD = 0.638)
C-95W-25-2		178.73	57.29	13.853		
C-95W-25-3		180.05	58.14	12.763		
C-95W-25-4		180.71	58.57	14.433		
C-95W-25-5		172.54	53.39	13.423		
C-95W-50-1	1.25	190.02	64.76	12.657	61.33 (SD = 2.024)	13.547 (SD = 0.469)
C-95W-50-2		180.71	58.57	13.764		
C-95W-50-3		184.83	61.27	14.043		
C-95W-50-4		183.43	60.35	13.632		
C-95W-50-5		185.50	61.71	13.636		

$K_0 = (\sigma_h - u_a)/(\sigma_v - u_a)$; σ_v = constant = 4 psi

Table 5.35 BE Test Results of Clay under K_0 Stress State at w = 27% (ψ = 235 kPa)

Specimen	K_0	Vs (m/s)	G_{max} (MPa)	D_{min} (%)	Avg G_{max} (MPa)	Avg D_{min} (%)
C-90W-00-1	0.0	127.78	29.29	13.346	29.20 (SD = 2.767)	14.175 (SD = 0.553)
C-90W-00-2		133.36	31.90	14.653		
C-90W-00-3		134.87	32.62	14.246		
C-90W-00-4		121.10	26.30	13.782		
C-90W-00-5		120.18	25.91	14.850		
C-90W-10-1	0.25	130.45	30.52	13.789	31.23 (SD = 1.392)	14.235 (SD = 0.516)
C-90W-10-2		133.73	32.08	14.568		
C-90W-10-3		134.87	32.62	13.457		
C-90W-10-4		133.74	32.08	14.577		
C-90W-10-5		126.77	28.82	14.783		
C-90W-25-1	0.625	134.11	32.26	13.786	32.99 (SD = 0.549)	14.133 (SD = 0.363)
C-90W-25-2		136.02	33.18	14.479		
C-90W-25-3		134.87	32.62	14.568		
C-90W-25-4		135.63	33.00	14.177		
C-90W-25-5		137.45	33.89	13.656		
C-90W-50-1	1.25	145.69	38.07	13.787	38.67 (SD = 1.137)	14.101 (SD = 0.375)
C-90W-50-2		148.40	39.50	13.898		
C-90W-50-3		147.48	39.01	14.267		
C-90W-50-4		143.21	36.79	14.762		
C-90W-50-5		149.32	39.99	13.789		

$K_0 = (\sigma_h - u_a)/(\sigma_v - u_a)$; σ_v = constant = 4 psi

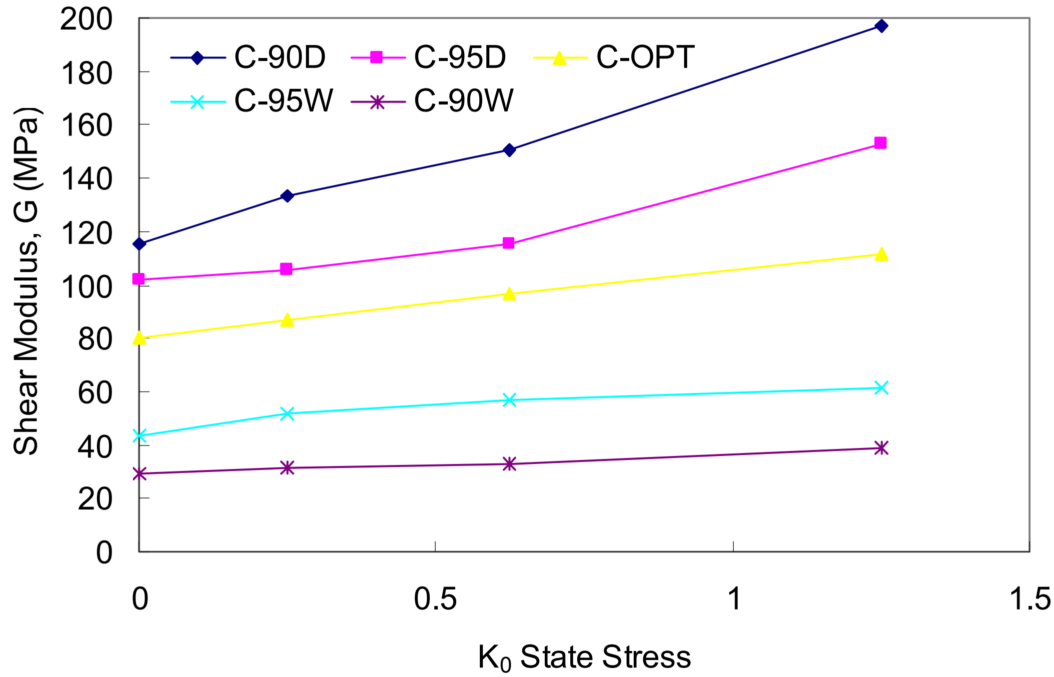

Figure 5.20 Variation of Average G with K_0 Stress State for Clay (TX/BE)

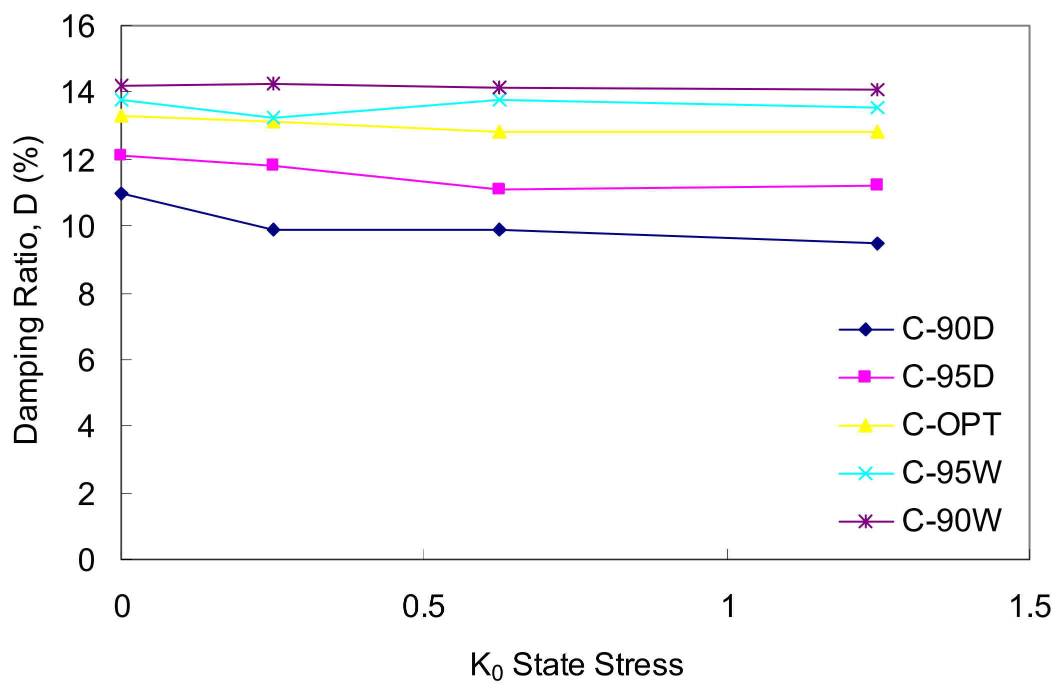

Figure 5.21 Variation of Average D with K_0 Stress State for Clay (TX/BE)

5.7 RC/BE Response

5.7.1 Sand

A series of RC/BE tests were conducted on several specimens of sand compacted at six moisture contents, 0%, 5%, 10%, 15%, 20%, and 24% in order to determine relationships between small-strain shear modulus (G_{max}) and small-strain damping ratio (D_{min}) with isotropic air confining pressure (σ_0) in the same confining chamber.

Tables 5.36 through 5.41 demonstrate the results of small-strain shear modulus (G_{max}) and small-strain damping ratio (D_{min}) of specimens at different isotropic confining pressure (σ_0) from both RC and BE methods.

Figures 5.22 and 5.33 show the variation of small-strain shear modulus (G_{max}) and damping ratio (D_{min}) with confining pressure (σ_0) at six moisture contents for sand from both RC and BE methods. It can be seen that G_{max} increases and D_{min} decreases with confinement σ_0. Also, it can be noted that at 0% moisture content the shear modulus from BE method is much higher than that from RC method, whereas values of shear modulus at higher moisture contents from both RC and BE methods are similar. This can be explained by the fact that the higher moisture content, the closer shear modulus values between both RC and BE methods are. Damping ratio from BE method is always higher than that from RC method.

Figures 5.34 through 5.37 show the variation of small-strain shear modulus and damping ratio with confinement at several moisture contents for sand from RC and BE methods, separately. As it can be observed from these figures, the shear modulus (G_{max}) decreases and damping ratio (D_{min}) increases with the amount of moisture content. Therefore, the shear modulus (G_{max}) increases and damping ratio (D_{min}) decreases with soil suction (ψ).

Table 5.36 RC/BE Test Results of Sand at w = 0% ($\psi \rightarrow \infty$)

Specimen	f_r (Hz)	V_{rms} (mV)$^{+}$	V_s (m/s)$^{++}$	$G_{max(RC)}$ (MPa)	$G_{max(BE)}$ (MPa)	$D_{min(RC)}$ (%)	$D_{min(BE)}$ (%)
S-00-00-1	54.12	60.92	163.74	26.37	45.82	4.804	6.532
S-00-00-2	56.41	55.91	174.26	28.64	51.89	4.224	5.383
S-00-00-3	53.74	59.42	168.25	26.00	48.38	4.125	4.928
S-00-00-4	53.55	60.21	173.02	25.82	51.16	4.554	5.837
S-00-00-5	53.36	58.33	171.20	25.64	50.09	3.530	6.274
S-00-10-1	59.26	47.47	171.82	31.61	50.45	4.788	5.930
S-00-10-2	58.50	51.53	173.02	30.81	51.16	3.987	6.437
S-00-10-3	58.12	52.39	176.14	30.41	53.02	4.216	6.219
S-00-10-4	57.93	49.02	174.89	30.21	52.27	4.436	5.357
S-00-10-5	58.69	49.78	173.64	31.01	51.53	4.546	5.437
S-00-25-1	60.59	43.42	177.42	33.05	53.80	4.554	5.839
S-00-25-2	60.21	46.97	177.12	32.64	53.61	4.433	6.291
S-00-25-3	59.83	49.03	176.79	32.22	53.41	4.234	5.343
S-00-25-4	59.64	50.11	175.51	32.02	52.64	4.573	5.674
S-00-25-5	60.97	42.91	176.14	33.47	53.02	3.857	5.328
S-00-50-1	61.16	52.43	179.38	33.67	54.99	4.769	5.839
S-00-50-2	61.35	49.29	180.71	33.88	55.81	4.322	5.932
S-00-50-3	61.92	49.54	178.08	34.52	54.20	4.123	5.637
S-00-50-4	62.30	48.52	178.73	34.94	54.59	4.039	5.148
S-00-50-5	61.82	53.59	181.39	34.41	56.23	4.373	5.342

+ V_{rms}: Accelerometer output from RC test

++ V_s: Shear-wave velocity from BE test

Table 5.37 RC/BE Test Results of Sand at w = 5% (ψ = 112 kPa)

Specimen	f_r (Hz)	V_{rms} (mV)	V_s (m/s)	$G_{max(RC)}$ (MPa)	$G_{max(BE)}$ (MPa)	$D_{min(RC)}$ (%)	$D_{min(BE)}$ (%)
S-05-00-1	53.74	62.75	135.63	26.00	31.44	4.152	8.403
S-05-00-2	54.88	63.38	134.11	27.12	30.74	5.362	6.124
S-05-00-3	55.65	63.99	135.25	27.88	31.26	5.451	6.383
S-05-00-4	57.93	62.57	132.26	30.21	29.89	4.956	7.738
S-05-00-5	58.50	64.28	131.89	30.81	29.73	4.213	6.839
S-05-10-1	59.26	64.83	132.62	31.61	30.06	3.779	5.902
S-05-10-2	57.93	65.44	138.65	30.21	32.85	4.726	6.743
S-05-10-3	58.88	64.14	137.85	31.21	32.47	4.321	7.234
S-05-10-4	59.64	62.16	140.27	32.02	33.63	4.329	7.489
S-05-10-5	59.83	64.21	138.25	32.22	32.66	4.038	7.345
S-05-25-1	59.83	65.34	145.21	32.22	36.04	3.491	5.849
S-05-25-2	60.21	64.55	144.79	32.64	35.83	4.546	6.847
S-05-25-3	60.59	62.85	142.36	33.05	34.63	4.375	6.472
S-05-25-4	59.64	65.01	141.94	32.02	34.43	4.678	6.227
S-05-25-5	60.38	61.84	141.52	32.82	34.23	4.245	7.472
S-05-50-1	59.83	65.79	145.21	32.22	36.04	3.663	7.121
S-05-50-2	60.21	64.60	146.09	32.64	36.47	4.343	7.438
S-05-50-3	60.59	64.44	146.52	33.05	36.69	4.733	5.728
S-05-50-4	61.35	61.23	146.97	33.88	36.91	3.432	6.428
S-05-50-5	61.73	59.31	148.31	34.31	37.59	4.028	6.282

Table 5.38 RC/BE Test Results of Sand at w = 10% (ψ = 68.7 kPa)

Specimen	f_r (Hz)	V_{rms} (mV)	V_s (m/s)	$G_{max(RC)}$ (MPa)	$G_{max(BE)}$ (MPa)	$D_{min(RC)}$ (%)	$D_{min(BE)}$ (%)
S-10-00-1	51.46	61.57	118.50	23.84	24.00	4.372	11.742
S-10-00-2	51.65	59.79	115.35	24.02	22.74	5.678	10.758
S-10-00-3	52.41	62.19	116.19	24.73	23.07	4.848	11.173
S-10-00-4	48.99	60.38	116.76	21.60	23.30	5.098	10.363
S-10-00-5	54.50	64.64	117.62	26.74	23.64	4.736	10.234
S-10-10-1	56.03	64.15	123.60	28.26	26.11	4.105	10.372
S-10-10-2	55.27	65.21	122.02	27.50	25.45	5.037	11.273
S-10-10-3	55.46	64.72	121.40	27.68	25.19	4.837	9.874
S-10-10-4	55.84	64.69	124.57	28.07	26.52	4.733	9.463
S-10-10-5	56.22	63.85	122.96	28.45	25.84	4.538	10.745
S-10-25-1	56.41	64.47	126.43	28.64	27.32	3.723	10.542
S-10-25-2	56.98	64.55	124.57	29.22	26.52	4.983	9.843
S-10-25-3	57.36	63.34	125.44	29.62	26.89	5.192	11.383
S-10-25-4	57.74	62.91	127.67	30.01	27.85	4.353	10.213
S-10-25-5	56.22	64.48	124.78	28.45	26.61	4.542	9.374
S-10-50-1	56.60	65.44	128.47	28.84	28.20	4.241	9.473
S-10-50-2	56.79	64.07	127.78	29.03	27.90	4.387	9.463
S-10-50-3	56.98	62.76	126.43	29.22	27.32	4.873	10.372
S-10-50-4	57.74	64.95	126.10	30.01	27.17	4.657	9.345
S-10-50-5	58.31	63.15	127.44	30.61	27.76	4.472	10.564

Table 5.39 RC/BE Test Results of Sand at w = 15% (ψ = 42.5 kPa)

Specimen	f_r (Hz)	V_{rms} (mV)	V_s (m/s)	$G_{max(RC)}$ (MPa)	$G_{max(BE)}$ (MPa)	$D_{min(RC)}$ (%)	$D_{min(BE)}$ (%)
S-15-00-1	47.85	63.66	101.27	20.61	17.53	4.911	12.353
S-15-00-2	48.23	63.99	100.42	20.94	17.23	5.378	11.489
S-15-00-3	47.47	62.67	100.63	20.28	17.31	5.284	11.374
S-15-00-4	45.95	63.19	105.90	19.00	19.17	4.967	10.847
S-15-00-5	51.08	64.99	107.01	23.49	19.57	5.536	11.874
S-15-10-1	51.27	65.82	114.34	23.66	22.34	4.803	11.746
S-15-10-2	51.46	65.59	114.62	23.84	22.45	4.933	11.983
S-15-10-3	51.65	64.91	112.99	24.02	21.82	4.738	11.573
S-15-10-4	52.03	65.67	113.80	24.37	22.13	4.722	12.083
S-15-10-5	50.89	65.88	115.35	23.32	22.74	5.012	10.217
S-15-25-1	51.65	65.65	113.26	24.02	21.92	3.582	11.839
S-15-25-2	51.46	65.59	114.62	23.84	22.45	4.732	11.746
S-15-25-3	52.03	65.67	115.35	24.37	22.74	4.656	11.537
S-15-25-4	52.41	64.91	116.19	24.73	23.07	4.758	11.463
S-15-25-5	52.79	64.88	115.08	25.09	22.63	4.832	10.874
S-15-50-1	52.03	63.09	114.89	24.37	22.56	4.509	10.376
S-15-50-2	52.41	64.19	115.35	24.73	22.74	4.783	11.243
S-15-50-3	52.79	64.35	116.19	25.09	23.07	4.347	10.567
S-15-50-4	53.17	63.47	116.76	25.45	23.30	4.435	10.372
S-15-50-5	53.55	64.02	117.62	25.82	23.64	4.374	10.738

Table 5.40 RC/BE Test Results of Sand at w = 20% (ψ = 7.04 kPa)

Specimen	f_r (Hz)	V_{rms} (mV)	V_s (m/s)	$G_{max(RC)}$ (MPa)	$G_{max(BE)}$ (MPa)	$D_{min(RC)}$ (%)	$D_{min(BE)}$ (%)
S-20-00-1	44.64	49.03	98.42	17.94	16.55	5.846	13.473
S-20-00-2	44.64	49.74	97.62	17.94	16.29	5.694	13.183
S-20-00-3	42.96	50.27	96.24	16.61	15.83	5.932	12.473
S-20-00-4	43.15	51.07	99.17	16.76	16.81	5.738	12.784
S-20-00-5	43.65	50.51	101.34	17.15	17.55	5.438	12.023
S-20-10-1	45.13	48.81	101.92	18.34	17.75	5.126	12.473
S-20-10-2	44.32	47.82	100.63	17.68	17.31	4.575	12.837
S-20-10-3	45.47	46.48	100.00	18.62	17.09	4.736	12.218
S-20-10-4	44.64	48.46	102.57	17.94	17.98	5.113	12.437
S-20-10-5	44.46	48.93	101.27	17.80	17.53	5.183	11.874
S-20-25-1	49.47	49.13	109.79	22.04	20.60	4.876	12.384
S-20-25-2	48.75	49.09	108.88	21.39	20.26	4.973	11.376
S-20-25-3	48.48	48.70	110.05	21.15	20.70	4.326	11.784
S-20-25-4	47.27	46.01	108.47	20.12	20.11	5.113	12.453
S-20-25-5	48.74	48.02	108.06	21.39	19.95	4.532	11.984
S-20-50-1	50.64	50.41	110.90	23.09	21.02	4.536	12.382
S-20-50-2	50.85	50.45	111.33	23.28	21.18	4.462	12.073
S-20-50-3	50.46	50.75	110.81	22.93	20.98	4.271	11.893
S-20-50-4	49.46	50.45	112.02	22.03	21.45	4.974	11.564
S-20-50-5	49.47	50.93	110.64	22.03	20.92	4.432	11.438

Table 5.41 RC/BE Test Results of Sand at w = 24% (ψ = 0.64 kPa)

Specimen	f_r (Hz)	V_{rms} (mV)	V_s (m/s)	$G_{max(RC)}$ (MPa)	$G_{max(BE)}$ (MPa)	$D_{min(RC)}$ (%)	$D_{min(BE)}$ (%)
S-24-00-1	41.47	48.38	92.28	15.48	14.55	5.748	13.273
S-24-00-2	42.37	47.68	92.94	16.16	14.76	5.533	13.193
S-24-00-3	39.67	48.01	95.48	14.17	15.58	5.118	12.839
S-24-00-4	40.87	48.48	93.85	15.04	15.05	5.773	12.647
S-24-00-5	41.19	43.59	90.71	15.27	14.06	5.285	12.364
S-24-10-1	44.49	46.27	98.02	17.82	16.42	4.873	11.932
S-24-10-2	43.58	47.67	99.17	17.10	16.81	5.368	11.237
S-24-10-3	45.49	45.78	101.27	18.63	17.53	5.457	11.674
S-24-10-4	44.86	47.44	100.42	18.11	17.23	4.446	11.847
S-24-10-5	44.39	47.34	97.03	17.74	16.09	4.783	11.463
S-24-25-1	47.47	48.12	109.71	20.29	20.57	4.436	11.244
S-24-25-2	48.57	48.69	107.98	21.23	19.92	4.873	11.374
S-24-25-3	46.48	48.82	108.96	19.45	20.29	4.778	11.637
S-24-25-4	46.49	47.64	110.22	19.45	20.76	5.592	11.038
S-24-25-5	46.78	48.53	103.39	19.70	18.27	5.016	11.237
S-24-50-1	48.48	49.59	110.22	21.16	20.76	4.635	11.746
S-24-50-2	49.49	48.38	110.54	22.05	20.88	4.833	12.098
S-24-50-3	47.47	50.97	111.34	20.29	21.19	4.281	11.533
S-24-50-4	47.97	49.77	110.84	20.71	20.99	4.562	11.328
S-24-50-5	48.68	48.82	111.75	21.33	21.34	4.921	10.784

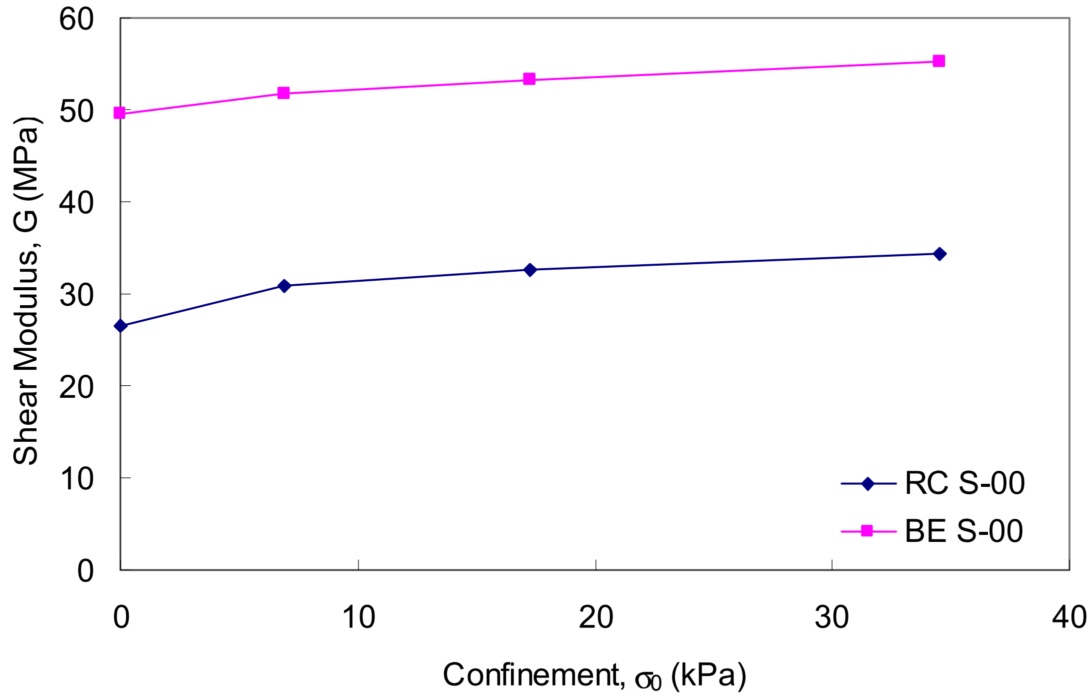

Figure 5.22 Variation of Shear Modulus with Confinement for Sand w=0% (RC/BE)

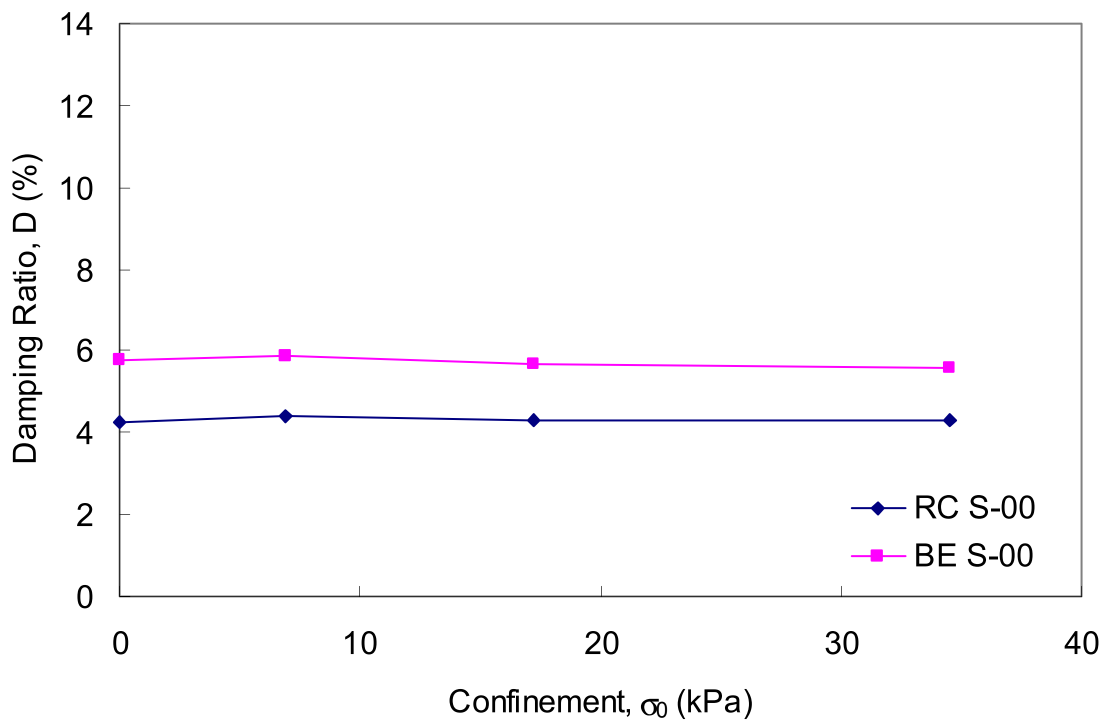

Figure 5.23 Variation of Damping Ratio with Confinement for Sand w=0% (RC/BE)

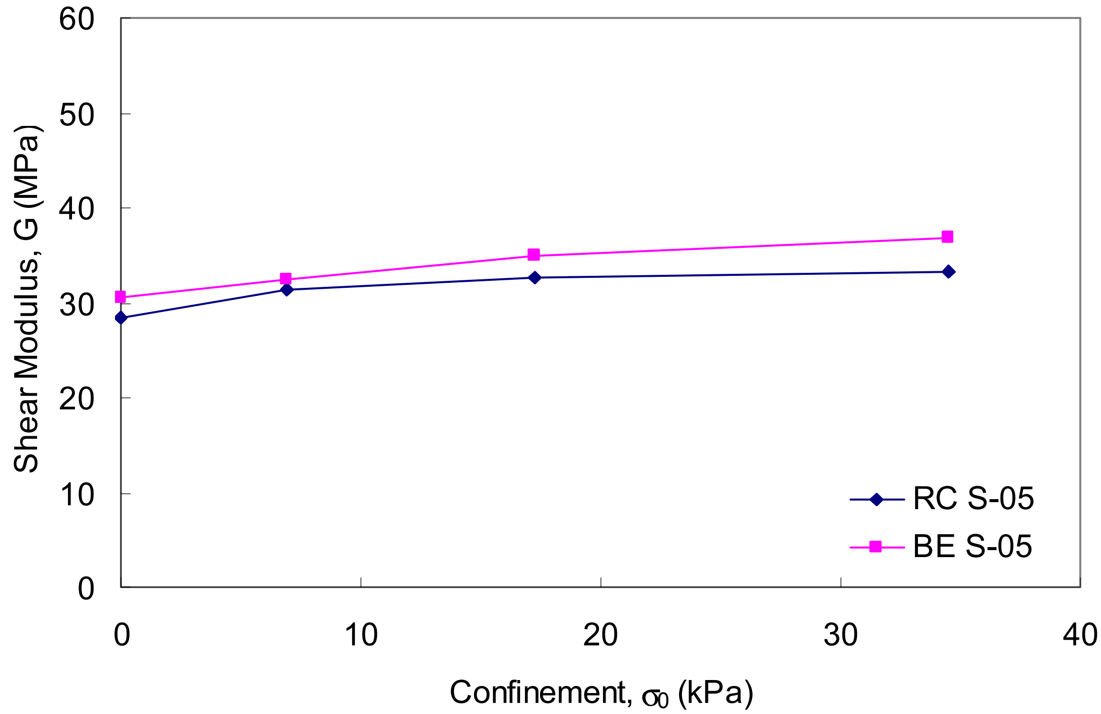

Figure 5.24 Variation of Shear Modulus with Confinement for Sand w=5% (RC/BE)

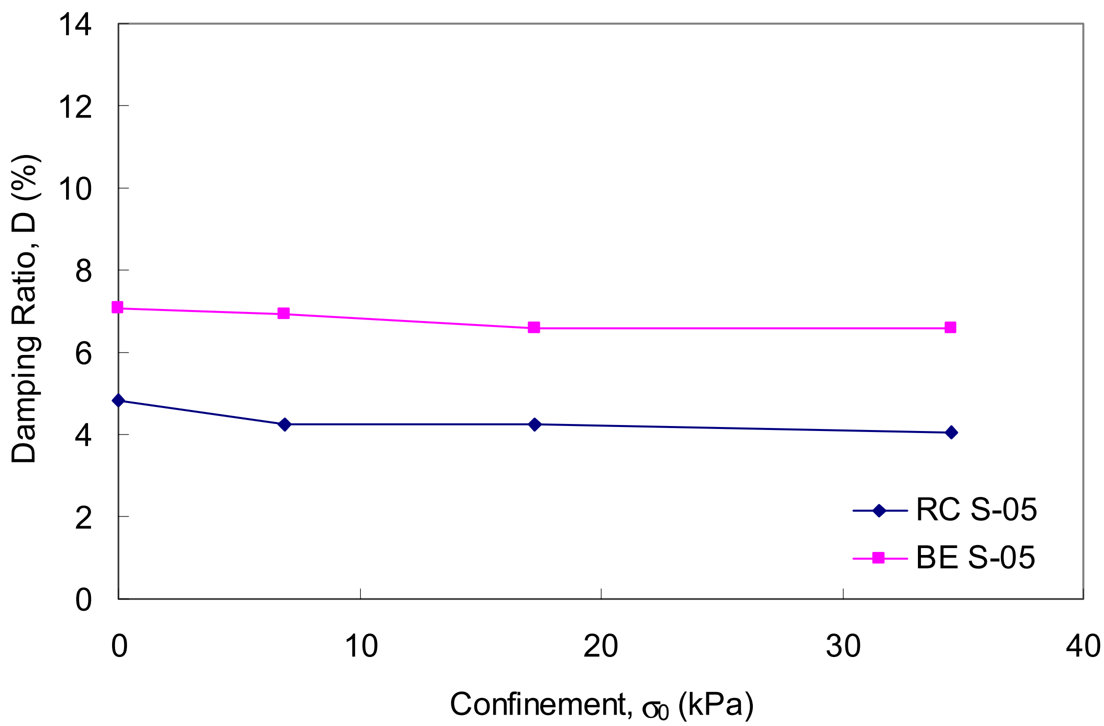

Figure 5.25 Variation of Damping Ratio with Confinement for Sand w=5% (RC/BE)

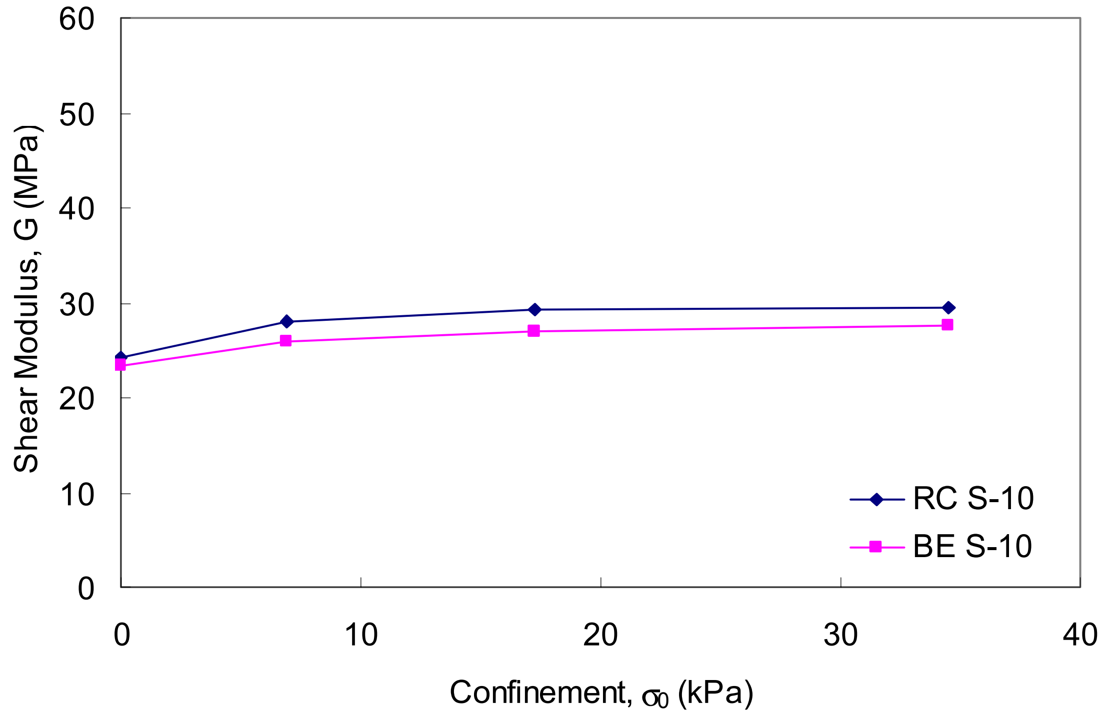

Figure 5.26 Variation of Shear Modulus with Confinement for Sand w=10% (RC/BE)

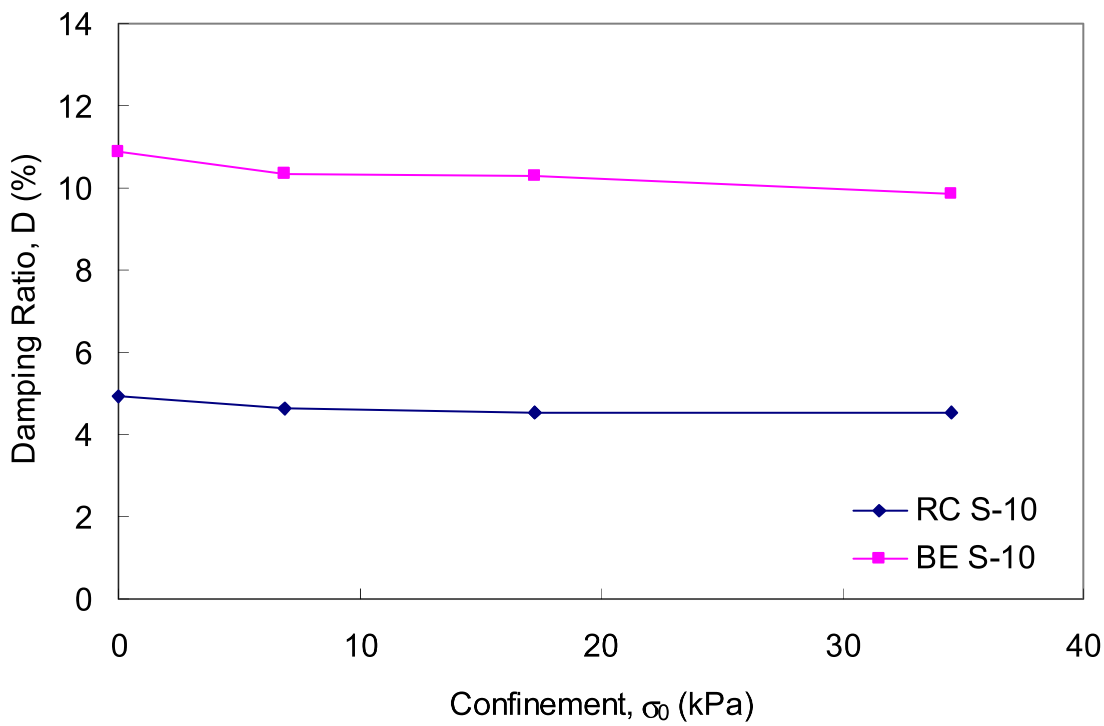

Figure 5.27 Variation of Damping Ratio with Confinement for Sand w=10% (RC/BE)

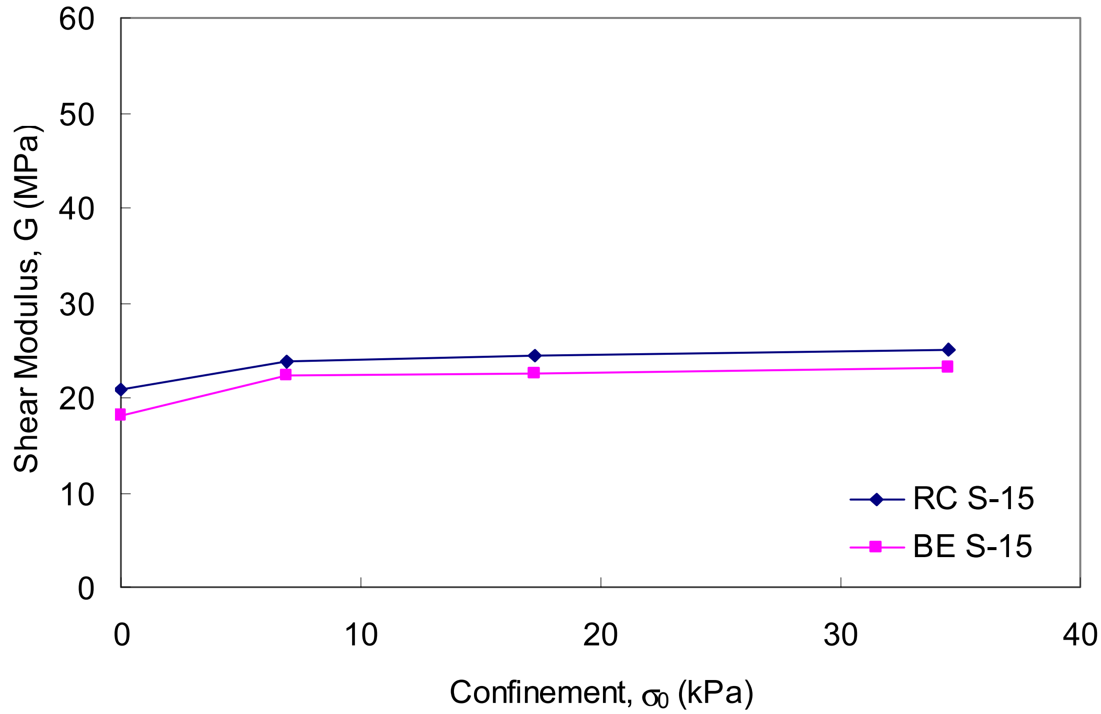

Figure 5.28 Variation of Shear Modulus with Confinement for Sand w=15% (RC/BE)

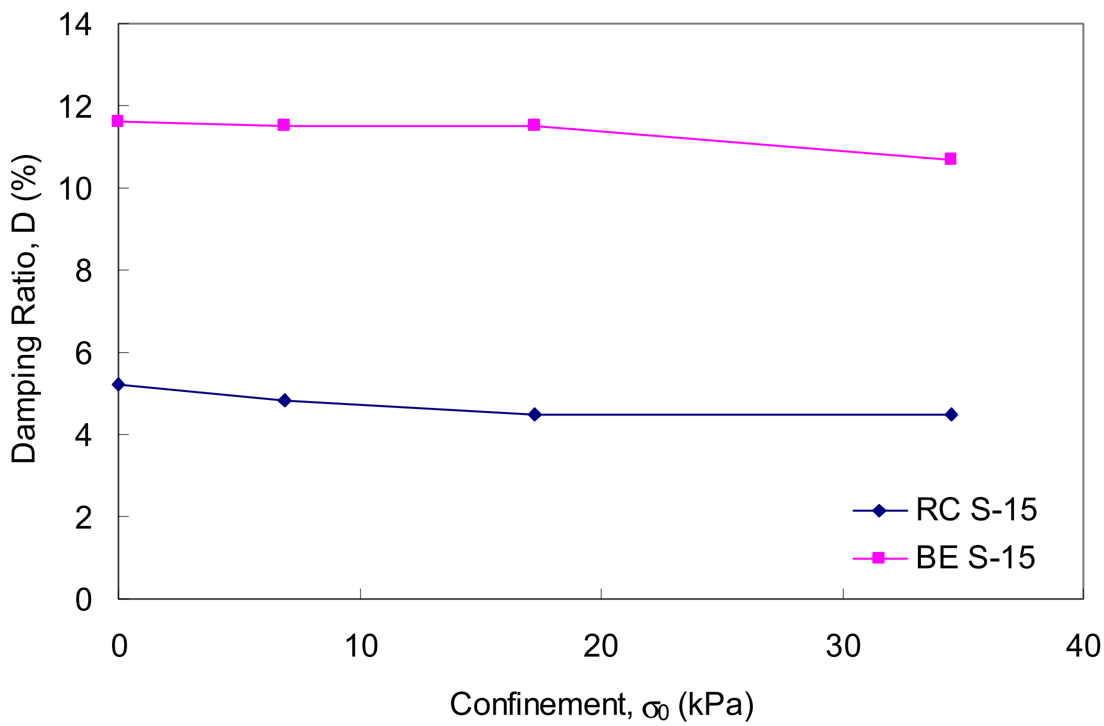

Figure 5.29 Variation of Damping Ratio with Confinement for Sand w=15% (RC/BE)

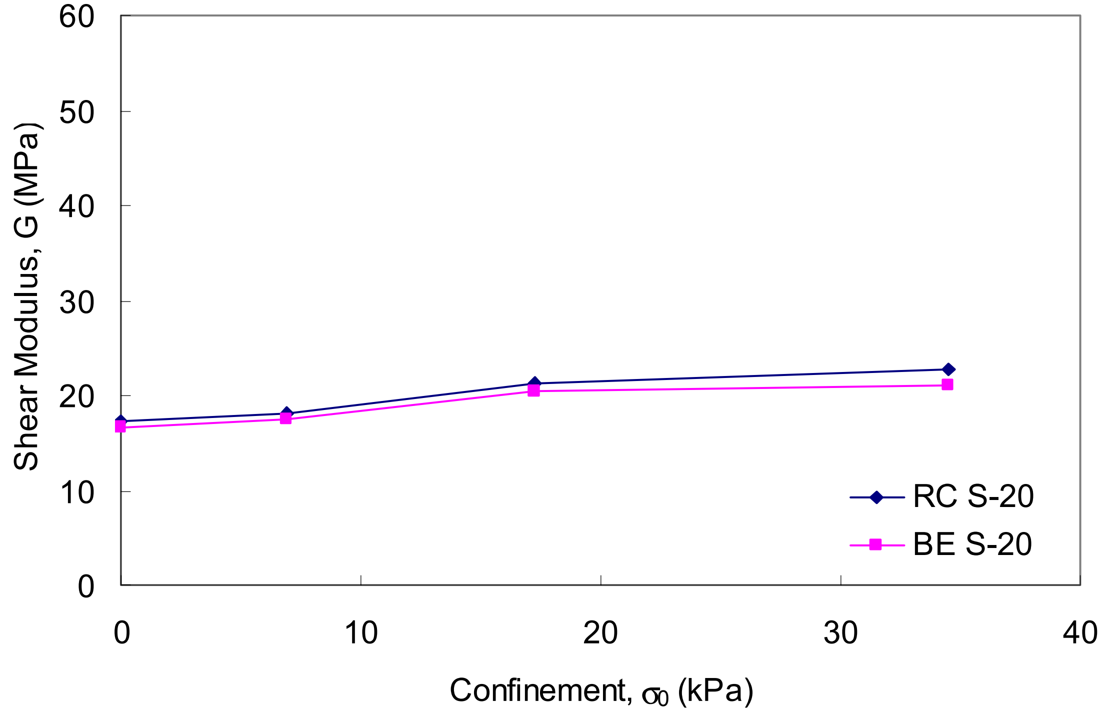

Figure 5.30 Variation of Shear Modulus with Confinement for Sand w=20% (RC/BE)

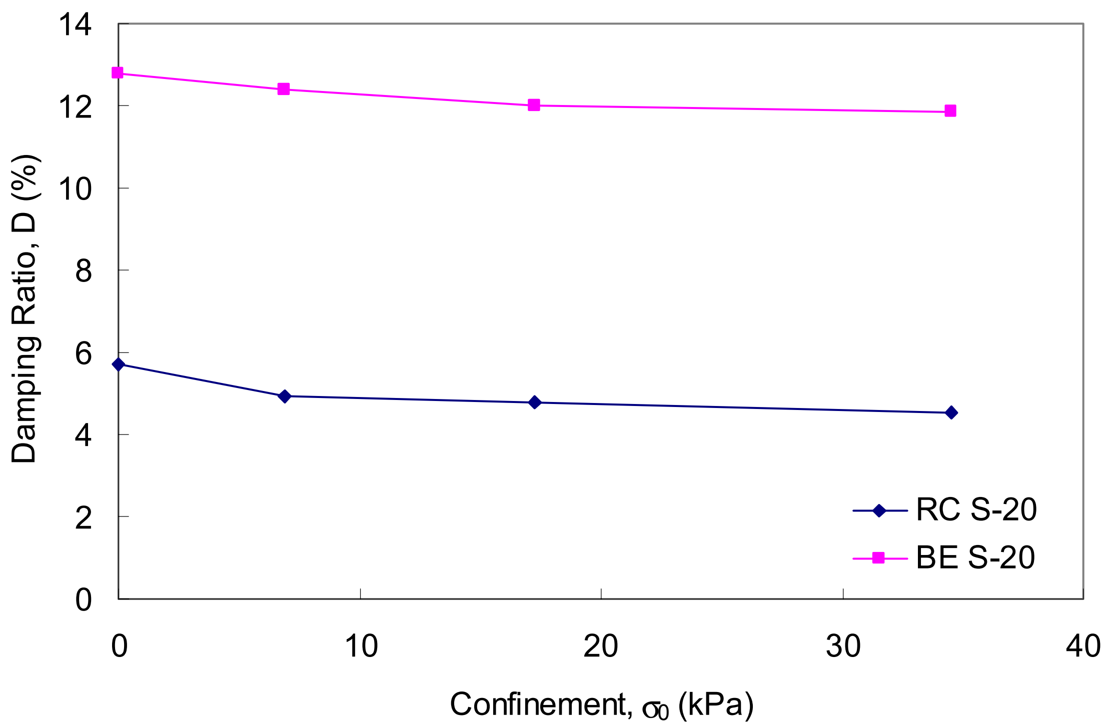

Figure 5.31 Variation of Damping Ratio with Confinement for Sand w=20% (RC/BE)

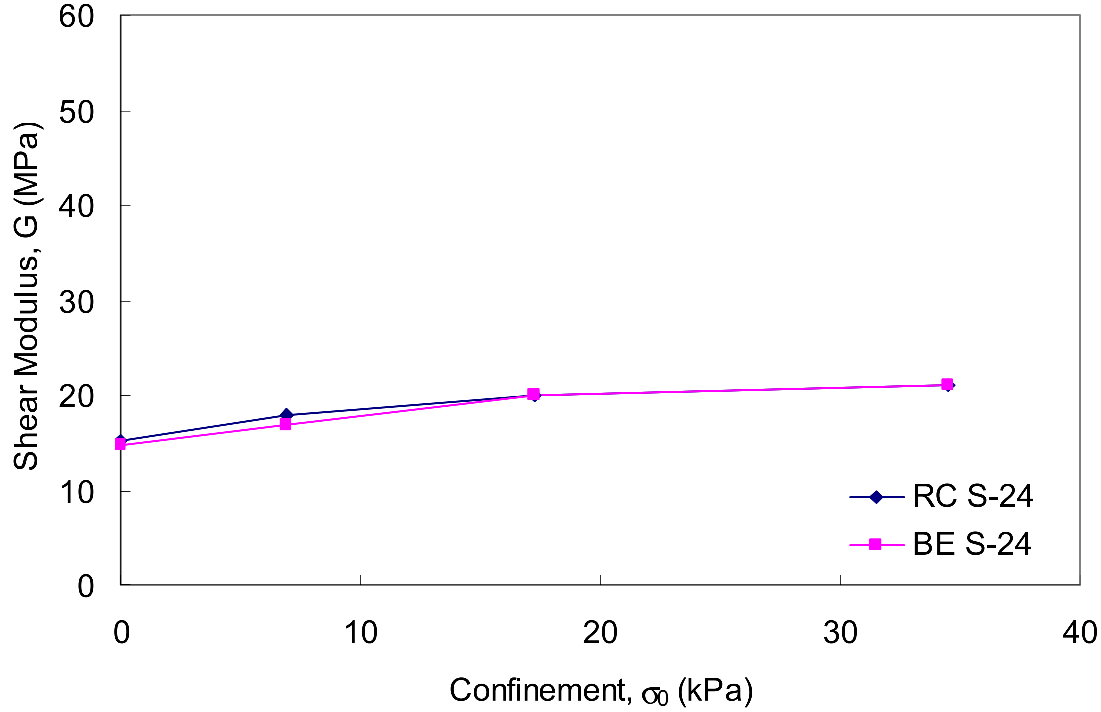

Figure 5.32 Variation of Shear Modulus with Confinement for Sand w=24% (RC/BE)

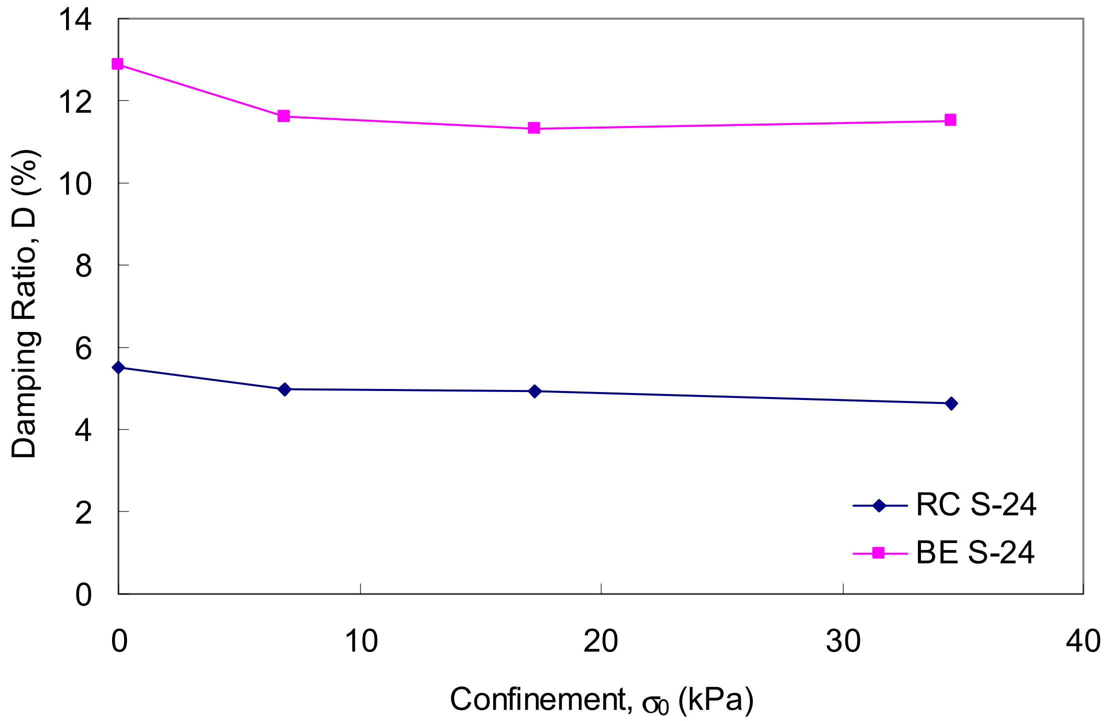

Figure 5.33 Variation of Damping Ratio with Confinement for Sand w=24% (RC/BE)

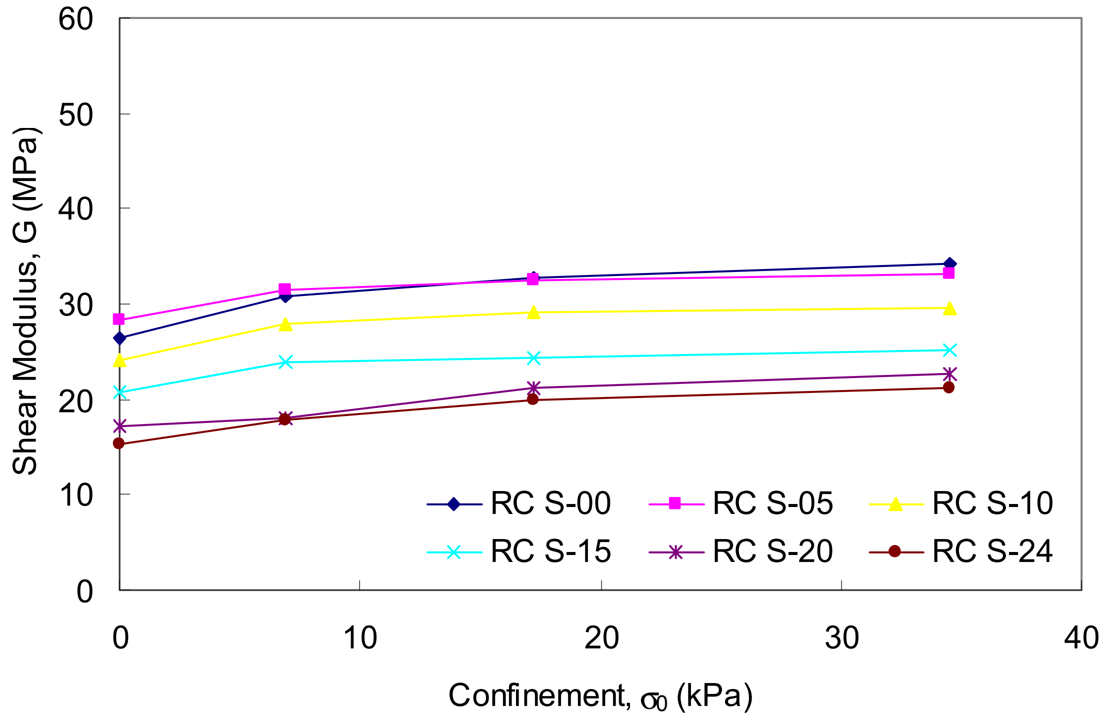

Figure 5.34 Variation of G_{max} with Confinement using RC Method for Sand (RC/BE)

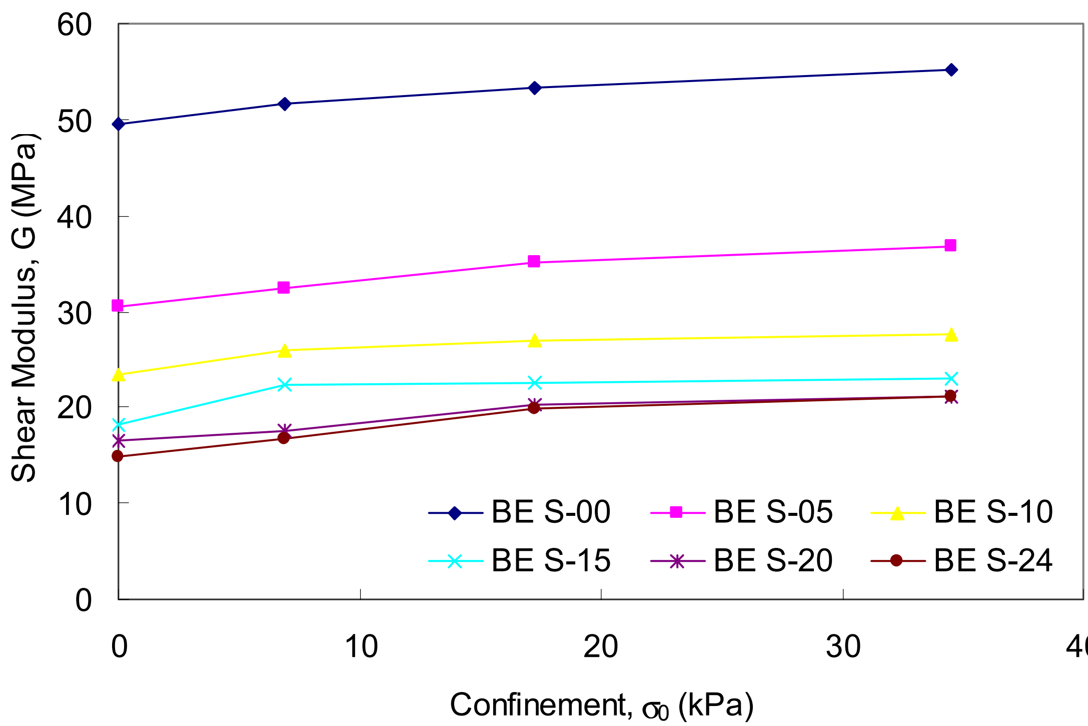

Figure 5.35 Variation of G_{max} with Confinement using BE Method for Sand (RC/BE)

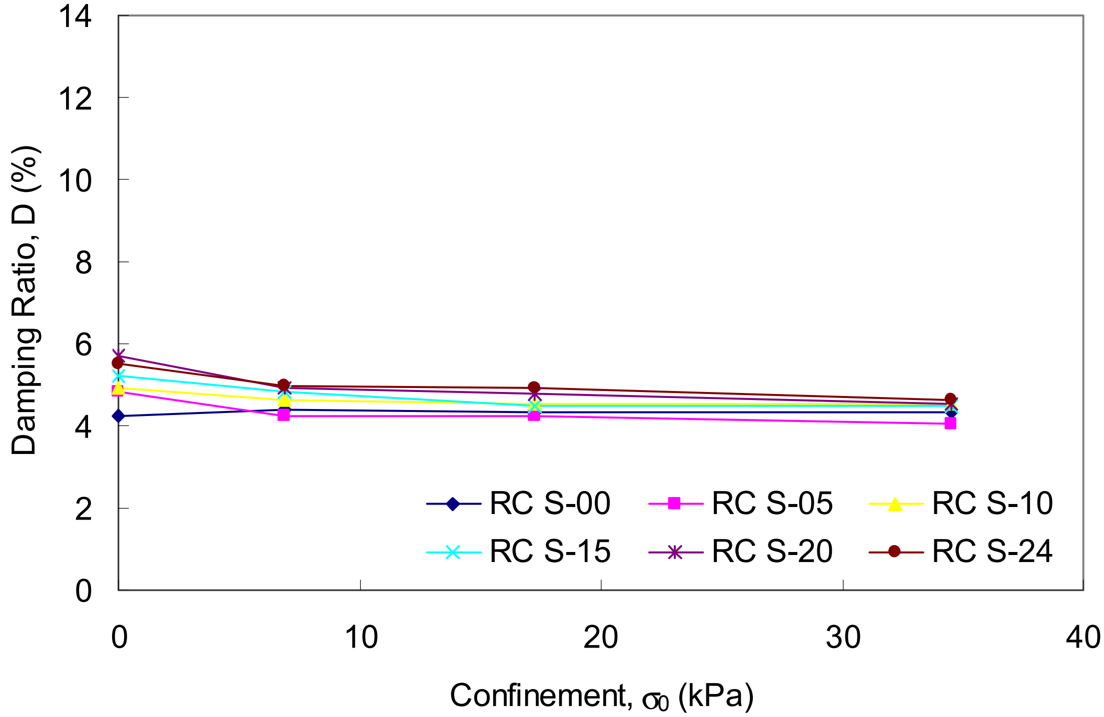

Figure 5.36 Variation of D_{min} with Confinement using RC Method for Sand (RC/BE)

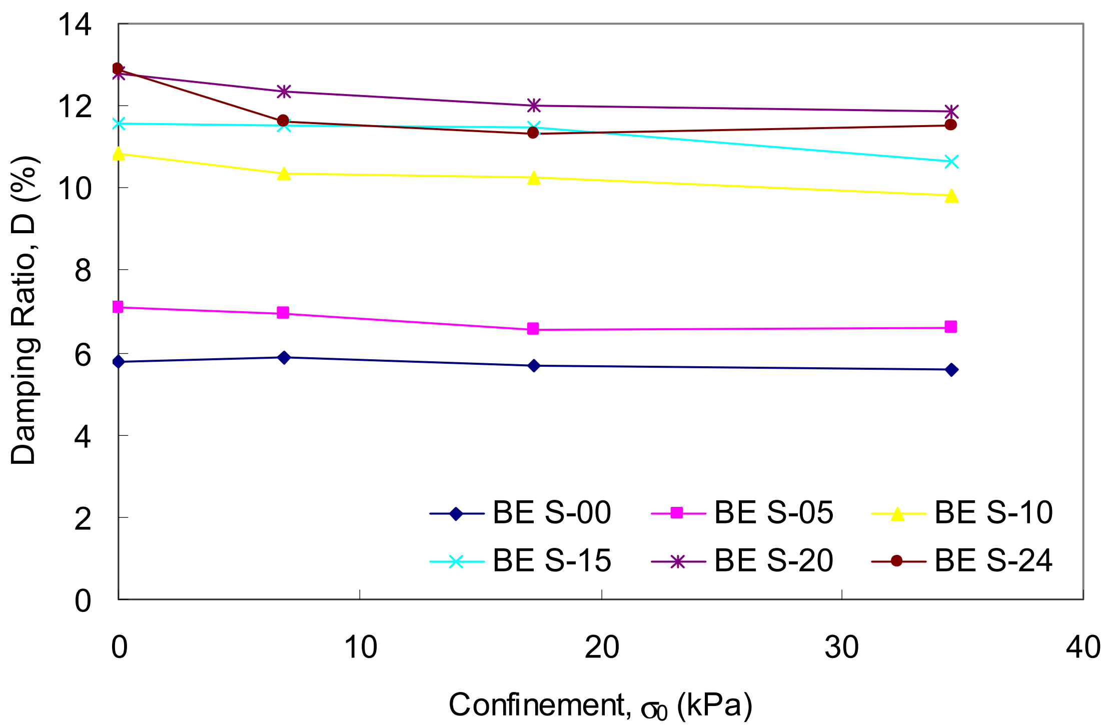

Figure 5.37 Variation of D_{min} with Confinement using BE Method for Sand (RC/BE)

5.7.2 Clay

A series of RC&BE tests were conducted on several specimens of clay compacted at 90% dry, 95% dry, optimum, 95% wet, and 90% wet of $\gamma_{d\text{-}max}$ (13%, 17%, 20%, 23%, and 27% moisture contents, respectively) in order to determine relationships between small-strain shear modulus (G_{max}) and damping ratio (D_{min}) with isotropic air confining pressure (σ_0) in the same confining chamber.

Tables 5.42 through 5.46 demonstrate the results of small-strain shear modulus (G_{max}) and small-strain damping ratio (D_{min}) of specimens at different isotropic confining pressure (σ_0) from both RC and BE methods.

Figures 5.38 and 5.47 show the variation of small-strain shear modulus (G_{max}) and damping ratio (D_{min}) with confining pressure (σ_0) at five moisture contents for sand from both RC and BE methods. It can be seen that G_{max} increases and D_{min} decreases with confinement σ_0. Also, it can be noted that at 13% moisture content, the shear modulus from BE method is much higher than that from RC method, and values of shear modulus from BE method is always higher than that from RC method, but the difference of values of shear modulus between RC and BE methods decreases with the amount of moisture content. This can be explained by the fact that the higher moisture content, the closer shear modulus values between both RC and BE methods. Damping ratio from BE is always higher than that from RC.

Figures 5.48 through 5.51 show the variation of G_{max} and D_{min} with confinement at several moisture contents for clay from RC and BE methods, separately. As it can be observed from these figures, the shear modulus (G_{max}) decreases and damping ratio (D_{min}) increases with amount of moisture content. Hence, the shear modulus (G_{max}) increases and damping ratio (D) decreases with soil suction (ψ).

Table 5.42 RC/BE Test Results of Clay at w = 13% (ψ = 2346 kPa)

Specimen	f_r (Hz)	V_{rms} (mV)	V_s (m/s)	$G_{max(RC)}$ (MPa)	$G_{max(BE)}$ (MPa)	$D_{min(RC)}$ (%)	$D_{min(BE)}$ (%)
C-90D-00-1	82.08	32.89	306.89	60.65	160.95	8.528	8.901
C-90D-00-2	81.51	32.42	310.81	59.81	165.09	8.372	9.201
C-90D-00-3	79.99	32.24	314.83	57.60	169.39	8.647	8.865
C-90D-00-4	81.13	33.38	316.85	59.26	171.56	8.356	8.473
C-90D-00-5	80.75	32.86	308.80	58.70	162.96	7.984	9.372
C-90D-10-1	84.17	33.40	318.96	63.78	173.86	8.512	8.675
C-90D-10-2	83.41	33.01	319.96	62.64	174.95	8.436	9.065
C-90D-10-3	83.22	35.65	325.32	62.35	180.87	8.647	9.123
C-90D-10-4	84.74	33.17	314.83	64.65	169.39	8.362	8.567
C-90D-10-5	84.38	33.71	323.13	64.10	178.43	8.362	8.382
C-90D-25-1	85.32	34.31	323.13	65.53	178.43	8.271	8.638
C-90D-25-2	85.51	34.22	327.48	65.82	183.27	8.463	8.273
C-90D-25-3	84.74	34.33	324.22	64.65	179.64	8.328	9.302
C-90D-25-4	85.02	34.04	322.11	65.08	177.31	8.364	7.894
C-90D-25-5	85.32	34.33	321.03	65.53	176.12	8.549	8.214
C-90D-50-1	86.46	34.25	327.48	67.29	183.27	8.501	8.643
C-90D-50-2	87.03	34.04	334.19	68.18	190.86	7.767	8.234
C-90D-50-3	86.65	34.33	336.54	67.59	193.55	8.574	9.047
C-90D-50-4	87.41	34.10	338.84	68.78	196.21	8.452	8.543
C-90D-50-5	86.08	34.26	329.73	66.70	185.80	8.352	7.784

Table 5.43 RC/BE Test Results of Clay at w = 17% (ψ = 1380 kPa)

Specimen	f_r (Hz)	V_{rms} (mV)	V_s (m/s)	$G_{max(RC)}$ (MPa)	$G_{max(BE)}$ (MPa)	$D_{min(RC)}$ (%)	$D_{min(BE)}$ (%)
C-95D-00-1	78.28	38.71	245.22	55.16	102.76	8.451	12.218
C-95D-00-2	77.90	38.64	240.37	54.63	98.74	7.234	12.678
C-95D-00-3	78.69	38.58	246.44	55.74	103.79	8.326	12.248
C-95D-00-4	77.33	38.17	242.77	53.83	100.72	7.687	11.098
C-95D-00-5	76.95	37.52	248.96	53.30	105.92	6.261	10.536
C-95D-10-1	79.23	39.18	258.19	56.51	113.92	7.257	11.944
C-95D-10-2	79.61	39.19	268.12	57.05	122.86	8.879	12.376
C-95D-10-3	79.80	39.20	262.34	57.33	117.61	7.579	11.438
C-95D-10-4	79.99	39.12	265.20	57.60	120.19	8.143	10.756
C-95D-10-5	79.04	39.05	256.80	56.24	112.70	7.897	11.219
C-95D-25-1	80.75	39.57	263.74	58.70	118.87	6.802	11.933
C-95D-25-2	80.56	39.48	272.61	58.43	127.00	7.863	10.876
C-95D-25-3	80.94	39.77	275.70	58.98	129.89	7.644	11.376
C-95D-25-4	81.32	39.61	271.06	59.53	125.56	8.236	10.019
C-95D-25-5	80.34	39.45	268.12	58.11	122.86	7.453	10.921
C-95D-50-1	82.27	38.95	275.70	60.93	129.89	6.245	9.619
C-95D-50-2	82.65	41.25	274.12	61.50	128.41	8.018	10.805
C-95D-50-3	82.88	39.85	278.80	61.83	132.84	7.192	11.987
C-95D-50-4	83.03	40.56	282.04	62.07	135.94	8.048	10.373
C-95D-50-5	82.45	40.20	245.22	61.20	134.40	8.358	11.176

Table 5.44 RC/BE Test Results of Clay at w = 20% (ψ = 953 kPa)

Specimen	f_r (Hz)	V_{rms} (mV)	V_s (m/s)	$G_{max(RC)}$ (MPa)	$G_{max(BE)}$ (MPa)	$D_{min(RC)}$ (%)	$D_{min(BE)}$ (%)
C-OPT-00-1	64.39	40.84	216.87	37.33	80.37	6.988	14.375
C-OPT-00-2	64.96	41.36	214.95	37.99	78.96	6.894	13.278
C-OPT-00-3	69.72	42.33	212.15	43.76	76.92	8.758	13.384
C-OPT-00-4	66.11	41.71	210.32	39.34	75.59	8.574	14.467
C-OPT-00-5	71.43	45.40	211.22	45.93	76.24	7.897	12.336
C-OPT-10-1	72.19	46.25	226.95	46.92	88.02	5.749	13.461
C-OPT-10-2	72.00	46.16	225.91	46.67	87.22	8.847	12.375
C-OPT-10-3	72.57	45.82	221.79	47.41	84.07	6.674	11.735
C-OPT-10-4	72.38	45.71	219.79	47.17	82.55	8.538	12.773
C-OPT-10-5	72.76	45.46	223.83	47.66	85.62	7.937	14.267
C-OPT-25-1	73.14	46.35	226.95	48.16	88.02	5.469	13.465
C-OPT-25-2	73.52	45.66	227.99	48.66	88.83	8.372	14.237
C-OPT-25-3	72.95	46.47	224.85	47.91	86.40	7.289	12.721
C-OPT-25-4	73.71	45.11	223.83	48.92	85.62	8.437	11.337
C-OPT-25-5	73.52	45.54	229.09	48.66	89.69	7.563	12.447
C-OPT-50-1	73.52	46.95	229.09	48.66	89.69	5.441	11.709
C-OPT-50-2	73.71	46.79	227.99	48.92	88.83	7.347	12.232
C-OPT-50-3	73.14	46.76	230.26	48.16	90.61	8.218	14.178
C-OPT-50-4	74.09	46.18	226.95	49.42	88.02	7.137	13.461
C-OPT-50-5	73.33	46.78	229.49	48.41	90.00	8.433	12.384

Table 5.45 RC/BE Test Results of Clay at w = 23% (ψ = 635 kPa)

Specimen	f_r (Hz)	V_{rms} (mV)	V_s (m/s)	$G_{max(RC)}$ (MPa)	$G_{max(BE)}$ (MPa)	$D_{min(RC)}$ (%)	$D_{min(BE)}$ (%)
C-95W-00-1	49.18	48.03	139.46	21.77	33.24	8.083	13.723
C-95W-00-2	48.80	49.74	141.52	21.44	34.23	8.938	14.594
C-95W-00-3	48.61	50.27	145.66	21.27	36.26	7.137	13.732
C-95W-00-4	54.50	45.07	144.57	26.74	35.72	7.837	12.538
C-95W-00-5	54.69	44.51	143.21	26.93	35.05	8.468	14.338
C-95W-10-1	56.03	44.81	150.14	28.26	38.52	8.355	13.717
C-95W-10-2	56.41	45.20	151.53	28.64	39.24	8.274	13.575
C-95W-10-3	56.98	43.48	148.75	29.22	37.81	8.138	12.936
C-95W-10-4	56.22	45.46	146.52	28.45	36.69	8.038	14.113
C-95W-10-5	56.79	44.93	145.66	29.03	36.26	7.137	12.083
C-95W-25-1	57.17	49.13	150.59	29.42	38.76	8.248	14.292
C-95W-25-2	56.98	49.09	152.00	29.22	39.48	8.028	13.673
C-95W-25-3	57.74	48.70	152.48	30.01	39.73	7.948	12.326
C-95W-25-4	58.12	46.01	152.95	30.41	39.98	7.830	14.113
C-95W-25-5	57.17	48.02	153.44	29.42	40.24	8.375	13.532
C-95W-50-1	57.55	48.41	155.89	29.81	41.53	8.328	11.327
C-95W-50-2	57.93	48.45	157.90	30.21	42.61	7.844	12.262
C-95W-50-3	58.12	47.75	157.40	30.41	42.34	7.938	14.171
C-95W-50-4	58.31	48.45	159.46	30.61	43.46	8.182	13.674
C-95W-50-5	58.50	46.93	154.90	30.81	41.00	8.022	12.332

Table 5.46 RC/BE Test Results of Clay at w = 27% (ψ = 235 kPa)

Specimen	f_r (Hz)	V_{rms} (mV)	V_s (m/s)	$G_{max(RC)}$ (MPa)	$G_{max(BE)}$ (MPa)	$D_{min(RC)}$ (%)	$D_{min(BE)}$ (%)
C-90W-00-1	48.04	58.28	130.45	20.77	29.08	8.476	15.039
C-90W-00-2	47.85	57.88	131.89	20.61	29.73	8.932	14.233
C-90W-00-3	47.47	58.01	133.74	20.28	30.57	8.827	14.518
C-90W-00-4	48.23	58.68	132.26	20.94	29.89	8.563	13.673
C-90W-00-5	48.42	53.69	131.17	21.10	29.40	8.328	13.585
C-90W-10-1	51.46	56.57	143.21	23.84	35.05	8.178	13.224
C-90W-10-2	51.27	57.37	140.69	23.66	33.82	8.237	14.468
C-90W-10-3	52.03	55.98	139.05	24.37	33.04	8.133	12.857
C-90W-10-4	51.65	57.14	143.93	24.02	35.40	8.028	12.446
C-90W-10-5	50.89	57.54	139.46	23.32	33.24	8.273	11.783
C-90W-25-1	52.60	58.02	145.21	24.91	36.04	8.563	13.307
C-90W-25-2	52.79	58.79	143.93	25.09	35.40	8.521	12.773
C-90W-25-3	52.98	58.72	144.79	25.27	35.83	8.216	14.178
C-90W-25-4	53.17	57.44	146.09	25.45	36.47	8.372	12.392
C-90W-25-5	52.79	58.63	146.52	25.09	36.69	8.437	11.216
C-90W-50-1	53.55	59.59	152.48	25.82	39.73	8.482	13.637
C-90W-50-2	53.74	58.48	150.14	26.00	38.52	8.127	12.833
C-90W-50-3	53.93	60.67	149.21	26.19	38.05	8.237	11.481
C-90W-50-4	54.50	59.37	150.59	26.74	38.76	8.173	12.562
C-90W-50-5	54.69	58.92	148.31	26.93	37.59	8.236	13.121

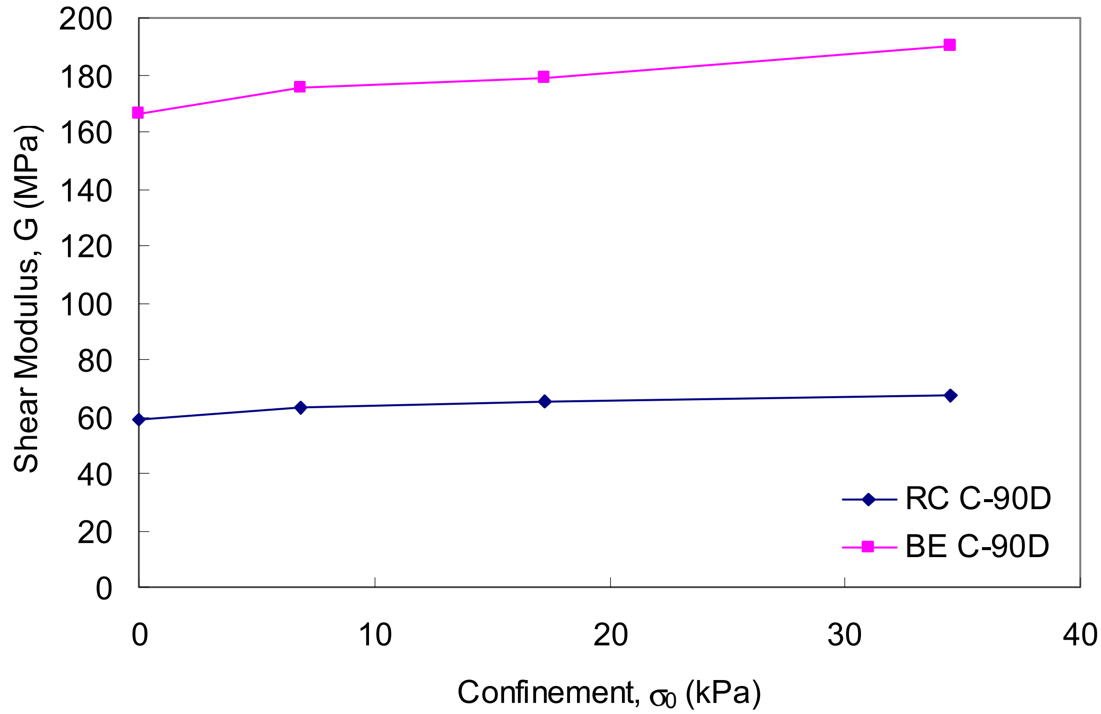

Figure 5.38 Variation of Shear Modulus with Confinement for Clay w=13% (RC/BE)

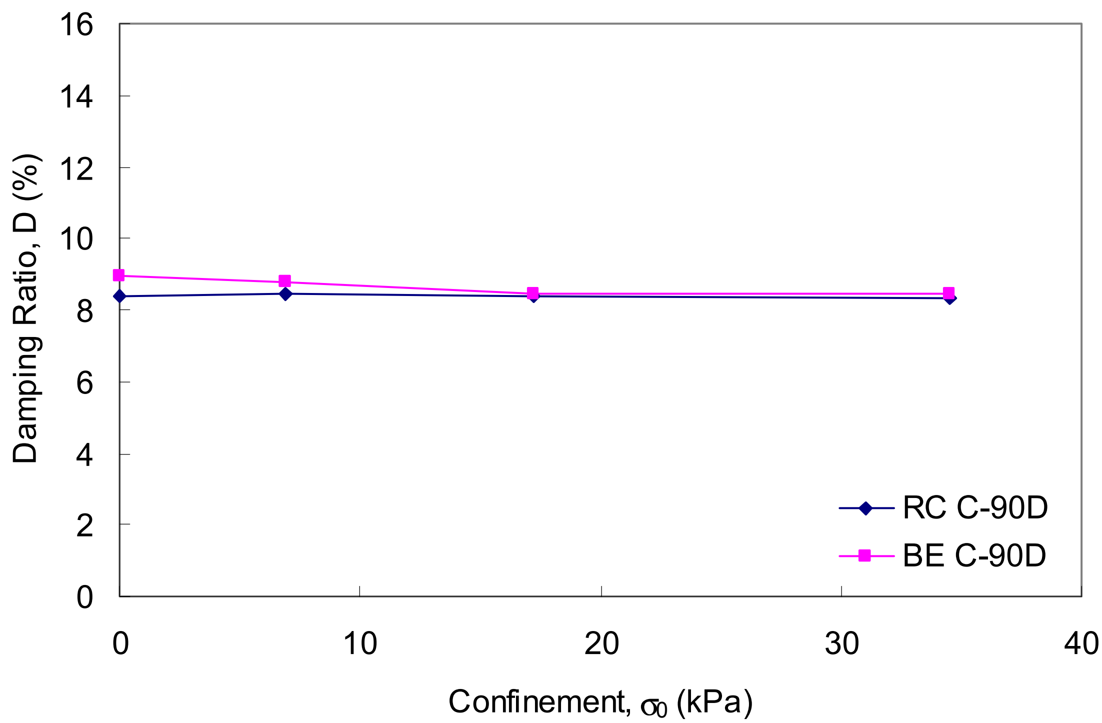

Figure 5.39 Variation of Damping Ratio with Confinement for Clay w=13% (RC/BE)

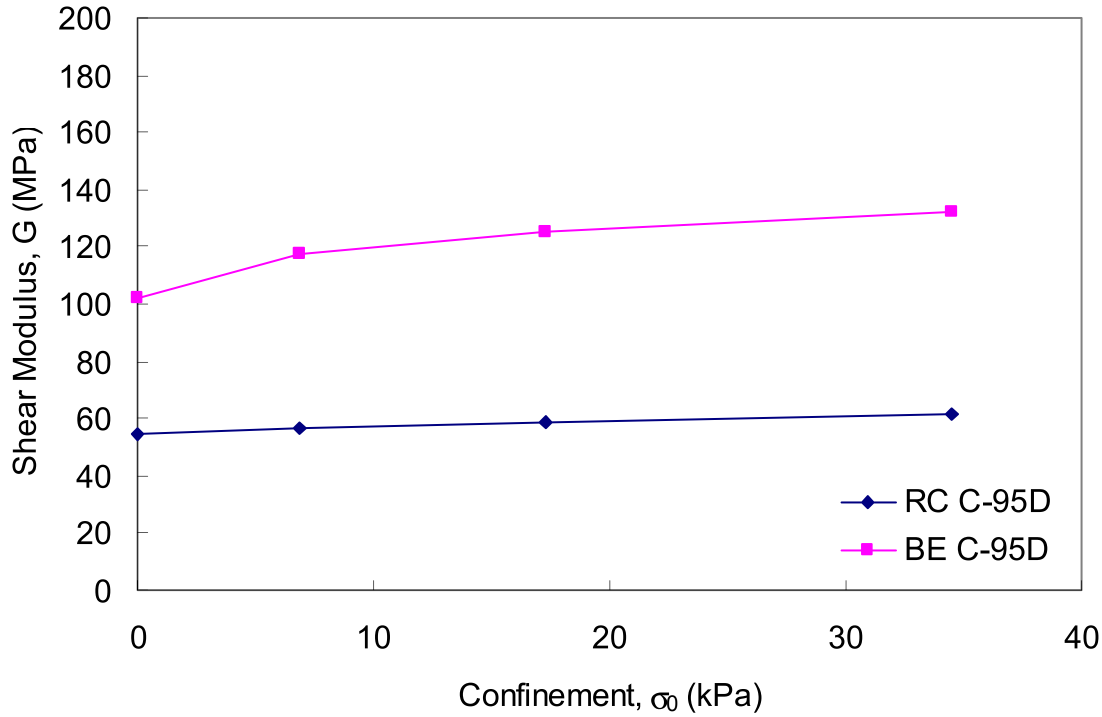

Figure 5.40 Variation of Shear Modulus with Confinement for Clay w=17% (RC/BE)

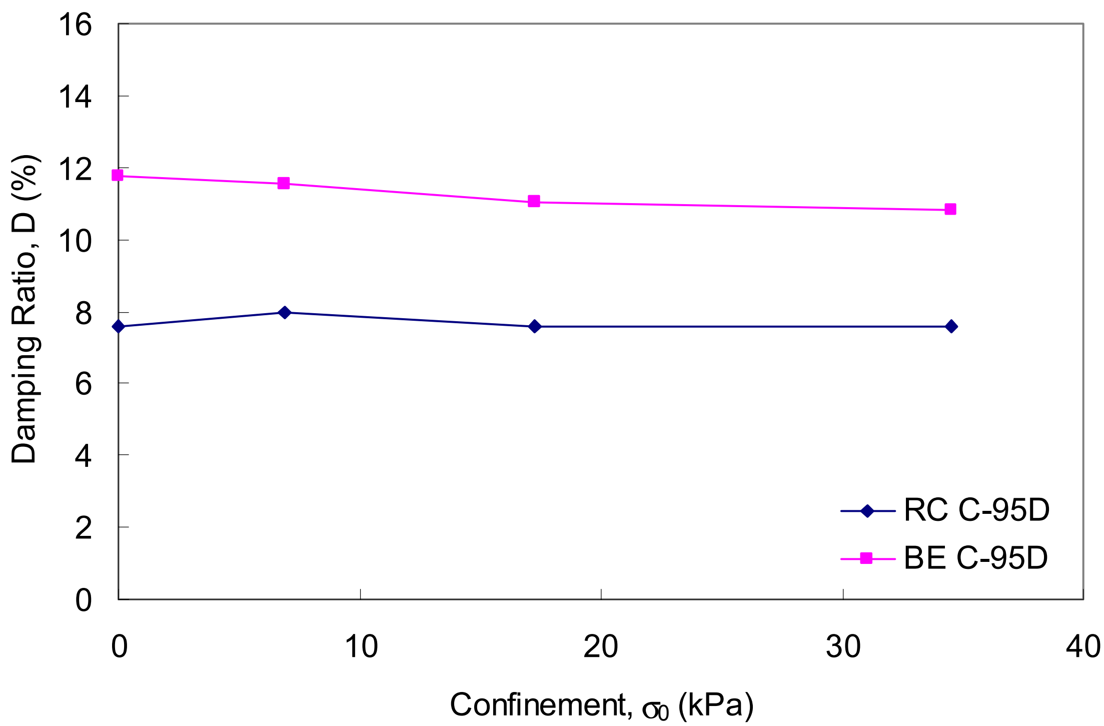

Figure 5.41 Variation of Damping Ratio with Confinement for Clay w=17% (RC/BE)

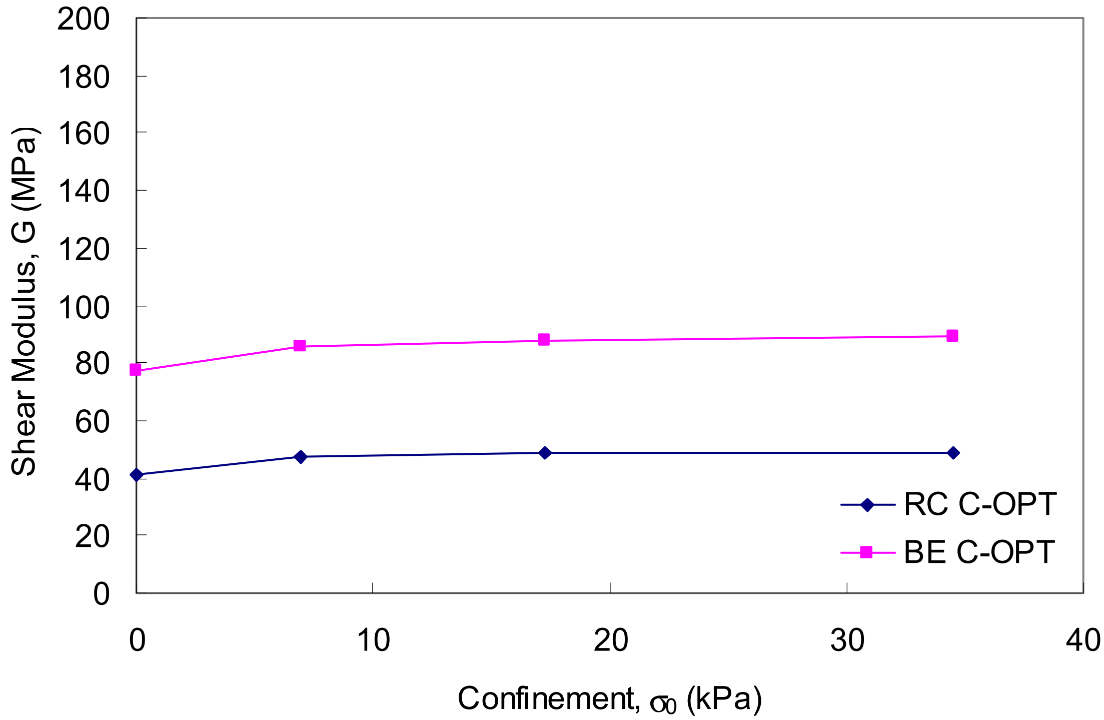

Figure 5.42 Variation of Shear Modulus with Confinement for Clay w=20% (RC/BE)

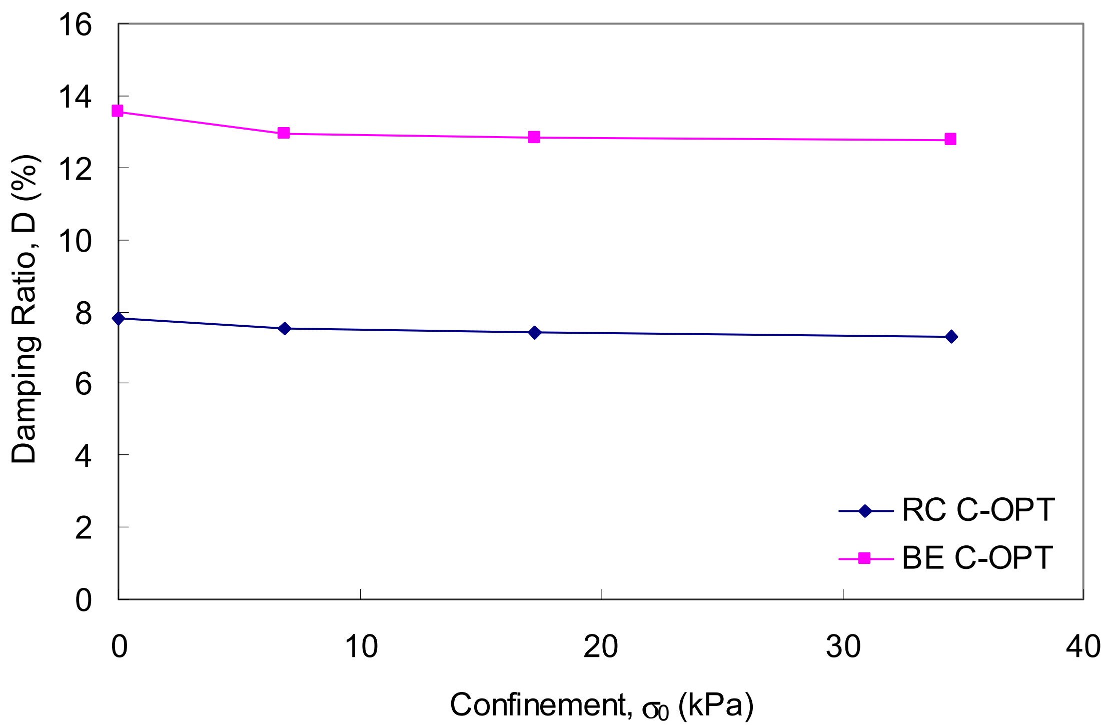

Figure 5.43 Variation of Damping Ratio with Confinement for Clay w=20% (RC/BE)

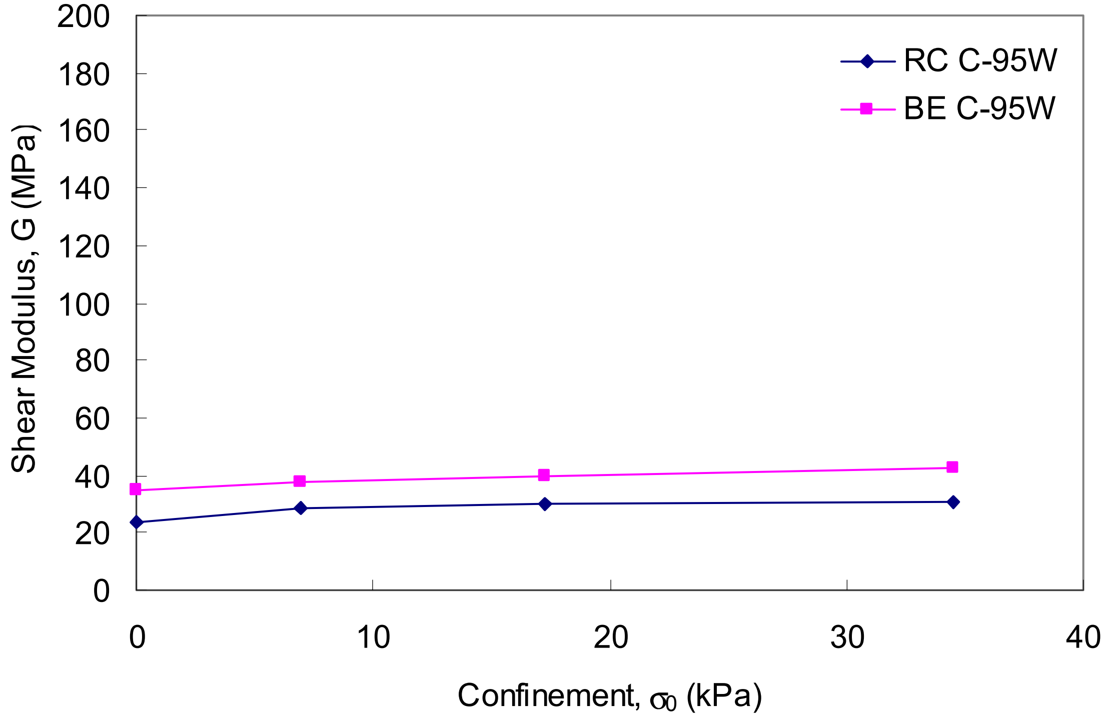

Figure 5.44 Variation of Shear Modulus with Confinement for Clay w=23% (RC/BE)

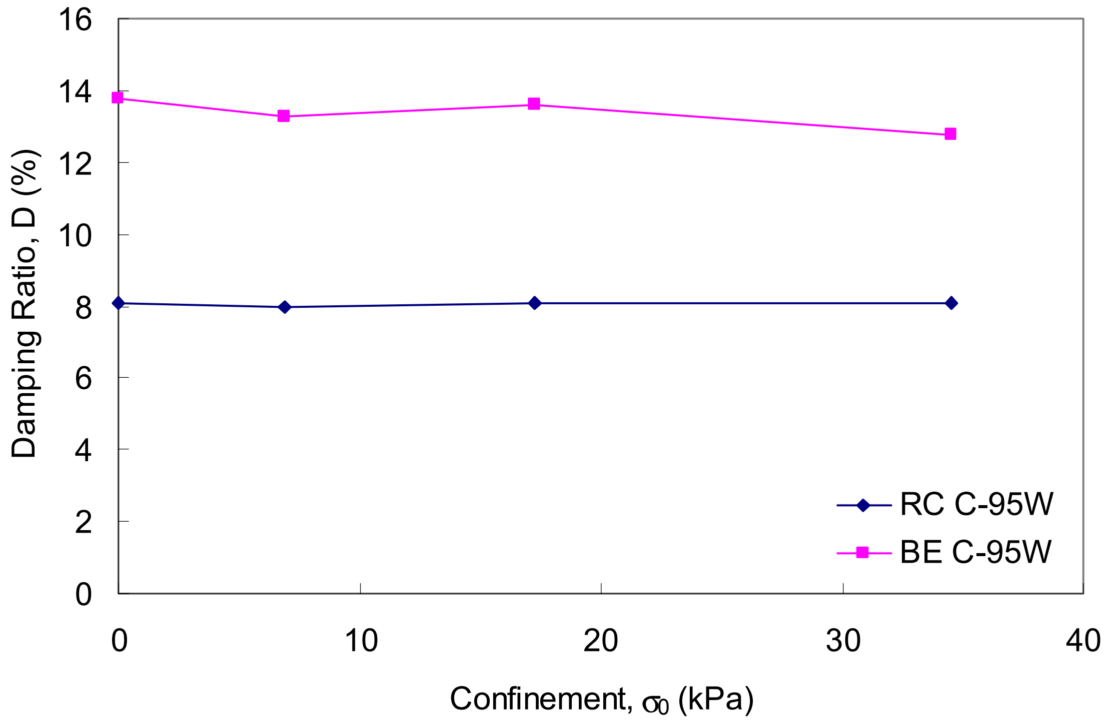

Figure 5.45 Variation of Damping Ratio with Confinement for Clay w=23% (RC/BE)

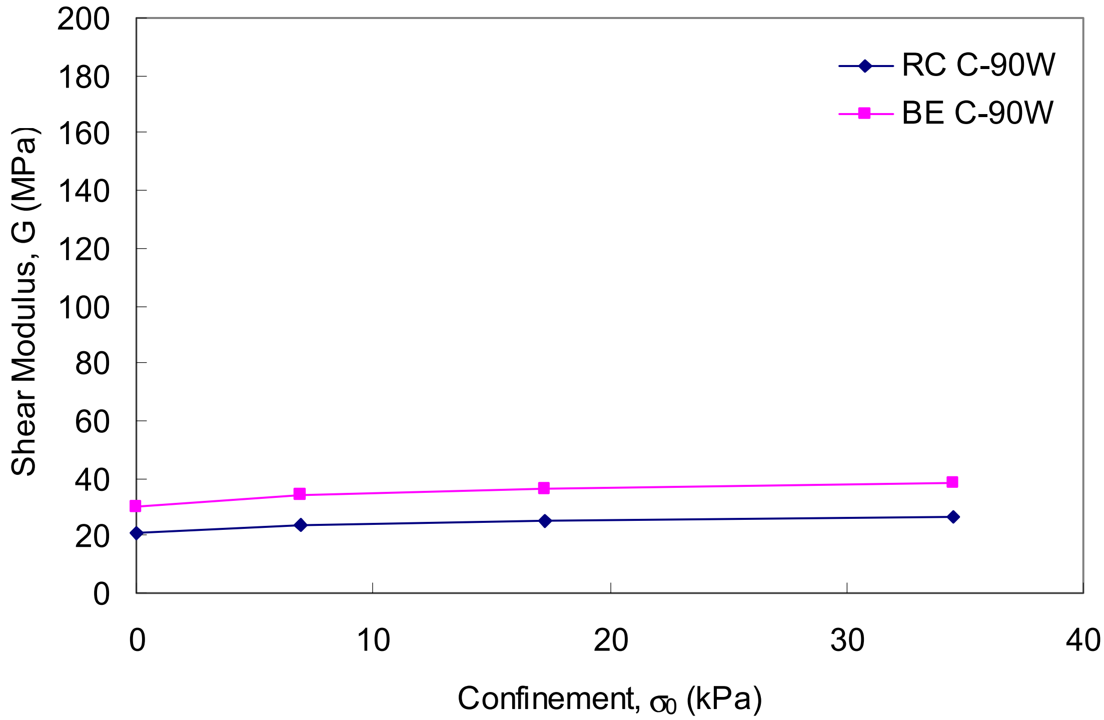

Figure 5.46 Variation of Shear Modulus with Confinement for Clay w=27% (RC/BE)

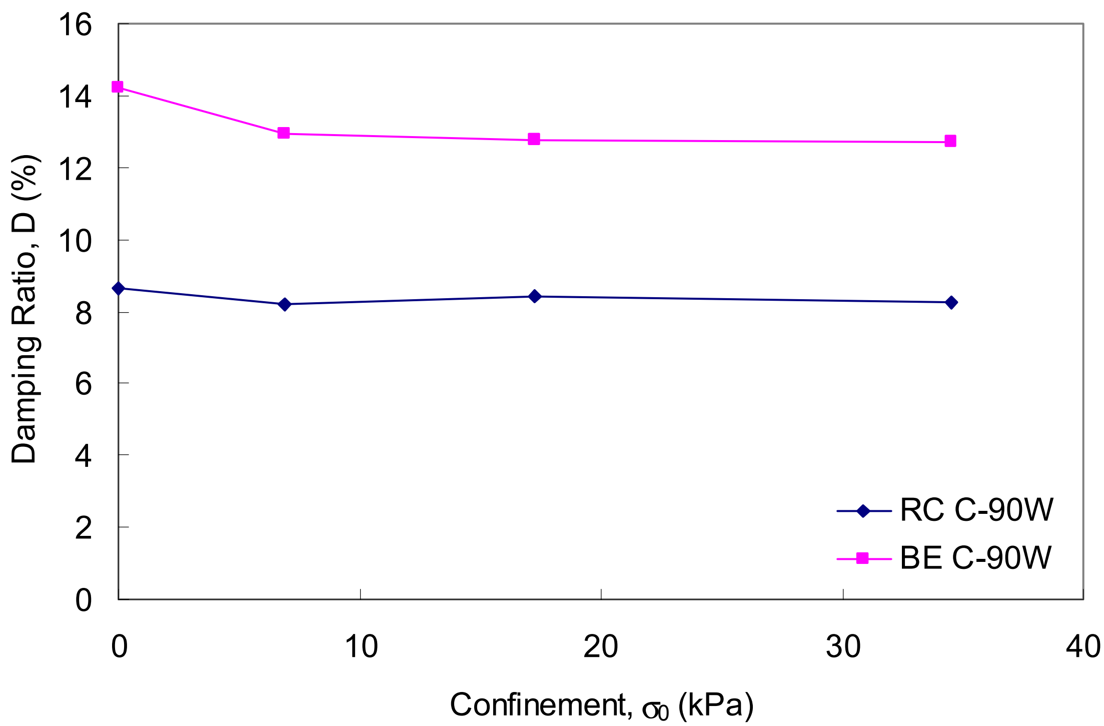

Figure 5.47 Variation of Damping Ratio with Confinement for Clay w=27% (RC/BE)

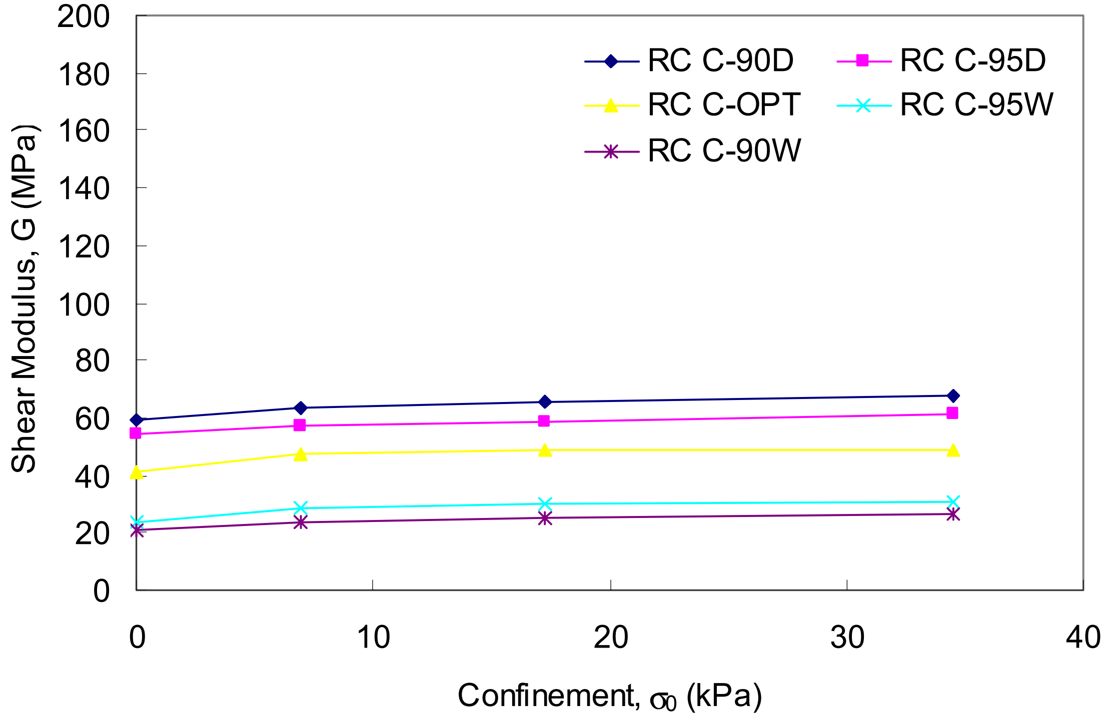

Figure 5.48 Variation of G_{max} with Confinement Using RC Method for Clay (RC/BE)

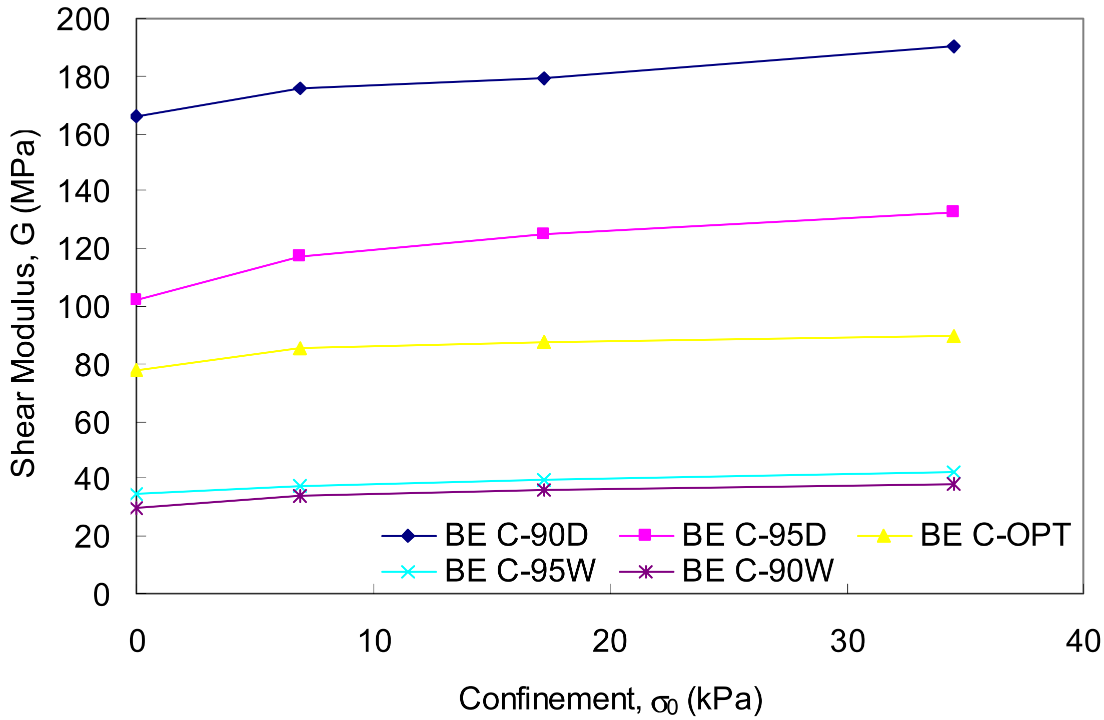

Figure 5.49 Variation of G_{max} with Confinement Using BE Method for Clay (RC/BE)

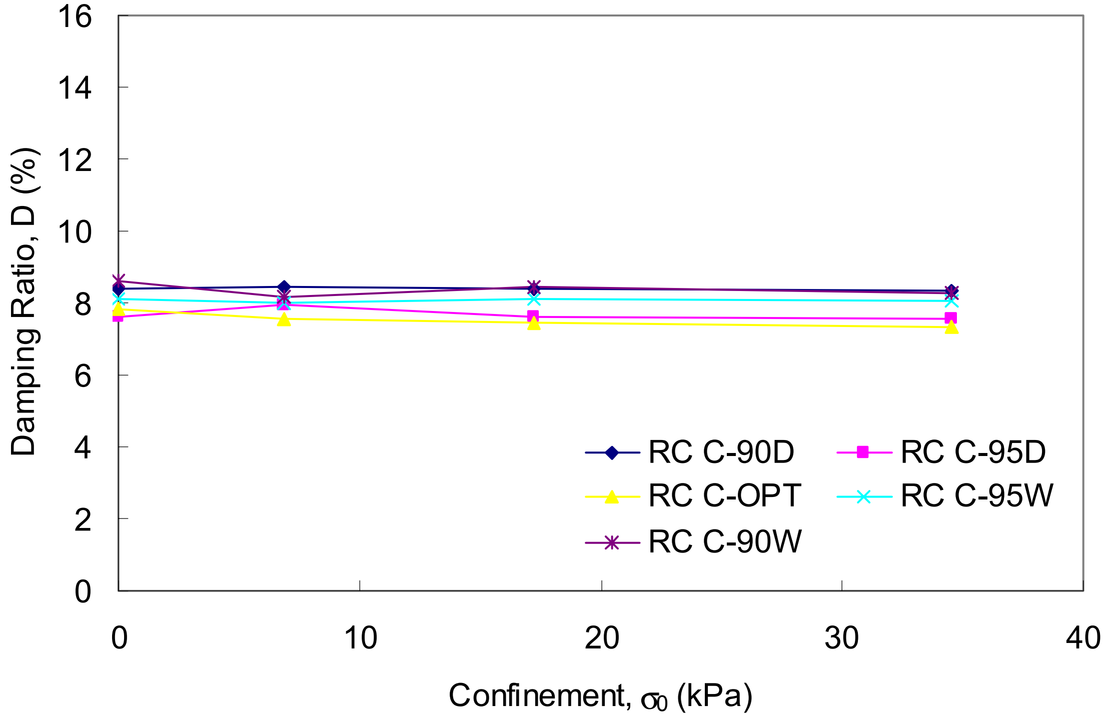

Figure 5.50 Variation of D_{min} with Confinement Using RC Method for Clay (RC/BE)

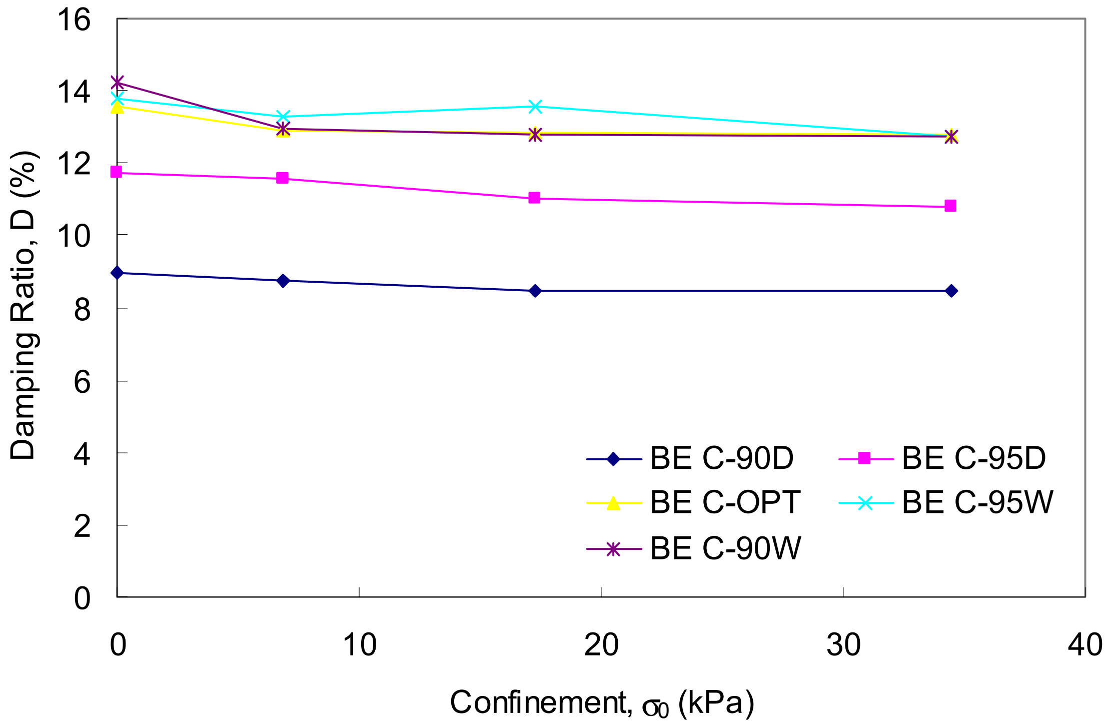

Figure 5.51 Variation of D_{min} with Confinement Using BE Method for Clay (RC/BE)

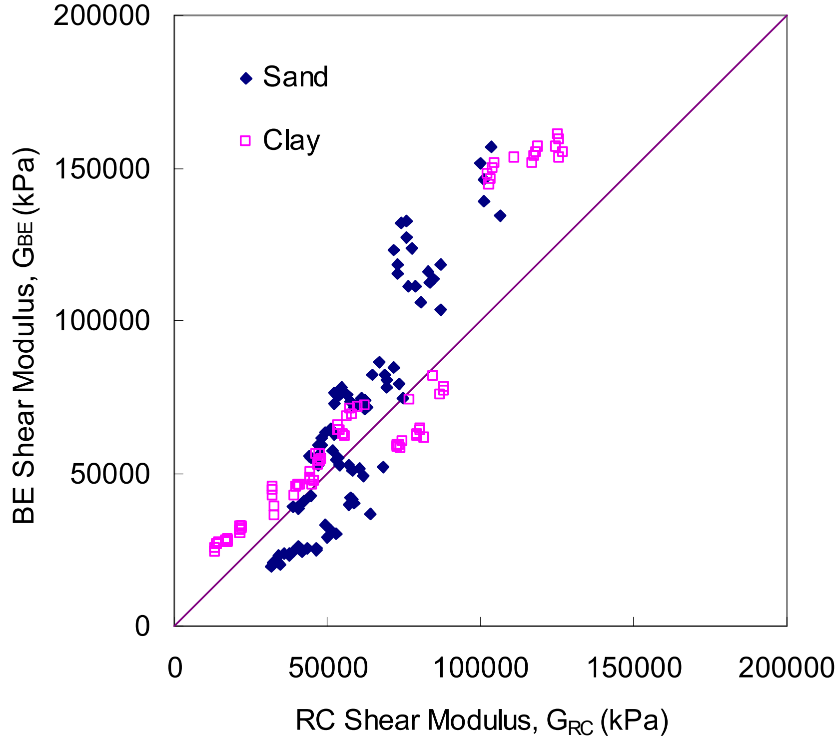

Figure 5.52 Variation of Shear Modulus from RC and TX/BE

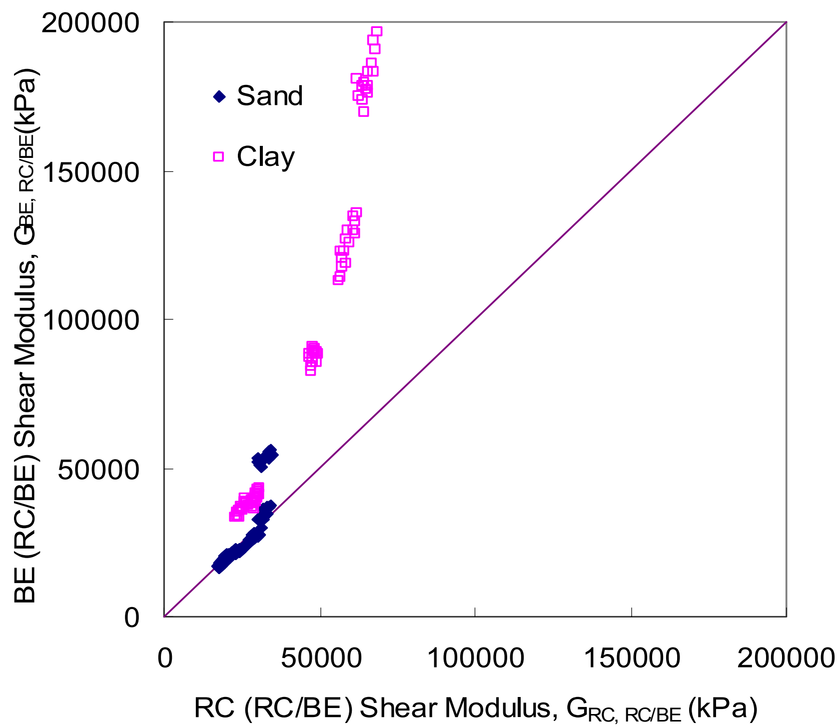

Figure 5.53 Variation of Shear Modulus of RC and BE from RC/BE

5.8 Assessment of Vertical Strain-Induced Suction Loss and Menisci Regeneration Patterns

5.8.1 Sand

A series of bender element (TX/BE) tests were conducted on several specimens of sand compacted at six moisture contents, 0%, 5%, 10%, 15%, 20%, and 24% in order to determine relationships between small-strain shear modulus (G_{max}) with elapse time at different low vertical strain. Specimen was tested at the confining pressure of 2.5-psi (17.25 kPa) at three strain levels (ε_v = 0%, 2%, and 4%). Then, shear modulus (G) was determined with elapse time of 24-h for each strain level.

Tables 5.47 through 5.52 demonstrate the results of small-strain shear modulus (G_{max}) of specimens with elapse time tested under the same confining pressure of 2.5-psi (17.25 kPa).

Figure 5.54 shows the variation of small-strain shear modulus (G_{max}) for sand at six moisture contents with elapse time. It can be seen that G_{max} tents to increases with elapse time at 0% strain, then G_{max} decreases with elapse time after applied 2% and 4% strain. This can be explained by the fact that the soil suction has been destroyed during applying the strain and cannot be regenerated with elapse time. Moreover, the small-strain shear modulus (G_{max}) increases immediately after applied the vertical displacement because the specimen was consolidated and hence the stiffer it becomes.

It can be observed from these figures that the specimen prepared at 0% moisture content give the highest values of G_{max} at any strain level when compared to any other specimen. Also, it can be noted that the shear modulus (G_{max}) decreases with the amount of moisture content. In other words, the shear modulus (G_{max}) increases with matric suction (ψ).

Table 5.47 Strain-dependent BE Results of Sand at w = 0% ($\psi \rightarrow \infty$)

Vertical strain (%)	Elapse time (hr)	V_s (m/s)	Load* (kgf)	Displacement (mm)	G_{max} (MPa)
0	0	248.96	0	0	105.92
	1	250.22			107.00
	2	250.22			107.00
	4	250.22			107.00
	6	250.22			107.00
	8	250.22			107.00
	12	250.22			107.00
	16	250.22			107.00
	20	250.22			107.00
	24	250.22			107.00
2	24	371.82	88.1	5.74	236.26
	25	371.82			236.26
	26	371.82			236.26
	28	368.84			232.48
	30	365.99			228.92
	32	363.10			225.31
	36	360.35			221.90
	40	352.24			212.03
	44	349.56			208.81
	48	347.00			205.78
4	48	460.48	195.37	11.48	362.37
	49	458.08			358.61
	50	455.71			354.90
	52	453.52			351.50
	54	451.20			347.90
	56	446.77			341.11
	60	440.21			331.17
	64	431.72			318.52
	68	429.61			315.41
	72	429.61			315.41

*Axial Load (σ_h = constant = 2.5 psi)

Table 5.48 Strain-dependent BE Results of Sand at w = 5% (ψ = 112 kPa)

Vertical strain (%)	Elapse time (hr)	V_s (m/s)	Load (kgf)	Displacement (mm)	G_{max} (MPa)
0	0	214.47	0	0	78.60
	1	214.47			78.60
	2	214.47			78.60
	4	214.47			78.60
	6	214.47			78.60
	8	214.47			78.60
	12	214.95			78.96
	16	214.95			78.96
	20	215.43			79.31
	24	215.43			79.31
2	24	354.87	70.34	5.74	215.21
	25	354.87			215.21
	26	353.59			213.67
	28	352.24			212.03
	30	349.56			208.81
	32	345.70			204.23
	36	341.92			199.79
	40	339.48			196.95
	44	339.48			196.95
	48	339.48			196.95
4	48	455.71	141.43	11.48	354.90
	49	455.71			354.90
	50	453.52			351.50
	52	451.20			347.90
	54	451.20			347.90
	56	451.20			347.90
	60	448.13			343.20
	64	448.13			343.20
	68	448.13			343.20
	72	448.89			344.36

*σ_h = constant = 2.5 psi

Table 5.49 Strain-dependent BE Results of Sand at w = 10% (ψ = 68.7 kPa)

Vertical strain (%)	Elapse time (hr)	V_s (m/s)	Load (kgf)	Displacement (mm)	G_{max} (MPa)
0	0	207.64	0	0	73.68
	1	207.64			73.68
	2	207.64			73.68
	4	207.64			73.68
	6	208.51			74.30
	8	208.51			74.30
	12	209.43			74.95
	16	210.32			75.59
	20	211.22			76.24
	24	211.22			76.24
2	24	323.08	38.79	5.74	178.38
	25	323.08			178.38
	26	323.08			178.38
	28	320.82			175.89
	30	318.67			173.54
	32	316.54			171.24
	36	312.31			166.69
	40	308.19			162.32
	44	306.13			160.16
	48	306.13			160.16
4	48	365.00	76.83	11.48	227.67
	49	365.00			227.67
	50	365.00			227.67
	52	362.00			223.94
	54	359.14			220.42
	56	356.33			216.99
	60	353.47			213.51
	64	347.97			206.92
	68	342.73			200.74
	72	337.56			194.73

*σ_h = constant = 2.5 psi

Table 5.50 Strain-dependent BE Results of Sand at w = 15% (ψ = 42.5 kPa)

Vertical strain (%)	Elapse time (hr)	V_s (m/s)	Load (kgf)	Displacement (mm)	G_{max} (MPa)
0	0	204.15	0	0	71.23
	1	204.15			71.23
	2	204.15			71.23
	4	203.32			70.64
	6	202.45			70.05
	8	200.78			68.89
	12	199.17			67.79
	16	195.96			65.62
	20	194.39			64.58
	24	192.10			63.07
2	24	290.08	49.63	5.74	143.80
	25	290.08			143.80
	26	290.08			143.80
	28	289.17			142.90
	30	289.17			142.90
	32	287.36			141.12
	36	285.63			139.42
	40	283.92			137.76
	44	283.92			137.76
	48	282.18			136.08
4	48	307.45	77.46	11.48	161.54
	49	307.45			161.54
	50	305.39			159.38
	52	303.35			157.26
	54	301.28			155.12
	56	297.28			151.02
	60	293.44			147.16
	64	289.64			143.37
	68	285.94			139.73
	72	282.34			136.23

*σ_h = constant = 2.5 psi

Table 5.51 Strain-dependent BE Results of Sand at w = 20% (ψ = 7.04 kPa)

Vertical strain (%)	Elapse time (hr)	V_s (m/s)	Load (kgf)	Displacement (mm)	G_{max} (MPa)
0	0	198.67	0	0	67.452
	1	198.67			67.452
	2	198.67			67.452
	4	198.67			67.452
	6	199.47			67.997
	8	200.30			68.568
	12	201.12			69.126
	16	202.79			70.284
	20	203.63			70.864
	24	203.63			70.864
2	24	265.23	56.17	5.74	120.22
	25	265.23			120.22
	26	262.30			117.58
	28	259.39			114.98
	30	255.16			111.26
	32	252.40			108.87
	36	252.91			109.31
	40	244.39			102.07
	44	241.94			100.03
	48	240.71			99.02
4	48	272.71	75.85	11.48	127.10
	49	272.71			127.10
	50	271.93			126.37
	52	270.26			124.82
	54	266.28			121.17
	56	260.86			116.29
	60	257.85			113.62
	64	253.49			109.82
	68	251.37			107.98
	72	248.58			105.60

*σ_h = constant = 2.5 psi

Table 5.52 Strain-dependent BE Results of Sand at w = 24% (ψ = 0.64 kPa)

Vertical strain (%)	Elapse time (hr)	V_s (m/s)	Load (kgf)	Displacement (mm)	G_{max} (MPa)
0	0	149.12	0	0	38.00
	1	149.12			38.00
	2	149.12			38.00
	4	149.12			38.00
	6	149.57			38.23
	8	150.04			38.47
	12	150.50			38.71
	16	151.44			39.19
	20	151.90			39.43
	24	151.90			39.43
2	24	168.12	36.47	5.74	48.30
	25	168.12			48.30
	26	166.94			47.63
	28	165.76			46.95
	30	164.02			45.97
	32	162.88			45.34
	36	163.09			45.45
	40	159.50			43.48
	44	158.45			42.91
	48	157.93			42.62
4	48	168.37	55.65	11.48	48.45
	49	168.37			48.45
	50	168.07			48.27
	52	167.43			47.91
	54	165.90			47.03
	56	163.78			45.84
	60	162.59			45.17
	64	160.84			44.21
	68	159.99			43.74
	72	158.85			43.12

*σ_h = constant = 2.5 psi

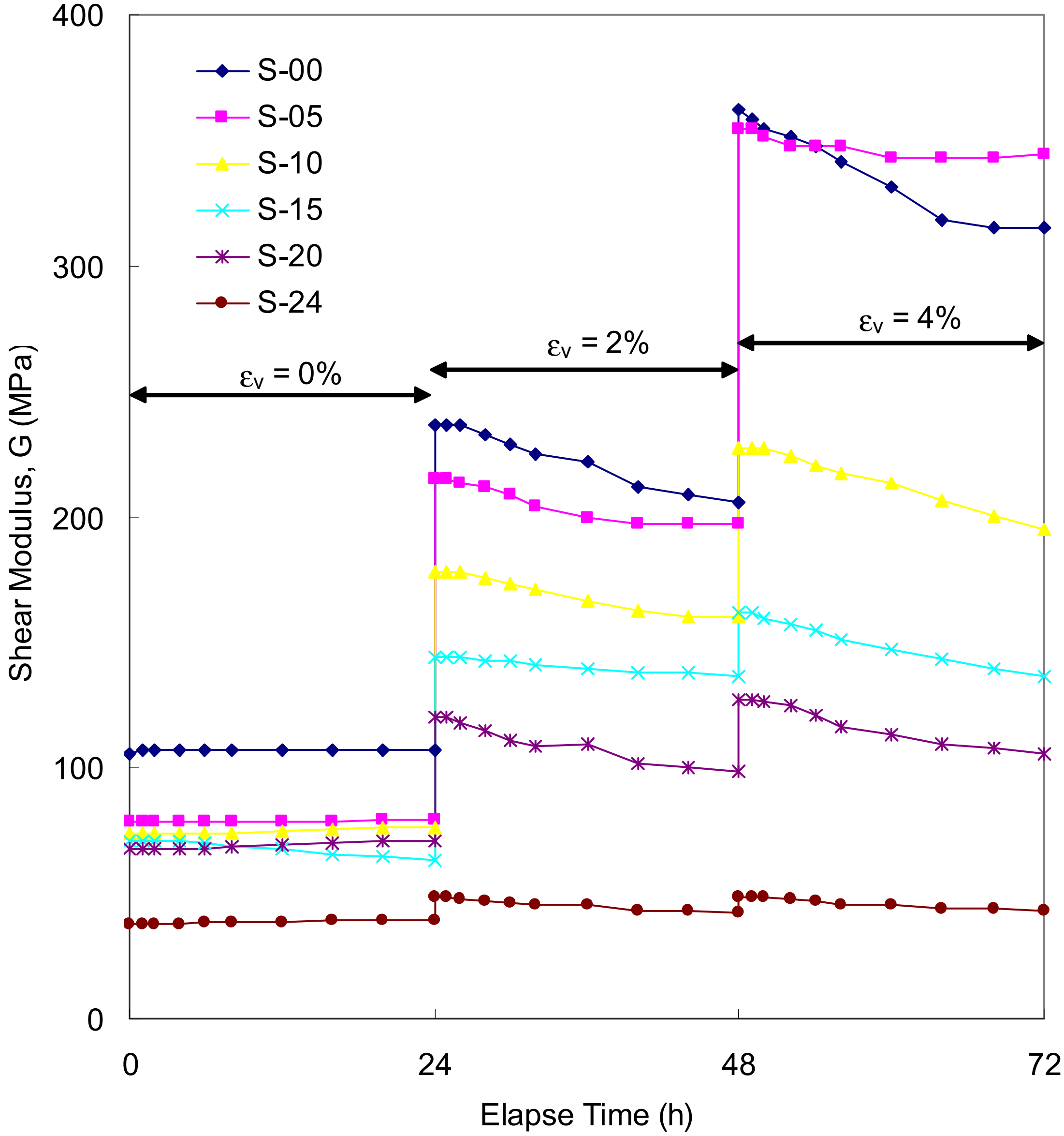

Figure 5.54 Time Variation in Shear Modulus of Sand
at Different Vertical Strain Levels

5.8.2 Clay

A series of bender element (TX/BE) tests were conducted on several specimens of clay compacted at 90% dry, 95% dry, optimum, 95% wet, and 90% wet of $\gamma_{d\text{-}max}$ (13%, 17%, 20%, 23%, and 27% moisture contents, respectively) in order to determine relationships between small-strain shear modulus (G_{max}) with elapse time at different low vertical strain. Specimen was tested at the confining pressure of 2.5-psi (17.25 kPa) at three strain levels (ε_v = 0%, 2%, and 4%). Then, shear modulus (G_{max}) was determined with elapse time of 24-h for each strain level.

Tables 5.53 through 5.57 demonstrate the results of small-strain shear modulus (G_{max}) of specimens with elapse time tested under the same confining pressure of 2.5-psi (17.25 kPa).

Figure 5.55 shows the variation of small-strain shear modulus (G_{max}) for clay at five moisture contents with elapse time. It can be seen that G_{max} increases with elapse time at 0% strain, then G_{max} decreases with elapse time after applied 2% and 4% strain. This can be explained by the fact that the soil suction has been destroyed during applying the strain and cannot be regenerated with elapse time. The small-strain shear modulus (G_{max}) decreases immediately after applied the vertical displacement because the clay specimen was destructed the shear strength and hence it becomes failure.

It can be observed from these figures that the specimen prepared at 13% moisture content still give the highest values of G_{max} at any strain level when compared to any other specimen. Moreover, it can be noted that the shear modulus (G_{max}) decreases with the amount of moisture content. In other words, the shear modulus G_{max} increases with matric suction (ψ).

Table 5.53 Strain-dependent BE Results of Clay at w = 13% (ψ = 2346 kPa)

Vertical strain (%)	Elapse time (hr)	V_s (m/s)	Load (kgf)	Displacement (mm)	G_{max} (MPa)
0	0	314.83	0	0	169.39
	1	314.83			169.39
	2	314.83			169.39
	4	314.83			169.39
	6	314.83			169.39
	8	314.83			169.39
	12	316.85			171.56
	16	316.85			171.56
	20	318.89			173.78
	24	318.89			173.78
2	24	323.08	132.77	5.74	178.38
	25	323.08			178.38
	26	323.08			178.38
	28	320.82			175.89
	30	316.54			171.24
	32	316.54			171.24
	36	316.54			171.24
	40	316.54			171.24
	44	316.54			171.24
	48	316.54			171.24
4	48	285.94	134.92	11.48	139.73
	49	284.10			137.93
	50	282.34			136.23
	52	280.60			134.55
	54	278.82			132.85
	56	277.12			131.24
	60	273.73			128.05
	64	272.09			126.52
	68	272.09			126.52
	72	270.42			124.97

*σ_h = constant = 2.5 psi

Table 5.54 Strain-dependent BE Results of Clay at w = 17% (ψ = 1380 kPa)

Vertical strain (%)	Elapse time (hr)	V_s (m/s)	Load (kgf)	Displacement (mm)	G_{max} (MPa)
0	0	281.43	0	0	135.35
	1	281.43			135.35
	2	281.43			135.35
	4	281.43			135.35
	6	283.04			136.90
	8	286.37			140.15
	12	288.04			141.78
	16	289.78			143.51
	20	291.49			145.20
	24	291.49			145.20
2	24	277.85	103.22	5.74	131.94
	25	277.85			131.94
	26	276.18			130.35
	28	276.18			130.35
	30	274.59			128.85
	32	274.59			128.85
	36	272.95			127.32
	40	271.39			125.87
	44	269.85			124.45
	48	269.85			124.45
4	48	264.04	121.43	11.48	119.14
	49	264.04			119.14
	50	262.52			117.77
	52	261.01			116.43
	54	261.01			116.43
	56	259.47			115.06
	60	261.58			116.93
	64	260.09			115.60
	68	257.10			112.96
	72	257.10			112.96

*σ_h = constant = 2.5 psi

Table 5.55 Strain-dependent BE Results of Clay at w = 20% (ψ = 953 kPa)

Vertical strain (%)	Elapse time (hr)	V_s (m/s)	Load (kgf)	Displacement (mm)	G_{max} (MPa)
0	0	258.19	0	0	113.92
	1	258.19			113.92
	2	259.54			115.12
	4	260.91			116.33
	6	262.34			117.61
	8	263.74			118.87
	12	266.63			121.49
	16	268.12			122.86
	20	269.58			124.20
	24	269.58			124.20
2	24	267.65	80.47	5.74	122.42
	25	267.65			122.42
	26	266.15			121.06
	28	263.15			118.34
	30	260.22			115.72
	32	257.40			113.22
	36	253.24			109.59
	40	251.85			108.39
	44	250.52			107.25
	48	250.52			107.25
4	48	280.60	100.52	11.48	134.55
	49	278.82			132.85
	50	277.12			131.24
	52	275.39			129.60
	54	272.09			126.52
	56	270.42			124.97
	60	267.19			122.00
	64	265.63			120.59
	68	265.63			120.59
	72	264.04			119.14

*σ_h = constant = 2.5 psi

Table 5.56 Strain-dependent BE Results of Clay at w = 23% (ψ = 635 kPa)

Vertical strain (%)	Elapse time (hr)	V_s (m/s)	Load (kgf)	Displacement (mm)	G_{max} (MPa)
0	0	152.48	0	0	39.73
	1	152.95			39.98
	2	153.43			40.23
	4	154.90			41.00
	6	156.39			41.80
	8	159.44			43.45
	12	160.50			44.02
	16	161.56			44.61
	20	162.11			44.91
	24	162.64			45.21
2	24	139.83	47.91	5.74	33.41
	25	140.24			33.61
	26	141.06			34.00
	28	141.95			34.43
	30	143.25			35.07
	32	144.57			35.72
	36	145.47			36.16
	40	145.92			36.39
	44	146.38			36.62
	48	146.38			36.62
4	48	140.28	54.45	11.48	33.63
	49	140.28			33.63
	50	139.84			33.42
	52	139.32			33.17
	54	138.55			32.80
	56	137.69			32.40
	60	137.28			32.21
	64	136.85			32.01
	68	136.44			31.81
	72	136.44			31.81

*σ_h = constant = 2.5 psi

Table 5.57 Strain-dependent BE Results of Clay at w = 27% (ψ = 235 kPa)

Vertical strain (%)	Elapse time (hr)	V_s (m/s)	Load (kgf)	Displacement (mm)	G_{max} (MPa)
0	0	145.66	0	0	36.26
	1	145.66			36.26
	2	145.66			36.26
	4	145.66			36.26
	6	146.09			36.47
	8	146.09			36.47
	12	146.09			36.47
	16	146.52			36.69
	20	146.97			36.91
	24	146.97			36.91
2	24	141.95	27.54	5.74	34.43
	25	142.37			34.64
	26	142.80			34.85
	28	143.25			35.07
	30	144.13			35.50
	32	144.57			35.72
	36	145.47			36.16
	40	146.38			36.62
	44	147.31			37.08
	48	147.76			37.31
4	48	128.30	34.2	11.48	28.13
	49	129.05			28.46
	50	130.58			29.14
	52	131.76			29.67
	54	132.80			30.14
	56	134.00			30.69
	60	134.80			31.05
	64	135.20			31.24
	68	135.61			31.43
	72	135.61			31.43

*σ_h = constant = 2.5 psi

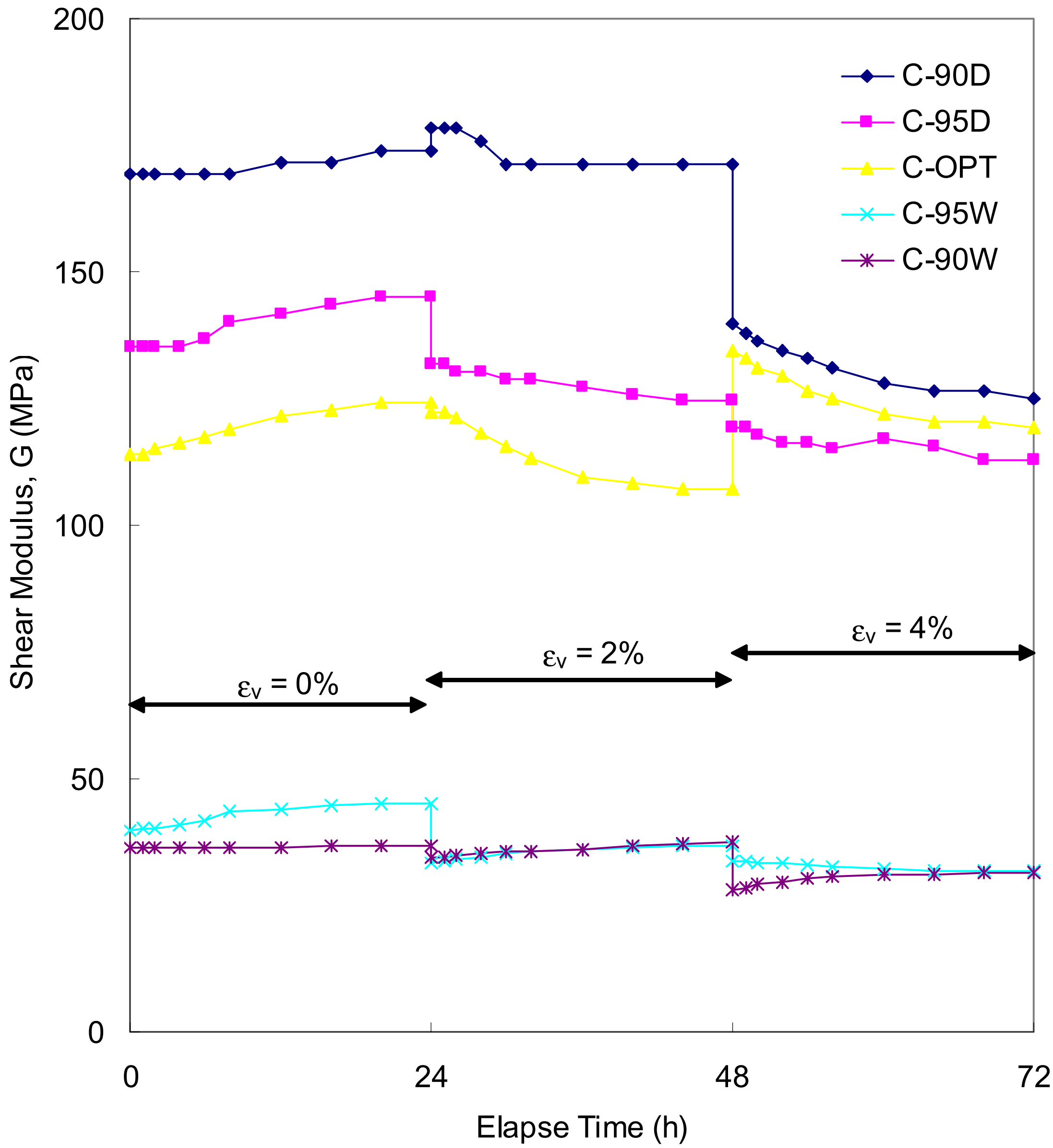

Figure 5.55 Time Variation in Shear Modulus of Clay at Different Vertical Strain Levels

5.9 Summary

This chapter presented the experimental program followed in this work and a comprehensive analysis of all PPE, RC, BE, and RC/BE test results, including effects of most relevant test variables on soil's shear modulus (G_{max}), material damping ratio (D_{min}) and soil water characteristic curve (SWCC). Chapter 6 presents the empirical models devised for prediction of shear modulus (G_{max}) and material damping ratio (D_{min}) with respect to confinement (σ_0), matric suction (ψ), and K_0 stress state, as well as the correction factor for interpreting the shear modulus and damping ratio from isotropic condition to any K_0 stress state condition.

CHAPTER 6

EMPIRICAL MODELS FOR SMALL-STRAIN STIFFNESS PROPERTIES

6.1 Introduction

This chapter presents the soil water characteristic curve (SWCC) function and the model for prediction of shear modulus (G) and material damping ratio (D) respected to confining pressure (σ_0), matric suction (ψ), and K_0 stress state on the present experimental results of poorly-graded sand (SP) and high plasticity clay (CH). Model constants obtained from these analyses are determined from different type of soil and test, based on the best-fit curve of shear modulus and damping ratio with respected to confining pressure, matric suction, and K_0 stress state. Predictions of these correlations are evaluated by comparing their predictions with the experimental results. Additionally, model of correction factor is created in order to predict the shear modulus and damping ratio at any K_0 stress state from isotropic confining pressure (K_0 = 1).

6.2 Soil-Water Characteristic Curve

A typical curve that describes the relationship between water content and pore water suction for silt is present in figure 6.1. Several defining parameters of the SWCC are shown, including air-entry suction head (ψ_a), residual water content (θ_r), and saturated water content (θ_s). Soils with larger particles sizes, including sands and silts, would develop a SWCC that plots to the left of the curve shown in figure 6.1, with a generally smaller air-entry suction head, smaller residual water content, and smaller value of the saturated water content compared with the curve in figure

6.1. Figure 6.2 also shows the typical of soil water characteristic curves for sandy soil, silty soil, and clayey soil.

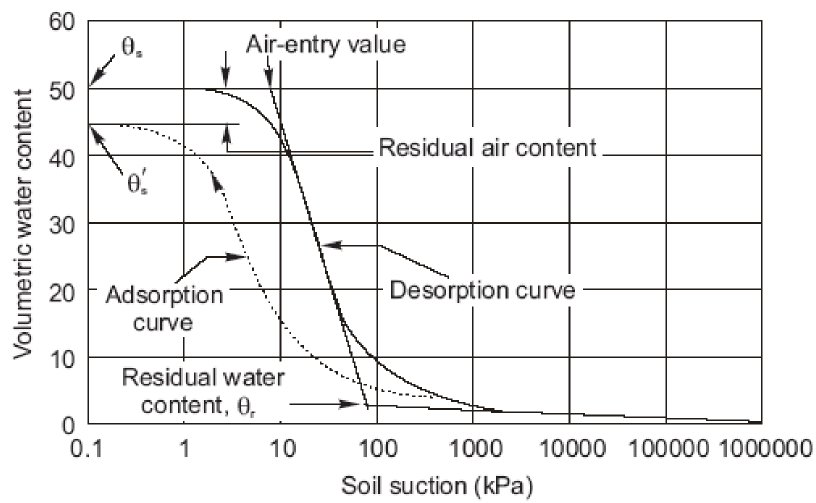

Figure 6.1 Typical SWCC for Silt with Adsorption and Desorption Curves (Fredlund and Xing, 1993)

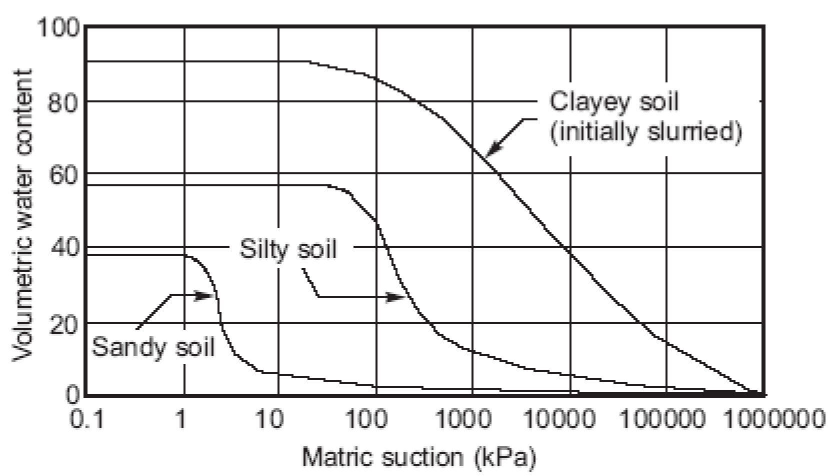

Figure 6.2 Typical SWCC for Sandy, Silty, and Clayey soil (Fredlund and Xing, 1993)

It is well known that the SWCC is hysteretic, with bounding curves defining the sorption (wetting) and desorption (drying) processes as shown in figure 6.1. However, standard practice is to determine only the desorption curve due to experimental difficulties associated with measurement of the sorption curve (Tinjum et al., 1997).

6.3 Soil-Water Characteristic Curve Models

Various equations have been proposed to represent SWCC. Commonly used models include the Brooks-Coreys, van Genuchtern, and Fredlund and Xing equations.

The Brooks-Corey (1964) model is

$$\frac{\theta_w - \theta_r}{\theta_s - \theta_r} = \left(\frac{\psi_a}{\psi}\right)^{\lambda} \tag{5.1}$$

where the optimized parameters are θ_r, ψ_a, and λ. λ = pore-size distribution index related to the slope of the curve.

The van Genuchten (1980) model is

$$\frac{\theta_w - \theta_r}{\theta_s - \theta_r} = \frac{1}{\left[1+\left(\frac{\psi}{\alpha}\right)^n\right]^m} \tag{5.2}$$

where the optimized parameters = θ_r, α, n, and m. Each of these parameters is described by Leong and Rahardjo (1997). The parameter α is the pivot point of the curve, and its value is the directly related to the value of the air-entry suction. As α increases, the air-entry suction also increases. The parameter n controls the slope of the SWCC about the pivot point, which occurs at a normalized volumetric water content (Θ) of 0.5, where $\Theta = (\theta_w - \theta_r)/(\theta_s - \theta_r)$. As n increases, the sloping portion of the curve between ψ_a and the knee (the point of inflection at the lower portion of the curve as it approaches a horizontal position) of the SWCC becomes steeper. The parameters m rotates the sloping portion of the curve. As m increases, the range of the curve between ψ_a and knee of the SWCC decreases. The stability of the curve-fitting process is improved by equating the parameter m to $1\text{-}n^{-1}$ (van Genuchten et al. 1991).

The Fredlund and Xing (1994) four parameter model is

$$\frac{\theta_w}{\theta_s} = \frac{1}{\left\{ \ln\left[e + \left(\frac{\psi}{a} \right)^b \right] \right\}^c} \tag{5.3}$$

where the optimized parameters = a, b, and c. the parameters a, b, and c of the Fredlund and Xing model are similar to the parameters α , n, and m in the van Genuchten model, respectively. Application of this model assumes that θ_r is small enough that it can be neglected. And, e = base of natural logarithm. This relationship was used in this study.

The unimodal soil water characteristic curve function was considered for use in this study because it commonly is used in simulating unsaturated liquid flow through porous media. The Fredlund and Xing (1994) model also was considered because it reportedly provides a better description of the soil water characteristic curve over a wide range of suctions (Leong and Rahardjo, 1997).

6.4 SWCC Results and Models

As the results of SWCC for sand and clay under constant K_0 condition from chapter 5, it can be noted that the confining pressure (σ_0) and K_0 stress state have no significant effects of the shape and the parameters of SWCC. Consequently, table 6.1 shows the optimized parameters a, b, and c of the Fredlund and Xing (1994) model for sand and clay in this experiment.

Table 6.1 Soil-Water Characteristic Curve Best-Fit Parameters

Soil	θ_s (%)	θ_r (%)	w_s (%)	w_r (%)	a	b	c	R^2
Sand	33.21	3.52	20.05	2.13	51.90	2.85	1.61	0.98
Clay	41.41	5.15	28.27	3.51	887	1.50	1.03	0.97

Figures 6.3 through 6.5 present the SWCC data and SWCC obtained and fit with the Fredlund and Xing model for sand and clay.

Table 6.2 shows the summary of relationship between matric suction and moisture content of all sand and clay specimens. Consequently, sandy and clayey soil specimens compacted at different moisture content can be determined the matric suction from SWCC fit with the Fredlund and Xing model (shown in table 6.1).

Table 6.2 Predicted Values of Matric Suction from Moisture Content

Soil Specimen	**Moisture Content, w (%)**	**Matric Suction (kPa)**
S-00	0	∞
S-05	5	111.99
S-10	10	68.72
S-15	15	42.50
S-20	20	7.04
S-24	24	0.64
C-90D	13	2346.01
C-95D	17	1379.65
C-OPT	20	953.24
C-95W	23	634.66
C-90W	27	234.74

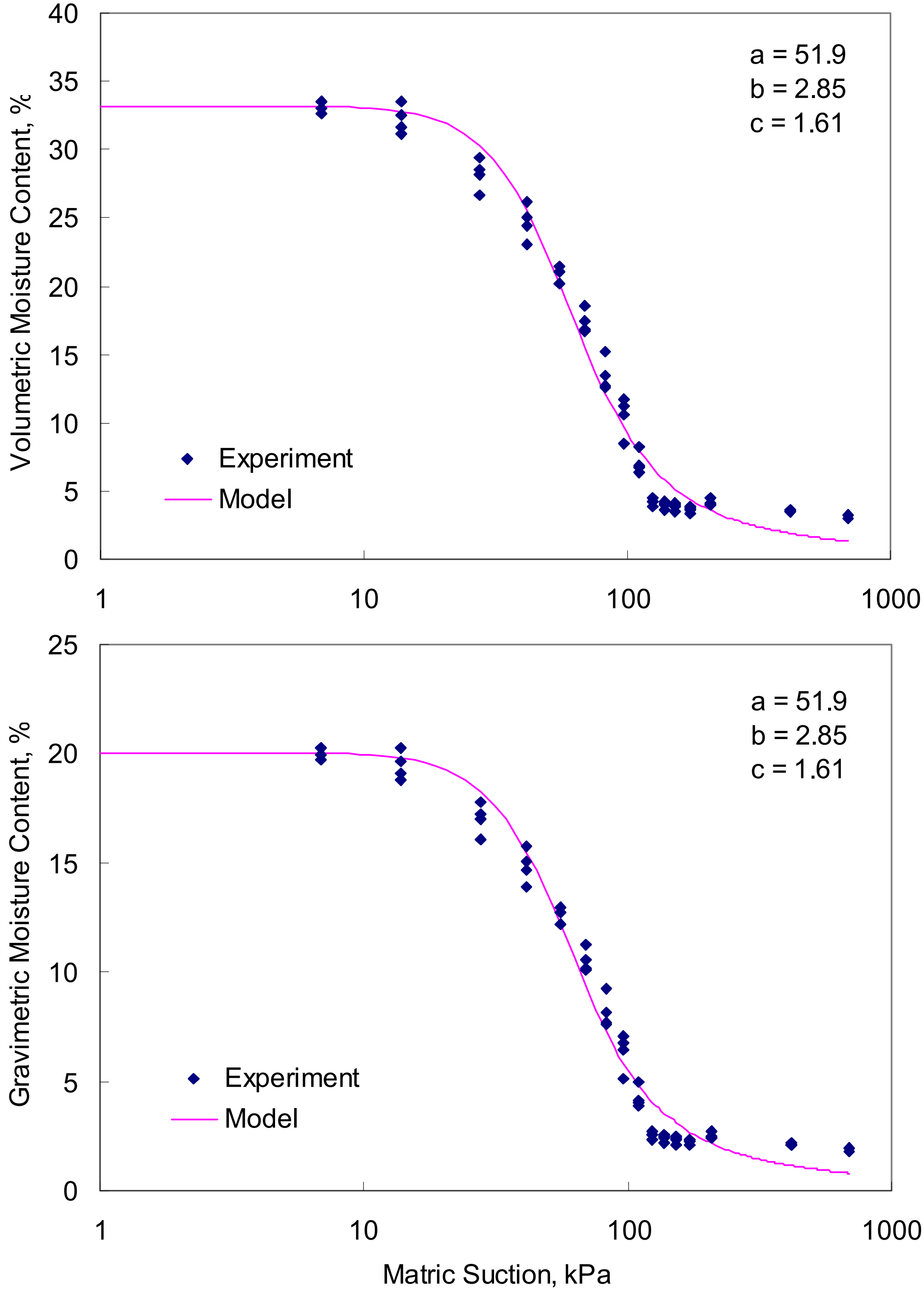

Figure 6.3 Experimental and Predicted SWCC for Sand

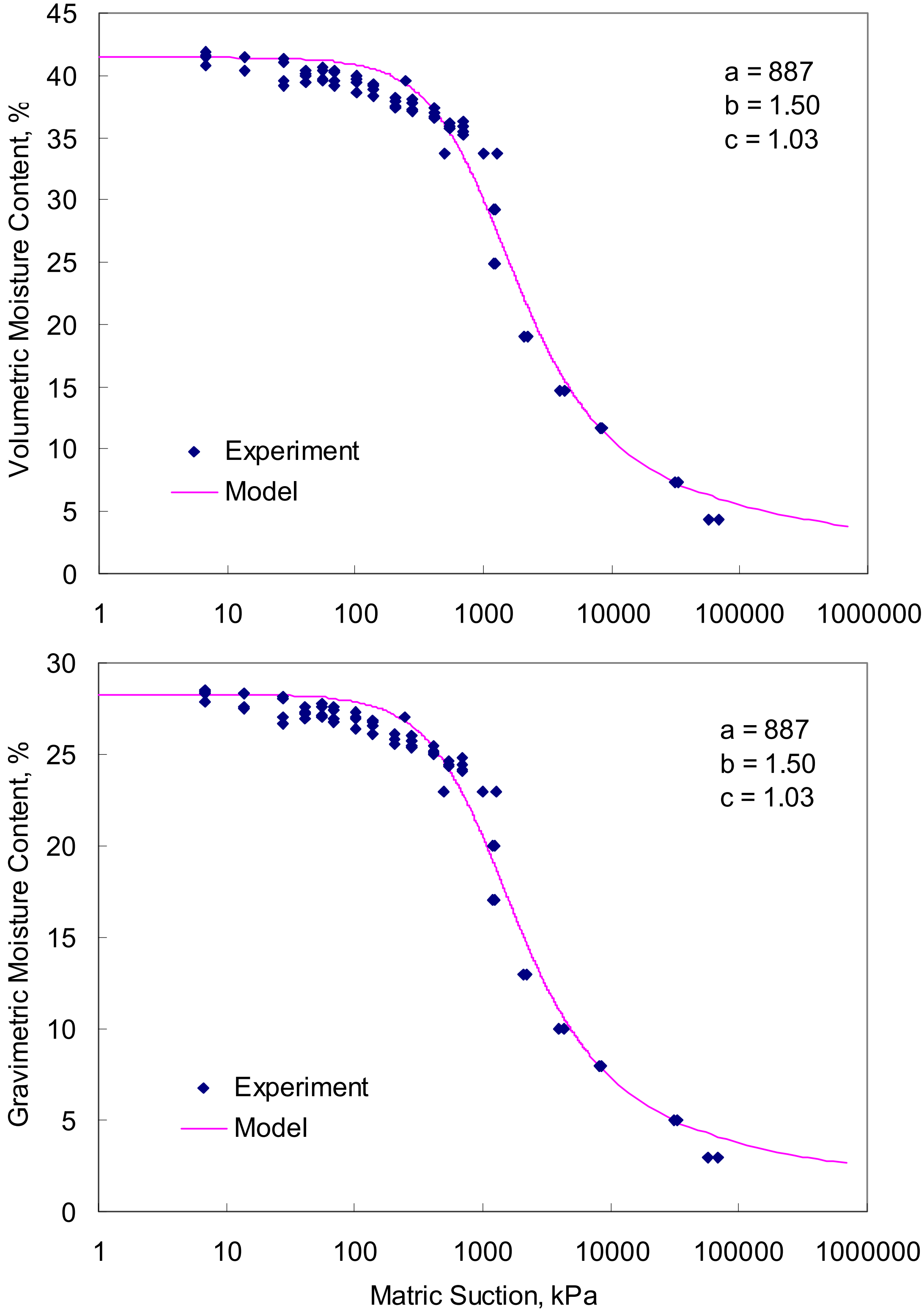

Figure 6.4 Experimental and Predicted SWCC for Clay

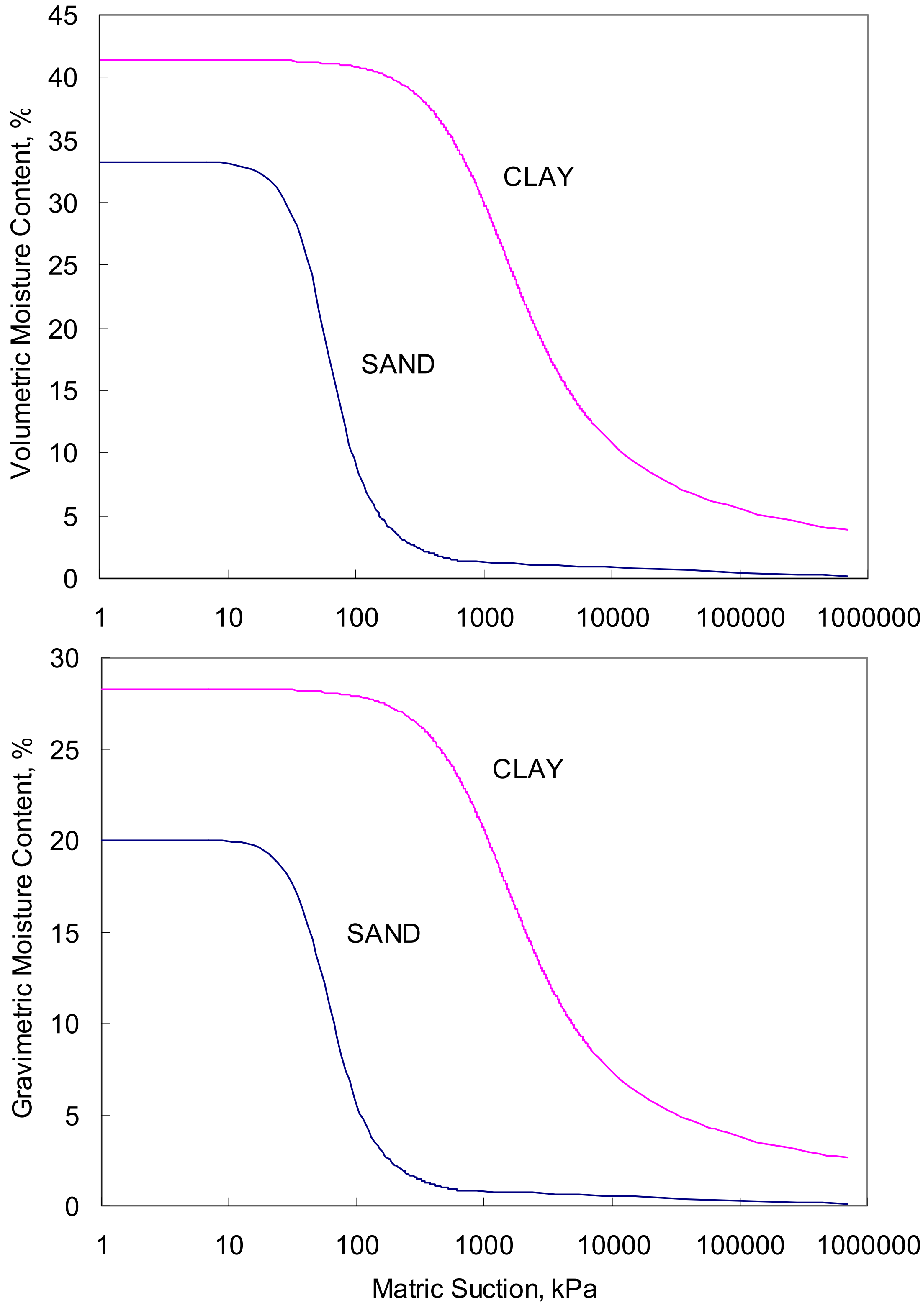

Figure 6.5 SWCC Model for Sand and Clay

6.5 Empirical Models for Shear Modulus and Damping Ratio

The saturated values of G for the tested silty sand can be modeled the equation first proposed by Hardin (1978):

$$\frac{G_0}{p_a} = S\left(\frac{p'}{p_a}\right)^n f(e) \tag{5.4}$$

where p_a is the atmospheric pressure, p' is the mean effective stress, and f(e) is a scaling function for void ratio-induced heterogeneity. The parameters S and n represent the stiffness of the material under the reference pressure and the sensitivity of the stiffness to the stress state, respectively (Hardin 1978). When f(e)=1 is assumed [the observed changes in void ratio of the tested soil are very limited (Vinale et al. 1999)], RC data yield S = 1298 and n = 0.57.

If the normalized shape of the G:suction relationship were unique, as resulting from the data of Cabarkapa et al. (1999), it would be possible to extend equation (5.4) to the unsaturated soil case by simply assuming S as suction dependent:

$$\frac{G_0}{p_a} = S(u_a - u_w)\left(\frac{p - u_a}{p_a}\right)^n f(e) \tag{5.5}$$

and f(e)=1. The above relationship does not agree with the experimental collected on silty sand. Therefore, an alternative formulation is proposed.

Thus, the models were created in this research by normalized the shear modulus (G) and damping ratio (D) with confining pressure (σ'_0) and plot the G/ σ'_0 with matric suction (ψ) at several confining pressure (σ'_0), and then produce the best fit model for those curves as shown in equations (5.6) for G and (5.7) for D:

$$\frac{G_0}{\sigma'_0} = f(\sigma'_0)\, g(\psi) \tag{5.6}$$

$$\frac{D}{\sigma'_0} = f(\sigma'_0)\, g(\psi) \tag{5.7}$$

6.5.1 Isotropic Stress State

Shear Modulus

As results from the data in figures 6.6 through 6.9, shown the variation of shear modulus (G) normalized by confining pressure (σ'_0) with matric suction (ψ) for sand and clay using resonant column (RC) and bender element (BE) testing devices individually, it can be created the prediction of shear modulus (G) with respect to confinement (σ'_0) and matric suction (ψ).

The prediction of G with respect to σ'_0 and ψ is presented in equation (5.7) and table 6.3 shows the constant parameters devised from the experimental data:

$$\frac{G}{\sigma_0} = A(\sigma_0)^B \left[\psi^{C\exp(D\sigma_0)}\right]\exp(E\psi) \tag{5.7}$$

where:

G = Shear modulus (kPa)

σ_0 = Confinement (kPa), $\sigma_0 \geq 1$ kPa

ψ = Matric suction (kPa)

A, B, C, D, and E = Constant as shown in table 6.3

Table 6.3 Constant Values for Prediction Model of Shear Modulus

Test	Soil Type	A	B	C	D	E	R^2
RC	Sand	18364	-0.6732	0	0	0.0034	0.98
RC	Clay	26.517	-0.2934	0.9243	-0.0057	0	0.99
BE	Sand	8000.7	-0.565	0.2311	-0.0017	0	0.94
BE	Clay	17382	-0.8516	0	0	0.0008	0.98

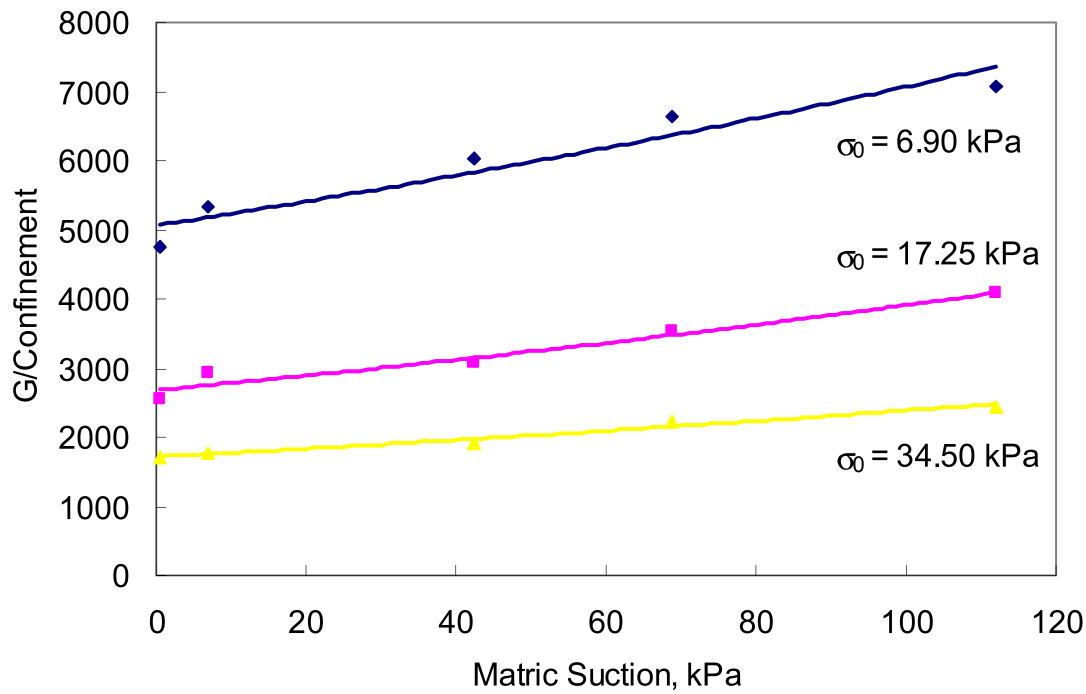

Figure 6.6 Normalized G by Confinement with Matric Suction for Sand (RC)

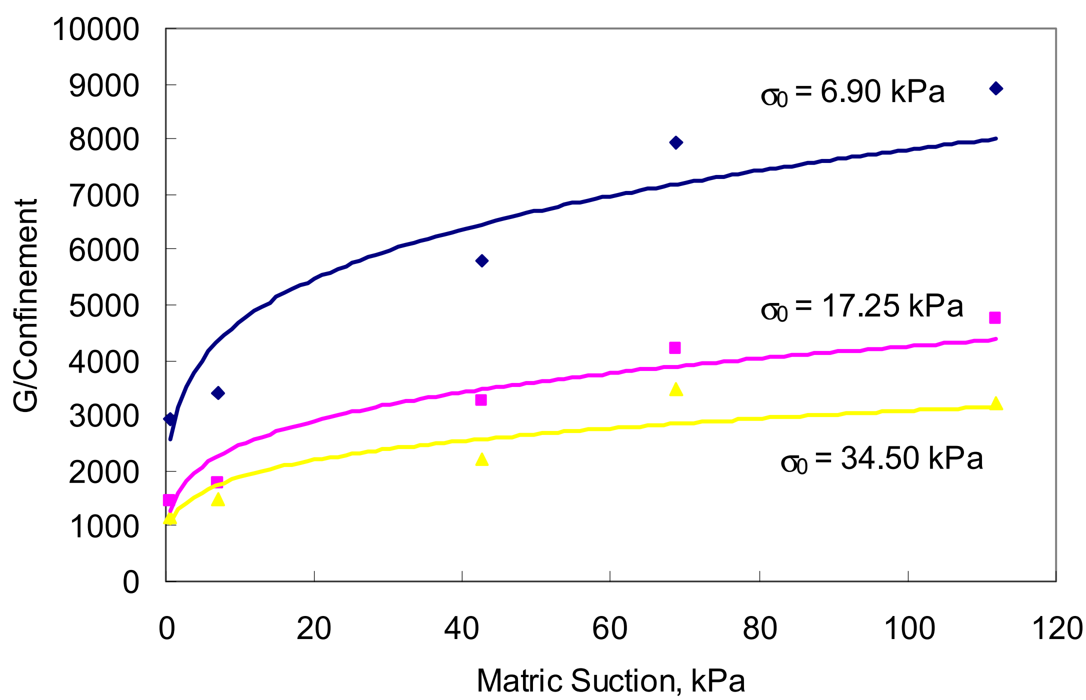

Figure 6.7 Normalized G by Confinement with Matric Suction for Sand (TX/BE)

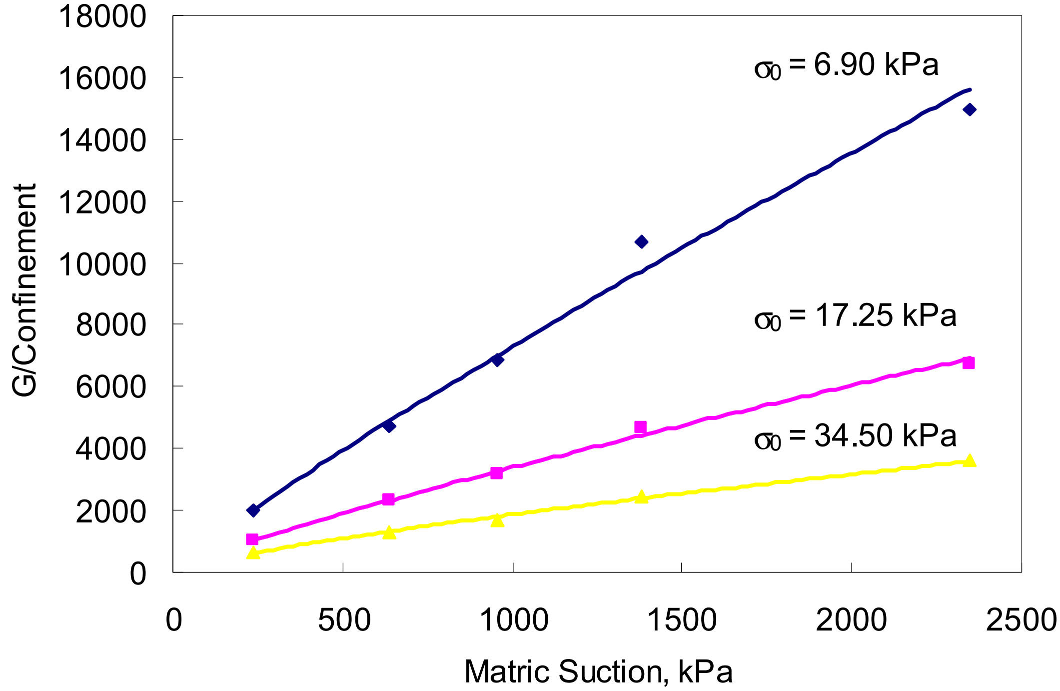

Figure 6.8 Normalized G by Confinement with Matric Suction for Clay (RC)

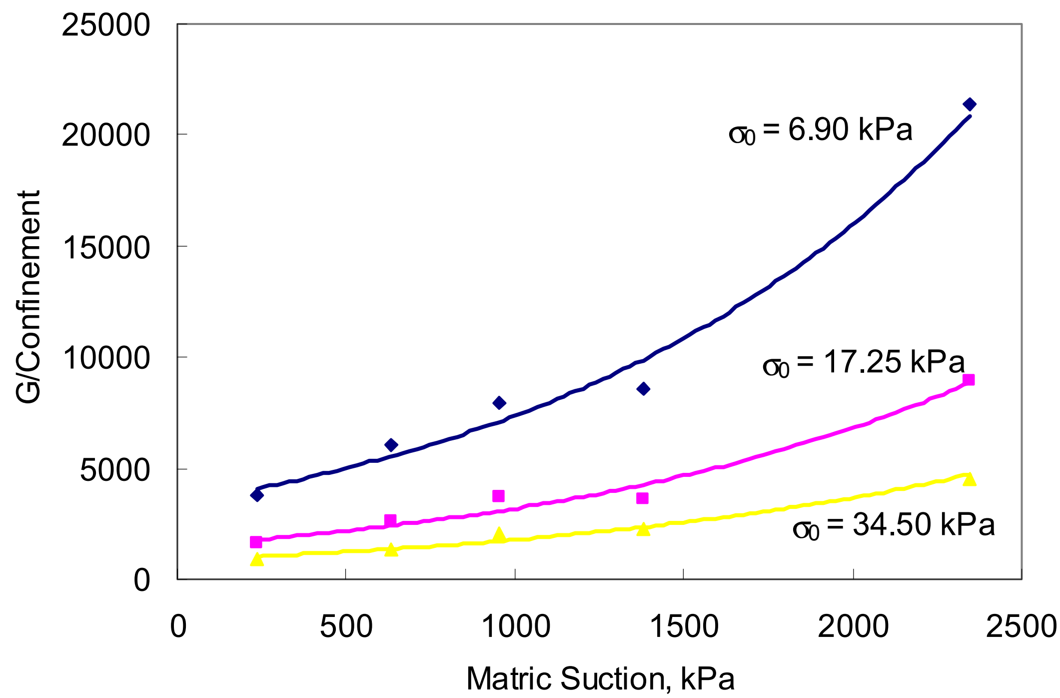

Figure 6.9 Normalized G by Confinement with Matric Suction for Clay (TX/BE)

Damping Ratio

As results from the data in figures 6.10 through 6.13, shown the variation of damping ratio (D) normalized by confining pressure (σ'_0) with matric suction (ψ) for sand and clay using resonant column (RC) and bender element (BE) testing devices individually, it can be created the prediction of damping ratio (D) with respect to confinement (σ'_0) and matric suction (ψ).

The prediction of damping ratio with respect to matric suction and confining pressure is presented in the following equation (5.8) and table 6.4 summarizes the best-fit constant parameters devised from the experimental data:

$$\frac{D}{\sigma_0} = P(\sigma_0)^Q \exp\left[R(\sigma_0)^T \psi\right] \tag{5.8}$$

where:

D = Damping ratio (%)

σ_0 = Confinement (kPa), $\sigma_0 \geq 1$ kPa

ψ = Matric suction (kPa)

P, Q, R, and T = Constant as shown in table 6.4

Table 6.4 Constant Values for Prediction Model of Damping Ratio

Test	Soil Type	P	Q	R	T	R^2
RC	Sand	5.4541	-0.9971	-0.0035	0.2563	0.95
RC	Clay	5.4237	-1.0697	0.0001	0	0.98
BE	Sand	9.9487	-1.035	-0.0059	0.0375	0.94
BE	Clay	15.507	-1.0231	-0.0002	0	0.98

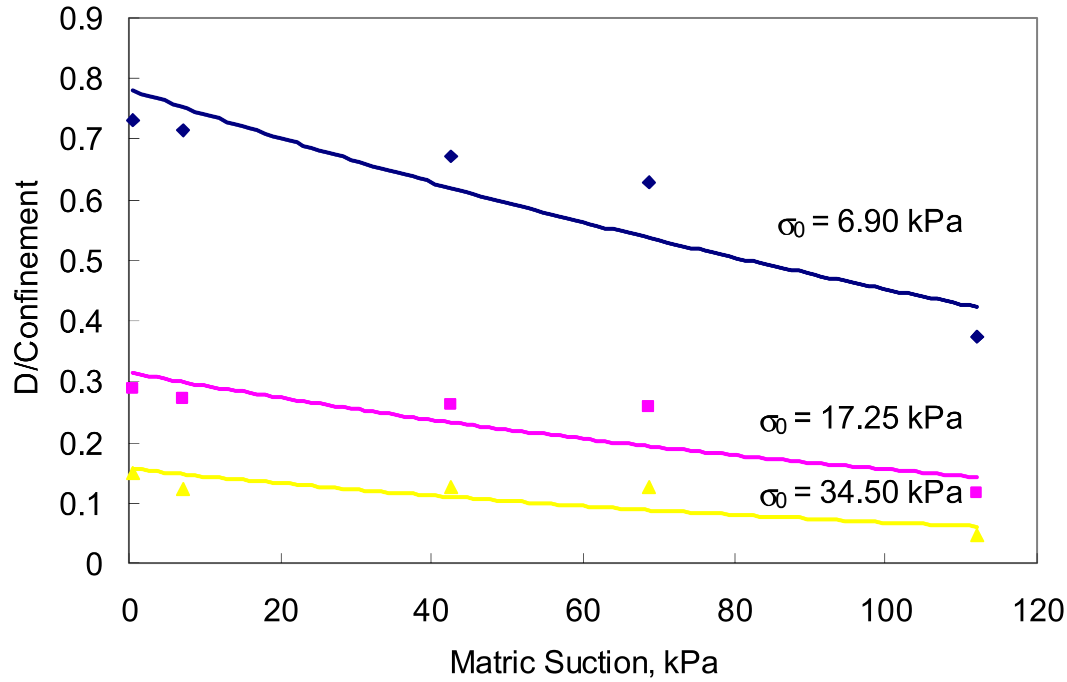

Figure 6.10 Normalized D by Confinement with Matric Suction for Sand (RC)

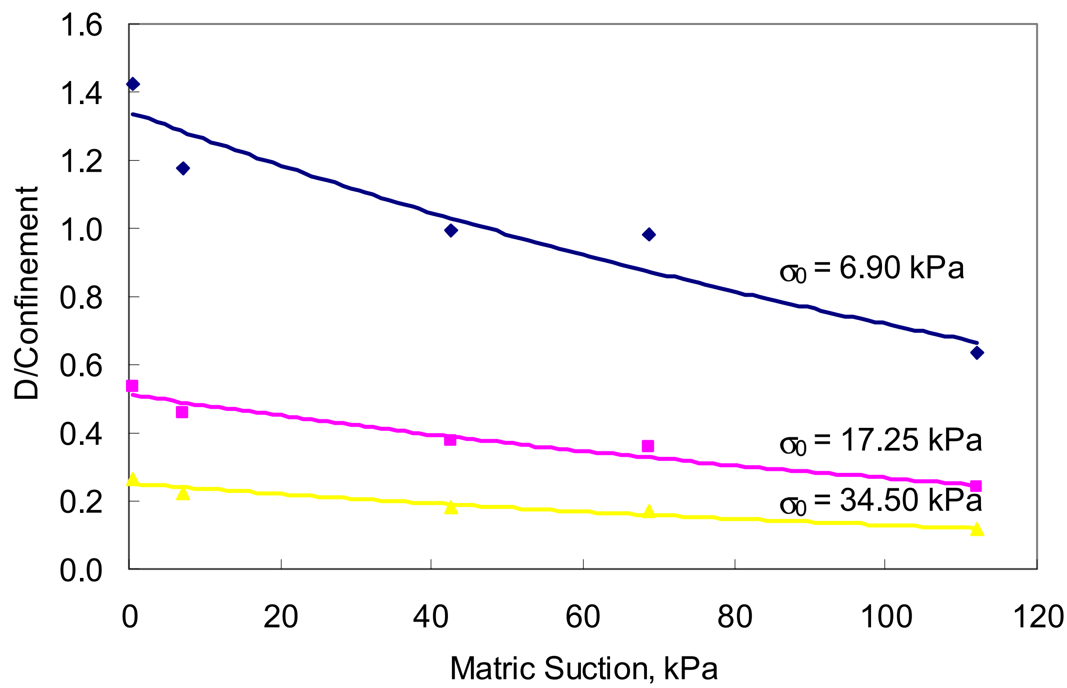

Figure 6.11 Normalized D by Confinement with Matric Suction for Sand (TX/BE)

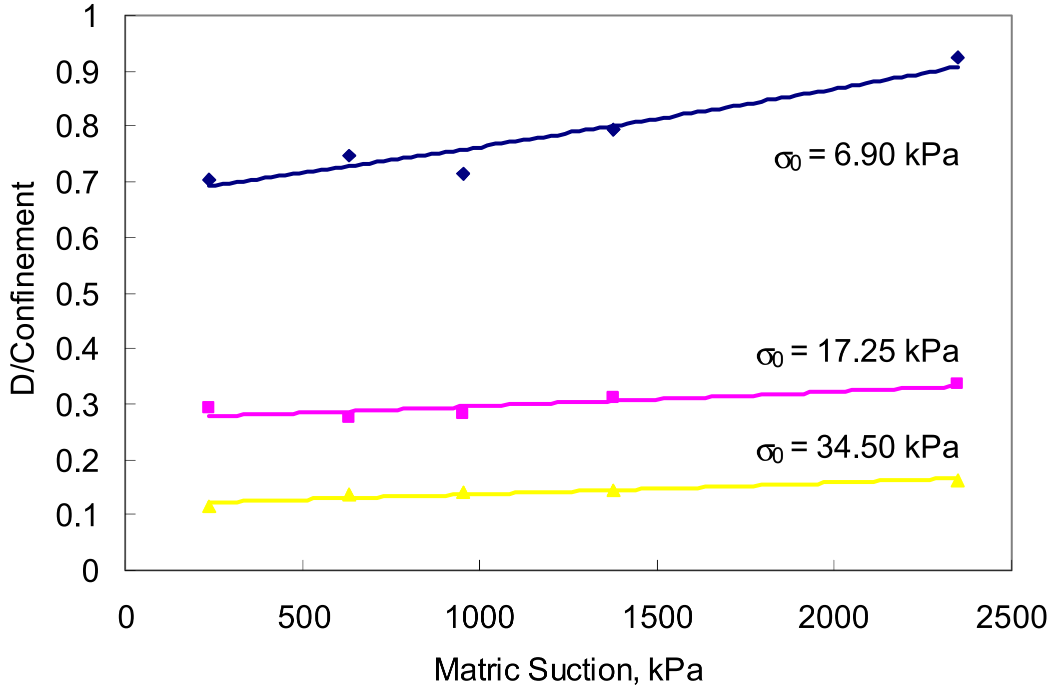

Figure 6.12 Normalized D by Confinement with Matric Suction for Clay (RC)

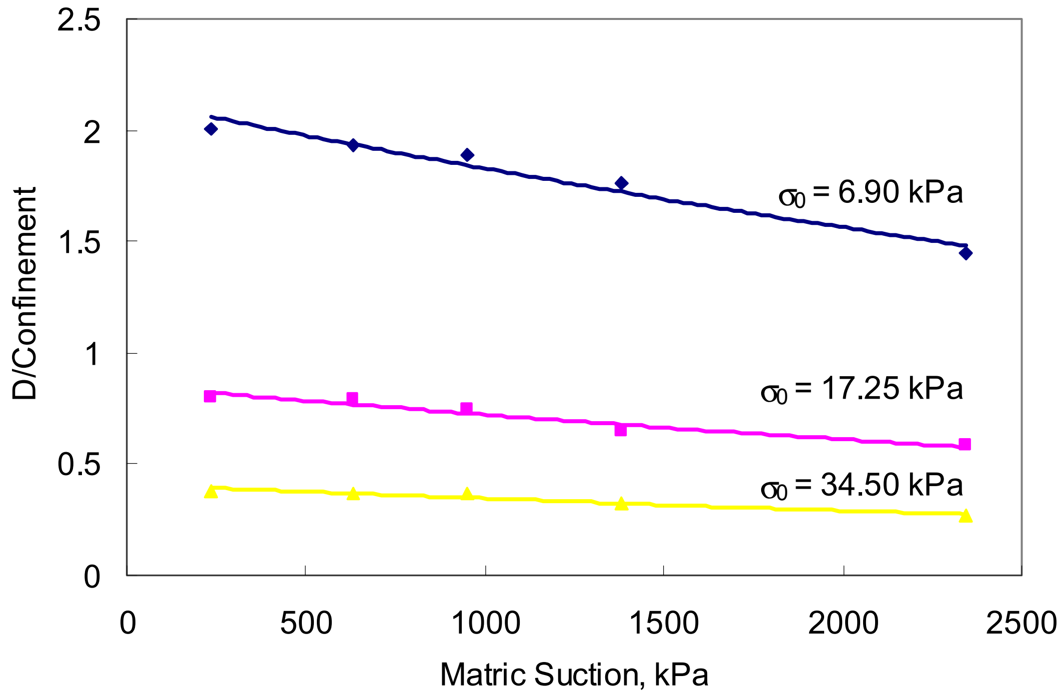

Figure 6.13 Normalized D by Confinement with Matric Suction for Clay (TX/BE)

6.5.2 Comparison of RC and BE Testing

This section is dedicated to present the bender element correction factor, $(CF)_{BE}$, for prediction model of shear modulus and damping ratio from bender element. The resonant column is well-known to determine the stiffness properties, shear modulus (G) and damping ratio (D), for a long period of time and the results from resonant column test are very consistent and reliable in geotechnical engineering, the prediction model of shear modulus and damping ratio from bender element needs to be corrected based on the results of prediction model from resonant column test.

Figures 6.14 and 6.15 show the comparison of the shear modulus and damping ratio results of prediction models from resonant column test and bender element test before making a correction. It can be noted that most of predicted shear modulus from bender element test are higher than that from resonant column test. Also, predicted damping ratio from bender element is more than that from resonant column.

As a result, the bender element correction factor, $(CF)_{BE}$, as shown in equations (5.10) and (5.12), is presented in order to interpret the result of prediction model of shear modulus and damping ratio from bender element test into the result of those from resonant column test.

Tables 6.5 and 6.6 show the constant values using in the bender element correction factor models and the r-square value of those models. It can be implied that these models are reliable because the r-square values of both sand and clay model is equal to 1. Precisely, the results from both methods are the same if r-square is equal to 1.

Figures 6.16 and 6.17 show the comparison of the shear modulus and damping ratio results of prediction models from resonant column test and bender element test before after making a correction by using equations (5.9) and (5.10)., as shown in the following paragraph:

Shear Modulus

$$G_{RC} = CF_{BE,G} \times G_{BE} \tag{5.9}$$

$$CF_{BE,G} = i(\sigma_0)^j \left[\psi^{l\exp(m\sigma_0)}\right]\exp(n\psi) \tag{5.10}$$

where:

$CF_{BE,G}$ = Bender element G correction factor

σ_0 = Confinement (kPa), $\sigma_0 \geq 1$ kPa

ψ = Matric suction (kPa)

i, j, l, m, and n = Constant as shown in table 6.5

Table 6.5 Constant Values of BE Correction Factor for Shear Modulus

Soil Type	i	j	l	m	n	R^2
Sand	2.2953	-0.1082	-0.2311	-0.0017	0.0034	1
Clay	1.5255E-3	0.5582	0.9243	-0.0057	-0.0008	1

Damping Ratio

$$D_{RC} = CF_{BE,D} \times D_{BE} \tag{5.11}$$

$$CF_{BE,D} = t(\sigma_0)^u \exp\left[v\psi(w\sigma_0{}^x + y\sigma_0{}^z)\right] \tag{5.12}$$

where:

$CF_{BE,D}$ = Bender element D correction factor

σ_0 = Confinement (kPa), $\sigma_0 \geq 1$ kPa

ψ = Matric suction (kPa)

t, u, v, w, x, y, and z = Constant as shown in table 6.6

Table 6.6 Constant Values of BE Correction Factor for Damping Ratio

Soil Type	t	u	v	w	x	y	z	R^2
Sand	0.5482	0.0379	1	-0.0035	0.2563	0.0059	0.0375	1
Clay	0.3498	-0.0466	0.0003	0.5	0	0.5	0	1

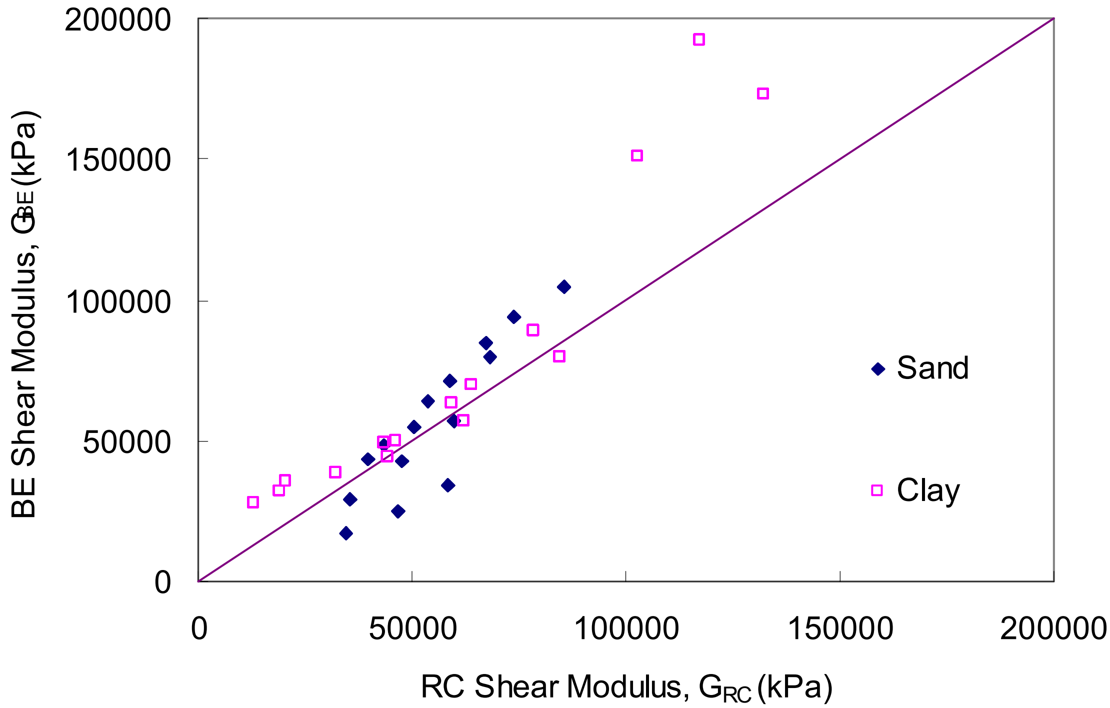

Figure 6.14 The Variation of G_{RC} and G_{BE} for Sand and Clay

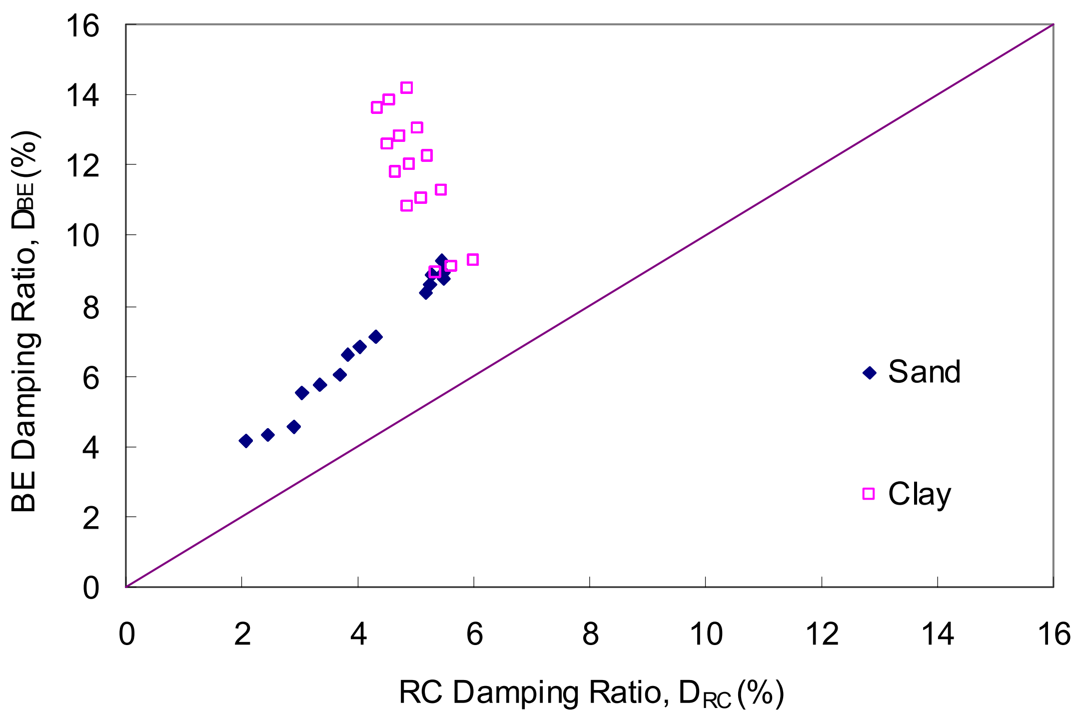

Figure 6.15 The Variation of D_{RC} and D_{BE} for Sand and Clay

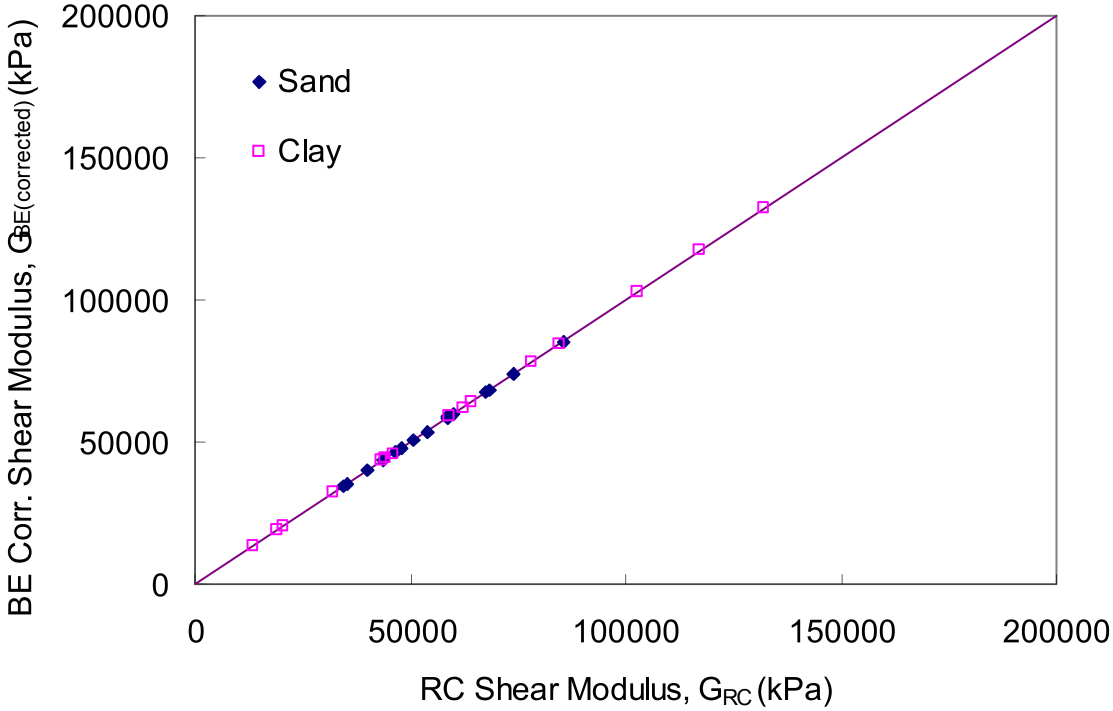

Figure 6.16 The Variation of G_{RC} and $G_{BE\ Corected}$ for Sand and Clay

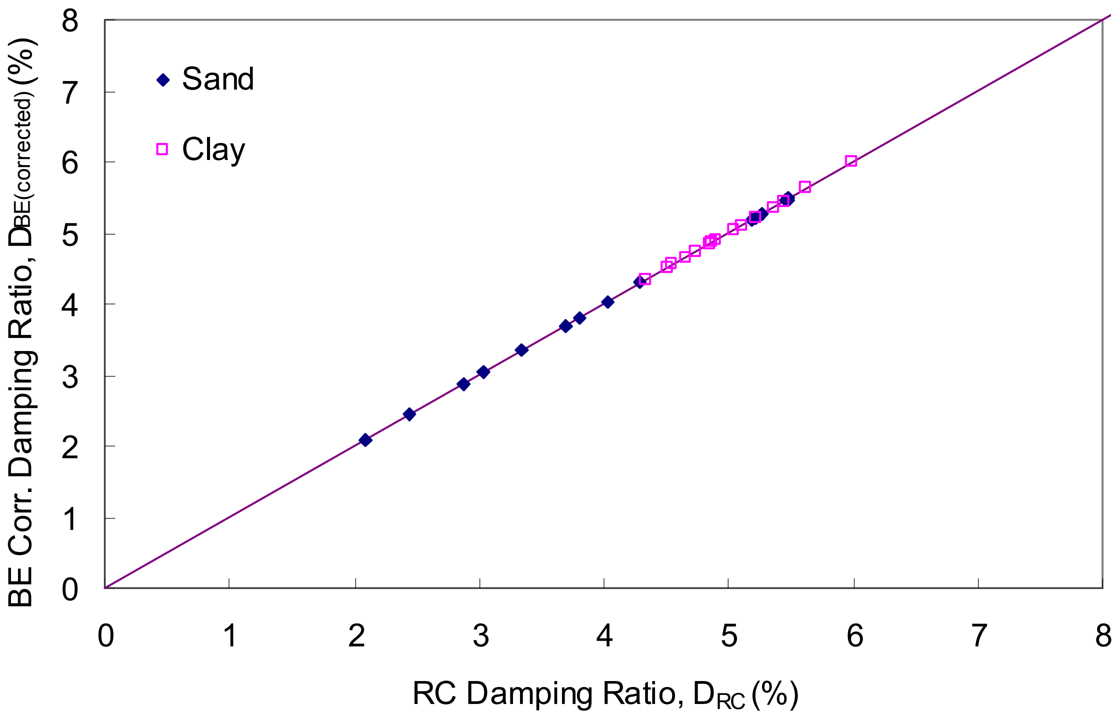

Figure 6.17 The Variation of D_{RC} and $D_{BE\ Corected}$ for Sand and Clay

6.5.3 K_0 Stress State Condition

Shear Modulus

As results from the data in figures 6.18 and 6.19, shown the variation of shear modulus (G) with K_0 stress state at different matric suction (ψ) for sand and clay using bender element (BE) testing devices in triaxial cell individually, it can be created the prediction of shear modulus (G) with respect to K_0 stress state and matric suction (ψ).

The prediction of shear modulus with respect to matric suction and K_0 stress state is presented in the following equation (5.13) and table 6.7 summarizes the best-fit constant parameters devised from the experimental data:

$$G = \left[I \ln(\psi) + J\right] \exp\left[(L\psi + M)K_0\right] \tag{5.13}$$

Where:

G = Shear modulus (MPa)

K_0 = K_0 stress state value

ψ = Matric suction (kPa)

I, J, L and M = Constant as shown in table 6.7

Table 6.7 Constant Values for Prediction Model of Shear Modulus under K_0 Stress State

Test	Soil Type	I	J	L	M	R^2
BE	Sand	2.6844	24.26	0.0009	0.4896	0.98
BE	Clay	40.323	-197.88	0.0001	0.1876	0.96

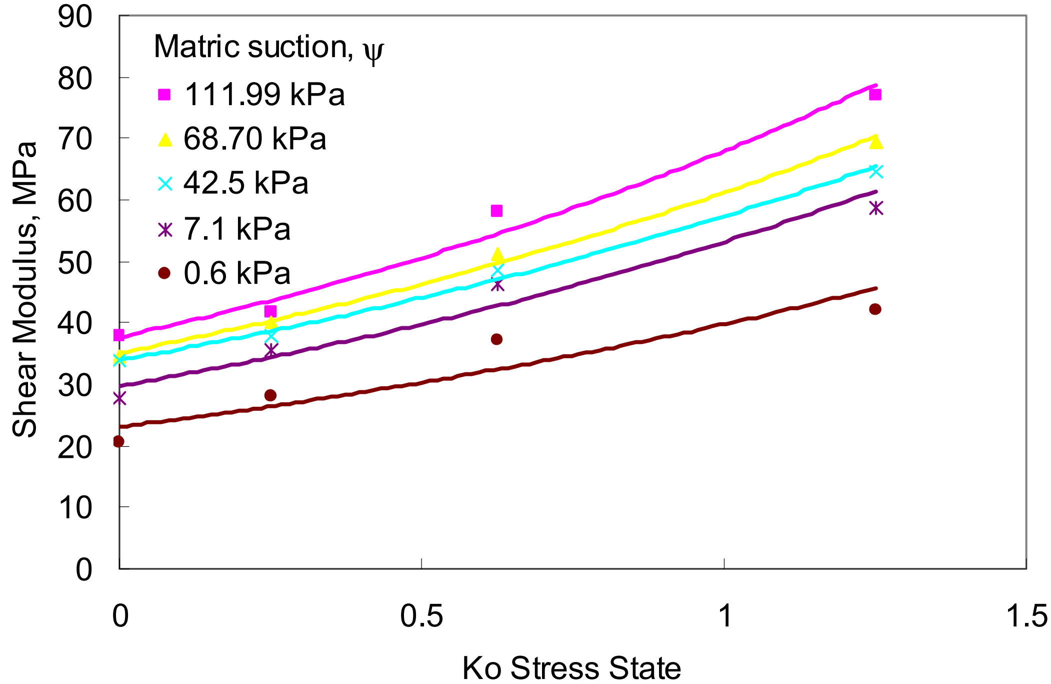

Figure 6.18 Variation of Shear Modulus with K_0 Stress State for Sand (TX/BE)

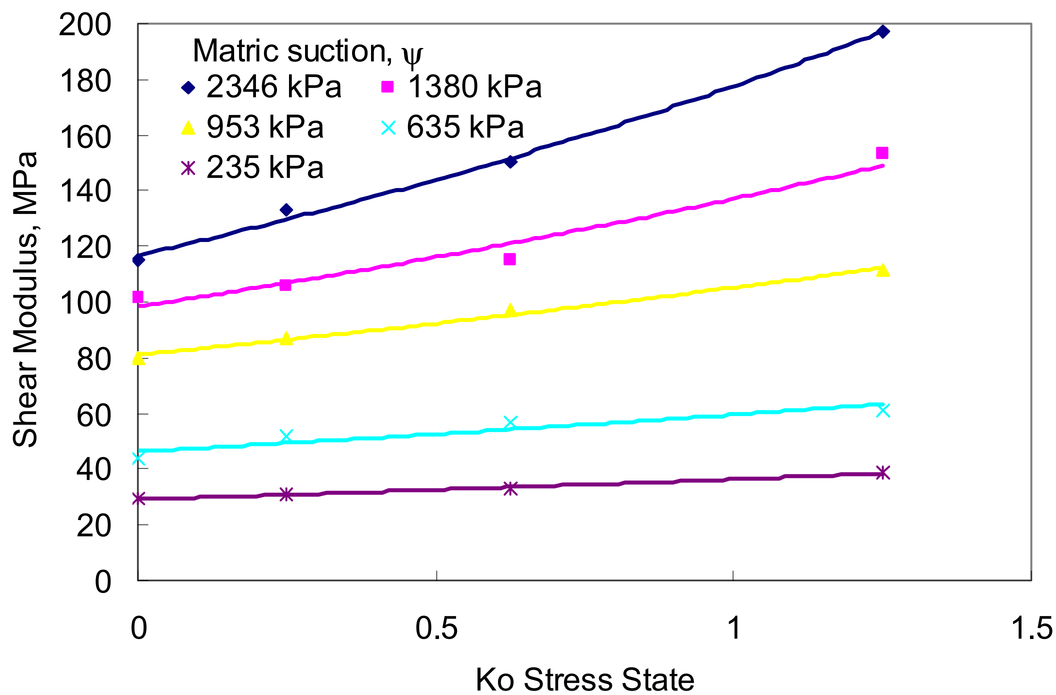

Figure 6.19 Variation of Shear Modulus with K_0 Stress State for Clay (TX/BE)

Damping Ratio

As results from the data in figures 6.120 and 6.21, shown the variation of damping ratio (D) with K_0 stress state at different matric suction (ψ) for sand and clay using bender element (BE) testing devices in triaxial cell individually, it can be created the prediction of damping ratio (D) with respect to K_0 stress state and matric suction (ψ).

The prediction of damping ratio with respect to matric suction and K_0 stress state is presented in the following equation (5.14) and table 6.8 summarizes the best-fit constant parameters devised from the experimental data:

$$D = W \exp(X\psi) \exp[(Y\psi + Z)K_0] \qquad (5.14)$$

where:

D = Damping ratio (%)

K_0 = K_0 stress state value

ψ = Matric suction (kPa)

W, X, Y, and Z = Constant as shown in table 6.8

Table 6.8 Constant Values for Prediction Model of Damping Ratio under K_0 Stress State

Test	Soil Type	W	X	Y	Z	R^2
BE	Sand	9.4498	-0.0061	0.00004	0.0835	0.77
BE	Clay	14.859	-0.0001	0.00005	-0.0138	0.80

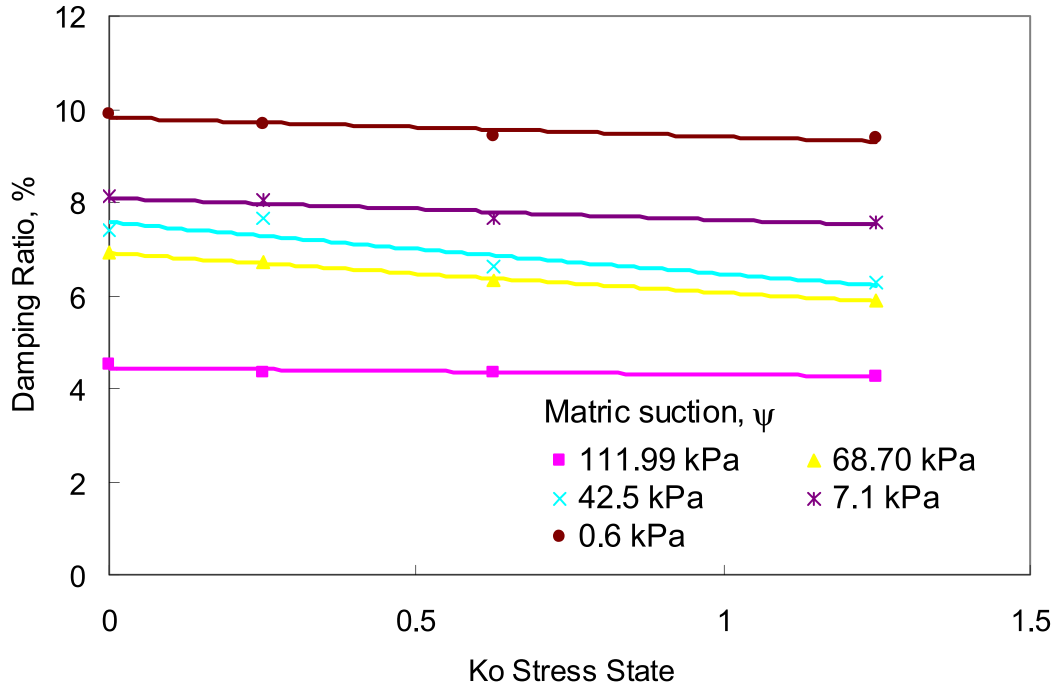

Figure 6.20 Variation of Damping Ratio with K_0 Stress State for Sand (TX/BE)

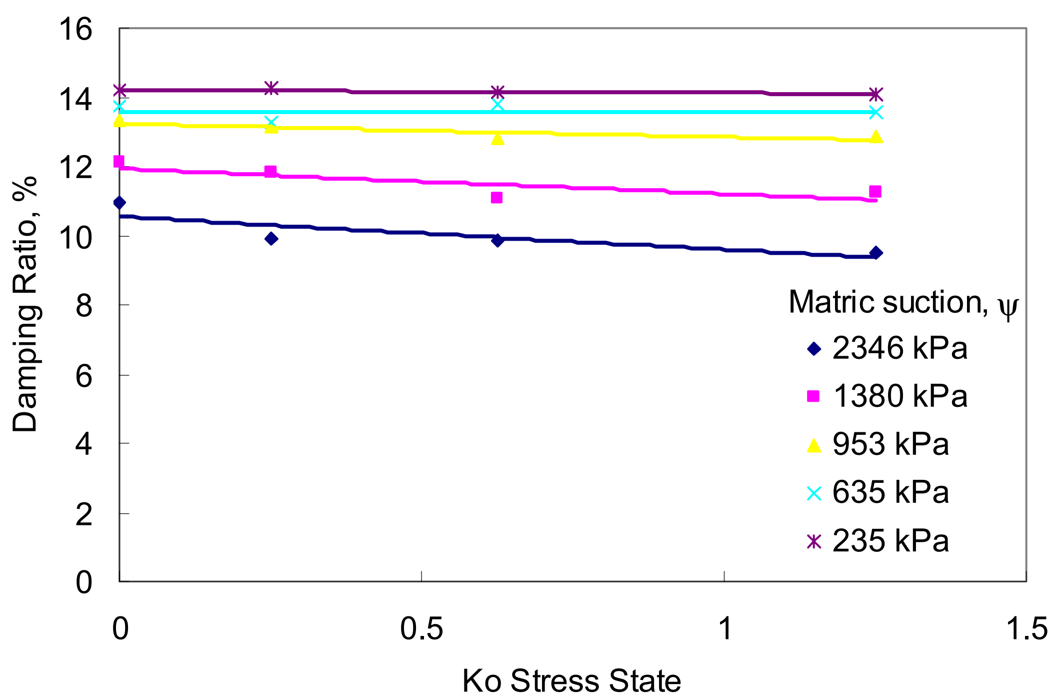

Figure 6.21 Variation of Damping Ratio with K_0 Stress State for Clay (TX/BE)

6.5.4 Correction Factor for Any K_0

From the previous prediction model of shear modulus (G) and damping ratio (D) with respect to confining pressure (σ_0) and matric suction (ψ), it can be noticed that shear modulus and damping ratio were determined only under the isotropic condition. After considering the factor of K_0 stress state, the prediction model of shear modulus (equation 5.7) and damping ratio (equation 5.8) needs to be corrected by the correction factor for any K_0 stress state as shown in the following paragraph.

As results from the data in figures 6.22 and 6.25, shown the variation of shear modulus (G) and damping ratio (D) with K_0 stress state at different matric suction (ψ) for sand and clay using bender element (BE) testing devices in triaxial cell, it can be created the correction factor for any K_0 stress state in order to correct the prediction model for shear modulus (G) and damping ratio (D) with respect to confining pressure (σ_0) and matric suction (ψ) from equations (5.16) and (5.19), respectively.

The correction factors for any given K_0 stress state to be applied to the empirically predicted values of shear modulus and damping ratio with respect to confinement and matric suction are presented in the following equations (5.17) and (5.20), and tables 6.9 through 6.12 summarize the best-fit constant parameters devised from the experimental data:

Shear Modulus

$$G_{K_0} = CF_{G,K_0} \times G_{K_0=1} \tag{5.15}$$

$$G_{K_0=1} = A(\sigma_0)^{1-B}\left[\psi^{C\exp(D\sigma_0)}\right]\exp(E\psi) \tag{5.16}$$

where:

G = Shear modulus (kPa)

σ_0 = Confinement (kPa), $\sigma_0 \geq 1$ kPa

ψ = Matric suction (kPa)

A, B, C, D, and E = Constant as shown in table 6.9

Table 6.9 Constant Values of Prediction Model for Shear Modulus (K_0=1)

Test	Soil Type	A	B	C	D	E	R^2
BE	Sand	8000.7	0.565	0.2311	-0.0017	0	0.94
BE	Clay	17382	0.8516	0	0	0.0008	0.98

$$CF_{G,K_0} = \left[(a\psi + b)K_0\right] + \left[c\exp(d\psi)\right] \tag{5.17}$$

where:

$CF_{G, Ko}$ = Correction Factor

K_0 = K_0 stress state value

ψ = Matric suction (kPa)

a, b, c and d = Constant as shown in table 6.10

Table 6.10 Constant Values of Correction Factor for Shear Modulus

Test	Soil Type	a	b	c	d	R^2
BE	Sand	0.0005	0.4097	0.5990	-0.0009	0.99
BE	Clay	0.00008	0.1785	0.8275	-0.0001	0.99

Damping Ratio

$$D_{K_0} = CF_{D,K_0} \times D_{K_0=1} \tag{5.18}$$

$$D_{K_0=1} = P(\sigma_0)^{1-Q} \exp\left[R(\sigma_0)^T \psi\right] \tag{5.19}$$

where:

D = Damping ratio (%), ψ = Matric suction (kPa)

σ_0 = Confinement (kPa), $\sigma_0 \geq 1$ kPa

P, Q, R, and T = Constant as shown in table 6.11

Table 6.11 Constant Values of Prediction Model for Damping Ratio (K_0=1)

Test	Soil Type	P	Q	R	T	R^2
BE	Sand	9.9487	1.035	-0.0059	0.0375	0.94
BE	Clay	15.507	1.0231	-0.0002	0	0.98

$$CF_{D,K_0} = \left[(p\psi + q)K_0\right] + \left[r\exp(t\psi)\right] \tag{5.20}$$

Where:

$CF_{D,\,Ko}$ = Correction Factor

K_0 = K_0 stress state value, ψ = Matric suction (kPa)

p, q, r and t = Constant as shown in table 6.12

Table 6.12 Constant Values of Correction Factor for Damping Ratio

Test	Soil Type	p	q	r	t	R^2
BE	Sand	0.00004	0.0810	0.9193	-0.00004	0.99
BE	Clay	0.00005	-0.0128	1.0142	-0.00005	0.99

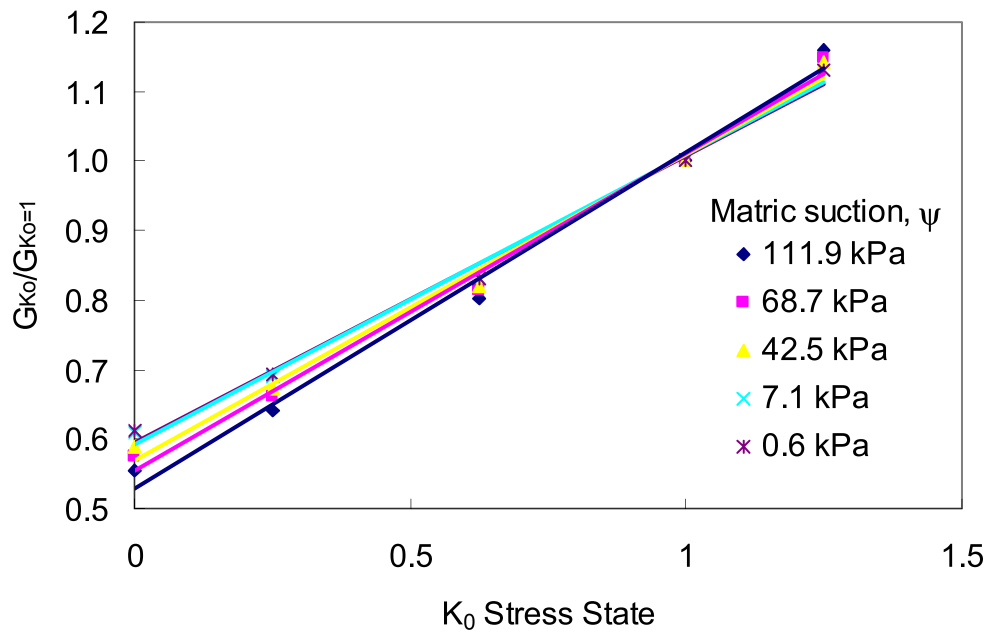

Figure 6.22 Variation of $G_{Ko}/G_{Ko=1}$ with K_0 Stress State for Sand (TX/BE)

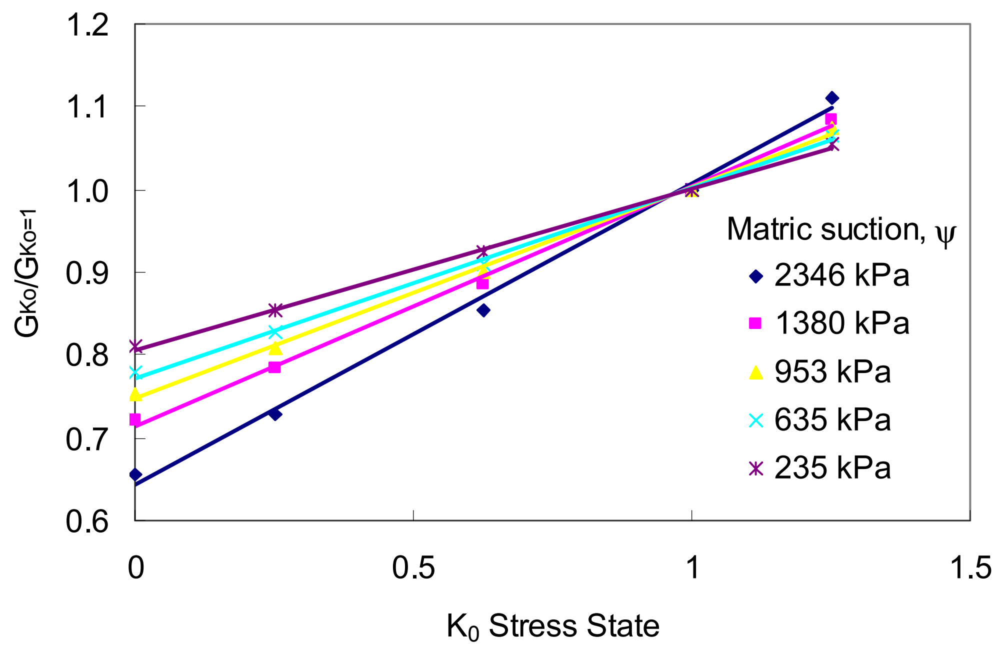

Figure 6.23 Variation of $G_{Ko}/G_{Ko=1}$ with K_0 Stress State for Clay (TX/BE)

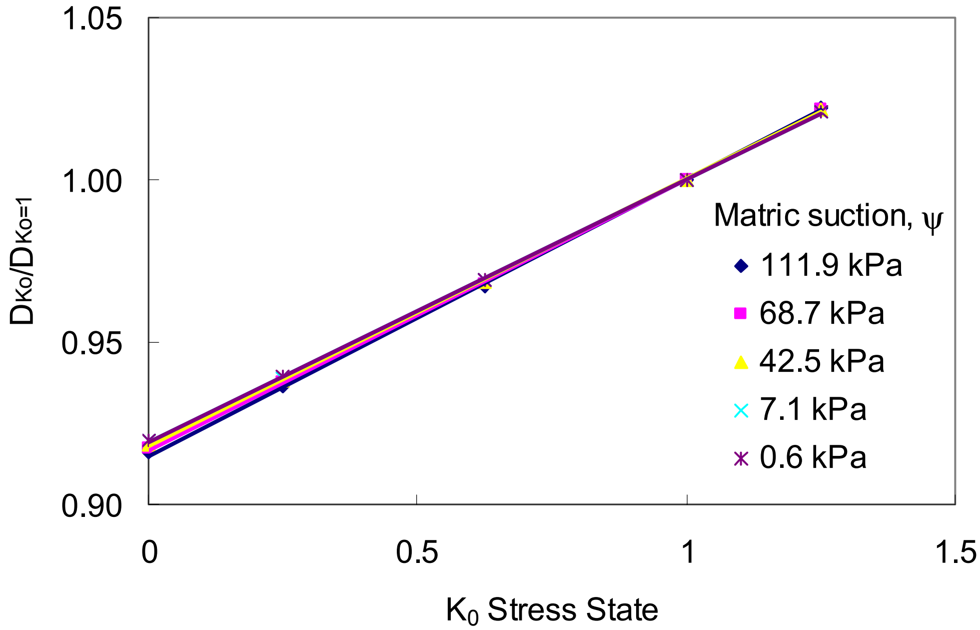

Figure 6.24 Variation of $D_{Ko}/D_{Ko=1}$ with K_0 Stress State for Sand (TX/BE)

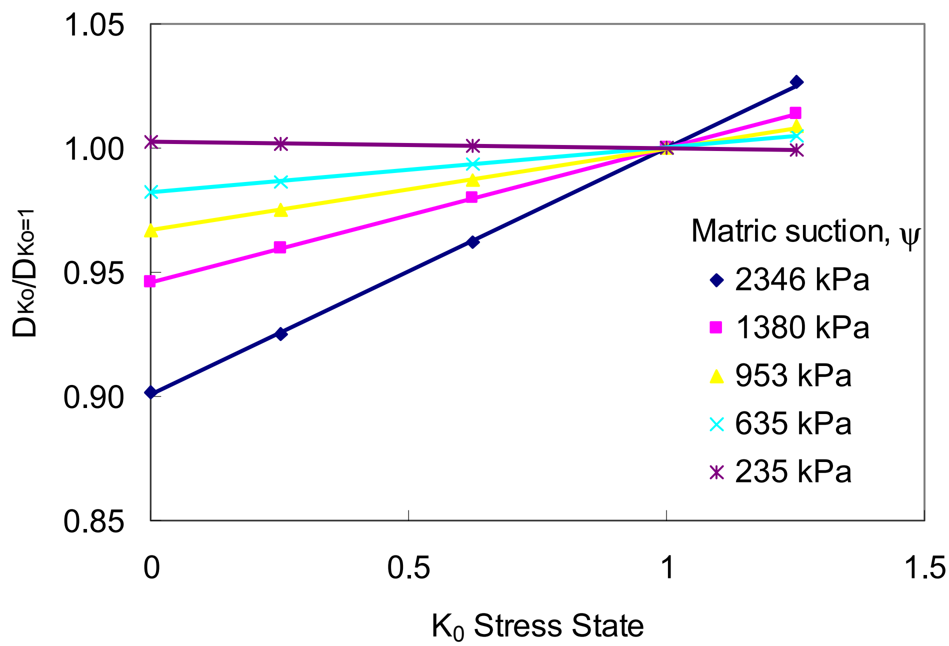

Figure 6.25 Variation of $D_{Ko}/D_{Ko=1}$ with K_0 Stress State for Clay (TX/BE)

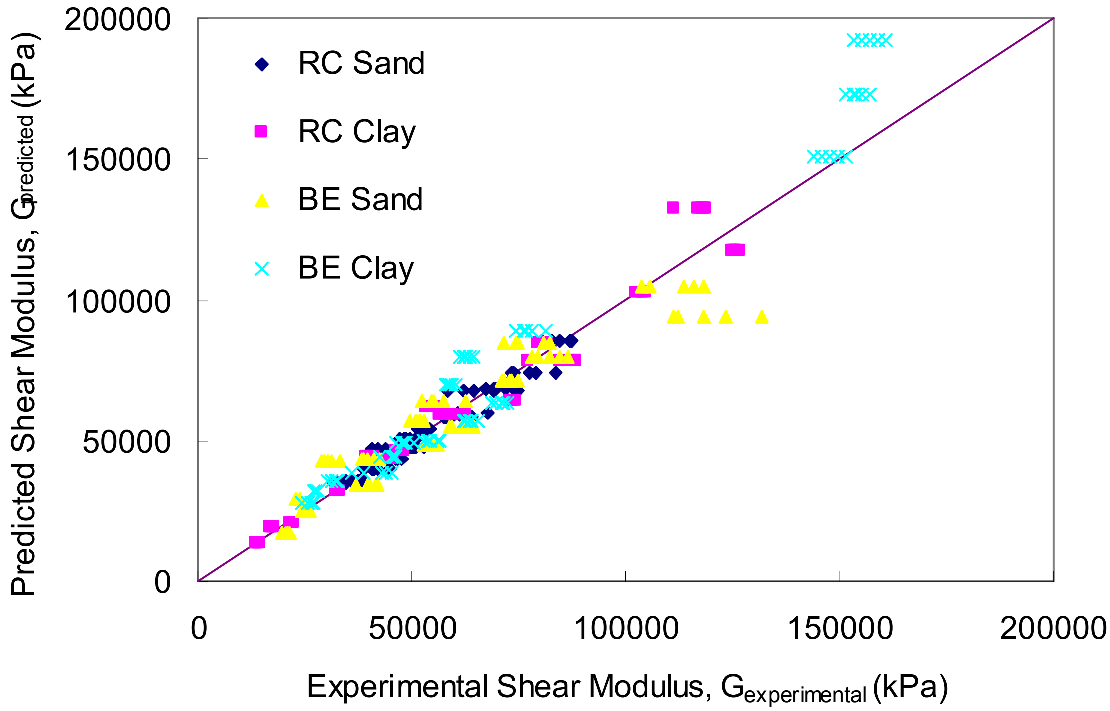

Figure 6.26 Comparisons between Shear Modulus from Experiment and Model

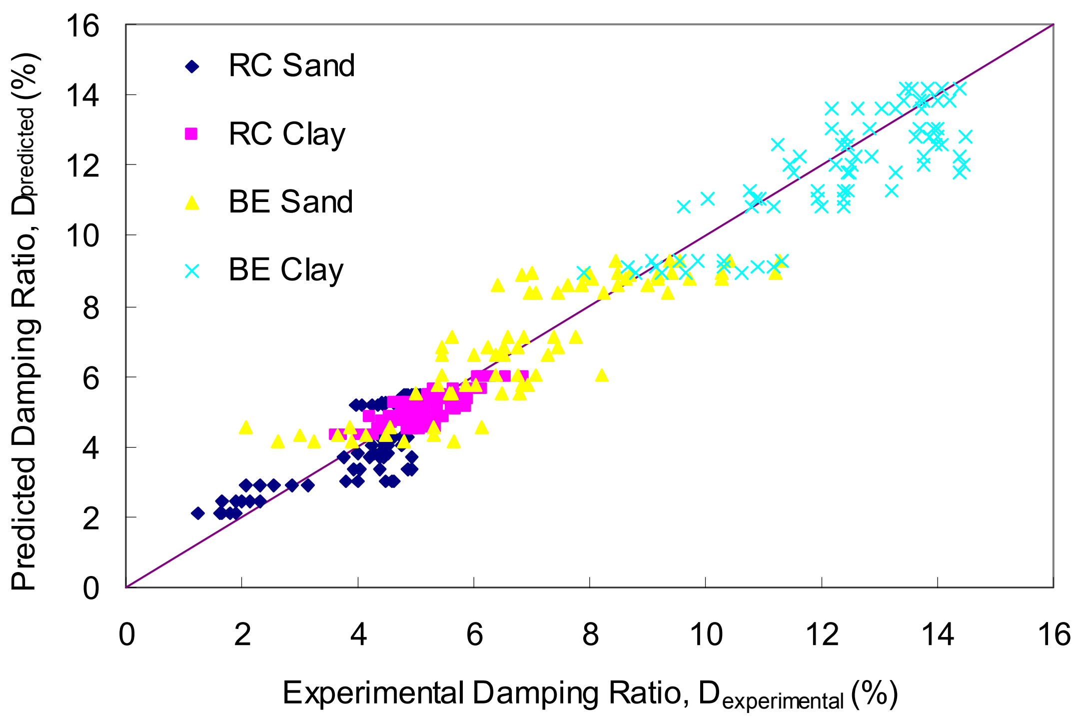

Figure 6.27 Comparisons between Damping Ratio from Experiment and Model

Figures 6.26 and 6.27 show the variation of predicted shear modulus (G) and damping ratio (D) with the results of shear modulus (G) and damping ratio (D) from experiment under isotropic confining pressure ($\sigma_1 = \sigma_3$). It can be observed that the predicted shear modulus is similar to the shear modulus from experiment, both resonant column and bender element techniques. Also, the prediction models of damping ratio for sand and clay from both RC and BE tests are reliable.

6.6 Summary

This chapter presented the SWCC models including the soil water characteristic parameters from Fredlund and Xing (1994) model and prediction models of shear modulus (G) and damping ratio (D) with respect to isotropic confining pressure (σ_0), matric suction (ψ), and K_0 stress state as well as all correction factors from resonant column and bender element testing techniques for sand and clay followed in this work and a briefly comprehensive analysis of model results. Chapter 7 compiles the main conclusions of this research effort, including some recommendations for future research work related to the topic investigated.

CHAPTER 7

SUMMARY, CONCLUSIONS, AND RECOMMENDATIONS

7.1 Summary

A series of Resonant Column Tests (ASTM D2325-68), Bender Element Tests (ASTM C 778), Pressure Plate Tests (ASTM D 4015-92), and Filter Paper Tests (ASTM D 5298) were conducted on several identically prepared specimens of poorly graded sand and high plasticity clay.

Soil specimens were prepared using different of moisture content and tested in the series of RC and BE tests at different confinements (0, 1, 2.5, and 5 psi or 0, 6.9, 17.25, and 34.5 kPa) to get the shear modulus (G_{max}) and damping ratio (D_{min}). Also, the new apparatus of PP tests with confining pressure were produced to perform the soil water characteristic curve (SWCC) at different net confinement in several stress states: (1) fixed-boundary condition, (2) constant K_o stress state condition, and (3) variable K_o stress state condition.

With the series of RC, BE, and PP tests, an attempt was made to assess the influence on stiffness properties of partially saturated soils, dynamic shear modulus (G_{max}), material damping ratio (D_{min}), and soil water characteristic curve (SWCC).

Findings from this research effort guide the relationship of shear modulus, damping ratio, and soil suction of sand and clay. Furthermore, it was created a new model of variation of shear modulus and damping ration with respected to soil suction (ψ), confinement (σ_0), and K_0 stress state including the correction factors of shear modulus and damping ratio for any K_0 stress state and the correction factors to interpret the results from bender element test to resonant column test.

7.2 Main Conclusions

The following paragraphs summarize the main concluding remarks from this research work.

Equipment performance and SWCC Testing

1. The series of RC, TX/BE, RC/BE and PPE tests conducted on compacted specimens of poorly graded sand (SP) and high plasticity clay (CH) yielded typical, repeatable values and behavioral trends reported in the literature on small-strain shear modulus (G_{max}), material damping (D_{min}), and soil-water characteristic curves (SWCC) for this type of materials, hence validating the feasibility of the RC, TX/BE, RC/BE and PPE testing setups at the Geotechnical Laboratories of The University of Texas at Arlington.

2. Net radial confinement (N.R.C.) was found to exert a paramount influence on the shape and position of the SWCC for poorly graded sand (SP) and high plasticity clay (CH) under controlled net radial confinement condition, despite the fact that all specimens featured similar moisture content and density prior to SWCC testing. This can be attributed to a sharp decrease in the average pore size (void ratio) of the soil mass as the N.R.C. is increased.

3. On the contrary, the initial (constant) K_0 stress state was found to exert no significant influence on the SWCC response of SP and CH soils under controlled K_0 stress state condition. In the present work, the selected range of the experimental variables was intended to reproduce in-situ stress states within a pavement or shallow foundation system (less than 5-psi confinement). Therefore, it is expected that higher levels of stress (more than 10-psi confinement) will have a considerable effect on the SWCC response of SP and CH soils. However, higher stress levels fall out of the scope of the originally intended work.

4. Likewise, the suction-dependent (variable) K_0 stress state was found to exert no significant influence on the SWCC response of SP and CH soils under controlled K_0 stress state condition. This can be explained by the possible fact that the average pore size (void ratio) of the soil mass, for the range of stress levels applied, did not experience major variations during SWCC testing.

5. Fredlund and Xing model was successfully applied to the SWCCs of poorly graded sand (SP) and high plasticity clay (CH). Best-fit curves from Fredlund and Xing model closely matched the experimental SWCC data with R-square values greater than 0.97.

Small-Strain Stiffness Properties

6. As it is generally expected, the small-strain shear modulus (G_{max}) of both poorly graded sand (SP) and high plasticity clay (CH), from the series of RC, TX/BE, and RC/BE tests devices, tend to increase with an increase in compaction-induced matric suction (ψ), isotropic confining pressure (σ_0) and/or K_0 stress state, with the sharpest increases observed in SP soils. This is obviously attributed to an increase in soil stiffness (increased rigidity of soil skeleton) due to an increase of either matric suction or confining pressure.

7. On the contrary, the small-strain damping ratio (D_{min}) of both poorly graded sand (SP) and high plasticity clay (CH), from the series of RC, TX/BE, and RC/BE tests devices, tend to decrease with an increase in compaction-induced matric suction (ψ), isotropic confining pressure (σ_0) and/or K_0 stress state, with the sharpest increases observed in SP soils. This also can be explained by an increase in soil stiffness (increased rigidity of soil skeleton) upon an increase in either matric suction or confining pressure.

8. Empirical models for the prediction of small-strain stiffness properties of SP and CH soils, with respect to compaction-induced matric suction (ψ), isotropic confining pressure (σ_0), and K_0 stress states, were devised with coefficients of determination greater than 0.95.

9. Values of small-strain shear modulus (G_{max}) obtained from RC and TX/BE tests conducted on identically prepared specimens of poorly graded sand (SP) were found to be similar. However, there is a significant difference in the G_{max} values obtained from both techniques when the gravimetric moisture content is close to zero (fully-dry conditions or extremely high matric suction ψ). The series of RC/BE tests corroborated this behavioral trend.

10. Values of small-strain shear modulus (G_{max}) obtained from TX/BE tests conducted on identically prepared specimens of high plasticity clay (CH) were always overestimated as compared to those from RC tests, with sharper differences at higher values of compaction-induced matric suction (ψ).

11. Similarly, values of small-strain material damping (D_{min}) obtained from TX/BE tests conducted on identically prepared specimens of high plasticity clay (CH) were always overestimated as compared to those from RC tests, with sharper differences at higher values of compaction-induced matric suction (ψ).

12. The correction factor models of predicted small-strain properties from TX/BE with respect to compaction-induced matric suction (ψ), isotropic confining pressure (σ_0), and K_0 stress states, were devised with coefficients of determination greater than 0.93.

Suction Loss and Menisci Regeneration Patterns

13. Axial strain levels (0, 2, and 4 % vertical strain levels) were found to exert a significant influence on small-strain shear modulus (G_{max}) response of poorly

graded sand (SP). An increase in the axial strain level resulted in an immediate increase in the G_{max} values obtained from bender element (TX/BE) tests, which can be considered as further evidence of the sharp increase in soil stiffness under higher K_o stress states. Sharpest increases are observed in those specimens compacted at higher compaction-induced matric suctions (ψ). However, under a constant level of axial deformation, the soil continues to loose stiffness within the first 24 hours of application of the corresponding vertical load, as evidenced by the steady decrease in G_{max} values from TX/BE tests conducted at different time intervals under a constant load. This can be attributed to the time-dependent effects of shearing on the initial compaction-induced water menisci within the compacted sandy specimen.

14. Axial strain levels (0, 2, and 4 % vertical strain levels) were also found to exert a significant influence on small-strain shear modulus (G_{max}) response of high plasticity clay (CH). However, contrary to the behavior of sandy soil, an increase in the axial strain level resulted in a sharp decrease in the G_{max} values obtained from bender element (TX/BE) tests. Under a constant level of axial deformation, the soil continues to loose stiffness within the first 24 hours of application of the corresponding vertical load, as evidenced by the steady decrease in G_{max} values from TX/BE tests conducted at different time intervals under a constant load. Both phenomena can be attributed to the more pronounced effect of shearing on strength-strain-stiffness response of clayey soils, which are not highly susceptible to changes in confinement.

15. Of particular interest is the G_{max} response of high plasticity clay (CH) within the first 24 hours after application of the 2.5-psi confinement, that is, under zero vertical strain ($\varepsilon_v = 0$). It appears that suction equalization (menisci formation) continues to take place immediately after compaction and even beyond the time of

application of the initial 2.5-psi confinement, as evidenced by the steady increase in G_{max} values from TX/BE tests conducted within the first 24 hours.

7.3 Recommendations for Future Work

Additional research efforts are recommended to further our understanding of the small-strain stiffness response of partially saturated soils considering higher stress levels and season dependent processes, such as wet-dry and freeze-thaw cycles. These recommendations are summarized as follows:

1. The use of more moisture content ranges and type of soil, so that the effects on stiffness properties can be used to predict the more behavior of the treated soils and the more accuracy and further correlate constant values of models with soil properties such as LL, PL, and γ_d, etc.

2. Further RC, TX/BE, and PPE testing for regression-based analysis of all experimental data, including analytical relationships between soil stiffness properties, moisture content, matric suction, and confining pressure at high level such as 10 and 20 psi pressures.

3. More study the influences of soil suction under strain-induced behavior on stiffness properties of partially unsaturated soil.

4. Axis translation suction control needs to be applied in the RC, TX/BE testing devices in order to precisely control the soil suction during determination of small-strain stiffness properties using RC and TX/BE testing techniques.

5. Modified pressure plate extractor needs to be adapted in order to study further on investigation and comparison the SWCC from both wetting and drying methods.

6. Study the influences of moisture content and matric suction in field and simulate to laboratory.

REFERENCES

1. AASHTO (1993). "Guide for design of pavement structures," American Association of State Highway and Transportation Officials, Washington, DC.
2. Abbiss, C. P. (1981). "Shear wave measurements of the elasticity of the ground." Geotechnique, 31(1), 91-104.
3. Agus, S. S., Leong, E. C., and Schanz, T., (2003). "Assessment of statistical models for indirect determination of permeability functions from soil-water characteristic curves." Geotechnique, Vol. 53, No. 2, 279-282.
4. Alonso, E.E., A. Gens & Josa (1990). "A constitutive model for partially saturated soils." Geotechnique 40(3), 405-430.
5. Arroyo, M., Muir Wood, D. & Greening, P. D. (2003). "Source near-field effects and pulse tests in soil samples." Geotechnique 53, No. 3, 337–345.
6. Assimaki, D, Kausel, E (2000). "Model for dynamic shear modulus and damping for granular soils" Journal of Geotechnical and Geoenvironmental Engineering, ASCE 126(10), 859-869.
7. ASTM (1993) "Test methods for modulus and damping of soils by the resonant column method," Standard D 4015-92, ASTM, Philadelphia, PA, pp. 581-593.
8. ASTM. (1994). "Standard test method for capillary-moisture relationships for fine-textured soils by pressure –membrane apparatus." Designation: D 3152-72, West Conshohocken, Pa.

9. ASTM D 854 (1994). “Standard test method of specific gravity of soils.” Annual Book of ASTM Standards, Vol. 04.08, ASTM International, West Conshohocken, PA.
10. Baxter, C. D. P. (1999). “Experimental study on the aging of sands.” Ph.D. Dissertation, Virginia Tech.
11. Bishop, A. W. & G.E. Blight (1963). “Some aspects of effective stress in saturated and partially saturated soils.” Geotechnique 13(3), 177-197.
12. Brignoli, E. G. M., Gotti, M., and Stokoe, K. H. II. (1996). “Measurement of shear waves in laboratory specimens by means of piezoelectric transducers.” Geotech. Test. J., 19(4), 384-397.
13. Brocanelli, D. & Rinaldi, V. (1998). “Measurement of low-strain material damping and wave velocity with bender elements in the frequency domain.” Canadian Geotechnical Journal, 35, 1032-1040.
14. Brooks, R. H., and Corey, A. T. (1964). “Hydraulic properties of porous media.” Hydro. Paper No. 3, Civ. Engrg. Dept., Colorado State University, Fort Collins, Colo.
15. Cabarkapa, Z., T. Cuccovillo & M Gunn (1999). “Some aspects of the pre-failure behaviour of unsaturated soil.” II International Conference on pre-failure behaviour of geomaterials, Turin 1, 159-165.
16. Craig A. Burger and Charles D. Shackelford (2001). “Soil-water characteristic curves and dual porosity of sand-diatomaceous earth mixtures”, J. Geotech. And Geoenvir. Engrg., ASCE, 129(9), 790-800.
17. Dano, C., Hareb, H., and Hicher, P. (2003). “Characterization of loire river sand in the small strain domain using new bender elements.” 16th ASCE Engrg. Mech. Conf., The University of Washington, Seattle.

18. Dyvik, R. & Madshus, Ch. (1985). "Lab measurements of G_{max} using bender elements." Advances in the Art of Testing Soils under Cyclic Conditions; Proc. ASCE, Detroit, 24 October 1985: 186-196. New York: ASCE.
19. Fredlund, D. G. & N. R. Morgernstern (1977). "Shear state variables for unsaturated soils." Journal of Geotechnical Engineering Division, ASCE 103(5), 447-466.
20. Fredlund, D. G. and Rahardjo, H. (1993). "Soil mechanics for unsaturated soils," John Wiley and Sons, Inc., New York.
21. Fredlund, D. G., and Xing, A. (1994). "Equation for the soil-water characteristic curve." Can. Geotech. J., 31(4), 521-532.
22. Fredlund, D. G., Xing, A., Huang, S., (1994). "Predicting the permeability functions for unsaturated soils using the soil-water characteristic curve." Can. Geotech. J. 31, 533-546.
23. Fredlund, M. D., Wilson, G. W., and Fredlund, D. G., (1997). "Prediction of the soil-water characteristic curve from the grain-size distribution curve." Proceedings of the 3rd Symposium on Unsaturated Soil, Rio de Janeiro, Brazil, 13-23.
24. Fredlund D. G. (1998). "Bringing unsaturated soil mechanics into engineering practice." II International Conference on Unsaturated Soils, UNSAT '98, Beijing 2, 1-36.
25. Fredlund, M. D., Fredlund, D. G., and Wilson, G. W. (2000). "An equation to represent grain-size distribution." Can. Geotech. J., 37(4), 817-827.
26. Gens, A., E.E. Alonso, J. Suriol & A. Lloret (1995). "Effect of structure on the volumetric behaviour of a compacted soil." I International Conference on unsaturated soils, UNSAT '95, Paris 2, 83-88.

27. Hardin, B. O., and Drnevich, V. P. (1972a). “Shear modulus and damping in soils: Measurement and parameter effects.” J. Soil Mech. and Found. Div., ASCE, 98(6), 603-624.
28. Hardin, B. O., and Drnevich, V. P. (1972b). “Shear modulus and damping in soils: Design equations and curves.” J. Soil Mech. and Found. Div., ASCE, 98(7), 667-692.
29. Hardin, B. O. (1978). “The nature of stress-strain behaviour for soils.” State of the Art, Geotechnical Engineering Division. Specialty Conference on Earthquake Engineering and Soil Dynamics, ASCE, Pasadena, California.
30. Hoyos, L. R. (1993). “Dynamic properties of puertorican residual soils using The resonant column device,” M.S. Thesis, The University. of Puerto Rico, Mayaguez, P.R., pp. 85-87.
31. Hoyos, L. R., Takkabutr, P., Puppala, A. J., (2005). “A pressure plate extractor device for assessment of SWCC under net radial confinement.” Proceeding of International Conference on Problematic Soils, Eastern Mediterranean University, Famagusta, N. Cyprus.
32. Huoo-ni, S. (1987). “Dynamic properties of sand under true triaxial stress states from resonant-column/torsional-shear tests,” PhD dissertation, The University of Texas, Austin, TX.
33. Isenhower, W. M. (1979). “Torsional simple Shear/resonant column properties of San Francisco bay mud,” Thesis GT80-1, Geotech. Engrg. Ctr., The University of Texas, Austin, TX.
34. Jovicic, M., Coop, R., and Simic, M. (1996), “Objective criteria for determining G_{max} from bender element tests,” Geotechnique, Vol. 46, No. 2, pp. 357-362.

35. Jovicic, V., and Coop, M. R. (1998), “The measurement of stiffness of clays with bender element tests in the triaxial apparatus,” Geotech. Testing J., 21(1), 3-10.
36. Kawaguchi, T., Mitachi, T., and Shibuya, S. (2001). “Evaluation of shear wave travel time in laboratory bender element test.” Proc., 15th Int. Conf. on Soil Mechanics and Geotechnics Engineering 155-158.
37. Kramer, Steven L. (1996), “Geotechnical earthquake engineering,” Prentice Hall, First Edition.
38. Kuwano, R., Connolly, T.M. and Kuwano, J. (1999), “Shear stiffness anisotropy measured by multi-directional bender element transducers.” Proceedings of the International Symposium on Pre-failure deformation characteristics of geomaterials, Torino, Balkema, 205-212.
39. Laird, J. P., and Stokoe, K. H. (1993). “Dynamic properties of remolded and undisturbed soil samples tested at high confining pressures.” Geotech. Engrg. Rep. GR93-6, Electrical Power Research Institute, Palo Alto, Calif.
40. Leong, E. C., and Rahardjo, H. (1997). “Review of soil-water characteristic curve equations.” J. Geotech. And Geoenvir. Engrg., ASCE, 123(12), 1106-1117.
41. Mancuso, C., Simonelli, A. L., and Vinale, F. (1998), “Numerical analysis of in situ S-wave measurements,” proceedings, Twelfth International Conference on Soil Mechanics and Foundation Engineering, Rio de Janeiro, Vol. 3, pp 277-280.
42. Miller, C. J., N. Yesiller, K. Yalso, and S. Merayyan (2002). “Impact of soil type and compaction conditions on soil water characteristic.” J. Geotech. and Geoenvir. Engrg, 128(9), 733-742.
43. Mitchell, J. K. (1993). “Fundamental of soil behavior,” John Wiley & Sons, New York.

44. Nelson, D. J. and Miller, J. D. (1992). “Expansive soils: problems and practice in foundation and pavement engineering,” John Wiley & Sons.
45. Ng, C., Pang, Y. (2000). “Experimental investigations of the soil-water characteristics of a volcanic soil.” Can. Geotech. J., 37, 1252-1264.
46. Pham, H. Q., Fredlund, D. G., and Barbour, S. L., (2003). “A practical hysteresis model for the soil-water characteristic curve for soils with negligible volume change.” Geotechnique, Vol. 53, No. 2, 293-298.
47. Pyl, L, Degrade, G (2000). “Measurement of material damping with bender elements in triaxial cell” Department of Civil Engineering, Structural Mechanics Division, K.U.Leuven, Belgium.
48. Richart, F. E., Hall, J. R. Jr., and Woods, R. D. (1970). “Vibration of soils and foundations,” Prentice-Hall, Inc., Englewood Cliffs, NJ.
49. Richart, F. E. (1975). “Some effects of dynamic soil properties on soil-structure interaction,” J. Geotech. Engrg. Div., ASCE, 101(12), pp. 1193-1240.
50. Rifat Bulut, Robert L. Lytton, and Warren K. Wray. “Soil suction measurement by filter paper.” ASCE.
51. Santamarina, J. C., and Fam, M. A. (1997). “Interpretation of bender element tests-discussion.” Geotechnique, 47(4), 873–875.
52. Schmertmann, J.H. (1992), “The mechanical aging of soils,” The Twenty-Fifth Karl Terzaghi Lecture, U.S./Brazil Geotechnical Engineering Workshop, Belo Horizonte, Brazil, pp. 1288-1330.
53. Shirley, D.J. & Hampton, L.D. (1978), “Shear-wave measurements in laboratory sediments”, Journal of Acoustics Soc. Am., 63(2), 607-613.
54. Sreedeep, S. and Singh, D. N., (2003). “Laboratory measurement of soil suction.” Indian Geotechnical Journal, Vol. 33, No. 3, 279-290.

55. Stoicescu, J. T., Haug, M. D., and Fredlund, D. G. (1998). “The soil-water characteristics of sand-bentonite mixtures used for liners and covers.” Proc., 2^{nd} Int. Conf. on Unsaturated Soils, International Academic Publishers, Beijing, Vol. 1, 143-148.
56. Stokoe, K. H. II, Anderson, A. M., Hoar, R. J., and Isenhower, W. M. (1978). “In-situ and laboratory shear velocity and modulus,” Proceedings from Earthquake Engineering and Soil Dynamics Conference, ASCE, III, The University of Texas, Austin, TX, pp. 1498-1502.
57. Stoke, K. H. and Huoo-Ni, S. (1985). “Effects of stress state and strain amplitude on shear modulus of dry sand,” Proceedings of the Second Symposium on the Interaction of Non-Nuclear Munitions with Structures, Panama City, FL, pp. 407-412.
58. Takkabutr, P. (2002). “Effects of cyclic drying and wetting on strength and stiffness properties of chemically stabilized sulfate-rich expansive clay.” M.S. Thesis, The University of Texas at Arlington, Arlington, Texas.
59. Thomann, J. G. and Hryciw, R. D., 1990, “Laboratory measurement of small strain shear modulus under K_0 conditions,” ASTM Geotechnical Testing Journal, Vol. 13, No. 2, pp. 97-105.
60. Tinjum, J. M., Benson, C. H., and Blotz, L. R. (1997). “Soil-water characteristic curves for compacted clays.” J. Geotech. Geoenvir. Engrg., 123(11), 1060-1069.
61. van Genuchten, M. T. (1980). “Closed-form equation for predicting hydraulic conductivity of unsaturated soils.” Soil Sci. Am. J., 44(5), 892-898.
62. van Genuchten, M. T., Leij, F. J., and Yates, S. R. (1991). “RETC code for quantifying hydraulic functions of soils.” EPA Rep. 600/2-91/065, U.S. Salinity Lab., Agr. Res. Service, U.S. Department of Agriculture, Riverside, Calif.

63. Vanapalli, S. K., D. G. Fredlund & D. E. Pufahl (1996). “The relationship between the soil-water characteristic curve and the unsaturated shear strength of a compacted glacial till.” Geotechnical Testing Journal 19(3), 259-268.
64. Vanapalli, S. K., Fredlund, D. G., Pufahl, D. E., Clifton, A. W., (1996). “Model for the prediction of shear strength with respect to soil suction. Can. Geotech. J. 33, 379-392.
65. Vanapalli, S. K., Pufahl, D. E., Fredlund, D. G., (1998). “The effect of stress on the soil-water characteristic behaviour of a compacted sandy-clay till. 51st Canadian Geotechnical Conference, Edmonton, 81-86.
66. Vanapalli, S., Fredlund, D., Pufahl, D. (1999). “The influence of soil structure and stress history on the soil-water characteristics of a compacted till. Geotechnique, 49(2), 143-159.
67. Viggiani, G., and Atkinson, J. H. (1995a). “Interpretation of bender element tests.” Geotechnique, 45(1), 149-154.
68. Vinale, F., A. d’Onofrio, C. Mancuso, F. Santucci De Magistris & F. Tatsuoka (1999). “The prefailure behaviour of soils as construction materials.” II International Conference on pre-failure behaviour of geomaterials, Turin.
69. Wang, X., Benson, C. H. (2004). “Leak-free pressure plate extractor for measuring the soil water characteristic curve.” Geotechnical Testing Journal, ASTM, 27(2), 163-172.
70. Wu, S., D. H. Gary & F. E. Richart (1985). “Capillary effects on dynamic modulus of sands and silts.” Journal of Geotechnical Engineering Division, ASCE 110(9), 1188-1203.

BIOGRAPHICAL INFORMATION

Phayak Takkabutr was born on September 28, 1977 at the City of Bangkok, Thailand. He received his bachelor degree in Civil Engineering from Kasetsart University, Thailand in March 1999. After graduating, he worked as a civil engineer at Thaiwat Engineering & Construction Co., Ltd, Thailand. Then, he received his master degree in Civil Engineering (Geotechnical Engineering) from The University of Texas at Arlington, Arlington, Texas USA in August 2002. With the great motivation and enthusiasm for developing higher-level skills and knowledge in the area of civil engineering, he decided to pursue Ph.D. graduate studies majoring in geotechnical engineering at The University of Texas at Arlington. In August 2002, he was admitted to the Department of Civil Engineering at The University of Texas at Arlington as a doctoral candidate. During his studies, he had the opportunity to work as a graduate research assistant under the supervision of Dr. Laureano Hoyos. Mr. Phayak Takkabutr has successfully completed all requirements for the Degree of Doctor of Philosophy in Civil Engineering and received the degree on August 12, 2006.